Surface Dimer Engineering and Properties of GaAs(N)(Bi) Alloys

by

Jordan M. Occena

A dissertation submitted in partial fulfillment
of the requirements for the degree of
Doctor of Philosophy
(Materials Science and Engineering)
in the University of Michigan
2018

Doctoral Committee:

Professor Rachel S. Goldman, Chair
Professor Cagliyan Kurdak
Dr. Andrew G. Norman, National Renewable Energy Laboratory
Associate Professor Pierre Ferdinand P. Poudeu

Jordan M. Occena

joccena@umich.edu

ORCID iD: 0000-0002-1160-2985

© Jordan M. Occena 2018

Acknowledgements

I would like to thank my advisor, Rachel Goldman, for her support throughout my studies at the University of Michigan, as well as Cagliyan Kurdak, Ferdinand Poudeu, and Andrew Norman for their time and guidance as members of my dissertation committee.

This dissertation would not have been possible without the support of my fellow group members, past and present. Thank you especially to Richard Field III, Simon Huang, Sunyeol Jeon, Tim Jen, Davide Del Gaudio, Christian Greenhill, Hongling Lu, Mingfei Zhang, Emily Rizzi, Jack Hu, and Andra Chen.

I gratefully acknowledge support from the National Science Foundation (Grant Nos. DMR 1006835, DMR 1410282, and DMR 1810280) the U. S. Department of Energy Office of Science Graduate Student Research (SCGSR) Program, and the University of Michigan Rackham Merit Fellowship Program.

Table of Contents

Acknowledgements .... **ii**

List of Figures .... **vii**

List of Tables .... **xxii**

List of Appendices .... **xxiii**

Abstract .... **xxiv**

Chapter 1 Introduction **1**

1.1 Overview 1

1.2 Optoelectronic applications in the near-infrared 2

1.3 Bandgap engineering with highly mismatched alloys 4

1.4 Band anti-crossing model 5

1.5 Epitaxy of dilute nitride and dilute bismide alloys: challenges 7

1.6 Influence of surface reconstruction on dilute nitride and dilute bismide epitaxy 9

1.7 Outline of the dissertation 10

1.8 Figures 13

1.9 References 21

Chapter 2 Experimental Procedures **29**

2.1 Overview 29

2.2 Molecular-beam epitaxy 30

2.2.1 Overview 30

2.2.2 MBE system details 30

2.2.3 Reflection high-energy electron diffraction 32

2.2.4 Temperature calibration 34

2.3 High-resolution x-ray diffraction 36

2.4 Hall effect measurements 37

2.5 Current-voltage and capacitance-voltage measurements 38

2.6 Ion beam analysis ... 38
2.7 Atomic force microscopy ... 39
2.8 Scanning electron microscopy ... 39
2.9 Transmission electron microscopy ... 40
2.10 Photoreflectance and photoluminescence ... 41
2.11 Figures ... 43
2.12 References ... 48

Chapter 3 Amphoteric Doping in GaAs(Bi) ... 50
3.1 Overview ... 50
3.2 Background ... 51
3.3 Experimental procedures ... 52
3.4 GaAs(Bi):Si surface reconstructions ... 53
3.5 GaAs(Bi):Si structural properties ... 54
3.6 Mechanism of conductivity-type transition ... 56
3.7 GaAs(Bi):Si surface morphologies and carrier transport properties ... 57
3.8 *n*-type and *p*-type Au/GaAs:Si Schottky diodes ... 59
3.9 Summary and conclusions ... 60
3.10 Figures ... 62
3.11 References ... 73

Chapter 4 GaAsNBi Alloys: Influence of Surface Reconstructoin in Bi-Enhanced N Incorporation ... 77
4.1 Overview ... 77
4.2 Background ... 78
4.3 Methods ... 79
4.4 Selection of the GaAsNBi growth temperature ... 81
4.5 Influence of N and Bi fluxes on Bi and N fractions ... 82
4.6 Interstitial N concentration ... 83
4.7 Dominant interstitial complex in GaAsNBi ... 85
4.8 Mechanism for Bi-enhanced N incorporation ... 86
4.9 Summary and conclusions ... 87
4.10 Figures ... 88
4.11 References ... 98

Chapter 5 Surfactant-Induced Chemical Ordering of GaAsN:Bi 102
5.1 Overview 102
5.2 Background 103
5.3 Experimental procedures 104
5.4 Surface morphologies and compositions 106
5.5 Exploring lateral phase separation 108
5.6 Exploring chemical ordering 108
5.7 Mechanisms for chemical ordering 111
5.8 Summary and conclusions 113
5.9 Figures 114
5.10 References 125

Chapter 6 Composition-Dependence of GaAsNBi Bandgaps 129
6.1 Overview 129
6.2 Background 130
6.3 Experimental procedures 130
6.4 Composition-dependence of out-of-plane misfit 132
6.5 Photoreflectance 132
6.6 Composition-dependence of bandgap 134
6.7 Photoluminescence and Stokes shift 135
6.8 Summary 137
6.9 Figures 138
6.10 References 145

Chapter 7 Summary and Suggestions for Future Work 148
7.1 Summary 148
7.2 Suggestions for future work 150
7.2.1 Growth of GaAsNBi on offcut substrates 150
7.2.2 Band offsets in GaAs/$GaAs_{1-x-y}N_xBi_y$/GaAs quantum wells 153
7.2.3 Annealing and irradiation of GaAs(N)(Bi) films 156
7.2.3.1 Background 156
7.2.3.2 UV irradiation of GaAs(N)(Bi) films 157
7.2.3.3 Influence of RTA and electron irradiation on optical properties 158
7.2.4 Influence of chemical ordering on electronic structure 160

7.2.5 Influence of chemical ordering on transport properties 161
7.3 Figures 162
7.4 References 174

Appendices 179

List of Figures

Figure 1.1 Energy bandgap versus lattice parameter for various group III-V binary compound semiconductors. Solid lines between points represent the bandgaps and lattice parameters for alloys of those binary compounds. Gray vertical bars indicate the lattice parameters of several commercially available substrates. Due to the giant bandgap bowing induced by alloying small fractions of N or Bi with GaAs, GaAsNBi alloys can access a wide range of bandgaps while remaining nearly lattice-matched to GaAs, as shown by the orange-shaded region. Adapted from Ref. 105. 13

Figure 1.2 The AM1.5 solar spectrum in gray, overlaid with blue, green, and magenta regions representing the portions of the solar spectrum that can be absorbed by a 3-junction photovoltaic cell with bandgaps of 1.70, 1.18, and 0.67 eV. Adapted and reprinted with permission from Ref. 17 (Copyright 2007, Cambridge University Press). 14

Figure 1.3 Illustration of the band anticrossing model for GaAsN. N induces a defect level, E^N, that interacts with the GaAs conduction band, E^C, to split the conduction band into two sub-bands, E_+ and E_-, effectively leading to a lowering of the GaAsN conduction band edge. Reprinted with permission from Ref. 17 (Copyright 2003, AIP Publishing). 15

Figure 1.4 Illustration of the valence band anticrossing model for GaAsBi. Bi induces a defect level that interacts with the GaAs valence band to split the heavy-hole (HH), light-hole (LH), and spin-orbit split-off (SO) bands into $E_+(HH_+, LH_+, SO_+)$ and $E_-(HH_-, LH_-, SO_-)$ sub-bands, effectively leading to a rise of the GaAsBi valence band edge. Reprinted with permission from Ref. 39 (Copyright 2007, AIP Publishing). 16

Figure 1.5 Schematics of the GaAsN band structure for different N local atomic environments, including (a) isolated N, as in the band anti-crossing model; (b) isolated N and N-N pairs; and (c) isolated N, N-N pairs, and N clusters, as in the linear combination of isolated resonant states model. Reprinted from Ref. 107 (Copyright 2017, Timothy Yu Cheng Jen). 17

Figure 1.6 X-ray rocking curves from GaAs layers grown at various temperatures, *T*. As the temperature is decreased, the diffraction peak shifts to lower angles, indicating in increase in lattice parameter associated with incorporation of arsenic antisites, As_{Ga}, in non-stoichiometric GaAs, $Ga_{1-\delta}As_{1+\delta}$. The mole fraction of As_{Ga}, δ, is estimated from the peak separation between each non-stoichiometric GaAs peak and the peak for GaAs grown at 525 °C. Adapted and reprinted with permission from Ref. 73 (Copyright 1990, Cambridge University Press)............................... 18

Figure 1.7 GaAs(Bi) films grown using either As dimers (As_2) or As tetramers (As_4), for various growth rates and group V/III beam-equivalent pressure (BEP) ratios. The range of Bi fractions achieved at each growth condition is labeled adjacent to each symbol. With As_2, negligible Bi incorporates for group V/III ratios > 6, while with As_4, significant Bi is incorporated even at group V/III ratios > 20. Adapted from Ref. 78 (Copyright 2015, Richard L. Field III)... 19

Figure 1.8 First-principles calculations of the variation of the bandgap of GaAsBi alloys for various Bi configurations as a function of Bi fraction. The bandgaps for isolated Bi atoms, [111] chains, Bi clusters, and special quasirandom structures (SQS) diverge with increasing Bi fraction. Photoluminescence (PL) measurements of bandgap are shown for comparison. Reprinted with permission from Ref. 50 (Copyright 2018, American Physical Society). 20

Figure 2.1 Schematic of the Modified Varian Gen II molecular-beam epitaxy system, containing seven solid sources (Ga, In, Al, Bi, Si, Be, As cracker) and a radio frequency N plasma source, each housed at one of the eight effusion cell ports. Each effusion cell source is directed at the sample center, angled 33° from the surface normal of the sample. Adapted from Ref. 11 (Copyright 2006, Matthew J. Reason). 43

Figure 2.2 Schematic of the Riber Compact 21 molecular-beam epitaxy system, containing seven solid sources (Ga, In, Al, Bi, Si, Be, As cracker), each housed in one of the effusion cell ports. Reprinted from Ref. 1 (Copyright 2015, Richard L. Field III). 44

Figure 2.3 Illustration of a (2x4) surface reconstruction, with dumbbells representing dimerized surface atoms, and its corresponding reflection high-energy electron diffraction pattern viewed along the 110 and $[\bar{1}10]$ directions. Adapted and reprinted with permission from Ref. 21 (Copyright 1991, AIP Publishing).. 45

Figure 2.4 Schematic of the high-resolution x-ray diffraction geometries used for measurements about the (a) symmetric (004) and (b) asymmetric (224) GaAs reflections. Adapted from Ref. 22. (Copyright 2003, Xiaojun Weng). 46

Figure 2.5 Schematic of the arrangement used for (a) resistivity and (b) Hall effect measurements of Van der Pauw specimens. 47

Figure 3.1 Columns III, IV, and V of the periodic table. Elements from group IV, such as Si, may act as *n*-type dopants in GaAs when substituting for Ga (group III) and as *p*-type dopants when substituting for As (group V). 62

Figure 3.2 Schematic of the layer structure of GaAs(Bi):(Si) samples discussed in Ch. 3, including layer thicknesses and substrate temperature, T_{sub}.............. 63

Figure 3.3 Reflection high-energy electron diffraction patterns collected along [110] and [$1\bar{1}0$] axes during GaAs(Bi):(Si) film growth. [(a), (b)] (2 x 4) pattern during GaAs growth at 600 °C; [(c), (d)] streaky (2 x 3) pattern during GaAs(Si) growth at 280 °C; [(e), (f)] dim (2 x chevron) pattern during *p*-type GaAs(Bi):Si growth at 280 °C, with arrows indicating the chevrons; [(g), (h)] streaky (1 x 3) pattern during *n*-type GaAs(Bi):Si growth at 280 °C. Reprinted with permission from Ref. 51 (Copyright 2016, AIP Publishing). 64

Figure 3.4 Representative high-resolution x-ray rocking curves for $GaAs_{1-x}Bi_x$ films, with x ranging from 0 to 0.048. For $x < 0.03$, Pendellosung fringes indicate high crystalline quality and coherent interfaces. As x increases, Pendellosung fringes disappear and the GaAsBi diffraction peak broadens. Reprinted with permission from Ref. 51 (Copyright 2016, AIP Publishing). 65

Figure 3.5 In-plane, $a_{\parallel}$, and perpendicular, $a_{\perp}$, lattice parameters and (b) FWHM of the (004) GaAsBi diffraction peak and upper bound for excess arsenic concentration, all as a function of Bi fraction, x. For $x < 0.04$, $a_{\perp}$ increases with increasing x, independent of doping type and concentration. For $x > 0.04$, $a_{\parallel}$ begins to increase while $a_{\perp}$ is nearly constant, suggesting that the film lattice has begun to relax to its intrinsic lattice parameter. For undoped GaAsBi and *n*-type GaAsBi:Si with $x < 0.04$, the FWHM of the GaAsBi peak is nearly constant; for $x > 0.04$, the FWHM increases with x. For *p*-type GaAsBi:Si, the FWHM of the GaAsBi peak increases monotonically with x. Reprinted with permission from Ref. 51 (Copyright 2016, AIP Publishing). 66

Figure 3.6 Conductivity type for GaAs(Bi):Si films: arsenic beam-equivalent pressure (BEP) vs. Ga BEP, with growth rate on the upper x-axis for the As-rich growth regime. A dashed line indicates the regime where the group V/III BEP ratio is equal to 10, “BEPratio10”. All GaAsBi:Si films above (below) the BEPratio10 line are n-type (p-type). In addition, along the BEPratio10 line, a conductivity type conversion from n-type to p-type occurs as the growth rate increases (from 0.25 to 2.0 μm/hr), consistent with the growth rate dependence of the stoichiometry threshold reported in Ref. 28. Schematics illustrate the (1 x 3) and (2 x 3) reconstructions observed for n-type conductivity and the (2 x 1) reconstruction observed for p-type conductivity. Reprinted with permission from Ref. 51 (Copyright 2016, AIP Publishing). 67

Figure 3.7 Surface reconstructions during Si incorporation in GaAs(Bi). Growth with a (2x1)' or (4x2)' reconstruction without As dimers results in *p*-type conductivity'' while growth with a (1x3), (2x3), or (2x4)' reconstruction containing As dimers results in *n*-type conductivity. '' 68

Figure 3.8 Conductivity vs. carrier concentration for bulk GaAs1-xBix:Si films, in comparison with literature reports for GaAsBi films doped with C or Be. The dotted lines form an envelope corresponding to mobilities of 2300 and 45 cm^2/(V-s). The n-type film mobilities are typically near the upper end of the range (~2300 cm^2/(V-s)) while the p-type film mobilities are typically near the lower end (~45 cm^2/(V-s)), all independent of Bi fraction. For our n-type films grown near the transition from n to p-type conductivity, mobilities lie near the mid-range of the envelope. The uncertainties in the conductivities and carrier concentrations are comparable to the size of the data points. See Ref. 36. See Ref. 37. See Ref. 38. See Ref. 39. See Ref. 40. Reprinted with permission from Ref. 51 (Copyright 2016, AIP Publishing). 69

Figure 3.9 Scanning electron microscopy, corresponding energy dispersive X-ray spectroscopy (EDS), and atomic force microscopy (AFM) images for [(a), (b), (c)] n-type GaAs$_{0.992}$Bi$_{0.008}$:Si, as well as p-type GaAs$_{0.991}$Bi$_{0.009}$:Si [(d), (e), (f)] before and [(g), (h), (i)] after etching with HCl:H20 (1:3). In the EDS images, red, green, and yellow correspond to Ga, As, and Bi, respectively. The gray-scale ranges displayed in the AFM images are (c) 10 nm, (f) 160 nm, and (i) 100 nm. Line-cuts of the tip height across the AFM images are shown beneath the images, with height axis from 0 to 250 nm. Reprinted with permission from Ref. 51 (Copyright 2016, AIP Publishing). 70

Figure 3.10 Schematic cross-section of the layer structures for n-type and p-type Au/GaAs:Si Schottky diodes containing a single quantum well (QW) of

GaAsN or GaAsBi. Silicon was used for both n-type and p-type doping, using the approach described in Section 3.6. For the n-type diodes, the GaAs:Si layers were grown at 580°C while for p-type diodes, GaAs:Si was grown at 280°C. 71

Figure 3.11 Current-voltage curves for n-type (red) and p-type (blue) Au/GaAs:Si Schottky diodes with and without single quantum wells of $GaAs_{1-x}N_x$ or $GaAs_{1-y}Bi_y$. The reverse leakage current densities are two to four orders of magnitude larger for the p-type diodes compared to the n-type diodes. 72

Figure 4.1 Schematic of the sample layer structure for both the N flux series and the Bi flux series. The dashed line indicates a growth interrupt during which the substrate temperature, T_{sub}, was ramped. 88

Figure 4.2 (004) high-resolution x-ray rocking curves for GaAsNBi films and GaAs buffer layers at growth temperatures ranging from 230 °C to 346 °C. At 230 °C, expansion of the low-temperature GaAs buffer layer lattice parameter due to excess As incorporation results in a diffraction peak approximately 100 arcsec to the left of the GaAs substrate peak. With increasing temperature, the non-stoichiometric GaAs peak moves to higher angle and eventually merges with the GaAs substrate peak, indicating a reduction in excess As incorporation. 89

Figure 4.3 Reflection high-energy electron diffraction patterns along the [110] and [1$\bar{1}$0] axes during GaAs(N)(Bi) film growth. [(a), (b)] (2 x 4) pattern following GaAs growth at 580°C; [(c), (d)] (2 x 3) pattern at 345 ± 15°C immediately prior to the GaAs(N)(Bi) growth; [(e), (f)] (1 x 3) pattern during GaAsNBi growth at 345 ± 15°C with Bi flux $\leq 5.7 \times 10^{-8}$ Torr; [(g), (h)] (2 x 1) pattern during GaAsNBi growth with Bi flux $\geq 5.7 \times 10^{-8}$ Torr. Reprinted with permission from Ref. 42 (Copyright 2017, AIP Publishing). 90

Figure 4.4 (004) high-resolution x-ray rocking curves for the (a) N flux series with x_N ranging from 0 to 0.023 and (b) Bi flux series with y_{Bi} ranging from 0 to 0.056. For all plots, the GaAs substrate peak is set to $\Delta\omega = 0$ arcseconds, thereby facilitating comparison of $\Delta\omega$ between the GaAs substrate and the GaAsNBi epilayers. Within the N flux series, y_{Bi} remains fixed as x_N is increased. However, within the Bi flux series, x_N increases as y_{Bi} increases, suggesting a Bi-induced enhancement of N incorporation. Reprinted with permission from Ref. 42 (Copyright 2017, AIP Publishing). 91

Figure 4.5 AFM images of the Bi flux series ((a)-(d)) and the N flux series ((e)-(f)). The colorscale range displayed is 3nm and the rms roughness is 0.3nm±0.05nm for all images, consistent with the typical <0.5nm rms roughness observed for layer-by-layer growth.' To confirm the absence of μm-sized surface droplets, SEM images were collected for areas of approximately 400 μm x 500 μm, as shown in (i)-(j). Features associated with dust were included to demonstrate that the images are in focus; the surfaces are otherwise featureless, without droplets. (a) – (h) are reprinted with permission from Ref. 42 (Copyright 2017, AIP Publishing). 92

Figure 4.6 Measured RBS yield versus backscattered particle energy for the Bi flux series. The vertical dashed lines indicate the energy window of ions backscattered from Bi atoms. As the Bi flux increases, the resulting Bi signal increases. (b) The portions of the RBS spectra enclosed in the box in (a) are shown in (b). Non-channeling data is overlaid with SIMNRA fitted spectra assuming uniform Bi depth profiles. Fitted Gaussian-shape spectra suggest uniform Bi incorporation throughout the GaAsNBi films. (c) Measured NRA yield versus emitted particle energy for the N flux series. The vertical dashed lines indicate the energy window of the protons emitted during the $^{14}N(\alpha,p)^{17}O$ reaction. As the N flux increases, the resulting N signal increases. Non-channeling data are overlaid with SIMNRA fitted spectra assuming a uniform N depth profile. Fitted Gaussian-shape non-channeling spectra suggest uniform N incorporation throughout the GaAsNBi film. Reprinted with permission from Ref. 42 (Copyright 2017, AIP Publishing). 93

Figure 4.7 Fractions of total N, x, substitutional N, x_{sub}, and interstitial N, x_{int} for the Bi flux series of GaAsN(Bi) films determined by channeling and non-channeling nuclear reaction analysis. The atomic concentrations corresponding to the mole fractions are shown on the right y-axis. Both x and x_{int} increase with Bi flux, suggesting a Bi-induced enhancement of N incorporation, with preferential incorporation in interstitial sites. Reprinted with permission from Ref. 42 (Copyright 2017, AIP Publishing). 94

Figure 4.8 Illustration of substitutional N, N_{As}; $(N\text{-}As)_{As}$, with the N-As pair aligned along the [010] direction; and $(N\text{-}N)_{As}$, with N_2 aligned along the [111] direction. 95

Figure 4.9 Total simulated NRA yields in the [100], [110], and [111] directions for (a) N_{sub}, (b) $(N\text{-}N)_{As}$, and (c) $(N\text{-}As)_{As}$. (d) Measured total NRA yield in each channeling direction. Similar yield trends of $Y_{[111]} > Y_{[110]} > Y_{[100]}$ are observed for (c) and (d), suggesting that $(N\text{-}As)_{As}$ is the dominant

interstitial complex in GaAsN alloys. Reprinted with permission from Ref. 42 (Copyright 2017, AIP Publishing). 96

Figure 4.10 Schematic of a $[\bar{1}10]$-oriented A-step with Ga dangling bonds and a [110]-oriented B-step edge with As dangling bonds. Bismuth increases the density of B-step edges with As dangling bonds, facilitating the formation of $(N\text{-}As)_{As}$. 97

Figure 5.1 Dimer-induced strain (DIS) mechanism for CuPt ordering, illustrated for a SiGe alloy. (a) Smaller Si atoms incorporate at compressively strained sites beneath surface dimers while larger Ge atoms incorporate at sites in tension between dimer rows, resulting in ordered rows of alternating Si and Ge, extending in the [110] direction (b) Upon growth of the next atomic bi-layer, the rows of alternating Si and Ge propagate in the $[\bar{1}11]$ direction, forming alternating Si and Ge $(1\bar{1}1)$ planes. Adapted with permission from Ref. 10 (Copyright 1990 by the American Physical Society).. 114

Figure 5.2 Schematic of the layer structures for (a) the temperature series (T-series) and (b) the Bi flux series. Dashed lines indicate growth interrupts during which the substrate temperature, T_{sub}, was ramped............................. 115

Figure 5.3 Reflection high-energy electron diffraction patterns collected during epitaxy of GaAsN:Bi. Patterns are shown along the [110] and $[1\bar{1}0]$ directions in [(a), (b)], [(e), (f)], [(g), (h)], [(i), (j)], and [(k), (l)] and along the [100] and [010] directions in [(c), (d)]. [(a), (b)] streaky (2x4) pattern during GaAs growth at 580°C; [(c), (d)] streaky c(4x4) pattern during annealing at $T_{GaAsN:Bi}$; [(e), (f)] streaky (1x3) pattern during GaAsN:Bi growth at low $T_{GaAsN:Bi}$ or low Bi beam equivalent pressure (BEP) values; [(g), (h)] streaky (2x1) pattern during GaAsN:Bi growth at higher $T_{GaAsN:Bi}$ and moderate Bi BEP values; [(i), (j)] spotty (3x3) pattern during GaAsN:Bi growth with the highest Bi BEP values. [(k), (l)] nearly-streaky (2x1) pattern during GaAsN growth...................................... 116

Figure 5.4 Plot of x-ray intensity vs. $\Delta\omega$ for rocking curves about the GaAs (004) reflection from the Bi flux series. For all plots, the GaAs substrate peak is set to $\Delta\omega = 0$ arcseconds, thereby facilitating comparison of $\Delta\omega$ between the GaAs substrate and the GaAsN:Bi epilayers. Corresponding atomic force microscopy (AFM) or scanning electron microscopy (SEM) images of the surface morphology are shown alongside in (b)-(f). For the AFM images, the colorscale ranges displayed are (b) 2nm, (c) 3 nm, (d) 2 nm, (e) 3 nm. (g) Energy-dispersive x-ray spectroscopy image corresponding to the SEM image in (f). In the mottled red-green region, Ga, As, and N

are present, while the blue regions are primarily bismuth. To confirm the absence of μm-sized surface droplets on films shown in (b)-(e), SEM images were collected for areas of approximately 200 μm x 250 μm, as shown in (h)-(k). Features associated with dust were included to demonstrate that the images are in focus; the surfaces are otherwise featureless, without droplets. 117

Figure 5.5 Plot of x-ray intensity vs. Δω for a coupled ω-2θ scan about the GaAs (004) reflection for the multilayer structure containing the GaAsN:Bi layers of the T-series. The GaAs substrate peak is set to Δω = 0 arcseconds. For each successive layer, as the temperature is decreased, x_N remains approximately constant while y_{Bi} increases slightly from 0.06 to 0.07. (Inset): Atomic force microscopy image of the top surface of the T-series, with $T_{GaAsN:Bi}$ = 260°C. The colorscale range displayed is 4 nm. To confirm the of absence of μm-sized surface droplets, an SEM image with area of approximately 200 μm x 250 μm is shown in the lower half of the inset. Features associated with dust were included to demonstrate that the image is in focus; the surface is otherwise featureless, without droplets. 118

Figure 5.6 X-ray reciprocal space map near the GaAs (002) reflection, with Q_z and Q_x along the [001] and [110] directions, respectively. The GaAs substrate peak is set to ΔQ_z = 0 and ΔQ_x = 0 to facilitate comparison with the GaAsNBi epilayer peak position. The color-scale represents the logarithm of the x-ray intensity. The lack of satellite peaks along the [110] direction about the GaAsNBi peak indicates a lack of lateral composition modulation. 119

Figure 5.7 Plots of x-ray intensity for ω-2θ scans about the GaAsN:Bi ½ (115) reflections for (a) tensile and (b) compressive GaAsN:Bi films. The presence of the ½ $(1\bar{1}5)$ reflection suggests ordering of the $(1\bar{1}1)$ planes. (c) representative [110] selected-area diffraction (SAD) pattern for the compressive GaAsN:Bi in (b), showing ½$(1\bar{1}1)$, ½$(1\bar{1}3)$, and ½$(1\bar{1}5)$ [½$(\bar{1}11)$, ½$(\bar{1}13)$, and ½$(\bar{1}15)$] reflections, indicating long-range ordering on $(1\bar{1}1)$ [$(\bar{1}11)$] planes. Additional $[1\bar{1}0]$ SAD patterns showed only ZB reflections, indicating an absence of long-range ordering on the {111}A planes. Similar SAD patterns were obtained for the tensile GaAsN:Bi. 120

Figure 5.8 High-angle annular dark field scanning transmission electron micrograph of the T-series, with alternating bright and dark layers consisting of GaAsN:Bi and GaAs, respectively. Selected-area diffraction patterns collected along the [110] zone axis for $T_{GaAsN:Bi}$ = 260°C, 300°C, 340°C,

and 380°C are shown in (b) – (e), respectively. The diffraction spots for {002}, {111}, and {220} are identified by closed circles, open circles, and triangles, respectively. Arrows in (d) and (e) indicate ½($1\bar{1}1$) and ½($\bar{1}11$) reflections corresponding to $CuPt_B$ ordering. 121

Figure 5.9 (a) High-resolution scanning transmission electron micrograph, collected near an interface between GaAs and ordered GaAsN:Bi. The magenta and cyan arrows in (a) indicate example ($\bar{1}11$) and ($1\bar{1}1$) planes with doubled periodicity in the [$\bar{1}11$] and [$1\bar{1}1$] directions, i.e. ($\bar{1}11$) and ($1\bar{1}1$) ordered domains. (b) Fast Fourier transform (FFT) of the image in (a), showing spots corresponding to the zincblende lattice and those at the ½($1\bar{1}1$) and ½($\bar{1}11$) positions. Inverse FFTs, using the spots circled in (b), with pixels near the top (18 ± 6%) and bottom (18 ± 7%) of the total grayscale range, are shown in (c), with magenta and cyan regions representing the ($\bar{1}11$) and ($1\bar{1}1$) ordered domains. For both the ($\bar{1}11$) and ($1\bar{1}1$) ordered domains, the distribution of domain sizes, fit with a logarithmic-normal (lognormal) distribution, is shown in (d). 122

Figure 5.10 Window for $CuPt_B$ ordering in GaAsN:Bi: Bi beam equivalent pressure (BEP) vs $T_{GaAsN:Bi}$. (1x3), (3x3), and (2x1) surface reconstructions are represented by squares, circles, and diamonds, respectively. Solid (open) symbols denote ordered (disordered) films. The dashed lines are a guide to the eye. 123

Figure 5.11 Proposed atomistic mechanism for $CuPt_B$ ordering in GaAsN:Bi. White, gray, green, blue, and red circles correspond to surface dimer, Ga, As, N, and Bi atoms, respectively. N and Bi atoms attach at step edges flowing in the [$\bar{1}10$] ([$1\bar{1}0$]) direction, leading to alternating N-rich/Bi-poor and N-poor/Bi-rich ($\bar{1}11$) [($1\bar{1}1$)] planes, highlighted by blue and red bars respectively. A fraction of N atoms share As lattice sites as $(N\text{-}As)_{As}$ complexes. 124

Figure 6.1 Contours of out-of-plane misfit, $\varepsilon_\perp$, presented on a plot of y_{Bi} and x_N for $GaAs_{1-x-y}N_xBi_y$ films. For circular symbols, x_N and y_{Bi} were determined by nuclear reaction analysis and Rutherford backscattering spectrometry (RBS) respectively. For square symbols, y_{Bi} was determined by RBS and x_N was determined by x-ray rocking curves (XRC), corrected to account for interstitial N. The percent out-of-plane misfit, $\varepsilon_\perp$, determined from (004) XRC, is labeled adjacent to each point. Dashed black lines represent contours of constant misfit, determined with a planar fit to the data points, indicating lattice-matching for a ratio $x_N/y_{Bi} = 0.83$. Lattice-matched ratios of $x_N/y_{Bi} = 0.59$ computed by Janotti et al., and $x_N/y_{Bi} = 0.49$ estimated

from x-ray diffraction determinations of x_N by Huang et al. are shown by gray lines. Cross symbols represent GaAsNBi films from Ref. 13. The uncertainty in the $\varepsilon_\perp$ contour lines is ± 0.04%, defined as the standard deviation between the fit and measured values of $\varepsilon_\perp$. 138

Figure 6.2 Photoreflectance (PR) spectra collected at 20 K from 100 nm thick $GaAs_{1-x-y}N_xBi_y$ films, with corresponding N and Bi fractions, x_N and $y_{Bi,}$ displayed above each spectrum for (a) the N flux series and (b) the Bi flux series. For each spectrum, a PR resonance attributed to the bandgap energy, E_g, is indicated by a black dashed line. With increasing x_N and/or y_{Bi}, the E_g values decrease monotonically. For some spectra, a second transition, attributed to strain-induced splitting of the light-hole and heavy-hole bands, is indicated by a red vertical dashed line. The energy of each resonance was determined by fitting each spectrum with the Aspnes formula (solid lines). The moduli of the PR resonances are shown as gray dashed lines below each PR spectrum.. 139

Figure 6.3 Photoreflectance (PR) spectra collected at 20 K from 400nm thick $GaAs_{1-x-y}N_xBi_y$ films from the Ch. 5 Bi-flux series, with corresponding N and Bi fractions, x_N and $y_{Bi,}$ displayed above each spectrum. With increasing x_N and/or y_{Bi}, the E_g values decrease monotonically. For some spectra, a second transition, attributed to strain-induced splitting of the light-hole and heavy-hole bands, is indicated by a red vertical dashed line. The energy of each resonance was determined by fitting each spectrum with the Aspnes formula (solid lines). For the film with $y_{Bi} = 0$, the photoluminescence (PL) spectrum is plotted in gray, showing that the feature at 1.2 eV in the corresponding PR spectrum is due to PL........ 140

Figure 6.4 Contours of bandgap energies, E_g, and out-of-plane misfit, $\varepsilon_\perp$, presented on a plot of y_{Bi} and x_N for $GaAs_{1-x-y}N_xBi_y$ films. Values of E_g determined from photoreflectance spectra collected at 20 K are labeled adjacent to each point. Solid lines of constant E_g were determined by a non-linear least-squares fit of Eqn. (6.4) to the data points. Dashed lines of constant $\varepsilon_\perp$, were determined as described for Fig. 1, with lattice-matching to GaAs at $x_N/y_{Bi} = 0.83$. The uncertainty in the E_g contour lines is ± 14 meV, defined as the standard deviation between the fit and the measured values of E_g. 141

Figure 6.5 (a) Photoluminescence spectra collected from a $GaAs_{0.959}N_{0.007}Bi_{0.034}$ film at measurement temperatures ranging from 7 to 125 K. With increasing measurement temperature, the PL peak energy decreases monotonically. (b) PL peak energy versus measurement temperature, compared to photoreflectance (PR)-determined bandgap energy, E_g, at 20 K. A solid

black line shows a projection of the E_g to high temperatures using the Varshni model with the parameters for GaAs. 142

Figure 6.6 Photoluminescence (PL) spectra collected at 7 K for selected $GaAs_{1-x-y}N_xBi_y$ films with photoreflectance spectra shown in Figure 6.2. A comparison of the PL-determined peak energies, E_{PL}, with the PR-determined bandgap energies, E_{PR}, in Figure 6.2 reveals similar values for the GaAsN film. For the GaAsNBi films, the difference between E_{PR} and E_{PL}, i.e. the Stokes shift, ranges from 0.15 to 0.18 eV, likely due to Bi-related states within the bandgap. Films with a (2x1) surface reconstruction observed by RHEED exhibit smaller Stokes shifts than those with a (1x3) reconstruction. 143

Figure 6.7 Photoluminescence (PL) spectra collected at 4 K from 400 nm thick $GaAs_{1-x-y}N_xBi_y$ films with photoreflectance spectra shown in Figure 6.3. The corresponding PR spectra are shown in Figure 6.3, and the Stokes shift, E_{PR} - E_{PL}, is listed alongside each spectrum, as well as the surface reconstruction observed by RHEED for each film during growth. For intermediate y_{Bi} in Figure 6.6 and Figure 6.7, films with a (2x1) reconstruction exhibit reduced Stokes shifts compared to films with a (1x3) reconstruction. 144

Figure 7.1 Schematic illustration of (a) the layer-by-layer growth mode on an exact (001) substrate, with island separation L_n, and (b) the step-flow growth mode on a substrate with offcut angle, θ, toward (111)B and lattice parameter a. The substrate offcut induces a regular array of terraces with width $W = (a/2)/tan(\theta)$, with step edges aligned along the [110] direction. 162

Figure 7.2 (004) high-resolution x-ray rocking curves for 100 nm thick $GaAs_{1-x}N_x$ and $GaAs_{1-x-y}N_xBi_y$ films grown on GaAs (001) substrates with offcuts from 0° to 10°(111)A. For all plots, the GaAs substrate peak is set to $\Delta\omega = 0$ arcseconds to facilitate comparison of $\Delta\omega$ between substrate and epilayer. The values of x_N and y_{Bi} are apparently independent of offcut angle. The full width at half maximum (FWHM) in arcseconds is shown adjacent to each peak. For comparison, films grown with similar layer structure and growth conditions in Figure 4.2 exhibit narrower substrate (20±5 arcsec) and epilayer (191±12 arcsec) peaks. The broadened diffraction peaks and weak or absent Pendellosung fringes suggest roughened substrate-epilayer interfaces. 163

Figure 7.3 Schematic of the layer structure for single quantum well (QW) diodes used in band offset measurements. Dashed lines indicate growth interrupts during which the substrate temperature, T_{sub}, was ramped. 164

Figure 7.4 Profile of the carrier concentration versus depth from the top Schottky contact of the structure shown in Figure 7.3, determined from capacitance-voltage measurements as described in Appendix G. The dashed black line shows a simulated carrier concentration profile from one-dimensional Schrödinger-Poisson calculations, assuming a conduction band offset (CBO) of 320 meV between GaAs and $GaAs_{0.964}N_{0.012}Bi_{0.024}$. 165

Figure 7.5 Photoluminescence (PL) spectra of GaAs/GaAsNBi/GaAs single quantum well (QW) structures at 4 K, with Bi fraction y_{Bi} = 0.024 and N fractions x_N = 0.012, 0.013, and 0.016. Emission from GaAs is apparent near 1.5 eV, with multiple features at lower energy associated with emission from the QWs. 166

Figure 7.6 High-resolution transmission electron microscopy images collected along the [110] zone axis from GaAs/GaAsNBi/GaAs single quantum well (QW) structures with Bi fraction y_{Bi} = 0.024 and N fractions x_N = 0.012, 0.013, and 0.016. Graded contrast in the lower half of the QWs suggests compositional grading. 167

Figure 7.7 (004) high-resolution x-ray rocking curves for $GaAs_{1-x-y}N_xBi_y$ films collected before and after ultraviolet irradiation. For all plots, the GaAs substrate peak is set to Δω = 0 arcseconds to facilitate comparison of Δω between substrate and epilayer. The full width at half maximum (FWHM) is listed next to each peak. No significant change in the peak FWHM or positions is apparent after irradiation. 168

Figure 7.8 Atomic force microscopy images of a GaAsNBi film collected (a) before and (b) after ultraviolet irradiation. The surface morphology and root mean square roughness, R_q = 0.3nm, are not significantly changed following irradiation. To confirm the of absence of µm-sized surface droplets, SEM images were collected for areas of approximately 200 µm x 250 µm, as shown in (c)-(d). Features associated with dust were included to demonstrate that the images are in focus; the surfaces are otherwise featureless, without droplets. 169

Figure 7.9 Photoluminescence (PL) spectra collected at 7 K for $GaAs_{1-x-y}N_xBi_y$ films from (a) the N flux series and (b) the Bi flux series, both as-grown (solid lines) and following rapid thermal annealing (RTA) for 60 s at 650 °C (dashed lines). For GaAsNBi films, a small increase in the PL peak intensity is observed following RTA, with negligible change in peak position. For the GaAsN film (y_{Bi} = 0), the RTA-induced enhancement in PL intensity is significantly larger and is accompanied by an increase in PL peak energy, suggesting that the presence of Bi modifies the influence

of annealing on luminescence. Further discussion of the as-grown film spectra is found in Section 6.7. 170

Figure 7.10 Photoluminescence (PL) spectra collected at 7 K from a GaAsNBi film, both as grown as well as following post-growth rapid thermal annealing (RTA) and/or electron irradiation. The PL peak intensity increases with RTA temperature up to 750°C and then decreases. The peak energy increases slightly up to 750°C, with a significant blue-shift for RTA temperature > 750°C. For electron irradiation alone, the PL intensity is reduced compared to the spectrum of the as-grown film. However, for electron irradiation plus RTA at 650 °C, the PL intensity is greater than that of the film that received only RTA at 650 °C, and negligible blue-shift is observed. 171

Figure 7.11 Photoluminescence (PL) spectra collected from a $GaAs_{0.959}N_{0.007}Bi_{0.034}$ film at temperatures ranging from 6 to 300 K, following electron irradiation and rapid thermal annealing (RTA) at 650°C for 1 min. The excitation power was 100 mW for spectra from 6K to 150K and 300 mW for 300K. The PL peak energy decreases with increasing temperature from 6K to 150K and then increases at 300K, suggesting the low temperature emission is produced by localized states. For comparison, PL spectra from the same film as-grown are shown in Figure 6.5, where the peak cannot be resolved above 100K. 172

Figure 7.12 First- and second-nearest-neighbor local atomic environments, viewed down the [110] direction, for a Bi solute atom in (a) disordered GaAsNBi, (b) ordered GaAsBi, and (c) ordered GaAsNBi. In the ordered GaAsNBi (GaAsBi) structure, atoms are arranged in alternating GaAsN (GaAs) and GaAsBi ($\bar{1}11$) planes, as discussed in Section 5.7. 173

Figure A.1 Pyrometer reading, T_{pyro}, versus CAR thermocouple reading, T_{CAR}, recorded for four molybdenum blocks in the Gen II MBE system. Solid lines represent linear least squares fits to the data points for each block. For substrate temperatures T_{sub} > 400°C, T_{pyro} was considered to accurately represent T_{sub}. For T_{sub} < 400°C, T_{sub} was determined from T_{CAR} using an extrapolation of the linear relationship between T_{CAR} and T_{pyro}. 180

Figure B.1 Natural logarithm of free carrier concentration, *n*, versus reciprocal Si cell temperature, *T*, for three GaAs:Si films. The solid line is a linear fit to the data, used to determine the Si cell temperature required to achieve a targeted carrier concentration. 182

Figure D.1 Nitrogen fractions, x, determined from x-ray rocking curves (XRC) and nuclear reactional analysis (NRA). The red line is a linear least squares fit, with slope x_{NRA}/x_{XRC} = 1.325. Therefore, to account for interstitial N in those samples for which only XRC data was available, we estimate a substitutional N fraction, $f_{N\text{-}sub}$ = 0.75, which corresponds to multiplying x_{XRC} by a factor of 1.325. 188

Figure E.1 Selected-area electron diffraction pattern collected along the $[\bar{1}10]$ direction from a GaAsNBi film grown with growth rate of 1 μm/h and substrate rotation speed of 10 rpm. Satellite spots along the [001] direction are indicated by red arrows. The spacing between each reflection and one of its satellite spots is one sixth of the (002) spacing. 192

Figure E.2 Chemically-sensitive (002) dark field transmission electron microscopy collected from the film in Figure C.1, showing a composition modulation with period 1.7 nm along the growth direction. 193

Figure E.3 Schematic showing the position-dependent and time-dependent flux variations as the sample is rotated during molecular-beam epitaxy. At the rotation center, indicated by the red dot, the relative fluxes are independent of time. However, at the off-rotation-center positions, the flux oscillates with a period corresponding to the sample rotation period. Therefore, oscillations in the composition, termed "composition modulations," are observed in the growth direction. Adapted and reprinted with permission from Ref. 4 (Copyright 2007, Elsevier). 194

Figure E.4 Schematic of the sample from which the GaAsNBi cross-sectional specimen shown in Figs. C.1 and C.2 was taken. Another specimen taken from the same sample at a location closer to the center of rotation does not exhibit satellite spots corresponding to substrate rotation-induced composition modulation. Relative locations of each specimen are indicated by red bars on the sample schematic. 195

Figure F.1 High-resolution scanning transmission electron micrograph, collected near an interface between GaAs and ordered GaAsNBi. (b) Fast Fourier transform (FFT) of the image in (a), showing spots corresponding to the zincblende lattice and those at the ½$(\bar{1}11)$ and ½$(1\bar{1}1)$ positions, indicating a doubling in periodicity in the $[\bar{1}11]$ and $[1\bar{1}1]$ directions. Green and blue circles indicate the ½$(1\bar{1}1)$ and ½$(\bar{1}11)$ spots, respectively. 199

Figure F.2 Conjugate pairs of (a) ½$(\bar{1}11)$ and (b) ½$(1\bar{1}1)$ spots in the FFT following application of the twin-oval masks. [(c), (d)] Fourier-filtered images produced by applying an inverse FFT to the conjugate pairs of spots in (a)

and (b). [(e), (f)] Thresholded images produced by selecting pixels from the top (18 ± 6%) and bottom (18 ± 7%) of the total grayscale range. [(g), (h)] Images of ordered domains after applying the dilation function to the images in (e) and (f). 200

List of Tables

Table H.1 Growth parameters for GaAs(Bi):(Si) films grown on the C21 MBE system, including growth rate, epilayer thickness, substrate temperature, As/Ga and Bi/As beam equivalent pressure (BEP) ratios, and silicon cell temperature. 204

Table H.2 Growth parameters for GaAs(N)(Bi) films grown on the Gen II MBE system, including growth rate, epilayer thickness, substrate temperature, As/Ga and Bi/As beam equivalent pressure (BEP) ratios, and nitrogen flow rate. 205

Table H.3 Si cell temperatures, T, and free carrier concentrations, n, of GaAs:Si films used in the Si doping calibration. 206

Table H.4 Parameters used to fit photoreflectance spectra with two resonances according to the Aspnes formula, $\frac{dR}{R}(E) = \mathrm{Re}\left[Ce^{i\vartheta}(E\text{-}E_0 + i\Gamma)^{-m}\right]$, as well as the goodness of fit, R^2. Samples RMBE 1368, 1367, and 1366 were fit with a single resonance. 207

Table I.1 Lattice parameters, a, bandgaps, E_g, and Poisson ratios, v, for GaAs, zincblende GaN, and GaBi (predicted). 209

Table I.2 Additional materials parameters for GaAs, including Varshni parameters, α and β, relative permittivity, ε_r, surface built-in potential, V_{BS}, and interface built-in potential, V_{BI}. 210

List of Appendices

Appendix A Temperature Calibration for T << 580 °C 179

Appendix B Doping Calibration 181

Appendix C Depletion Correction for Hall Effect Measurements 183

Appendix D N Interstitial Correction for XRC 187

Appendix E Substrate-Rotation-Induced Composition Modulations 189

Appendix F FFT Analysis of Ordered Domain Sizes 197

Appendix G Capacitance-Voltage Carrier Concentration Profiling 201

Appendix H Tabulated Data 203

Appendix I Materials Parameters 209

Abstract

Due to the significant bandgap narrowing induced by dilute fractions of N and Bi in III-V semiconductors, emerging dilute nitride-bismide semiconductor alloys are of significant interest for long-wavelength applications ranging from temperature-insensitive laser diodes to ultra-high efficiency multijunction photovoltaic cells. However, both dilute nitride and dilute bismide devices have exhibited significant sensitivity to the local atomic environments of N or Bi solute atoms, while their incorporation mechanisms are not well understood. In this work, we investigate the role of the surface reconstruction on doping, alloy formation, and electronic and optical properties of GaAs(N)(Bi) alloys.

For GaAs(Bi), we examine the influence of surface reconstruction on silicon dopant incorporation and electronic properties. Si incorporation into GaAs(Bi) with an (*n*x3) surface reconstruction leads to n-type conductivity, while growth with a (2x1) reconstruction leads to p-type conductivity. We hypothesize that the presence or absence of surface arsenic dimers prevents or enables dopant incorporation into arsenic lattice sites. We consider the influence of bismuth anions on arsenic-dimer mediated dopant incorporation and the resulting electronic transport properties, demonstrating the applicability of this mechanism to mixed anion semiconductor alloys.

For GaAsNBi alloys, we examine the influence of Bi and N fluxes on N and Bi incorporation. The incorporation of Bi is found to be independent of N flux, while the total N incorporation and the fraction of N atoms occupying non-substitutional lattice sites increase with

increasing Bi flux. A comparison of channeling nuclear reaction analysis with Monte Carlo – molecular dynamics simulations indicates that the non-substitutional N primarily incorporate as $(N\text{-}As)_{As}$ interstitial complexes. We discuss the influence of Bi adatoms on the formation of arsenic-terminated [110]-oriented step edges with a (1x3) surface reconstruction and the resulting enhancement in total N incorporation via the formation of additional $(N\text{-}As)_{As}$.

We also consider the influence of Bi as an incorporating surfactant on chemical ordering in GaAsN:Bi alloys. While epitaxy with a (2x1) reconstruction leads to random GaAsN formation, the introduction of a Bi flux induces long-range chemical ordering of the {111} planes. We propose a mechanism in which Bi enhances the formation of dimer rows aligned along the [110] direction in the (2x1) surface reconstruction, facilitating N incorporation beneath surface dimers and Bi incorporation between dimer rows to form alternating N-rich and Bi-rich {111} planes. These findings suggest a route to tailoring the local atomic environment of N and Bi atoms in a wide range of emerging dilute nitride-bismide alloys.

Finally, we have examined the alloy composition dependence of the energy bandgap and electronic states in GaAsNBi alloys. Using direct measurements of N and Bi mole fractions, via ion beam analysis, in conjunction with direct measurements of the out-of-plane misfit via x-ray rocking curves, we determine a new "magic ratio" for lattice-matching of GaAsNBi alloys with GaAs substrates. In addition, using a combination of photoreflectance and photoluminescence spectroscopy, we determine a new map of the composition- and misfit-dependence of the energy bandgaps, along with revealing the energetic position of Bi-related states at approximately 0.18 eV above the valence band maximum.

Chapter 1

Introduction

1.1 Overview

Highly mismatched alloys (HMAs) consist of highly immiscible solute atoms with distinctly different size and/or electronegativity, often with alloy properties that deviate significantly from those of the solvent. In semiconductors and insulators, incorporation of dilute fractions of highly mismatched solute atoms leads to dramatic reductions of the host bandgap energy. In addition, the band structure of HMAs is predicted to be strongly influenced by the local atomic environments of solute atoms. The incorporation of solute atoms is governed by surface conditions during epitaxy; therefore, an understanding of the mechanistic links between surface reconstruction and alloy formation is key to tuning the optoelectronic properties of HMAs.

For dilute nitride and dilute bismide HMAs, the incorporation of dilute fractions of N and/or Bi leads to a large bandgap reduction – approximately 150 meV for a N mole fraction of $x_N = 0.01$[1] and 84 meV for a Bi mole fraction of $y_{Bi} = 0.01$[2,3] – which allows GaAsN and GaAsBi alloys to access a range of wavelengths in the near-infrared with relatively small change in lattice parameter. Consequently, dilute nitride and dilute bismide alloys are being pursued for a variety of applications, from temperature-insensitive laser diodes to ultra-high efficiency multijunction photovoltaic cells,[4,5,6,7] Co-alloying both N and Bi with GaAs is expected to further extend the

accessible wavelength range, while maintaining lattice-matching to GaAs substrates and allowing independent control of the conduction and valence band offsets in heterostructures.[6,7]

However, experimental work in recent years has revealed numerous challenges to achieving high-quality epitaxial growth of dilute nitride and dilute bismide alloys. For GaAsN, degradation of electron transport properties and optical efficiency with increasing N fraction has been attributed to the formation of a high concentration of N-related interstitial complexes.[8,9] For GaAsBi, significant Bi incorporation has required low growth temperatures and near-Ga-rich conditions, leading to detrimental formation of point defects associated with non-stoichiometric GaAs,[10] as well as Ga or Bi surface droplets.[11,12,13,14] Both dilute nitride and dilute bismide alloys have exhibited significant sensitivity to the local atomic environments of N or Bi solute atoms. In the case of GaAsNBi alloys, relatively few experimental studies have been reported to date. Realizing the enhanced bandgap and strain engineering possibilities predicted for GaAsNBi will require an understanding of the mechanisms of alloy formation during co-incorporation of N and Bi.

This chapter begins by highlighting applications for dilute nitride and dilute bismide HMAs in optoelectronic devices operating in the near infrared. We then describe the extraordinary composition-dependence of bandgap energy in HMAs compared to conventional semiconductor alloys and review theoretical models for the influence of N and Bi on the GaAs band structure. We discuss the challenges associated with epitaxial growth of dilute nitride and dilute bismide alloys, with a review of the available experimental findings for GaAsNBi alloys. The chapter concludes with an outline of the dissertation.

1.2 Optoelectronic applications in the near-infrared

Epitaxially grown compound semiconductor alloys that combine elements from group III and group V of the periodic table are at the heart of many modern optoelectronic devices, from solid-state lighting and optical data storage to fiber-optic telecommunications and ultra-high-efficiency solar cells.[15,16] In particular, optoelectronic devices operating in the near-infrared (near-IR) wavelength range from approximately 0.8 to 3 μm have developed tremendous technological importance in recent years. For example, rapid growth of the internet and demand for high-speed data transmission has spurred the widespread use of fiber-optic telecommunications networks, which rely on lasers emitting at 1.3 or 1.55 μm. The bandgaps corresponding to these wavelengths (0.95 eV and 0.8 eV) have traditionally been achieved using InGaAsP or InAlGaAs alloys on InP substrates. Because of the temperature-sensitivity of the bandgap and optical efficiency in these materials, many applications require energy-intensive active cooling during operation, which accounts for the majority of the device power consumption.[5] Furthermore, while use of GaAs substrates, rather than InP substrates, would be more economical and allow improvement of electrical and optical confinement of carriers,[6] materials capable of both lattice-matching to GaAs and emitting at 1.3 or 1.55 μm have not been available historically using conventional III-V semiconductor alloys.

Wavelengths in the near-IR range also make up a significant portion of the solar spectrum, as shown in the plot of solar irradiance vs wavelength in Figure 1.2.[17] Consequently, optimizing solar energy harvesting requires materials with bandgap energies within or below this range. The highest-efficiency solar cells demonstrated to date use a multi-junction structure consisting of three or more semiconductor alloy layers with different bandgaps, each selected to absorb a separate portion of the solar spectrum, as shown in Figure 1.2.[18] Detailed balance calculations of the limiting efficiency in devices with four or more junctions predict that the power conversion

efficiency can be pushed past 50% if a layer with a bandgap close to 1eV is included; [17,19] however identifying a suitable material that possesses both a bandgap near 1eV and a lattice parameter close to that of the GaAs or Ge substrate has been challenging.

1.3 Bandgap engineering with highly mismatched alloys

Access to the wide variety of energy bandgaps required for various optoelectronic applications can be achieved by alloying III-V binary compounds. In Figure 1.1, elemental and binary semiconductors are shown as points on a plot of bandgap energy versus lattice parameter. The bowed lines connecting points indicate the bandgaps and lattice parameters of ternary compounds formed by alloying binary compounds, e.g., $In_xGa_{1-x}As$ formed by alloying GaAs and InAs. The lattice parameter of the alloy typically follows Vegard's Law, expressed as a linear interpolation of the lattice parameters of the binary compounds. The bandgap, E_g, of an alloy $A_{1-x}B_x$ can typically be described by a linear interpolation between the bandgaps of its binary constituents, A and B, modified by a bowing parameter, b:[20]

$$E_g(A_{1-x}B_x) = (1-x)E_g(A) + xE_g(B) - bx(1-x) \tag{1.1}$$

For conventional III-V alloys, the value b is typically fractions of an eV.[20] However, for HMAs, b can be several eV and is often composition-dependent.[21] In highly mismatched III-V-N and III-V-Bi alloys, large bowing parameters, $b_{GaAsN} = 7.5 - 40$ eV[22,23] and $b_{GaAsBi} = 2 - 9$ eV,[24,25] enable significant bandgap reductions with relatively small changes in lattice parameter.

The discovery in the early 1990s[26] that dilute concentrations of N induce a steep bandgap reduction (~ 150 meV for $x_N = 0.01$)[1] opened up new possibilities for bandgap engineering, offering access to a range of technologically important bandgaps below that of GaAs with only a small deviation from the GaAs lattice parameter. Indeed, with the addition of In and/or Sb to

compensate the tensile strain introduced by N, dilute nitride alloys enabled 1.3 μm and 1.55 μm GaAs-based laser diodes,[27,28,29] as well as the first lattice-matched solar cell to reach 44% efficiency.[30,31].

A few years after the first studies of $GaAs_{1-x}N_x$, the first synthesis of $GaAs_{1-y}Bi_y$[32] revealed that dilute concentrations of Bi also induce a steep bandgap reduction in GaAs, ~ 84 meV for $y_{Bi} = 0.01$.[2,3] Thus, Bi incorporation into GaAs offers another route to accessing bandgaps in the near-infrared with only a small deviation from the GaAs lattice parameter. Furthermore, it has been proposed that dilute bismide alloys used in the active region of laser diodes could exhibit temperature-insensitive bandgaps[32,33,34,35] and reduced non-radiative Auger recombination,[36] both of which would enable telecommunications lasers without the energy-intensive active cooling required for conventional InGaAsP lasers.

Co-incorporation of N and Bi to form $GaAs_{1-x-y}N_xBi_y$ quaternary alloys presents the possibility of leveraging the advantages of both dilute nitride and dilute bismide alloys. The bandgap reduction associated with Bi incorporation (84 meV for $y_{Bi} = 0.01$)[2,3] is much larger than that of Sb (21 meV) or In (16 meV),[37] such that use of Bi to compensate the tensile strain introduced by N allows lattice-matching to GaAs or Ge substrates while greatly extending the accessible wavelength range. In addition, because N primarily influences the conduction band (CB) edge while Bi primarily influences the valence band (VB) edge, as discussed in Section 1.4, GaAsNBi alloys are expected to allow versatile tuning of the band alignment at heterojunctions.[6,7]

1.4 Band anti-crossing model

The composition-dependence of the bandgaps of GaAsN, GaAsBi, and other HMAs is often described using the band anticrossing (BAC) model[38] or valence band anticrossing (VBAC)

model.[39] According to the BAC model, the incorporation of N into GaAs introduces localized N impurity states, forming a resonant defect level above the GaAs conduction band edge (CBE) with energy E_N. Interaction between the defect level, E_N, and the GaAs CBE induces a splitting of the conduction band into E_+ and E_- sub-bands, as shown in Figure 1.3. As the N fraction increases, the splitting between E_+ and E_- increases, effectively leading to a reduction of the bandgap as the CBE follows the E_- energy level. For the incorporation of Bi in GaAs, an analogous VBAC model has been used to model the reduction of the bandgap with Bi fraction by assuming a Bi-induced defect level splits the heavy-hole (HH), light-hole, and SO bands of the GaAs valence band into six valence sub-bands, $E_+(HH_+, LH_+, SO_+)$ and $E_-(HH_-, LH_-, SO_-)$, as shown in Figure 1.4.

While the BAC model has been widely used to explain the composition dependence of the bandgap of dilute nitride semiconductor alloys, it fails to account for other reported properties of dilute nitride alloys, including the composition-dependence of the electron effective mass[40] and the electron gyromagnetic ratio.[41] These properties have been accounted for theoretically using a linear combination of isolated nitrogen states (LCINS) model,[42,43] in which a variety of local atomic environments for the N solute atoms are considered, including isolated N atoms, N pairs, and larger N clusters, as illustrated in Figure 1.5. Indeed, a number of studies have highlighted the significant dependence of dilute nitride alloy properties on the local atomic environment of N solute atoms. Pseudopotential calculations of the dependence of bandgap on N atomic arrangement predict that clustering or anti-clustering of N atoms can lead to significant local variations in the bandgap of GaAsN.[44] The observation of a Stokes shift and significantly broadened photoreflectance features at low temperature,[45] as well as S-shaped temperature-dependence of photoluminescence emission,[46,47,48] has been attributed to localization of carriers at local conduction band minima due to differing local N atomic environments. In addition, measurements

of enhancements in carrier transport properties[8] and optical efficiencies[49] of dilute nitride alloys upon thermal annealing have been correlated with changes to the concentrations of N interstitials and In-N bonds, respectively – i.e., with modifications of the local N atomic configurations.

A similar strong dependence of band structure on the local Bi atomic environment has been predicted for dilute bismide alloys. For example, density functional theory (DFT) calculations comparing isolated Bi atoms and 2-, 3-, or 4-atom Bi clusters predict local variations in the bandgap and valence band splitting on the order of hundreds of meV, as shown in Figure 1.8.[50,51] Broadening of spontaneous emission and modal gain spectra,[52,53] as well as S-shaped temperature dependence of photoluminescence emission,[54,55,56,57] have been attributed to these local variations in the local Bi atomic configuration and the corresponding local variations in the band structure.[58,59]

1.5 Epitaxy of dilute nitride and dilute bismide alloys: challenges

Incorporation of either N or Bi into GaAs poses significant challenges. Implementation of dilute nitride alloys in devices has been hindered by N-induced degradation of electron mobility and optical efficiency. The electron mobility of GaAsN alloys decreases rapidly with increasing N fraction.[8,60] The reduction in electron mobility has been attributed in part to the presence of a significant fraction of N interstitials[9,61,62] which act as carrier trapping and scattering centers.[8] Low luminescence efficiency in as-grown dilute nitride alloys has also been attributed to N interstitials,[9] which have been reported to predominantly take the form of N-N pairs or N-As occupying As lattice sites.[63,64,65,66,67,68] Post-growth thermal annealing can improve both the carrier transport properties and the optical efficiency, which has been correlated with a reduction in N interstitial

concentration.[8,9,69] In addition, epitaxy of GaAsN within a "forbidden window" of temperatures and growth rates can lead to significant surface roughening. [4,70]

For GaAsBi alloys, negligible Bi is incorporated for molecular beam epitaxy at temperatures above 400 °C, and the low growth temperatures employed lead to an increased concentration of points defects related to excess As incorporation, including As antisites, As_{Ga}.[71,72] The concentration of As_{Ga} in non-stoichiometric GaAs can be estimated from an increase in the lattice parameter of the non-stoichiometric layer compared to a stoichiometric GaAs substrate.[72] While the concentration of As_{Ga} tends to increase with decreasing temperature, as shown in Figure 1.6,[73] epitaxy at higher temperatures reportedly leads to increased compositional inhomogeneity[74] and reduced Bi solubility.[75,76] Furthermore, for GaAsBi epitaxy using As_2, significant Bi incorporation can only be achieved near to the threshold between As-rich and Ga-rich conditions, i.e., the stoichiometric threshold.[3,11] Near the stoichiometric threshold, and for high Bi fluxes, Ga, Bi, or Ga-Bi surface droplets often form,[11,13] which can roughen the surface and induce compositional inhomogeneities.[12,14] Growth using As_4 has been found to enable Bi incorporation under more As-rich conditions, as shown in Figure 1.7.[77,76,78,79] In addition, significant broadening of optical emission in dilute bismides[52,53,58,59] is thought to be related to the non-uniform local configurations of Bi atoms, including reports of clustering[80,81,82] and short[83,84] and long[85,86,87] range chemical ordering of Bi atoms.

GaAsNBi alloys have the potential to combine the advantages of both dilute nitrides and dilute bismides: access to a wide range of bandgaps in the near- and mid-infrared, independent control of conduction and valence band offsets, lattice-matching to GaAs or Ge substrates, and optical emission with reduced temperature sensitivity. However, epitaxy of high-quality GaAsNBi alloys also must overcome the combined challenges of N and Bi incorporation. To date, there have

been relatively few reports on the synthesis of GaAsNBi alloys. To accommodate Bi incorporation, growth of GaAsNBi alloys has been limited to temperatures between 350 – 400 °C for MBE[37,88,89,90,91,92,93,94] and 400 – 450 °C for metal-organic vapor phase epitaxy (MOVPE).[95,96] with group V/III ratios close to the transition between As-rich and Ga-rich conditions. Reports of optical measurements including photoluminescence, photoreflectance, and spectroscopic ellipsometry have indicated support for the bandgap reduction and spin-orbit splitting predicted for N and Bi co-incorporation. Measurements by nuclear reaction analysis and time-resolved terahertz spectroscopy have suggested a significant concentration of N interstitials[97] and suppressed electron mobility,[98] though the origins of these properties remain unknown.

1.6 Influence of surface reconstruction on dilute nitride and dilute bismide epitaxy

The surface reconstruction during epitaxy has been reported to influence both N and Bi incorporation in GaAs. For example, growth of GaAsN with a (2x1) reconstruction has been reported to increase substitutional N incorporation compared to growth with a (3x1) or (2x4) reconstruction.[62] Introduction of a non-incorporating Bi flux during GaAsN growth has been found to smooth the surface and induce a (1x3) reconstruction, accompanied by enhanced N incorporation,[99,100] though the mechanism of the enhanced N incorporation has not been resolved. For Bi incorporation in GaAsBi alloys, growth on a (2x1) reconstruction has been correlated with enhanced photoluminescence intensity and x-ray diffraction Pendellösung fringes compared to growth on a (1x3) reconstruction.[101] Scanning tunneling microscopy (STM) studies of the Bi-induced (1x3) surface indicate disordered dimer rows and an increased ratio of [110]-oriented to [$1\bar{1}0$]-oriented step edges.[102] On the other hand, STM studies of the Bi-induced (2x1) surface reconstruction have suggested well-ordered rows of Bi dimers extending in the [110]

direction,[103,104] which has been proposed to lead to chemical ordering of the {111} planes in GaAsBi.[85,104] For epitaxy of GaAsNBi alloys, the role of surface reconstruction in N and Bi co-incorporation remains unknown.

1.7 Outline of the dissertation

This dissertation is organized as follows. In Chapter 2, we describe the experimental techniques used during this research, including molecular-beam epitaxy, reflection high-energy electron diffraction, high-resolution x-ray diffraction, Hall effect measurements, ion beam analysis, atomic force microscopy, electron microscopy, photoluminescence spectroscopy, and photoreflectance spectroscopy.

Chapter 3 begins with a review of earlier studies of Si doping of GaAs and the epitaxial conditions that produce n-type or p-type conductivity in GaAs:Si. Next, we describe the experimental techniques we used to investigate the electronic and structural properties of Si-doped GaAs and GaAsBi films. Si incorporation in GaAs(Bi) with an (n x 3) reconstruction leads to n-type conductivity, while growth with a (2 x 1) reconstruction leads to p-type conductivity. We hypothesize that the presence or absence of surface arsenic dimers prevents or enables dopant incorporation into arsenic lattice sites. We finish with a discussion of the surface morphologies and carrier transport properties of n-type and p-type Si-doped GaAsBi alloys. These findings suggest Si is a promising alternative to C or Be for p-type doping of GaAs and related alloys.

In Chapter 4, we review reports of the influence of Bi on N incorporation and discuss epitaxial conditions for co-incorporation of N and Bi in GaAsNBi alloys. We then describe the epitaxial conditions used for growth of GaAsNBi alloys and the combined experimental and computational methods used to investigate N and Bi incorporation in two sets of GaAsNBi films:

a N flux series and a Bi flux series. The incorporation of Bi is found to be independent of N flux, while the total N incorporation and the fraction of N atoms occupying non-substitutional lattice sites increase with increasing Bi flux. A comparison of channeling nuclear reaction analysis along the [100], [110], and [111] directions with Monte Carlo-Molecular Dynamics simulations indicates that the non-substitutional N primarily incorporate as $(N\text{-}As)_{As}$ interstitial complexes. We discuss the influence of Bi adatoms on the formation of arsenic-terminated [110]-oriented step-edges on a (1x3) surface reconstruction, and the resulting enhancement in total N incorporation via the formation of additional $(N\text{-}As)_{As}$. These insights provide a pathway to tailored N incorporation in GaAsNBi and related alloys.

In Chapter 5, we review evidence for the dependence of dilute nitride and dilute bismide alloy properties on the local environments of N and Bi solute atoms and propose long-range chemical ordering as a route to tuning the N and Bi local atomic environments. We introduce two sets of GaAsN:Bi alloys, a Bi flux series and a temperature series, distinct from those in Ch. 4, and examine their surface reconstructions, compositions and surface morphologies. We reveal the presence of long-range chemical ordering in GaAsNBi and demonstrate its dependence on a (2x1) surface reconstruction accompanied by a Bi flux. We propose that Bi enhances the formation of dimer rows aligned along the [110] direction in the (2x1) surface reconstruction, which in turn drives the formation of alternating N-rich and Bi-rich {111} planes.

In Chapter 6, we discuss the composition-dependence of lattice misfit and optical properties in GaAsNBi alloys. Using our analyses of the N flux series and the Bi flux series of GaAsNBi films from Ch. 4, we present a new map of the out-of-plane misfit, and a new N/Bi ratio for lattice-matching of GaAsNBi alloys with GaAs substrates. Using ion beam measurements of alloy composition and photoreflectance measurements of bandgaps, we map the bandgap energies

of GaAsNBi as a function of N and Bi fractions. In addition, a comparison of photoluminescence and photoreflectance reveals a Stokes shift, revealing the presence of Bi-related localized states approximately 0.18 eV above the valence band edge. Finally, in Chapter 7, we present a summary and suggestions for future work.

1.8 Figures

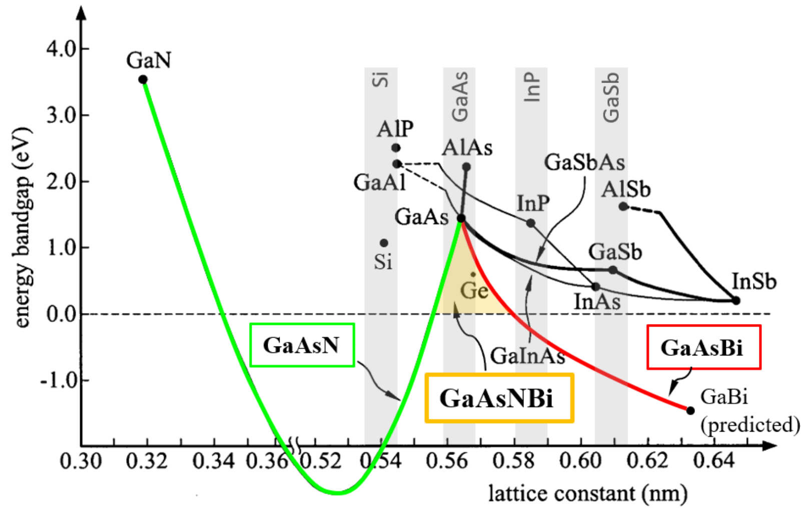

Figure 1.1 Energy bandgap versus lattice parameter for various group III-V binary compound semiconductors. Solid lines between points represent the bandgaps and lattice parameters for alloys of those binary compounds. Gray vertical bars indicate the lattice parameters of several commercially available substrates. Due to the giant bandgap bowing induced by alloying small fractions of N or Bi with GaAs, GaAsNBi alloys can access a wide range of bandgaps while remaining nearly lattice-matched to GaAs, as shown by the orange-shaded region. Adapted from Ref. 105.

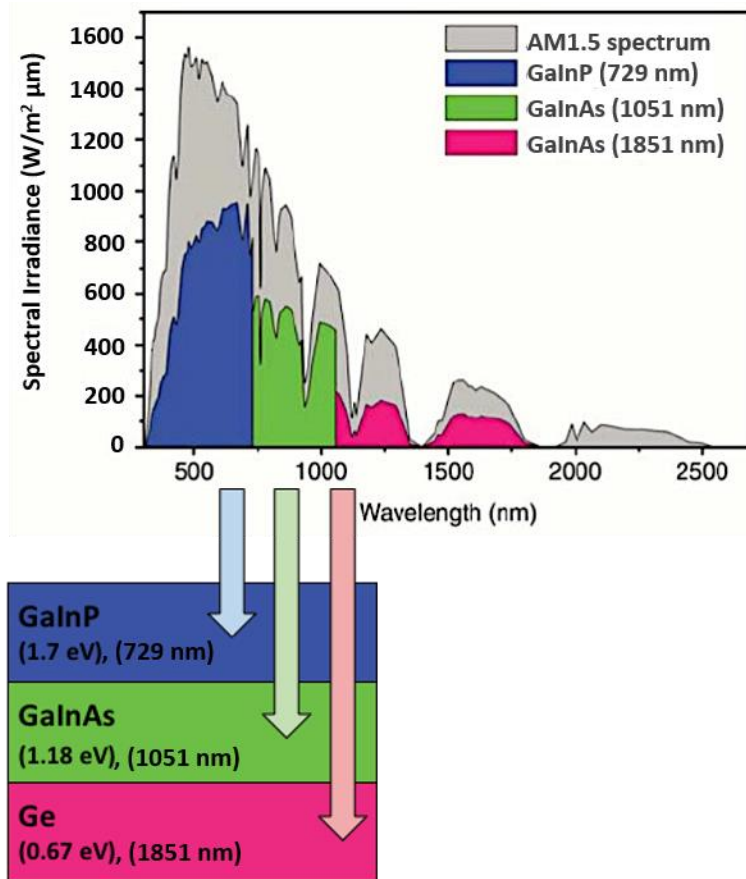

Figure 1.2 The AM1.5 solar spectrum in gray, overlaid with blue, green, and magenta regions representing the portions of the solar spectrum that can be absorbed by a 3-junction photovoltaic cell with bandgaps of 1.70, 1.18, and 0.67 eV. Adapted and reprinted with permission from Ref. 17 (Copyright 2007, Cambridge University Press).

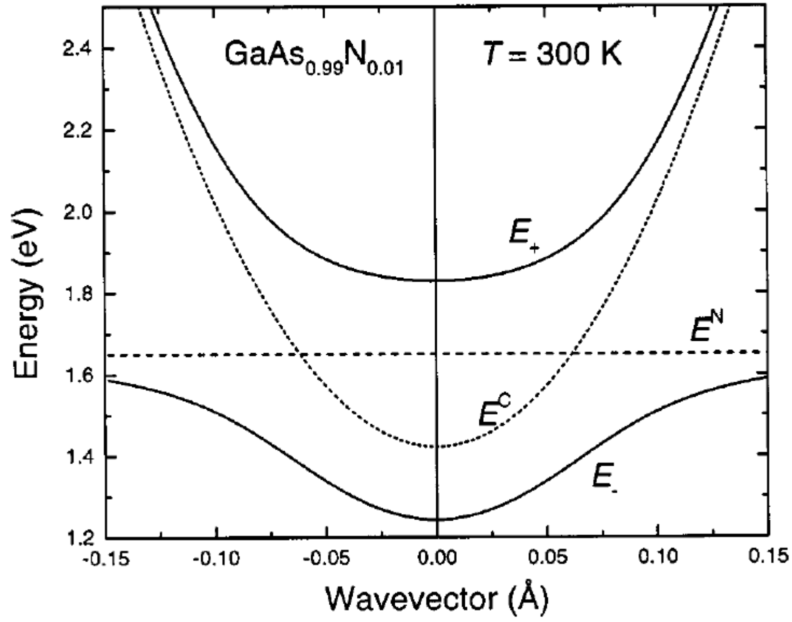

Figure 1.3 Illustration of the band anticrossing model for GaAsN. N induces a defect level, E^N, that interacts with the GaAs conduction band, E^C, to split the conduction band into two sub-bands, E_+ and E_-, effectively leading to a lowering of the GaAsN conduction band edge. Reprinted with permission from Ref. 106 (Copyright 2003, AIP Publishing).

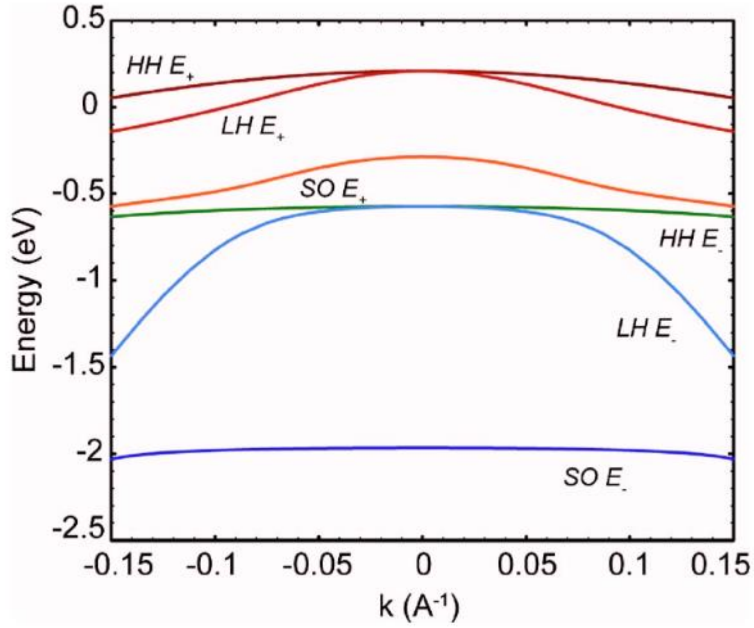

Figure 1.4 Illustration of the valence band anticrossing model for GaAsBi. Bi induces a defect level that interacts with the GaAs valence band to split the heavy-hole (HH), light-hole (LH), and spin-orbit split-off (SO) bands into E_+(HH_+ , LH_+, SO_+) and E_-(HH_-, LH_-, SO_-) sub-bands, effectively leading to a rise of the GaAsBi valence band edge. Reprinted with permission from Ref. 39 (Copyright 2007, AIP Publishing).

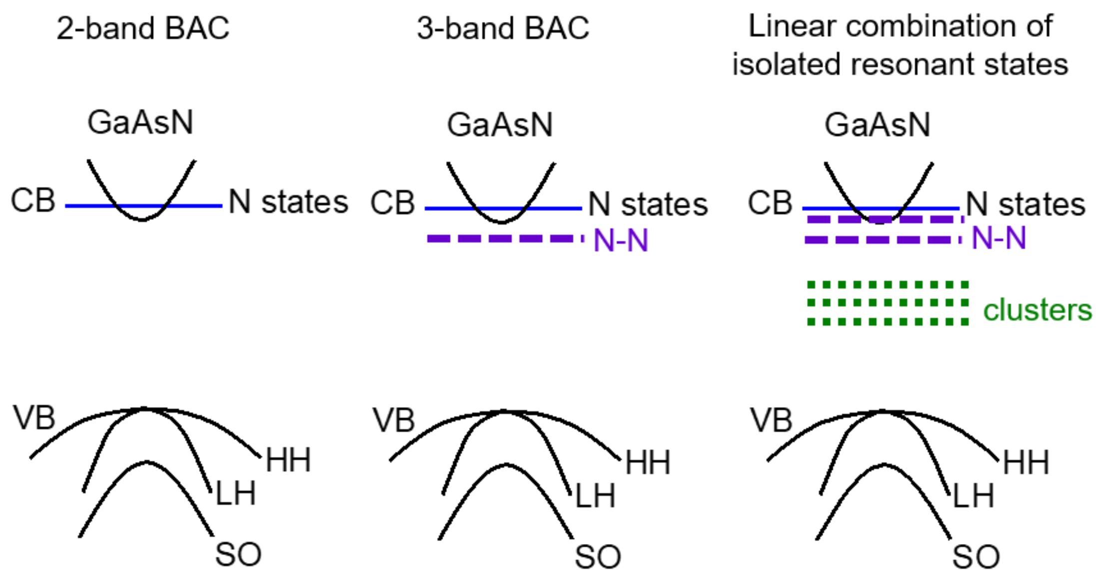

Figure 1.5 Schematics of the GaAsN band structure for different N local atomic environments, including (a) isolated N, as in the band anti-crossing model;[38] (b) isolated N and N-N pairs; and (c) isolated N, N-N pairs, and N clusters, as in the linear combination of isolated resonant states model.[42] Reprinted from Ref. 107 (Copyright 2017, Timothy Yu Cheng Jen).

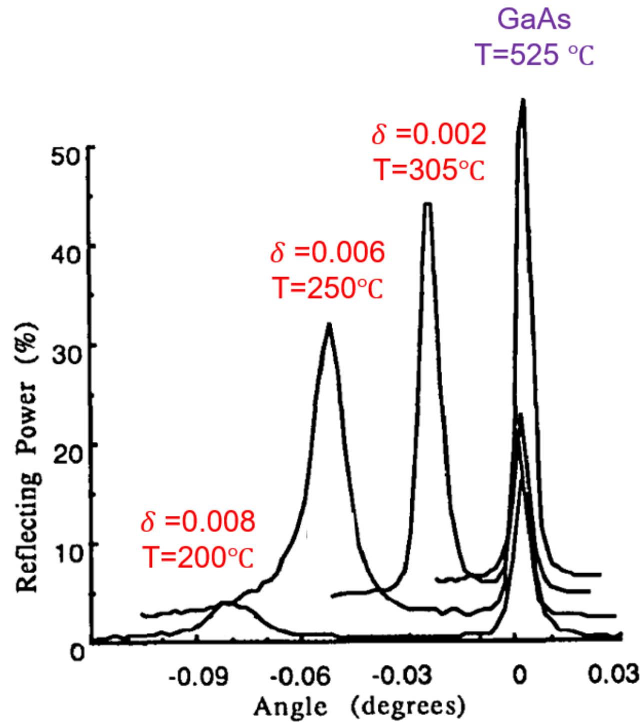

Figure 1.6 X-ray rocking curves from GaAs layers grown at various temperatures, *T*. As the temperature is decreased, the diffraction peak shifts to lower angles, indicating in increase in lattice parameter associated with incorporation of arsenic antisites, As_{Ga}, in non-stoichiometric GaAs, $Ga_{1-\delta}As_{1+\delta}$. The mole fraction of As_{Ga}, δ, is estimated from the peak separation between each non-stoichiometric GaAs peak and the peak for GaAs grown at 525 °C.[72] Adapted and reprinted with permission from Ref. 73 (Copyright 1990, Cambridge University Press).

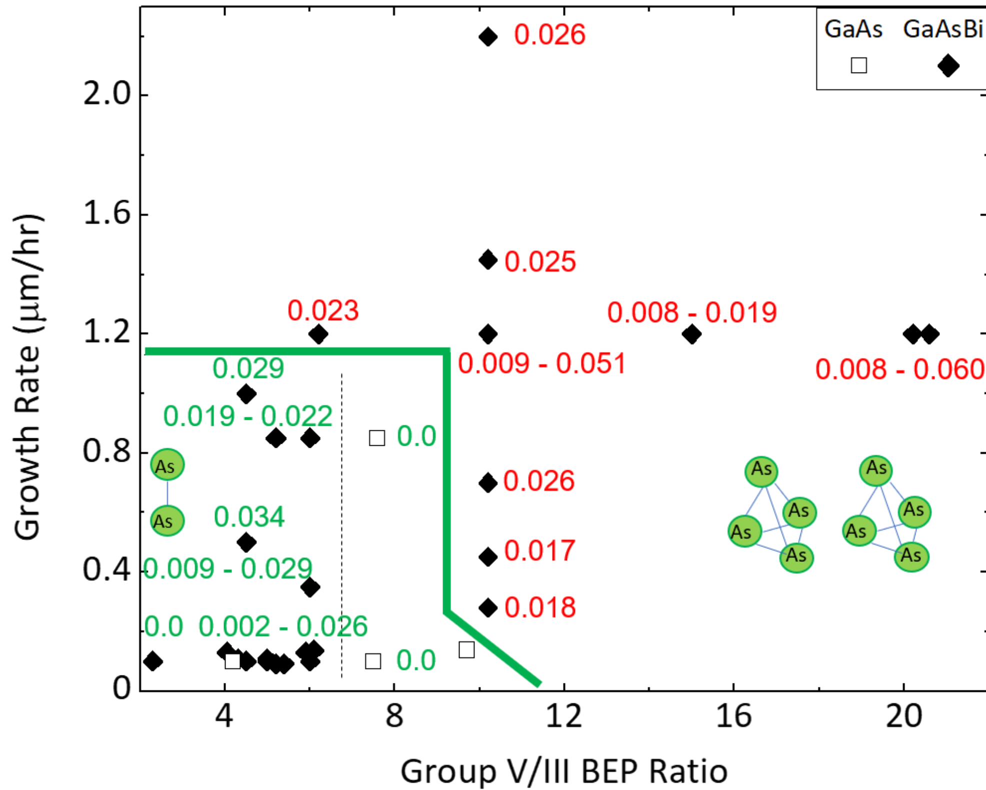

Figure 1.7 GaAs(Bi) films grown using either As dimers (As_2) or As tetramers (As_4), for various growth rates and group V/III beam-equivalent pressure (BEP) ratios. The range of Bi fractions achieved at each growth condition is labeled adjacent to each symbol. With As_2, negligible Bi incorporates for group V/III ratios > 6, while with As_4, significant Bi is incorporated even at group V/III ratios > 20. Adapted from Ref. 78 (Copyright 2015, Richard L. Field III).

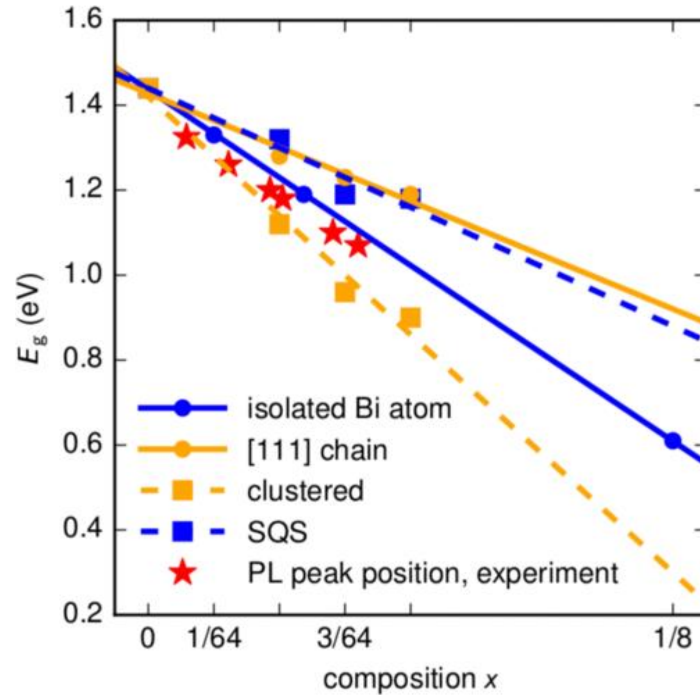

Figure 1.8 First-principles calculations of the variation of the bandgap of GaAsBi alloys for various Bi configurations as a function of Bi fraction. The bandgaps for isolated Bi atoms, [111] chains, Bi clusters, and special quasirandom structures (SQS) diverge with increasing Bi fraction. Photoluminescence (PL) measurements[108] of bandgap are shown for comparison. Reprinted with permission from Ref. 50 (Copyright 2018, American Physical Society).

1.9 References

[1] M. Kondow, K. Uomi, K. Hosomi, and T. Mozume, "Gas-Source Molecular Beam Epitaxy of GaNxAs1-x Using a N Radical as the N Source", Jpn. J. Appl. Phys. 33, L1056 (1994).

[2] S. Francoeur, M.J. Seong, A. Mascarenhas, S. Tixier, M. Adamcyk, and T. Tiedje, "Band gap of GaAs1-xBix, 0 < x < 3.6%", Appl. Phys. Lett. 82, 3874 (2003).

[3] S. Tixier, M. Adamcyk, T. Tiedje, S. Francoeur, A. Mascarenhas, P. Wei, and F. Schiettekatte, "Molecular Beam Epitaxy Growth of GaAs1-xBix", Appl. Phys. Lett. 82, 2245 (2003).

[4] S.R. Bank, H. Bae, L.L. Goddard, H.B. Yuen, M.A. Wistey, R. Kudrawiec, and J.S. Harris, "Recent Progress on 1.55-µm Dilute-Nitride Lasers", IEEE J. Quantum Elect. 43, 773 (2007).

[5] I.P. Marko and S.J. Sweeney, "Progress Toward III–V Bismide Alloys for Near- and Midinfrared Laser Diodes", IEEE J. Quantum Elect. 23, 1 (2017).

[6] C.A. Broderick, M. Usman, S.J. Sweeney, and E.P. O'Reilly, "Band Engineering in Dilute Nitride and Bismide Semiconductor Lasers", Semicon. Sci. Tech. 27, 094011 (2012).

[7] S.J. Sweeney and S.R. Jin, "Bismide-Nitride Alloys: Promising for Efficient Light Emitting Devices in the near- and Mid-Infrared", J. Appl. Phys. 113, 043110 (2013).

[8] Y. Jin, R.M. Jock, H. Cheng, Y. He, A.M. Mintarov, Y. Wang, C. Kurdak, J.L. Merz, and R.S. Goldman, "Influence of N Interstitials on the Electronic Properties of GaAsN Alloys", Appl. Phys. Lett. 95, 062109 (2009).

[9] S.G. Spruytte, C.W. Coldren, J.S. Harris, W. Wampler, P. Krispin, K. Ploog, and M.C. Larson, "Incorporation of Nitrogen in Nitride-Arsenides: Origin of Improved Luminescence Efficiency after Anneal", J. Appl. Phys. 89, 4401 (2001).

[10] P.M. Mooney, K.P. Watkins, Z. Jiang, A.F. Basile, R.B. Lewis, V. Bahrami-Yekta, M. Masnadi-Shirazi, D.A. Beaton, and T. Tiedje, "Deep Level Defects in N-Type GaAsBi and GaAs Grown at Low Temperatures", J. Appl. Phys. 113, 133708 (2013).

[11] G. Vardar, S.W. Paleg, M.V. Warren, M. Kang, S. Jeon, and R.S. Goldman, "Mechanisms of Droplet Formation and Bi Incorporation during Molecular Beam Epitaxy of GaAsBi", Appl. Phys. Lett. 102, 042106 (2013).

[12] C.R. Tait, L. Yan, and J.M. Millunchick, "Droplet Induced Compositional Inhomogeneities in GaAsBi", Appl. Phys. Lett. 111, 042105 (2017).

[13] A.J. Ptak, R. France, D.A. Beaton, K. Alberi, J. Simon, A. Mascarenhas, and C.-S. Jiang, "Kinetically Limited Growth of GaAsBi by Molecular-Beam Epitaxy", J. Cryst. Growth 338, 107 (2012).

[14] A.W. Wood, K. Collar, J. Li, A.S. Brown, and S.E. Babcock, "Droplet-Mediated Formation of Embedded GaAs Nanowires in MBE $GaAs_{1-x}Bi_x$ Films", Nanotechnology 27, 115704 (2016).

[15] S. Mokkapati and C. Jagadish, "III-V Compound SC for Optoelectronic Devices", Mater. Today 12, 22 (2009).

[16] J.A. del Alamo, "Nanometre-Scale Electronics with III–V Compound Semiconductors", Nature 479, 317 (2011).

[17] F. Dimroth and S. Kurtz, "High-Efficiency Multijunction Solar Cells", MRS Bull. 32, 230 (2007).

[18] M.A. Green, Y. Hishikawa, E.D. Dunlop, D.H. Levi, J. Hohl-Ebinger, and A.W.Y. Ho-Baillie, "Solar Cell Efficiency Tables (Version 52)", Prog. Photovoltaics 26, 427 (2018).

[19] R.R. King, D. Bhusari, A. Boca, D. Larrabee, X.-Q. Liu, W. Hong, C.M. Fetzer, D.C. Law, and N.H. Karam, "Band Gap-Voltage Offset and Energy Production in next-Generation Multijunction Solar Cells", Prog. Photovoltaics 19, 797 (2011).

[20] I. Vurgaftman, J.R. Meyer, and L.R. Ram-Mohan, "Band Parameters for III–V Compound Semiconductors and Their Alloys", J. Appl. Phys. 89, 5815 (2001).

[21] J. Wu, W. Shan, and W. Walukiewicz, "Band Anticrossing in Highly Mismatched III–V Semiconductor Alloys", Semicond. Sci. Technol. 17, 860 (2002).

[22] G. Pozina, I. Ivanov, B. Monemar, J.V. Thordson, and T.G. Andersson, "Properties of Molecular-Beam Epitaxy-Grown GaNAs from Optical Spectroscopy", J. Appl. Phys. 84, 3830 (1998).

[23] U. Tisch, E. Finkman, and J. Salzman, "The Anomalous Bandgap Bowing in GaAsN", Appl. Phys. Lett. 81, 463 (2002).

[24] A. Janotti, S.-H. Wei, and S.B. Zhang, "Theoretical Study of the Effects of Isovalent Coalloying of Bi and N in GaAs", Phys. Rev. B 65, 115203 (2002).

[25] X. Lu, D.A. Beaton, R.B. Lewis, T. Tiedje, and Y. Zhang, "Composition Dependence of Photoluminescence of GaAs1−xBix Alloys", Appl. Phys. Lett. 95, 041903 (2009).

[26] M. Weyers, M. Sato, and H. Ando, "Red Shift of Photoluminescence and Absorption in Dilute GaAsN Alloy Layers", Jpn. J. Appl. Phys. 31, L853 (1992).

[27] R. Fehse, S. Tomic, A.R. Adams, S.J. Sweeney, E.P. O'Reilly, A. Andreev, and H. Riechert, "A Quantitative Study of Radiative, Auger, and Defect Related Recombination Processes in 1.3-μm GaInNAs-Based Quantum-Well Lasers", IEEE J. Sel. Top. Quant. 8, 801 (2002).

[28] N. Tansu, Jeng-Ya Yeh, and L.J. Mawst, "High-Performance 1200-Nm InGaAs and 1300-Nm InGaAsN Quantum-Well Lasers by Metalorganic Chemical Vapor Deposition", IEEE J. Sel. Top. Quant. 9, 1220 (2003).

[29] S.R. Bank, H.P. Bae, H.B. Yuen, M.A. Wistey, L.L. Goddard, and J.S. Harris, "Room-Temperature Continuous-Wave 1.55 μm GaInNAsSb Laser on GaAs", Electron. Lett. 42, 156 (2006).

[30] V. Sabnis, H. Yuen, and M. Wiemer, "High-Efficiency Multijunction Solar Cells Employing Dilute Nitrides", AIP Conf. Proc. 1477, 14 (2012).

[31] M.A. Green, K. Emery, Y. Hishikawa, W. Warta, and E.D. Dunlop, "Solar Cell Efficiency Tables (Version 41)", Prog. Photovoltaics 21, 1 (2013).

[32] K. Oe and H. Okamoto, "New Semiconductor Alloy GaAs1-xBix Grown by Metal Organic Vapor Phase Epitaxy", Jpn. J. Appl. Phys. 37, L1283 (1998).

[33] K. Oe and H. Asai, "Proposal on a Temperature-Insensitive Wavelength Semiconductor Laser", IEICE T. Electron. E79-C, 1751 (1996).

[34] J. Yoshida, T. Kita, O. Wada, and K. Oe, "Temperature Dependence of $GaAs_{1-x}Bi_x$ Band Gap Studied by Photoreflectance Spectroscopy", Jpn. J. Appl. Phys. 42, 371 (2003).

[35] M. Yoshimoto, W. Huang, G. Feng, and K. Oe, "New Semiconductor Alloy GaNAsBi with Temperature-Insensitive Bandgap", Phys. Status Solidi B 243, 1421 (2006).

[36] Z. Batool, K. Hild, T.J.C. Hosea, X. Lu, T. Tiedje, and S.J. Sweeney, "The Electronic Band Structure of GaBiAs/GaAs Layers: Influence of Strain and Band Anti-Crossing", J. Appl. Phys. 111, 113108 (2012).

[37] S. Tixier, S.E. Webster, E.C. Young, T. Tiedje, S. Francoeur, A. Mascarenhas, P. Wei, and F. Schiettekatte, "Band Gaps of the Dilute Quaternary Alloys GaNxAs1−x−yBiy and Ga1−yInyNxAs1−x", Appl. Phys. Lett. 86, 112113 (2005).

[38] W. Shan, W. Walukiewicz, J. Ager, E. Haller, J. Geisz, D. Friedman, J. Olson, and S. Kurtz, "Band Anticrossing in GaInNAs Alloys", Phys. Rev. Lett. 82, 1221 (1999).

[39] K. Alberi, O.D. Dubon, W. Walukiewicz, K.M. Yu, K. Bertulis, and A. Krotkus, "Valence Band Anticrossing in GaBixAs1−x", Appl. Phys. Lett. 91, 051909 (2007).

[40] T. Dannecker, Y. Jin, H. Cheng, C.F. Gorman, J. Buckeridge, C. Uher, S. Fahy, C. Kurdak, and R.S. Goldman, "Nitrogen Composition Dependence of Electron Effective Mass in GaAs1−xNx", Phys. Rev. B 82, 125203 (2010).

[41] G. Pettinari, F. Masia, A. Polimeni, M. Felici, A. Frova, M. Capizzi, A. Lindsay, E.P. O'Reilly, P.J. Klar, W. Stolz, G. Bais, M. Piccin, S. Rubini, F. Martelli, and A. Franciosi, "Influence of Nitrogen-Cluster States on the Gyromagnetic Factor of Electrons in GaAs1-xNx", Phys. Rev. B 74, 245202 (2006).

[42] E.P. O'Reilly, A. Lindsay, and S. Fahy, "Theory of the Electronic Structure of Dilute Nitride Alloys: Beyond the Band-Anti-Crossing Model", J. Phys.-Cond. Mat. 16, S3257 (2004).

[43] E.P. O'Reilly, A. Lindsay, P.J. Klar, A. Polimeni, and M. Capizzi, "Trends in the Electronic Structure of Dilute Nitride Alloys", Semicon. Sci. Tech. 24, 033001 (2009).

[44] L. Bellaiche and A. Zunger, "Effects of Atomic Short-Range Order on the Electronic and Optical Properties of GaAsN, GaInN, and GaInAs Alloys", Phys. Rev. B 57, 4425 (1998).

[45] R. Kudrawiec, G. Sęk, K. Ryczko, J. Misiewicz, P. Sundgren, C. Asplund, and M. Hammar, "The Nature of Optical Transitions in Ga0.64In0.36As1−xNx/GaAs Single Quantum Wells with Low Nitrogen Content (X≤0.008)", Solid State Commun. 127, 613 (2003).

[46] M.-A. Pinault and E. Tournié, "On the Origin of Carrier Localization in Ga1−xInxNyAs1−y/GaAs Quantum Wells", Appl. Phys. Lett. 78, 1562 (2001).

[47] I.A. Buyanova, W.M. Chen, and B. Monemar, "Electronic Properties of Ga(In)NAs Alloys", MRS Internet J. Nitride Semicond. Res. 6, 2 (2001).

[48] J. Misiewicz, P. Sitarek, K. Ryczko, R. Kudrawiec, M. Fischer, M. Reinhardt, and A. Forchel, "Influence of Nitrogen on Carrier Localization in InGaAsN/GaAs Single Quantum Wells", Microelectr. J. 34, 737 (2003).

[49] V. Lordi, H.B. Yuen, S.R. Bank, M.A. Wistey, J.S. Harris, and S. Friedrich, "Nearest-Neighbor Distributions in Ga1−xInxNyAs1−y and Ga−xInxNyAs1−y−zSbz Thin Films upon Annealing", Phys. Rev. B 71, 125309 (2005).

[50] L.C. Bannow, O. Rubel, S.C. Badescu, P. Rosenow, J. Hader, J.V. Moloney, R. Tonner, and S.W. Koch, "Configuration Dependence of Band-Gap Narrowing and Localization in Dilute GaAs1−xBixAlloys", Phys. Rev. B 93, 205202 (2016).

[51] L.C. Bannow, S.C. Badescu, J. Hader, J.V. Moloney, and S.W. Koch, "Valence Band Splitting in Bulk Dilute Bismides", Appl. Phys. Lett. 111, 182103 (2017).

[52] I.P. Marko, P. Ludewig, Z.L. Bushell, S.R. Jin, K. Hild, Z. Batool, S. Reinhard, L. Nattermann, W. Stolz, K. Volz, and S.J. Sweeney, "Physical Properties and Optimization of GaBiAs/(Al)GaAs Based near-Infrared Laser Diodes Grown by MOVPE with up to 4.4% Bi", J. Phys. D Appl. Phys. 47, 345103 (2014).

[53] I.P. Marko, C.A. Broderick, S. Jin, P. Ludewig, W. Stolz, K. Volz, J.M. Rorison, E.P. O'Reilly, and S.J. Sweeney, "Optical Gain in GaAsBi/GaAs Quantum Well Diode Lasers", Sci. Rep. 6, 28863 (2016).

[54] R. Kudrawiec, M. Syperek, P. Poloczek, J. Misiewicz, R.H. Mari, M. Shafi, M. Henini, Y.G. Gobato, S.V. Novikov, J. Ibáñez, M. Schmidbauer, and S.I. Molina, "Carrier Localization in GaBiAs Probed by Photomodulated Transmittance and Photoluminescence", J. Appl. Phys. 106, 023518 (2009).

[55] A.R. Mohmad, F. Bastiman, C.J. Hunter, R.D. Richards, S.J. Sweeney, J.S. Ng, J.P.R. David, and B.Y. Majlis, "Localization Effects and Band Gap of GaAsBi Alloys: Localization Effects and Band Gap of GaAsBi Alloys", Phys. Status Solidi B 251, 1276 (2014).

[56] M.K. Shakfa, D. Kalincev, X. Lu, S.R. Johnson, D.A. Beaton, T. Tiedje, A. Chernikov, S. Chatterjee, and M. Koch, “Quantitative Study of Localization Effects and Recombination Dynamics in GaAsBi/GaAs Single Quantum Wells”, J. Appl. Phys. 114, 164306 (2013).

[57] T. Wilson, N.P. Hylton, Y. Harada, P. Pearce, D. Alonso-Álvarez, A. Mellor, R.D. Richards, J.P.R. David, and N.J. Ekins-Daukes, “Assessing the Nature of the Distribution of Localised States in Bulk GaAsBi”, Sci. Rep. 8, 6457 (2018).

[58]M. Usman, C. Broderick, Z. Batool, K. Hild, T. Hosea, S. Sweeney, and E. O’Reilly, “Impact of Alloy Disorder on the Band Structure of Compressively Strained GaBiAs”, Phys. Rev. B 87, 115104 (2013).

[59] J. Hader, S.C. Badescu, L.C. Bannow, J.V. Moloney, S.R. Johnson, and S.W. Koch, “Extended Band Anti-Crossing Model for Dilute Bismides”, Appl. Phys. Lett. 112, 062103 (2018).

[60] M. Reason, Y. Jin, H.A. McKay, N. Mangan, D. Mao, R.S. Goldman, X. Bai, and C. Kurdak, “Influence of N on the Electronic Properties of GaAsN Alloy Films and Heterostructures”, J. Appl. Phys. 102, 103710 (2007).

[61] P. Wei, M. Chicoine, S. Gujrathi, F. Schiettekatte, J.-N. Beaudry, R.A. Masut, and P. Desjardins, “Characterization of GaAs1−xNx Epitaxial Layers by Ion Beam Analysis”, J. Vac. Sci. Technol. A 22, 908 (2004).

[62] M. Reason, H.A. McKay, W. Ye, S. Hanson, R.S. Goldman, and V. Rotberg, “Mechanisms of Nitrogen Incorporation in GaAsN Alloys”, Appl. Phys. Lett. 85, 1692 (2004).

[63] P. Carrier, S.-H. Wei, S. B. Zhang, and S. Kurtz, “Evolution of Structural Properties and Formation of N-N Split Interstitials in GaAs 1 − x N x Alloys”, Phys. Rev. B 71, 165212 (2005).

[64] K. Laaksonen, H.-P. Komsa, T. T. Rantala, and R. M. Nieminen, “Nitrogen Interstitial Defects in GaAs”, J. Phys. Condens. Matter 20, 235231 (2008).

[65] S.B. Zhang and S.H. Wei, “Nitrogen Solubility and Induced Defect Complexes in Epitaxial GaAs:N”, Phy. Rev. Lett. 86, 1789 (2001).

[66] E. Arola, J. Ojanen, H.-P. Komsa and T. T. Rantala, “Atomic and Electronic Structures of N Interstitials in GaAs”, Phys. Rev. B 72, 045222 (2005).

[67] T. Jen, G. Vardar, Y.Q. Wang, and R.S. Goldman, “Identifying the Dominant Interstitial Complex in Dilute GaAsN Alloys”, Appl. Phys. Lett. 107, 221904 (2015).

[68] J. Li, X. Han, C. Dong, and C. Fan, “Formation Energies of Substitutional NAs and Split Interstitial Complexes in Dilute GaAsN Alloys with Different Growth Orientations”, Appl. Phys. A 124, 108 (2018).

[69] P. Krispin, V. Gambin, J.S. Harris, and K.H. Ploog, “Nitrogen-Related Electron Traps in Ga(As,N) Layers (⩽3% N)”, J. Appl. Phys. 93, 6095 (2003).

[70] M. Reason, N.G. Rudawski, H.A. McKay, X. Weng, W. Ye, and R.S. Goldman, “Mechanisms of GaAsN Growth: Surface and Step-Edge Diffusion”, J. Appl. Phys. 101, 083520 (2007).

[71] S. O’Hagan and M. Missous, “Effect of As4/Ga Flux Ratio on Electrical and Optical Properties of Low-Temperature GaAs Grown by Molecular Beam Epitaxy”, J. Appl. Phys. 75, 7835 (1994).

[72] X. Liu, A. Prasad, J. Nishio, E.R. Weber, Z. Liliental-Weber, and W. Walukiewicz, “Native Point Defects in Low-Temperature-Grown GaAs”, Appl. Phys. Lett. 67, 279 (1995).

[73] C.R. Wie, K. Xie, T.T. Bardin, J.G. Pronko, D.C. Look, K.R. Evans, and C.E. Stutz, “Characterization of MBE GaAs Layers Grown at 200°C–300°C”, MRS Proc. 198, 383 (1990).

[74] T.B.O. Rockett, R.D. Richards, Y. Gu, F. Harun, Y. Liu, Z. Zhou, and J.P.R. David, “Influence of Growth Conditions on the Structural and Opto-Electronic Quality of GaAsBi” J. Cryst. Growth 477, 139 (2017).

[75] R.B. Lewis, M. Masnadi-Shirazi, and T. Tiedje, “Growth of High Bi Concentration $GaAs_{1-x}Bi_x$ by Molecular Beam Epitaxy”, Appl. Phys. Lett. 101, 082112 (2012).

[76] W. Bennarndt, G. Boehm, and M.-C. Amann, “Domains of Molecular Beam Epitaxial Growth of Ga(In)AsBi on GaAs and InP Substrates”, J. Cryst. Growth 436, 56 (2016).

[77] R.L. Field, J. Occena, T. Jen, D. Del Gaudio, B. Yarlagadda, C. Kurdak, and R.S. Goldman, “Influence of Surface Reconstruction on Dopant Incorporation and Transport Properties of GaAs(Bi) Alloys”, Appl. Phys. Lett. 109, 252105 (2016).

[78] R.L. Field III, "Growth and Electronic Properties of GaAsN and GaAsBi Alloys", Ph.D. thesis. University of Michigan, 2015, p. 117.

[79] R.D. Richards, F. Bastiman, C.J. Hunter, D.F. Mendes, A.R. Mohmad, J.S. Roberts, and J.P.R. David, “Molecular Beam Epitaxy Growth of GaAsBi Using As2 and As 4”, J. Cryst. Growth 390, 120 (2014).

[80] J. Puustinen, M. Wu, E. Luna, A. Schramm, P. Laukkanen, M. Laitinen, T. Sajavaara, and M. Guina, “Variation of Lattice Constant and Cluster Formation in GaAsBi”, J. Appl. Phys. 114, 243504 (2013).

[81] D.L. Sales, E. Guerrero, J.F. Rodrigo, P.L. Galindo, A. Yáñez, M. Shafi, A. Khatab, R.H. Mari, M. Henini, S. Novikov, M.F. Chisholm, and S.I. Molina, “Distribution of Bismuth Atoms in Epitaxial GaAsBi”, Appl. Phys. Lett. 98, 101902 (2011).

[82] N. Baladés, D.L. Sales, M. Herrera, C.H. Tan, Y. Liu, R.D. Richards, and S.I. Molina, “Analysis of Bi Distribution in Epitaxial GaAsBi by Aberration-Corrected HAADF-STEM”, Nanoscale Res. Lett. 13, 125 (2018).

[83] G. Ciatto, M. Thomasset, F. Glas, X. Lu, and T. Tiedje, “Formation and Vanishing of Short Range Ordering in GaAs1−xBix Thin Films”, Phys. Rev. B 82, 201304 (2010).

[84] A. Beyer, N. Knaub, P. Rosenow, K. Jandieri, P. Ludewig, L. Bannow, S.W. Koch, R. Tonner, and K. Volz, “Local Bi Ordering in MOVPE Grown Ga(As,Bi) Investigated by High Resolution Scanning Transmission Electron Microscopy”, Appl. Mater. Today 6, 22 (2017).

[85] A.G. Norman, R. France, and A.J. Ptak, Atomic Ordering and Phase Separation in MBE GaAs1-xBix”, J. Vac. Sci. Technol. B 29, 03C121 (2011).

[86] D.F. Reyes, F. Bastiman, C.J. Hunter, D.L. Sales, A.M. Sanchez, J.P.R. David, and D. González, “Bismuth Incorporation and the Role of Ordering in GaAsBi/GaAs Structures”, Nanoscale Res. Lett. 9, 23 (2014).

[87] M. Wu, E. Luna, J. Puustinen, M. Guina, and A. Trampert, “Observation of Atomic Ordering of Triple-Period-A and -B Type in GaAsBi”, Appl. Phys. Lett. 105, 041602 (2014).

[88] M. Yoshimoto, W. Huang, Y. Takehara, A. Chayahara, Y. Horino, J. Saraie, and K. Oe, “Molecular Beam Epitaxy of Quaternary Semiconductor Alloy GaNAsBi”, in *16th Conf. P. Indium Phosph.* (IEEE, Kagoshima, Japan, 2004), pp. 501–504.

[89] M. Yoshimoto, W. Huang, and K. Oe, "MBE-Grown GaNAsBi Matched to GaAs with 1.3-μm Emission Wavelength", MRS Proceedings 829, B11.6. (2004).

[90] M. Yoshimoto, W. Huang, Y. Takehara, J. Saraie, A. Chayahara, Y. Horino, and K. Oe, “New Semiconductor GaNAsBi Alloy Grown by Molecular Beam Epitaxy”, Jpn. J. Appl. Phys. 43, L845 (2004).

[91] W. Huang, K. Oe, G. Feng, and M. Yoshimoto, “Molecular-Beam Epitaxy and Characteristics of GaNyAs1−x−yBix”, J. Appl. Phys. 98, 053505 (2005).

[92] M. Yoshimoto, W. Huang, G. Feng, and K. Oe, “New Semiconductor Alloy GaNAsBi with Temperature-Insensitive Bandgap”, Phys. Status Solidi B 243, 1421 (2006).

[93] M. Yoshimoto, W. Huang, G. Feng, Y. Tanaka, and K. Oe, “Molecular-Beam Epitaxy of GaNAsBi Layer for Temperature-Insensitive Wavelength Emission”, J. Cryst. Growth 301–302, 975 (2007).

[94] G. Feng, K. Oe, and M. Yoshimoto, “Influence of Thermal Annealing Treatment on the Luminescence Properties of Dilute GaNAs-Bismide Alloy”, Jpn. J. Appl. Phys. 46, L764 (2007).

[95] Z.L. Bushell, P. Ludewig, N. Knaub, Z. Batool, K. Hild, W. Stolz, S.J. Sweeney, and K. Volz, “Growth and Characterisation of Ga(NAsBi) Alloy by Metal–Organic Vapour Phase Epitaxy”, J. Cryst. Growth 396, 79 (2014).

[96] L. Nattermann, P. Ludewig, E. Sterzer, and K. Volz, “Exploiting Strain to Enhance the Bi Incorporation in GaAs-Based III/V Semiconductors Using MOVPE”, J. Cryst. Growth 470, 15 (2017).

[97] P. Wei, S. Tixier, M. Chicoine, S. Francoeur, A. Mascarenhas, T. Tiedje, and F. Schiettekatte, “Ion Beam Characterization of GaAs(1-x-y)NxBi(y) Epitaxial Layers”, Nucl. Instrum. Meth. B 219–220, 671 (2004).

[98] D.G. Cooke, F.A. Hegmann, E.C. Young, and T. Tiedje, “Electron Mobility in Dilute GaAs Bismide and Nitride Alloys Measured by Time-Resolved Terahertz Spectroscopy”, Appl. Phys. Lett. 89, (2006).

[99] S. Tixier, M. Adamcyk, E.C. Young, J.H. Schmid, and T. Tiedje, “Surfactant Enhanced Growth of GaNAs and InGaNAs Using Bismuth”, J. Cryst. Growth 251, 449 (2003).

[100] T. Liu, S. Chandril, A.J. Ptak, D. Korakakis, and T.H. Myers, “Bismuth Surfactant Effects for GaAsN and Beryllium Doping of GaAsN and GaInAsN Grown by Molecular Beam Epitaxy", J. Cryst. Growth 304, 402 (2007).

[101] M. Masnadi-Shirazi, D.A. Beaton, R.B. Lewis, X. Lu, and T. Tiedje, “Surface Reconstructions during Growth of GaAs1−xBix Alloys by Molecular Beam Epitaxy”, J. Cryst. Growth 338, 80 (2012).

[102] A. Duzik, J.C. Thomas, J.M. Millunchick, J. Lång, M.P.J. Punkkinen, and P. Laukkanen, “Surface Structure of Bismuth Terminated GaAs Surfaces Grown with Molecular Beam Epitaxy”, Surf. Sci. 606, 1203 (2012).

[103] P. Laukkanen, M.P.J. Punkkinen, H.-P. Komsa, M. Ahola-Tuomi, K. Kokko, M. Kuzmin, J. Adell, J. Sadowski, R.E. Perälä, M. Ropo, T.T. Rantala, I.J. Väyrynen, M. Pessa, L. Vitos, J. Kollár, S. Mirbt, and B. Johansson, “Anomalous Bismuth-Stabilized (2×1) Reconstructions on GaAs(100) and InP(100) Surfaces”, Phys. Rev. Lett. 100, 086101 (2008).

[104] F. Bastiman, A.G. Cullis, J.P.R. David, and S.J. Sweeney, “Bi Incorporation in GaAs(100)-2×1 and 4×3 Reconstructions Investigated by RHEED and STM”, J. Cryst. Growth 341, 19 (2012).

[105] C.-H. Chiou, P.-H. Wu, S.-F. Chen, I.-L. Chen, J.-T. Hsu, A.-Y. Tzeng, and C.-H. Wu, "Solar cell with superlattice structure and fabricating method thereof", US20070151595 A1 (5 July 2007).

[106] I. Vurgaftman and J.R. Meyer, “Band Parameters for Nitrogen-Containing Semiconductors”, J. Appl. Phys. 94, 3675 (2003).

[107] T. Jen, "Ion Beam Analysis of Solute Incorporation in GaAsN and GaAsNBi Alloys", Ph.D. Thesis, University of Michigan, 2017, p. 19.

[108] B. Breddermann, A. Bäumner, S.W. Koch, P. Ludewig, W. Stolz, K. Volz, J. Hader, J.V. Moloney, C.A. Broderick, and E.P. O′Reilly, “Luminescence Properties of Dilute Bismide Systems”, J. Lumin. 154, 95 (2014).

Chapter 2

Experimental Procedures

2.1 Overview

This chapter describes the experimental procedures used to synthesize and characterize the alloys studied in this work. We begin by describing the Gen II and C21 molecular-beam epitaxy (MBE) systems, including the reflection high-energy electron diffraction (RHEED) systems used for calibrations and in-situ measurements during MBE growth. We then proceed to describe several characterization techniques used in this dissertation. Following growth, high-resolution x-ray diffraction (XRD) was used to examine alloy composition and strain. The surface morphologies were examined by atomic force microscopy (AFM) and scanning electron microscopy (SEM). Resistivity, carrier concentration, and mobility were determined by room-temperature Hall effect measurements. For quaternary alloys, ion beam analysis, including Rutherford backscattering spectrometry (RBS) and nuclear reaction analysis (NRA), was used to measure the Bi and N concentrations, respectively. Chemical ordering was investigated using transmission electron microscopy (TEM) of [110] and [$\bar{1}$10] cross-sections. Optical properties were measured using photoluminescence and photoreflectance, through collaborations with Dr. Emil-Mihai Pavelescu at IMT-Bucharest and Dr. Robert Kudrawiec and Dr. Wojciech Linhart at the Wroclaw University of Science and Technology.

2.2 Molecular-beam epitaxy

2.2.1 Overview

Molecular-beam epitaxy (MBE) is a vapor deposition technique that enables growth of high-quality epitaxial films and heterostructures. The process is performed in ultra-high vacuum such that evaporation or sublimation from heated solid or liquid source materials produces molecular beams, which interact with a heated single-crystalline substrate to form epitaxial films. The Si-doped GaAs and GaAsBi films described in Ch. 3 of this thesis were grown in a Riber Compact 21 (C21) MBE system. GaAsN, GaAsBi, and GaAsNBi alloys in Ch. 4 – 6 were grown in a Modified Varian Gen II MBE system.

2.2.2 MBE system details

Both the Gen II and C21 MBE systems, shown schematically in Figure 2.1 and Figure 2.2, respectively, consist of separately pumped load-lock, buffer, and growth chambers. Samples are transferred between chambers using trolleys and magnetic transfer arms. The pressure in each chamber is monitored by an ionization gauge. An additional ionization gauge in the growth chamber of each MBE system is mounted in the sample position to measure beam-equivalent pressures. The Gen II MBE growth chamber is pumped by a Varian sputter-ion pump and a CTI CryoTorr 8 cryopump while the C21 MBE growth chamber is pumped by a Riber sputter-ion pump and a Riber titanium sublimation pump. Each growth chamber contains a cryoshroud and a cryopanel, through which liquid nitrogen is flowed during growth. The cryoshroud is located near the source flange and wraps around each source to thermally isolate the hot effusion cells. The

cryopanel is located behind and to either side of the substrate holder and serves to inhibit re-evaporation of molecules deposited on the walls of the chamber, helping to achieve a base pressure < 3×10^{-10} Torr. Each growth chamber contains a STAIB electron source for in-situ reflection high-energy electron diffraction (RHEED) and a Stanford Research Systems residual gas analyzer (RGA) for in-situ mass spectrometry. During growth, the sample is held by a manipulator referred to as the CAR (continuous azimuthal rotation) or ARM (azimuthal rotation manipulator) and rotated to improve sample uniformity. All samples discussed in this dissertation were grown with azimuthal rotation of 10 rpm, unless otherwise noted in the growth logs. Both MBE systems are equipped with high-purity gallium (99.99999%), indium (99.99999%), aluminum (99.99995%), bismuth (99.9999%), silicon (99.9999%), and beryllium (99.99%) contained in pyrolytic boron nitride crucibles, which are housed in Knudsen effusion cells.

Arsenic (99.99995%) is supplied by a cracker source in which solid arsenic is housed in a bulk zone and passes through a cracker zone before entering the growth chamber. The cracking zone temperature determines whether predominantly As_4 or As_2 molecules are supplied. For growth with As_2, the cracking zone is elevated to a temperature of 1000 °C to crack each As_4 tetramer into two As_2 dimers. For all films discussed in this dissertation, the cracking zone was maintained at a temperature of 600 °C during growth, such that predominantly As_4 molecules were supplied, enabling Bi incorporation for a wider range of As/Ga ratios, as shown in Figure 1.7. A more detailed comparison between growth with As_2 and growth with As_4 can be found in Ch. 4 of the Ph.D. dissertation of Dr. Richard L. Field III.[1] We note that the exact ratio of As_2 to As_4 for each cracking zone temperature has not been measured directly. Additional details about the method used to

select the cracking zone temperatures can be found in Appendix C of the Ph.D thesis of Dr. Simon Huang.[2]

The Gen II MBE also contains a Riber RF-N 450 radio frequency nitrogen plasma source, which generates a reactive N plasma from high-purity N_2 gas (99.9999%). N_2 gas is filtered by an Entegris 0.003 μm purifier prior to entering the plasma source, and the flow rate is regulated by an MKS mass flow controller. The plasma source is pumped by a Varian Turbo-V 70LP turbomolecular pump and is separated from the growth chamber by a gate valve, which remains closed except during N deposition. To protect the growth chamber ion pump from the flux of ions introduced by the plasma source, the ion pump gate valve is closed ~30 s prior to growth of the N-containing layer and reopened ~30 s following completion of the layer. The N plasma is ignited prior to growth, and a detailed description of the procedure for igniting the N plasma can be found in Appendix B of the Ph.D. thesis of Dr. Tim Jen.[17] For N-containing samples in this dissertation, the plasma source was operated at a power of 350 W with N_2 flow rates from 0.15 to 0.35 sccm. The partial pressure of active N in the growth chamber was monitored using RGA detection of 14 amu particles.

2.2.3 Reflection high-energy electron diffraction

Reflection high-energy electron diffraction (RHEED) provides in-situ information about the morphology and atomic structure of the sample surface. RHEED is used prior to growth for growth rate (GR) and incorporation rate ratio (IRR) calibrations, as well as during growth for in-situ monitoring of the surface reconstruction. For RHEED measurements, an electron beam is accelerated toward the sample surface at a grazing

incidence angle (~ 1°). Electrons diffracted from the sample surface form a diffraction pattern on a phosphor screen; this pattern is then captured by a charge coupled device (CCD) camera. The Gen II MBE is equipped with an IMI-Tech IMB-1040FT camera, and the C21 MBE with an IMI-Tech IMB-40FT camera. Both the Gen II MBE and the C21 MBE are equipped with STAIB RHEED sources, which are operated at accelerating voltages of 18 keV and 12 keV, respectively.

To calibrate the GR, the intensity of the central spot of the RHEED diffraction pattern is monitored during growth of GaAs on a (001)-oriented substrate, displaying an oscillating intensity versus time. The growth rate is then estimated assuming that one oscillation corresponds to the time required for growth of a single bilayer of GaAs.[3] For Ga-limited growth, the Ga flux is adjusted to achieve the desired growth rate. To calibrate the As flux, we monitor the so-called incorporation rate ratio (IRR).[4,5] The IRR is determined by monitoring the time required for an As-rich (2x4) surface reconstruction to recover after being deprived of an As flux. The sample is oriented with the RHEED electron beam along the [110] direction and a few seconds of GaAs growth is initiated, resulting in a (2x) diffraction pattern for As-rich conditions. At time t_1, The As shutter is closed for a few seconds, causing the surface to become Ga-rich with a (4x) RHEED pattern. The As shutter is reopened at time t_2, causing the surface reconstruction to return to a (2x) pattern a few seconds later, at time t_3. The IRR is then calculated as $(t_3 - t_1)/(t_2 - t_1)$.[6] The As flux was adjusted to achieve IRR values in the range 1.3 – 1.8, which typically result in smooth surface morphologies for GaAs and AlAs growth.[6]

During epitaxial growth, atoms adsorbed on the sample surface rearrange to minimize surface energy, forming a surface reconstruction that often differs from the

structure of the bulk crystal lattice.[7] Because the RHEED electron beam is incident upon the sample surface at a glancing angle, the beam interacts with only the top few monolayers of the film,[8] and the resulting diffraction pattern represents the periodicity of the surface reconstruction.[9] In this work, we describe surface reconstructions using the standard notation (*M*x*N*), in which the lattice parameter of the surface unit cell along the $[\bar{1}10]$ ([110]) direction is represented as a multiple, *M* (*N*), of the bulk lattice parameter. Figure 2.3 shows an example of a (2x4) surface reconstruction and its corresponding RHEED pattern along the [110] and $[\bar{1}10]$ directions.

2.2.4 Temperature calibration

During growth, each substrate was indium-bonded to a molybdenum block, and the substrate temperature was measured by means of a thermocouple in contact with the back of the Mo block. Depending on the thermal conductivity and thickness of the substrate wafer and the degree of contact between the thermocouple and the substrate with the block, there can be an offset > 200 °C between the thermocouple reading, T_{CAR}, and the actual temperature at the surface of the growing film, T_{sub}. Therefore, multiple calibrations were used to correlate T_{CAR} and T_{sub}.

On GaAs substrates, the native oxide desorbs at a temperature of approximately 580 °C.[10] For each sample, the RHEED pattern was monitored as the GaAs substrate was gradually heated upon first being introduced to the growth chamber. Prior to oxide desorption, the pattern appears dim and diffuse because it is obscured by the surface oxide. The oxide desorption at 580 °C is indicated by a sudden sharpening of the spots in the RHEED pattern; T_{CAR} when this occurred was assumed to correspond to T_{sub} = 580 °C for

the Gen II MBE system (600 °C for the C21 MBE system, as described in Section 2.2.4 of the Ph.D. thesis of Dr. Richard L. Field III).

For growth at temperatures well below 580 °C in the Gen II MBE, an Ircon Modline 3 infrared pyrometer was used to calibrate T_{CAR}. The pyrometer was mounted on a viewport at the center of the source flange, with a direct line of sight to the sample surface. Calibration of the emissivity of the pyrometer was performed by first growing 300 nm of undoped GaAs and leaving the sample in the growth chamber overnight. Liquid nitrogen was left running to prevent redeposition of molecules adsorbed on the walls of the chamber. On the following day, T_{CAR} was raised gradually, with the RHEED pattern initially showing a (2x4) reconstruction before changing to a (3x1) reconstruction. The (2x4) to (3x1) transition temperature was assumed to correspond to T_{sub} = 500 °C. [11] Further increase of T_{CAR} eventually resulted in the (3x1) pattern abruptly changing to a (4x2) pattern, which was assumed to correspond to 595 °C.[11] The emissivity of the pyrometer was then adjusted so that the pyrometer read 595 °C. After calibration of the pyrometer emissivity, the pyrometer reading, T_{pyro}, was assumed to accurately represent T_{sub} for temperatures > 400 °C, which is the lower detection limit of the pyrometer. To correlate T_{pyro} with T_{CAR}, pyrometer and thermocouple readings were collected for a range of temperatures 450 °C < T_{sub} < 600 °C. A plot of T_{pyro}, versus T_{CAR} then exhibited a linear relationship, which was fit using a linear regression with R^2 value > 0.99. For temperatures < 400 °C, T_{sub} was determined from T_{CAR} using an extrapolation of the linear fit. This calibration was performed for each molybdenum block used. Additional details of the T_{pyro}-T_{CAR} calibration can be found in Appendix A. On the C21 MBE system, the offset between

T_{CAR} and T_{sub} is smaller, and T_{CAR} was used as T_{sub} for $T < 300$ °C, as described in Section 2.2.4 of the Ph.D. thesis of Dr. Richard L. Field III.

2.3 High-resolution x-ray diffraction

High-resolution x-ray diffraction (XRD) measurements were used to examine the composition and strain in $GaAs_{1-x-y}N_xBi_y$ layers. XRD measurements were performed using $CuK\alpha_1$ radiation in either a Bede D1 diffractometer at the University of Michigan or a Rigaku Smartlab diffractometer at the National Renewable Energy Laboratory (NREL). Three types of XRD scans are discussed in this dissertation. In $\Delta\omega$ scans, also called rocking curves, the sample is "rocked" about the substrate Bragg angle with the x-ray source and detector held fixed. In ω-2θ scans, variation of the source and detector angles is coupled to maintain a constant diffraction vector, allowing measurement of parallel planes with a range of lattice spacings. In reciprocal space mapping (RSM), an analyzer crystal is used to limit the angular acceptance of the detector, and a series of ω-2θ scans with a range of ω offsets are collected to produce a 2-dimensional map of reciprocal space in which the influences of strain and tilt can be separated.

For most films, $\Delta\omega$ scans were collected for two sets of reflections, the symmetric (004) and the asymmetric glancing-incidence (224), illustrated in Figure 2.4, to determine the in-plane and out-of-plane lattice parameters. For ternary alloys, the N (Bi) fraction was determined assuming a linear interpolation between the GaAs and GaN (GaBi) lattice parameters. Since the binary compound GaBi has not been synthesized, a calculated value[12] of 6.324 Å was used for the GaBi lattice parameter. For quaternary alloys, N and Bi fractions were typically determined by ion beam analysis, as described in Section 2.6. In

some cases, the N fractions of quaternary alloys were determined by fitting dynamical diffraction simulations to XRD data using the Rocking-Curve Analysis by Dynamical Simulation (RADS) software following determination of the Bi fraction by Rutherford backscattering spectrometry. XRD was performed either by the author, by Dr. Tim Jen, or by Emily Rizzi.

2.4 Hall effect measurements

The carrier mobilities and free carrier concentration of GaAs and GaAsBi films in Ch. 3 were determined using room-temperature Hall effect measurements. Samples were cleaved into 4 x 4 mm or 5 x 5 mm squares and prepared in the van der Pauw geometry.[13] Indium contacts were deposited on each corner of the square and annealed for two minutes at 420 °C in nitrogen. The Ohmic nature of the contacts was verified using a Hewlett Packard 4156B semiconductor parameter analyzer. Hall effect and resistivity measurements were conducted using a Keithley 224 programmable current source and a Hewlett Packard 34420A voltmeter. For resistivity measurements, current was passed between two adjacent contacts, and voltage was measured parallel to the current flow, across the other two contacts of the van der Pauw sample, as shown in Figure 2.5(a). For Hall effect measurements, an external magnetic field of magnitude 0.12 Tesla was applied perpendicular to the sample surface. A current was passed between two diagonally opposed contacts, and voltage was measured across the remaining two contacts, perpendicular to the current flow, as shown in Figure 2.5(b). Free carrier concentration and mobility were then determined using the procedures described in ASTM standard F76.[14] Hall effect measurements were performed either by the author or by Dr. Richard L. Field III.

2.5 Current-voltage and capacitance-voltage measurements

Current-voltage (I-V) and capacitance-voltage (C-V) measurements were used to determine the rectifying characteristics and carrier concentration profiles of Schottky diode structures, as discussed in Ch. 3 and Ch. 7. Both I-V and C-V measurements were performed using a Keithley 4200 semiconductor parameter analyzer and an Alessi probe station managed by the Lurie Nanofabrication Facility. C-V measurements were performed with an AC voltage of 30 mV and a frequency of 1 MHz, with the DC bias swept from 1 to -12 V. For I-V measurements, the DC bias was typically swept from -1 to 1 V. Measurements were performed in the dark to avoid influence from photogenerated carriers. I-V and C-V measurements were performed by Mingfei Zhang, Jack Hu, Andra Chen, and the author.

2.6 Ion beam analysis

Rutherford backscattering spectroscopy (RBS) and nuclear reaction analysis (NRA) were used to analyze the concentrations of N and Bi solute atoms incorporated substitutionally or interstitially in $GaAs_{1-x-y}N_xBi_y$ films. In both RBS and NRA, a beam of He^{2+} ions, i.e. α particles, is accelerated into the sample under a static electric potential. Ion beam energies of 4.46 to 4.88 MeV were used. For RBS, elastically backscattered He^{2+} ions were collected by a silicon surface barrier detector positioned at 167° with respect to the incident ion beam. For NRA, the nuclear reaction $^{14}N(\alpha,p)^{17}O$, which describes α particles reacting with ^{14}N nuclei to produce protons, *p*, and ^{17}O nuclei, was used.[15] Emitted protons were collected by a silicon surface barrier detector located at 135° with respect to the incident ion beam. Both RBS and NRA data were analyzed using the simulation of

nuclear reaction analysis (SIMNRA) code, an analytical simulation program in which multiple small-angle scattering events are treated as energy broadening.[16] The ion beam measurements were performed by Dr. Tim Jen, and additional details regarding the ion beam analysis can be found in Chapter 2 and Appendix D of his Ph.D. thesis.[17]

2.7 Atomic force microscopy

The surface morphology of films was examined by atomic force microscopy (AFM). AFM images were collected in a Veeco Dimension Icon AFM in ScanAsyst mode, which consists of a modified tapping mode with a proprietary control algorithm for tuning the scan parameters to maintain constant peak force. Bruker ScanAsyst-Air triangular silicon tips with tip radius < 12nm, tip length = 115 µm, spring constant = 0.4 N/m, and resonant frequency = 70 kHz were used to image areas of 1×1 μm^2 and 3×3 μm^2. Following measurements, image “flattening” and feature height analysis were formed using either Nanoscope Analysis or Gwyddion software. The AFM measurements were performed in part by the author and in part by Dr. Tim Jen, Emily Rizzi, Brandon Carter, Theodore Jimson, and Hongling Lu.

2.8 Scanning electron microscopy

Scanning electron microscopy (SEM) was used to examine sub-micron surface features on GaAs, GaAsBi, and GaAsNBi films in Ch. 3 and Ch. 5. SEM images were collected either at the Michigan Center for Materials Characterization (MC)^2 or the National Renewable Energy Laboratory (NREL). At both facilities, the instrument used was a FEI Nova Nanolab 200 equipped with an energy dispersive x-ray spectroscopy

(XEDS) detector, a Ga^+ focused ion beam (FIB), and an Omniprobe manipulator. Some additional SEM images were collected using a JEOL IT500 microscope in the Van Vlack Undergraduate Laboratory. Images were collected using acceleration voltages ranging from 3 kV to 20 kV and beam currents from 98 pA to 2.4 nA. SEM imaging was also used in conjunction with FIB to prepare cross-sectional foils for transmission electron microscopy analysis, as described in Section 2.9.

2.9 Transmission electron microscopy

Transmission electron microscopy (TEM) was used to examine the microstructure and composition of $GaAs_{1-x-y}N_xBi_y$ layers in Ch. 5. Three different instruments were used for TEM imaging: a FEI Tecnai $G^2$30 Super Twin TEM at NREL operating at 300 kV, a FEI Tecnai F20 Ultra Twin scanning TEM (STEM) at NREL operating at 200 kV, and a JEOL 3100R05 double C_s-corrected STEM at $(MC)^2$ operating at 300 kV. All TEM imaging was performed either by the author or by Dr. Andrew G. Norman. All TEM specimens were prepared by the author at NREL.

Cross-sectional TEM specimens normal to the [110] and $[1\bar{1}0]$ directions were prepared either by conventional mechanical polishing and dimpling[18] or by a FIB lift-out process. For mechanically-polished samples, two cleaved sample pieces were first glued together with (001) surfaces facing inward using EPO-TEK epoxy. This "sandwich" specimen was then thinned perpendicular to the glue line (along a <110> direction) using 600 grit SiC papers and a Gatan disc grinder to form a ~100 µm thick foil. Next the specimen was dimple-polished on a Model D500i Dimpler using a 1 µm diamond suspension followed by a 0.05 µm alumina suspension to produce a concave dimple on one

side of the foil with thickness of < 10 μm at its center. The dimpled specimen was glued to a 3 mm diameter slotted Cu grid and then ion-milled until perforated using Ar^+ ions in a Fischione 1010 ion mill, with accelerating voltage of 3.5 kV, current of 5.0 mA, and incident angle of 10°. The specimen was cooled with liquid nitrogen and continuously rotated during ion milling. A final polishing step was performed at 1.0 kV and 3.0 mA following perforation.

Some cross-sectional TEM specimens were prepared by a conventional FIB lift-out technique[19,20] using a Ga^+ FIB in a Nova Nanolab 200 SEM. A platinum bar with approximate dimensions 20 μm × 2 μm × 1 μm was deposited on the sample surface as a protective cap. FIB milling at 30 kV and 0.92 - 2.8 nA was used to mill trenches on either side of the Pt cap and cut out a foil approximately 20 μm long by 5 μm tall, which was Pt-welded to an Omniprobe 3-post Cu lift-out grid. Thinning of the foil was performed with the FIB at 30kV and 93 – 460 pA. Final cleaning of the foil in the SEM was performed at 3 kV and 110 pA. Following removal from the SEM, the TEM specimen was further thinned and cleaned in a liquid-nitrogen-cooled Fischione Model 1040 NanoMill, using an Ar^+ FIB at 500 eV and 150 μA, with incident angle 10°.

2.10 Photoreflectance and photoluminescence

To investigate the optical properties of $GaAs_{1-x-y}N_xBi_y$ alloys, both photoreflectance (PR) and photoluminescence (PL) measurements were performed. PR measurements were performed by Dr. Wojciech M. Linhart in Dr. Robert Kudrawiec’s group at the Wroclaw University of Science and Technology. The PR spectra were collected at 20 K in a closed-cycle helium cryostat, using a semiconductor laser with wavelength 532 nm as the pump

beam and a 150 W tungsten halogen bulb as the probe beam. Both pump and probe were focused onto the sample with a diameter of ~2mm. The pump beam was modulated by a mechanical chopper at a frequency of 290 Hz, and the PR signal was collected using a lock-in amplifier. PL measurements were performed by Dr. Emil-Mihai Pavelescu at the National Institute for Research and Development in Microtechnologies (IMT-Bucharest). PL measurements were performed for temperatures from 7 – 300 K, using a continuous-wave laser with wavelength of 532 nm and excitation powers of 100 or 300 mW. Additional PL measurements were performed by Patricia Dippo at the National Renewable Energy Laboratory, using a 532 nm continuous-wave laser with excitation powers of 0.5 to 10 mW.

2.11 Figures

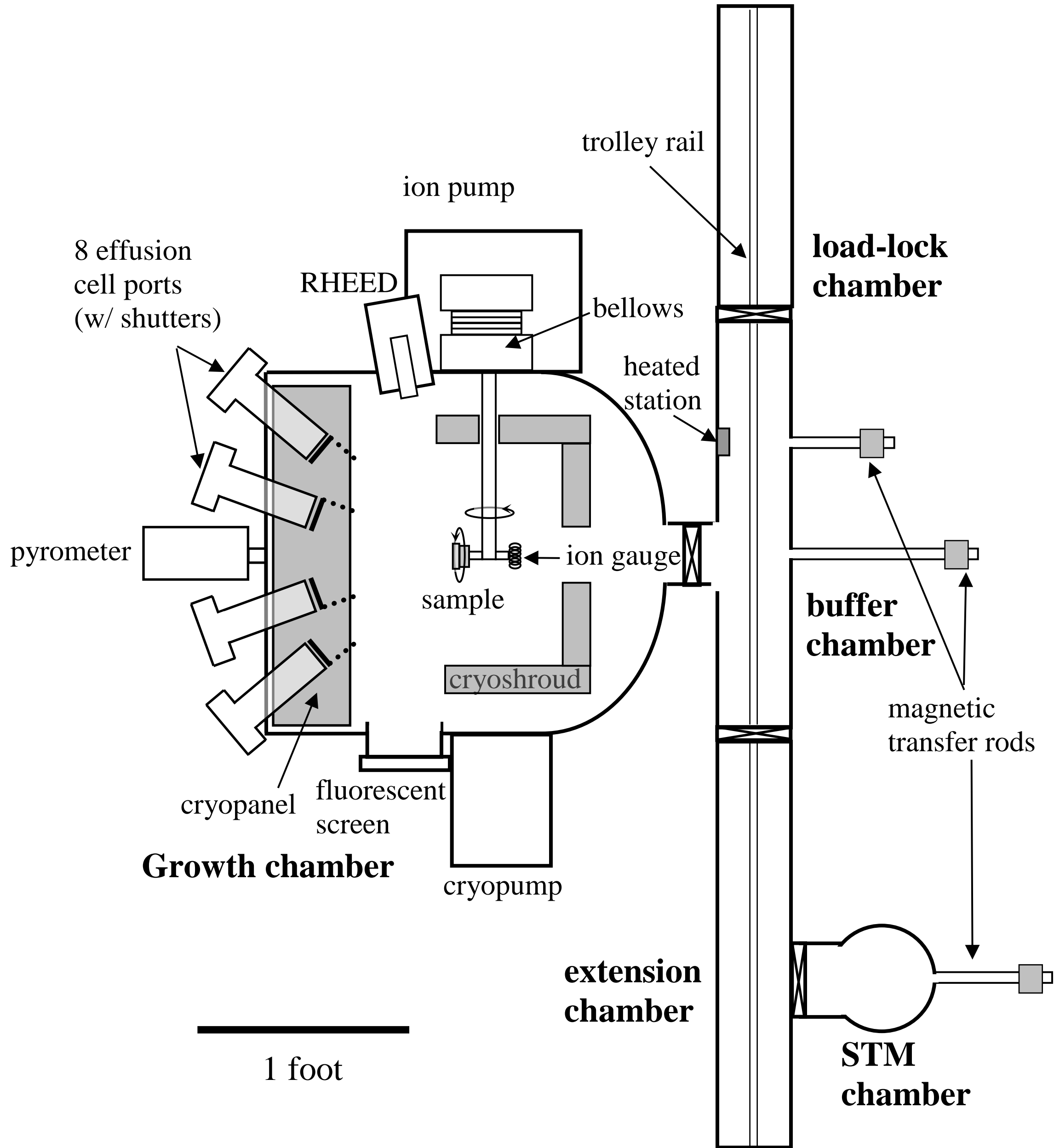

Figure 2.1 Schematic of the Modified Varian Gen II molecular-beam epitaxy system, containing seven solid sources (Ga, In, Al, Bi, Si, Be, As cracker) and a radio frequency N plasma source, each housed at one of the eight effusion cell ports. Each effusion cell source is directed at the sample center, angled 33° from the surface normal of the sample. Adapted from Ref. 11 (Copyright 2006, Matthew J. Reason).

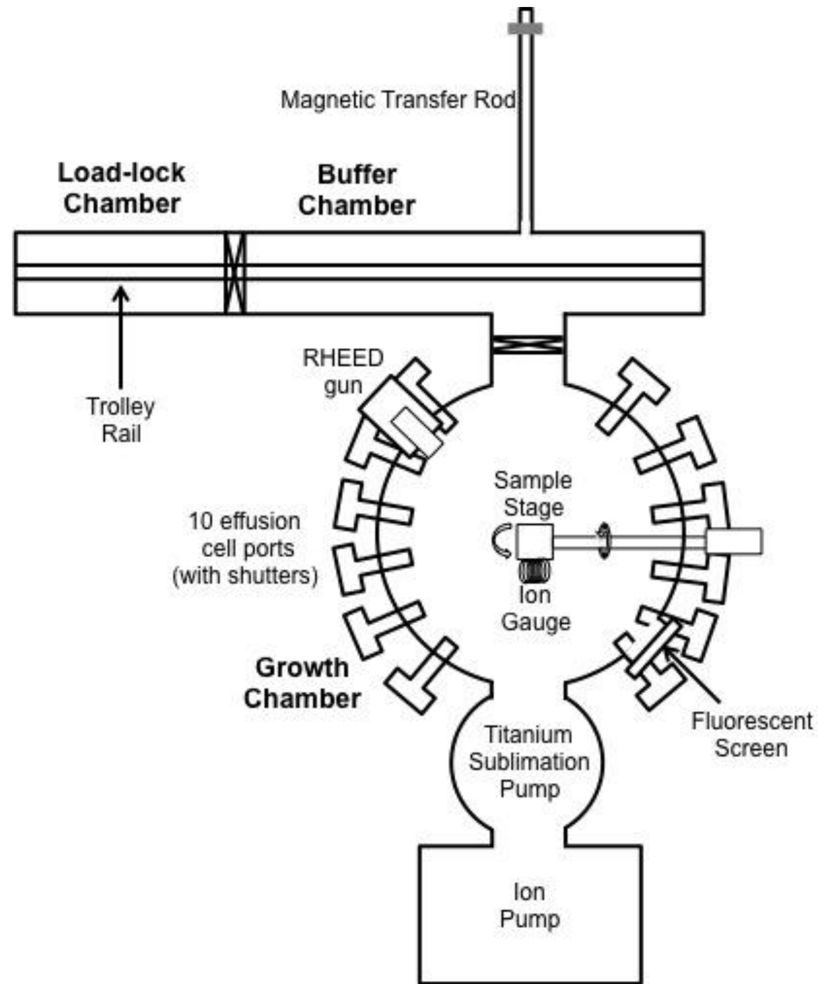

Figure 2.2 Schematic of the Riber Compact 21 molecular-beam epitaxy system, containing seven solid sources (Ga, In, Al, Bi, Si, Be, As cracker), each housed in one of the effusion cell ports. Reprinted from Ref. 1 (Copyright 2015, Richard L. Field III).

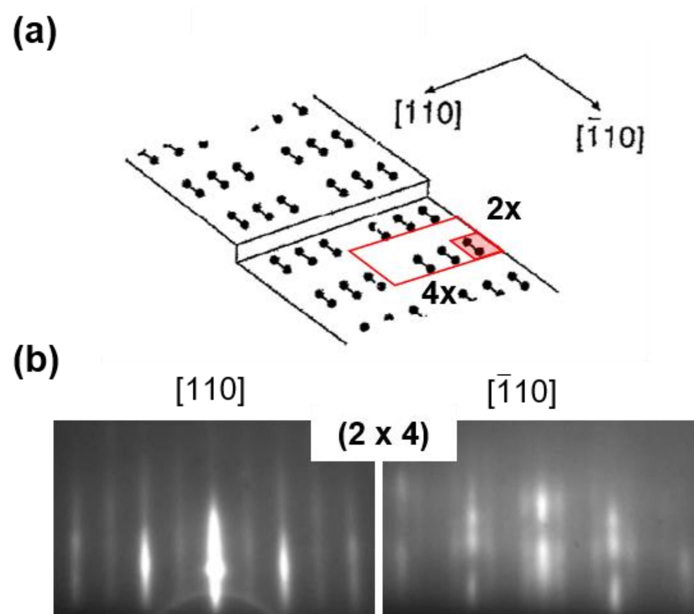

Figure 2.3 (a) Illustration of a (2x4) surface reconstruction, with dumbbells representing dimerized surface atoms, and (b) its corresponding reflection high-energy electron diffraction pattern viewed along the [110] and [$\bar{1}$10] directions. (a) is adapted and reprinted with permission from Ref. 21 (Copyright 1991, AIP Publishing).

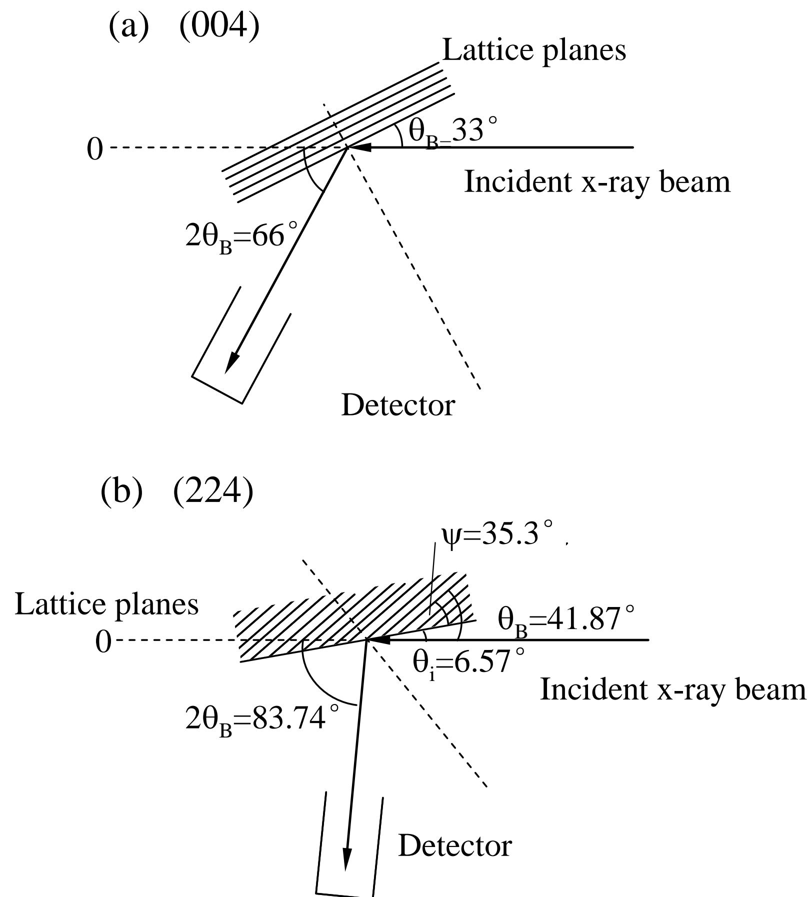

Figure 2.4 Schematic of the high-resolution x-ray diffraction geometries used for measurements about the (a) symmetric (004) and (b) asymmetric (224) GaAs reflections. Adapted from Ref. 22 (Copyright 2003, Xiaojun Weng).

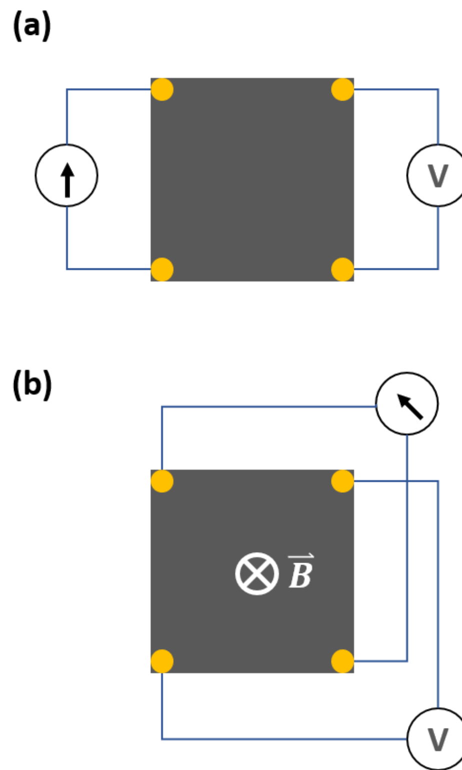

Figure 2.5 Schematic of the arrangement used for (a) resistivity and (b) Hall effect measurements of Van der Pauw specimens.

2.12 References

[1] R.L. Field III, "Growth and Electronic Properties of GaAsN and GaAsBi Alloys", Ph.D. thesis, University of Michigan, 2015, p. 54, 107-108, 117.

[2] Simon Huang, "Formation, Structure, and Properties of InAs/GaAs Quantum Dots", Ph.D. thesis, University of Michigan, 2015, p. 127-128.

[3] J.H. Neave, B.A. Joyce, P.J. Dobson, and N. Norton, "Dynamics of Film Growth of GaAs by MBE from Rheed Observations", Appl. Phys. A Solids Surf. 31, 1 (1983).

[4] T.P. Chin, B.W. Liang, H.Q. Hou, M.C. Ho, C.E. Chang, and C.W. Tu, Appl. Phys. Lett. 58, 254 (1991).

[5] H.Q. Hou and C.W. Tu, "Determination of V/III Ratios on Phosphide Surfaces during Gas Source Molecular Beam Epitaxy", Appl. Phys. Lett. 60, 1872 (1992).

[6] S.R. Bank, An Introduction to MBE, http://lase.ece.utexas.edu/mbe.php; accessed 29 July 2018.

[7] A. Kahn, "Semiconductor Surface Structures", Surf. Sci. Rep. 3, 193 (1983).

[8] P.A. Maksym and J.L. Beeby, "A Theory of Rheed", Surf. Sci. 110, 423 (1981).

[9] J.E. Mahan, K.M. Geib, G.Y. Robinson, and R.G. Long, "A Review of the Geometrical Fundamentals of Reflection High-energy Electron Diffraction with Application to Silicon Surfaces", J. Vac. Sci. Technol. A 8, 3692 (1990).

[10] E.C. Larkins and J.S. Harris Jr., "Molecular Beam Epitaxy of High Quality GaAs and AlGaAs" in *Molecular Beam Epitaxy: Applications to Key Materials*, edited by R.F.C. Farrow (Noyes, Park Ridge, New Jersey, 1995), pp. 114–274.

[11] M. Reason, "Structure and Properties of Dilute Nitride GaAsN Alloy Films", Ph.D Thesis, Ch. 2, University of Michigan, 2006, p. 27, 48.

[12] A. Janotti, S.-H. Wei, and S.B. Zhang, "Theoretical Study of the Effects of Isovalent Coalloying of Bi and N in GaAs", Phys. Rev. B 65, (2002).

[13] L.J. Van der Pauw, "A Method of Measuring Specific Resistivity and Hall Effect of Discs of Arbitrary Shape", Philips Res. Repts. 26, 220 (1958).

[14] AFM Standards, Designation F 76, "Standard Test Methods for Measuring Resistivity and Hall Coefficient and Determining Hall Mobility in Single-Crystal Semiconductors".

[15] J.R. Tesmer and M.A. Nastasi, *Handbook of Modern Ion Beam Materials Analysis* (Materials Research Society, 1995).

[16] M. Mayer., W. Eckstein, H. Langhuth, F. Schiettekatte, and U. von Toussaint. "Computer Simulation of Ion Beam Analysis: Possibilities and Limitations", Nucl. Instrum. Meth. B 269, 3006 (2011).

[17] T. Jen, "Ion Beam Analysis of Solute Incorporation in GaAsN and GaAsNBi Alloys", Ph.D. Thesis, University of Michigan, 2017, p. 43-46, 164-179.

[18] J.C. Bravman and R. Sinclair, "The Preparation of Cross-Section Specimens for Transmission Electron Microscopy", J. Electron Micr. Tech. 1, 53 (1984).

[19] L.A. Giannuzzi and F.A. Stevie, "A Review of Focused Ion Beam Milling Techniques for TEM Specimen Preparation", Micron 30, 197 (1999).

[20] R.M. Langford and C. Clinton, "In Situ Lift-out Using a FIB-SEM System", Micron 35, 607 (2004).

[21] M.D. Pashley, K.W. Haberern, and J.M. Gaines, "Scanning Tunneling Microscopy Comparison of GaAs(001) Vicinal Surfaces Grown by Molecular Beam Epitaxy", Appl. Phys. Lett. 58, 406 (1991).

[22] X. Weng, "Structural, Electronic, and Optical Properties of Narrow Gap Compound Semiconductors", Ph.D. Thesis, University of Michigan, 2003, p.64.

Chapter 3

Amphoteric Doping in GaAs(Bi)

3.1 Overview

This chapter describes investigations of the incorporation of Si as a dopant in GaAs and GaAsBi. The objective of this work is to identify the influence of surface reconstruction on the incorporation of silicon and the resulting transport properties of Si-doped GaAs(Bi) films. These studies enable us to demonstrate an opportunity for using Si as both an n- and p-type dopant in GaAs and related alloys.

The chapter begins with a review of earlier studies of Si doping of GaAs and the epitaxial conditions that produce n-type or p-type conductivity in GaAs:Si. Next, we describe the experimental techniques we used to investigate the electronic and structural properties of Si-doped GaAs and GaAsBi films. Si incorporation in GaAs(Bi) with an (n x 3) reconstruction leads to n-type conductivity, while growth with a (2 x 1) reconstruction leads to p-type conductivity. We hypothesize that the presence or absence of surface arsenic dimers prevents or enables dopant incorporation into arsenic lattice sites. We finish with a discussion of the surface morphologies and carrier transport properties of n-type and p-type Si-doped GaAsBi alloys and the application of amphoteric Si doping in Au/GaAs:Si Schottky diodes. These findings suggest Si is a promising alternative to C or Be for p-type doping of GaAs and related alloys.

3.2 Background

Elements from column IV of the periodic table, including C, Ge, and Si, may act as either donors or acceptors in III-V semiconductors, depending on their incorporation into group III or group V lattice sites, as shown in Figure 3.1 During molecular-beam epitaxy (MBE) of GaAs, C most often occupies an As site, leading to p-type conductivity.[1,2,3] On the other hand, Ge may occupy a Ga lattice site, Ge_{Ga}, or an As lattice site, Ge_{As}, resulting in *n*-type or *p*-type conductivity, respectively.[4,5] Typically, Si occupies a Ga lattice site, Si_{Ga}, resulting in n-type conductivity.[6,7] However, when Si is able to outcompete arsenic for group V sites, p-type conductivity is observed. For example, due to the high density of Ga dangling bonds on (n11)A ($n \leq 3$) GaAs surfaces, Si-doping typically leads to p-type conductivity, with a transition to n-type conductivity occurring as the V/III flux ratio is increased.[8,9,10] However, for (001) GaAs surfaces, Si-doping typically leads to n-type conductivity, with a transition to p-type conductivity using a shuttering sequence or V/III flux ratios near the transition from anion-rich to cation-rich conditions, i.e., the stoichiometry threshold.[11,12,13] For growth at 600°C, Zhang *et al.* observed a transition from n-type to p-type conductivity at the so-called stoichiometry threshold, corresponding to (2 x 4) and (4 x 2) GaAs surface reconstructions, respectively.[13] For lower substrate temperatures (520°C), Quivy *et al.* obtained p-type GaAs:Si by alternate surface exposure to As, then Ga plus Si, leading to (2 x 4) and (4 x 2) surface reconstructions, respectively.[11] For the lowest substrate temperatures (270°C), a transition from n-type to p-type conductivity has been reported for GaAs growth near the stoichiometry threshold.[12] To date, the atomistic mechanisms for this transition have not yet been considered. We hypothesize that the presence or absence of surface arsenic dimers prevents or enables

dopant incorporation into arsenic lattice sites. We consider the influence of bismuth anions on arsenic-dimer mediated dopant incorporation and the resulting electronic transport properties, demonstrating the applicability of this mechanism to mixed anion semiconductor alloys.

3.3 Experimental procedures

GaAs(Bi):Si alloy films were grown on semi-insulating (001) GaAs substrates by MBE, using solid Ga, As_4, Bi, and Si sources. The surface reconstruction was monitored in-situ with a reflection high-energy electron diffraction (RHEED) source operating at 12 keV. For all films, the substrate temperature was measured by a thermocouple in contact with the back of each molybdenum block, calibrated by setting the oxide desorption temperature to 600 °C, as described in Section 2.2.4. The sample layer structure is illustrated in Figure 3.2. Following growth of a 500-nm thick GaAs buffer at 600 °C, the substrate temperature was lowered to 280 °C during growth of 250- to 550-nm thick GaAs layers. Finally, 400-nm GaAs(Bi):Si layers, with or without Si and Bi, were grown at various growth rates (0.25 to 2.0 μm/hr), Group V/III beam equivalent pressure (BEP) ratios (6 to 20), and Bi:As BEP ratios (0 to 0.03). The Si cell temperature was chosen to target $n = 1 \times 10^{18}$ or 7×10^{18} cm^{-3} in GaAs:Si control films, based on a doping calibration described in Appendix B.

For the GaAs(Bi):Si alloys, the surface morphology was examined *ex-situ* with AFM and SEM. The in-plane and out-of-plane strain and lattice parameters were determined from an analysis of (004) and (224) high resolution x-ray rocking curves (HRXRCs), in both $\varphi = 0°$ and $\varphi = 180°$ configurations, as described in Section 2.3.

HRXRCs were performed in a Bede D1 system, with a monochromator which contains two Si channel cut crystals, consisting of (220) reflections in the duMond-Hart-Bartels (+,-,-,+) configuration,[14] which select the CuKα_1 line with a beam divergence of 12 arcseconds. To determine the Bi fraction, x, we use a linear interpolation of the measured GaAs (5.6533 Å) and computed GaBi (6.324 Å) lattice parameters.[15] In many cases, x was also determined using Rutherford backscattering spectrometry (RBS) measurements in conjunction with simulation of nuclear reaction analysis (SIMNRA) code;[16] the HRXRC and RBS determinations of x agree to within ± 0.005 for $x < 0.04$ and ± 0.01 for $x > 0.04$. For all the GaAs(Bi):Si films, resistivity and Hall measurements were performed at room temperature using the van der Pauw configuration.[17] $In_{0.52}Sn_{0.48}$ Ohmic contacts were applied to the corners of 4 mm x 4 mm cleaved squares and annealed at 420 °C for 2 minutes in nitrogen. Sheet resistivity, free carrier concentration, and carrier mobility were determined by the van der Pauw method, as described in Section 2.4. The composition profiles across the surface droplets were determined using EDS and/or Auger electron spectroscopy, in respective scanning electron microscopes (SEM), as described in Section 2.8. Finally, for select films, surface Ga droplets were removed via surface etching with HCl:H_2O (1:3),[18,19] followed by subsequent AFM, SEM, EDS, and resistivity and Hall measurements.

3.4 GaAs(Bi):Si surface reconstructions

To monitor the surface reconstruction, RHEED patterns were collected along the [110] and $[1\bar{1}0]$ directions, as shown in Figure 3.3. During GaAs growth at 600 °C, a streaky (2 x 4) pattern is observed, indicating Group V termination of the surface [Figure

3.3(a) and Figure 3.3(b)]. As the substrate temperature is lowered to 280°C, the RHEED pattern transforms to a streaky (2 x 3) pattern [Figure 3.3(c) and Figure 3.3(d)], independent of the presence of Si. In some cases, spotty (2 x 1) RHEED patterns with chevrons [Figure 3.3(e) and Figure 3.3(f)] emerge during growth of GaAs(Bi):Si films; these films exhibit p-type conductivity. In other cases, within 10s of GaAs(Bi):Si growth, streaky (n x 3) patterns [Figure 3.3(g) and Figure 3.3(h)] appear, with (2 x chevron) patterns emerging following at least 45 s of growth; these films exhibit n-type conductivity.

3.5 GaAs(Bi):Si structural properties

We now discuss the structure and composition of the GaAs(Bi):(Si) films. A representative series of HRXRCs about the (004) GaAs diffraction peak are shown in Figure 3.4 for $GaAs_{1-x}Bi_x$ films with x ranging from 0 to 0.048. For all films, diffraction peaks associated with GaAsBi and GaAs are observed, with the peak separations increasing with increasing x. For low x, Pendellosung fringes are apparent, indicating smooth epilayer surfaces and interfaces.[20,21] As x increases, the Pendellosung fringes disappear and the GaAsBi diffraction peak broadens, presumably due to roughening of the surfaces and interfaces due to misfit strain relaxation.[22] In Figure 3.5(a) we plot the in-plane ($a_{\parallel}$) and perpendicular ($a_{\perp}$) lattice parameters as a function of x for GaAs(Bi) films, with and without Si. For $x < 0.04$, $a_{\parallel}$ remains constant while $a_{\perp}$ increases linearly with x, consistent with a pseudomorphically strained film. For $x > 0.04$, $a_{\parallel}$ begins to increase while $a_{\perp}$ remains nearly constant, suggesting that the film lattice has begun to relax to its intrinsic lattice parameter. We note that both $a_{\parallel}$ and $a_{\perp}$ are independent of free carrier type and Si concentration.

Since the GaAs(Bi) layers are grown at low temperatures, the dopant incorporation and transport properties may be influenced by As antisites, [As_{Ga}], as discussed in Section 1.5. [As_{Ga}] is often determined from HRXRC measurements of an increase in the lattice parameter of the low non-stoichiometric GaAs layer according to $\Delta a/a$ = 1.24 x 10^{-23} [As_{Ga}], where a is the lattice parameter of the GaAs substrate, Δa is the difference between a and the non-stoichiometric GaAs lattice parameter, and [As_{Ga}] is in cm^{-3}.[23] We estimate an upper bound for [As_{Ga}] using the FWHM of the GaAs HRXRC peak. For all the GaAs layers, [As_{Ga}] < 3×10^{19} cm^{-3}, approximately an order of magnitude lower concentration than standard non-stoichiometric GaAs.[23] Similarly, for the GaAsBi layers, we consider the FWHM of the GaAsBi film peak as an upper bound for [As_{Ga}]. In Figure 3.5(b), the FWHM of the GaAsBi diffraction peak and corresponding [As_{Ga}] upper bound are shown as a function of x. For undoped GaAsBi and n-type GaAsBi:Si with $x < 0.04$, the FWHM of the GaAsBi peak is typically 48 ± 7 arcseconds, corresponding to an [As_{Ga}] upper bound of ~ $(3.0 \pm 0.5) \times 10^{19}$ cm^{-3}. For Bi fraction in excess of x = 0.04, the FWHM increases to 500 ± 100 arcseconds, corresponding to an [As_{Ga}] upper bound of ~ $(3.0 \pm 0.6) \times 10^{20}$ cm^{-3}. For p-type GaAsBi films, the FWHM increases from 150 to 500 arcseconds, corresponding to the [As_{Ga}] upper bound increasing from 1 to 3×10^{20} cm^{-3}. In undoped GaAs with [As_{Ga}] up to 10^{20} cm^{-3}, free electron concentrations up to 3×10^{16} cm^{-3} have been reported.[24,25] Since the carrier concentrations of our n-type and p-type GaAs(Bi):Si films exceed 10^{17} cm^{-3}, it is expected that compensation by excess-As-induced free carriers is insignificant for the GaAs(Bi) films.

3.6 Mechanism of conductivity-type transition

The conductivity types for GaAs(Bi):Si films are summarized in Figure 3.6, a plot of arsenic BEP vs. gallium BEP, with growth rate on the upper *x*-axis for the As-rich growth regime. A dashed line indicates where the group V/III BEP ratio is equal to 10, "BEPratio10". All GaAsBi:Si films above [below] the BEPratio10 line are grown on (*n* x 3) [(2 x 1)] reconstructed surfaces and are *n*-type [*p*-type]. A similar transition from (*n* x 3) to (2 x 1) with decreasing group V/III ratio has been reported for GaAsBi growth with As_2.[26] In addition, along the BEPratio10 line, a conversion from *n*-type to *p*-type conductivity occurs as the growth rate increases (from 0.25 to 2.0 μm/hr) and the surface reconstruction changes from (*n* x 3) to (2 x 1). This growth-rate-dependence of the transition to a (2x1) surface reconstruction is consistent with the growth-rate-dependence of the stoichiometry threshold reported for GaAsBi growth using As_2.[27]

We next discuss a mechanism for the transition from *n*-type to *p*-type conductivity. During growth on a (1 x 3) or (2 x 3) reconstructed surface,[28] shown in Figure 3.7, Si must break an As dimer in order to occupy a group V site; thus, Si more easily incorporates into group III sites, resulting in n-type conductivity. However, for a (2 x 1) reconstruction without As dimers,[29,30,31] Si incorporation into group V sites is enabled, leading to p-type conductivity. This arsenic-dimer mediated dopant incorporation mechanism also explains previous reports of conductivity type conversion in GaAs. Zhang[13] and Quivy[11] observed an n-type to p-type conductivity conversion following the transition from a (2 x 4) to a (4 x 2) reconstruction, associated with the presence[32] and absence[33] of surface As dimers, as shown in Figure 3.7 In the case of Fukushima,[12] the conductivity type conversion occurred at an As_4/Ga BEP ratio of 12, with substrate temperature of 270°C, which typically

correspond to a transition from an (n x 3) to a (2 x 1) surface reconstruction, associated with the presence and absence of surface As dimers.

3.7 GaAs(Bi):Si surface morphologies and carrier transport properties

This surface-reconstruction-induced transition in conductivity type provides the opportunity to examine Si as both an n-type and p-type dopant in III-V semiconductor compounds, especially for alloys such as GaAsBi, that are typically grown at similarly low temperatures near the stoichiometric threshold.[34] In Figure 3.8, we plot conductivity, σ, as a function of carrier concentration for our GaAs(Bi):Si films, in comparison with those of literature reports for GaAsBi films with various n-type and p-type dopants.[35,36,37,38,39] In the plot of σ vs. n, dashed lines form an envelope corresponding to mobilities of 2300 and 45 $cm^2/(V\text{-}s)$. The n-type film mobilities are typically near the upper end of the range, ~2300 $cm^2/(V\text{-}s)$, while the p-type film mobilities are typically near the lower end, ~45 $cm^2/(V\text{-}s)$, all independent of Bi fraction. For the n-type films, the mobilities are consistent with those of conventionally grown GaAs.[40] Indeed, as shown in the SEM and AFM images in Figure 3.9(a) and Figure 3.9(c), n-type GaAsBi films are smooth and droplet-free.

In Figure 3.9(d) and Figure 3.9(f), representative SEM and AFM images are shown for p-type GaAs(Bi):Si films, which contain sub-micron diameter surface droplets. A corresponding EDS image, with red, green, and yellow representing Ga, As, and Bi, shown in Figure 3.9(e). The surface droplets are composed primarily of Ga, often with segregated patches of Bi, consistent with similar 2D EDS mapping of GaAsBi films.[27] Droplets presumably begin to form at the start of GaAs(Bi):Si growth and gradually develop, leading to both a dimming of the RHEED pattern and the appearance of chevrons, likely associated

with crater formation, similar to earlier reports of curved crystalline surface formation during growth.[41,42] AFM reveals that the droplets are displaced from 20 ± 10 nm deep craters [circled in Figure 3.9(f)], consistent with reports of Ga droplets deposited at 350 °C.[43] Following removal of the droplets via chemical etching, the surface craters are retained, as shown in Figure 3.9(g). The corresponding EDS image in Figure 3.9(h) confirms the absence of Ga-rich regions within the craters. Furthermore, for the *p*-type GaAsBi:Si film shown in Figure 3.9, the carrier concentration is 2.1 ± 0.2 x 10^{18} cm^{-3}, the hole mobility is 29.5 ± 1.5 cm^2/(V-s), and the conductivity is 9.8 ± 0.6 S/cm, both before and after etching. The apparent lack of influence of the Ga surface droplets on the GaAs(Bi):Si film transport properties suggests that our 20 ± 2% droplet surface coverage is below the percolation threshold for conductivity, typically >70%.[44,45]

The *p*-type GaAs(Bi):Si films with high hole concentrations (p = 2 - 6 x 10^{18} cm^{-3}) exhibit mobilities consistent with conventionally grown GaAs.[46] For lower hole concentrations, p ~ 2 x 10^{17} cm^{-3}, GaAs(Bi):Si hole mobilities are lower than those of typical GaAs but similar to those reported for GaAsBi doped with Be or C.[37,38,39] Since similar hole mobilities are observed in the *p*-type films, independent of the presence of Bi, the hole mobility reduction is likely related to point defects intrinsic to Ga-rich growth, such as As vacancies.[47] The *n*-type GaAsBi films grown at the lowest group V/III BEP ratios are compensated, with mobilities near the mid-range of the envelope in Figure 3.8.[48] Since the group V/III BEP ratios of these compensated films lie very close to the transition from *n*-type to *p*-type conductivity, it is likely that Si donors are compensated by Si acceptors. For Si incorporation in GaAs (111), compensation is similarly observed near the

n-type to *p*-type transition and is attributed to Si occupying a mixture of group III and group V lattice sites.[9]

3.8 *n*-type and *p*-type Au/GaAs:Si Schottky diodes

In this section we discuss current-voltage characteristics of *n*-type and *p*-type Au/GaAs:Si Schottky diodes containing single quantum wells (QWs) of $GaAs_{1-x}N_x$ or $GaAs_{1-y}Bi_y$. The diodes were grown in preparation for measurement of GaAs(N)(Bi)/GaAs band offsets, as described further in Section 7.2.2. The layer structures of the diodes are shown in Figure 3.10. Silicon was used as the dopant for both *n*-type and *p*-type layers; for *n*-type diodes, the GaAs:Si was grown at 580°C, while for *p*-type diodes the GaAs:Si layers were grown at 280°C, using the approach described in Section 3.6. To determine x_N (y_{Bi}) in the QWs, x_N (y_{Bi}) in alloy reference samples consisting of thick (200 to 500 nm) layers of GaAsN (GaAsBi) grown under conditions essentially identical to those of the QWs were determined via the analysis of (004) high resolution x-ray rocking curves, using the method described in Section 2.3. The current-voltage (I-V) characteristics of the diodes were examined using the method described in Section 2.5.

In Figure 3.11, I-V characteristics are shown for *n*-type diodes with and without $GaAs_{1-x}N_x$ QWs in red and *p*-type diodes with and without $GaAs_{1-y}Bi_y$ QWs in blue. For each diode, the N or Bi fraction and the ideality factor,[49] *n*, are displayed in the legend. The *n*-type diode without a QW (x = 0) exhibits nearly ideal diode performance, with an ideality factor close to one and reverse leakage current less than 100 μA/cm^2 at a voltage of -1.0 V. The *n*-type diodes containing a GaAsN QW have a slightly lower current density than the *n*-type diode without a QW at forward bias but otherwise exhibit similar rectifying

performance, with nearly identical reverse leakage current density. The small reduction in current density at forward bias is likely due to series resistance introduced by the undoped QW region, with no apparent dependence on the N fraction.

The reverse leakage current densities of the *p*-type diodes at -1.0 V are two to five orders of magnitude larger than those observed in the *n*-type diodes. Diodes with *p*-type doping also exhibit larger ideality factors. The *p*-type diodes with a GaAsBi QW exhibit lower reverse leakage current density and lower ideality factor than the *p*-type diode without a QW, suggesting that the poor rectifying characteristics are not caused by the GaAsBi layer. Since the *p*-type GaAs:Si layers were grown at 280°C while the *n*-type GaAs:Si layers were grown at 580°C, it is likely that the poor rectifying characteristics in the *p*-type diodes are associated with non-stoichiometric GaAs point defects, such as As antisites and Ga vacancies,[23] that occur in higher concentrations at low temperatures, as discussed in Section 1.5. Further work is needed to determine the origin of the high reverse leakage current density in the *p*-type diodes.

3.9 Summary and conclusions

In summary, we report on the influence of surface reconstruction on Si doping type and transport properties of GaAs(Bi) alloys. A transition from n-type to p-type conductivity is observed as the surface reconstruction transitions from (*n* x 3) to (2 x 1). We hypothesize that the presence (absence) of surface arsenic dimers prevents (enables) dopant incorporation into arsenic lattice sites, resulting in n-type (p-type) conductivity. We consider the influence of bismuth anions on arsenic-dimer mediated dopant incorporation and the resulting electronic transport properties, demonstrating the applicability of this

mechanism to mixed anion semiconductor alloys. In addition, we examine the I-V characteristics of *n*-type and *p*-type Au/GaAs:Si Schottky diodes and find large reverse leakage current densities in *p*-type diodes, likely associated with formation of non-stoichiometric GaAs at low growth temperatures.

3.10 Figures

III	IV	V
5 B	6 C	7 N
13 Al	14 Si	15 P
31 Ga	32 Ge	33 As
49 In	50 Sn	51 Sb
81 Ti	82 Pb	83 Bi

Figure 3.1 Columns III, IV, and V of the periodic table. Elements from group IV, such as Si, may act as *n*-type dopants in GaAs when substituting for Ga (group III) and as *p*-type dopants when substituting for As (group V).

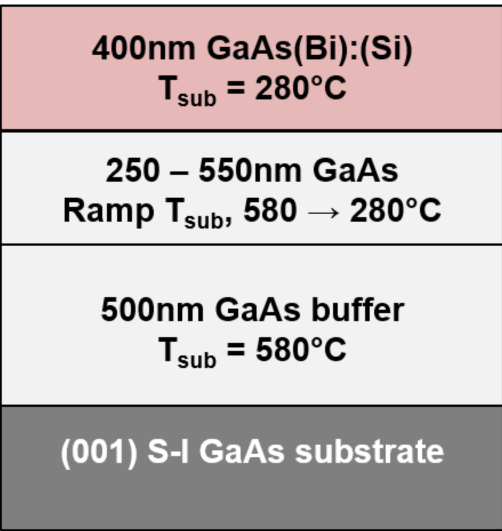

Figure 3.2 Schematic of the layer structure of GaAs(Bi):(Si) samples discussed in Ch. 3, including layer thicknesses and substrate temperature, $T_{sub.}$

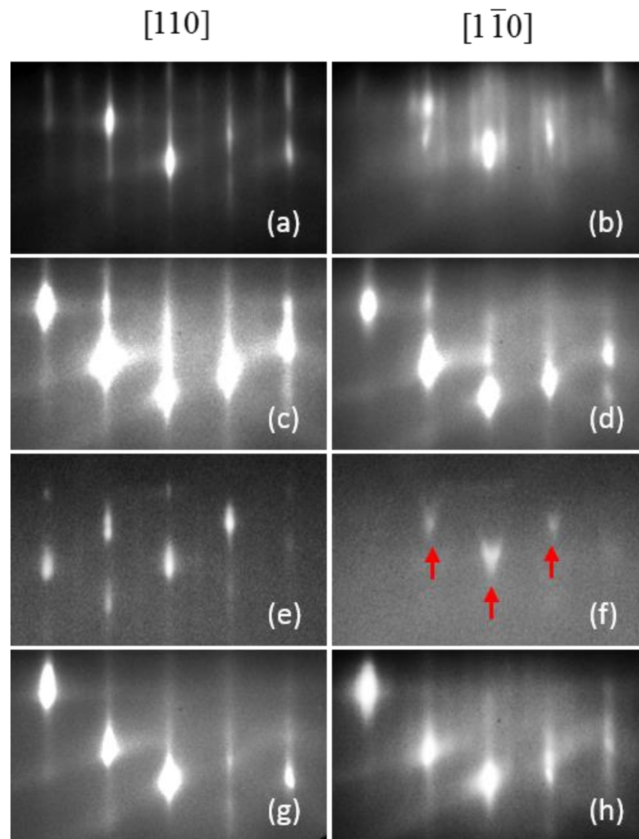

Figure 3.3 Reflection high-energy electron diffraction patterns collected along [110] and [1$\bar{1}$0] axes during GaAs(Bi):(Si) film growth. [(a), (b)] (2 x 4) pattern during GaAs growth at 600 °C; [(c), (d)] streaky (2 x 3) pattern during GaAs(Si) growth at 280 °C; [(e), (f)] dim (2 x chevron) pattern during *p*-type GaAs(Bi):Si growth at 280 °C, with arrows indicating the chevrons; [(g), (h)] streaky (1 x 3) pattern during *n*-type GaAs(Bi):Si growth at 280 °C. Reprinted with permission from Ref. 50 (Copyright 2016, AIP Publishing).

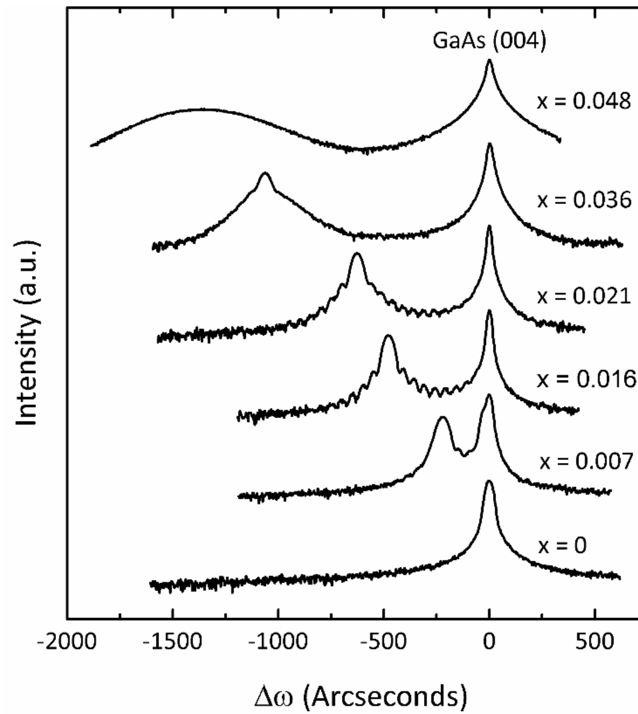

Figure 3.4 Representative high-resolution x-ray rocking curves for $GaAs_{1-x}Bi_x$ films, with x ranging from 0 to 0.048. For $x < 0.03$, Pendellosung fringes indicate high crystalline quality and coherent interfaces. As x increases, Pendellosung fringes disappear and the GaAsBi diffraction peak broadens. Reprinted with permission from Ref. 50 (Copyright 2016, AIP Publishing).

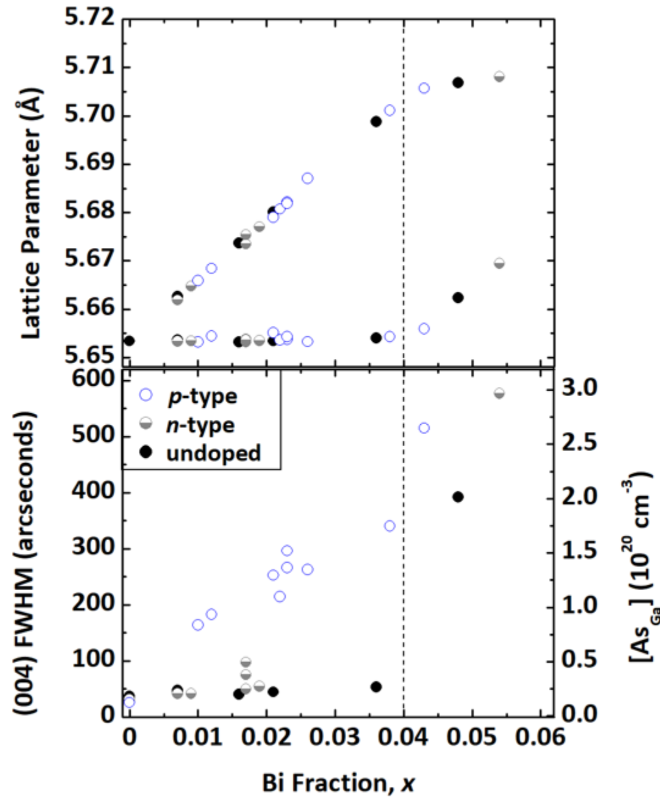

Figure 3.5 In-plane, $a_{/\!/}$, and perpendicular, $a_{\perp}$, lattice parameters and (b) FWHM of the (004) GaAsBi diffraction peak and upper bound for excess arsenic concentration, all as a function of Bi fraction, x. For $x < 0.04$, $a_{\perp}$ increases with increasing x, independent of doping type and concentration. For $x > 0.04$, $a_{/\!/}$ begins to increase while $a_{\perp}$ is nearly constant, suggesting that the film lattice has begun to relax to its intrinsic lattice parameter. For undoped GaAsBi and n-type GaAsBi:Si with $x < 0.04$, the FWHM of the GaAsBi peak is nearly constant; for $x > 0.04$, the FWHM increases with x. For p-type GaAsBi:Si, the FWHM of the GaAsBi peak increases monotonically with x. Reprinted with permission from Ref. 50 (Copyright 2016, AIP Publishing).

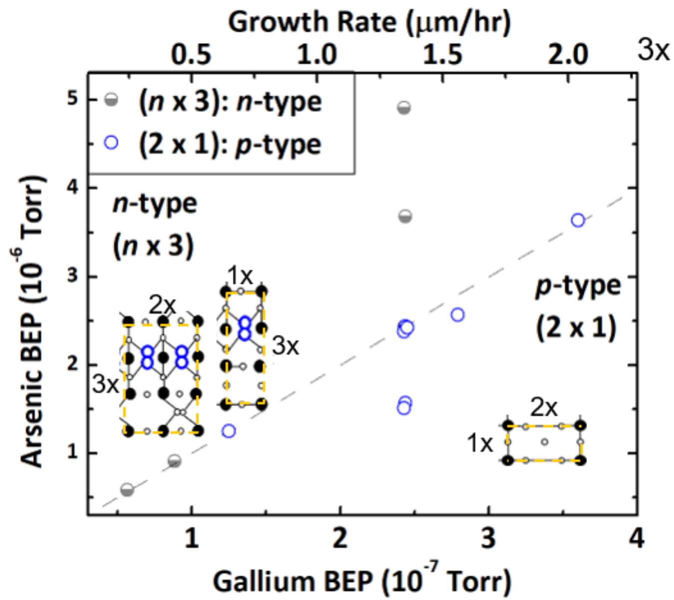

Figure 3.6 Conductivity type for GaAs(Bi):Si films: arsenic beam-equivalent pressure (BEP) vs. Ga BEP, with growth rate on the upper x-axis for the As-rich growth regime. A dashed line indicates the regime where the group V/III BEP ratio is equal to 10, "BEPratio10". All GaAsBi:Si films above (below) the BEPratio10 line are n-type (p-type). In addition, along the BEPratio10 line, a conductivity type conversion from n-type to p-type occurs as the growth rate increases (from 0.25 to 2.0 μm/hr), consistent with the growth rate dependence of the stoichiometry threshold reported in Ref. 27. Schematics illustrate the (1 x 3) and (2 x 3) reconstructions observed for n-type conductivity and the (2 x 1) reconstruction observed for p-type conductivity. Reprinted with permission from Ref. 50 (Copyright 2016, AIP Publishing).

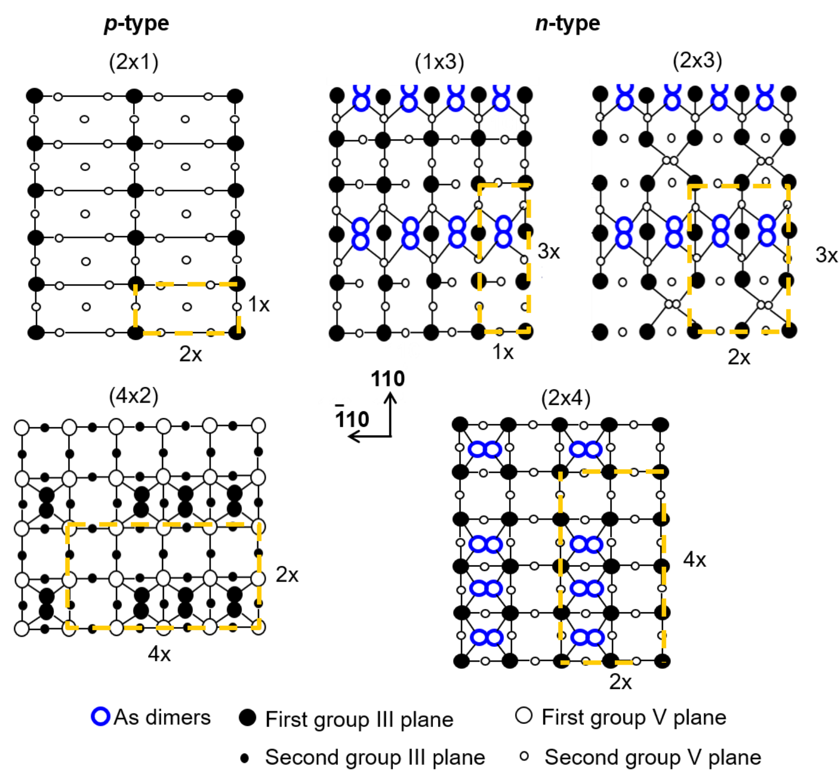

Figure 3.7 Surface reconstructions during Si incorporation in GaAs(Bi). Growth with a (2x1)[29,] or (4x2)[51,] reconstruction without As dimers results in *p*-type conductivity[11,13,50] while growth with a (1x3),[28] (2x3),[52] or (2x4)[51,] reconstruction containing As dimers results in *n*-type conductivity. [11,13,50]

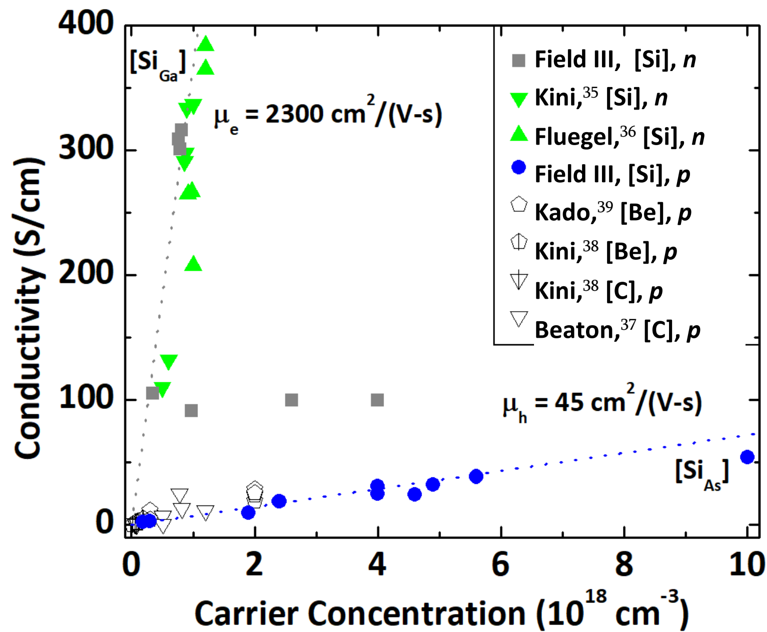

Figure 3.8 Conductivity vs. carrier concentration for bulk GaAs1-xBix:Si films, in comparison with literature reports for GaAsBi films doped with C or Be. The dotted lines form an envelope corresponding to mobilities of 2300 and 45 cm^2/(V-s). The n-type film mobilities are typically near the upper end of the range (~2300 cm^2/(V-s)) while the p-type film mobilities are typically near the lower end (~45 cm^2/(V-s)), all independent of Bi fraction. For our n-type films grown near the transition from n to p-type conductivity, mobilities lie near the mid-range of the envelope. The uncertainties in the conductivities and carrier concentrations are comparable to the size of the data points. See Ref. 35. See Ref. 36. See Ref. 37. See Ref. 38. See Ref. 39. Reprinted with permission from Ref. 50 (Copyright 2016, AIP Publishing).

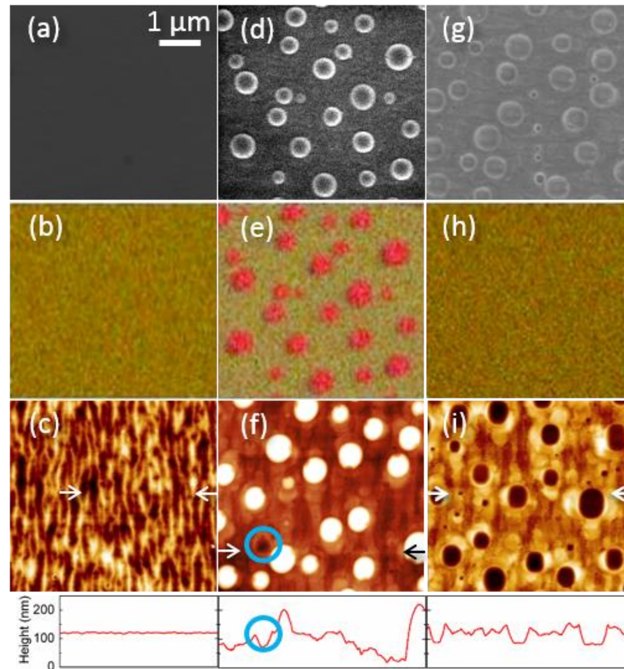

Figure 3.9 Scanning electron microscopy, corresponding energy dispersive X-ray spectroscopy (EDS), and atomic force microscopy (AFM) images for [(a), (b), (c)] n-type $GaAs_{0.992}Bi_{0.008}$:Si, as well as p-type $GaAs_{0.991}Bi_{0.009}$:Si [(d), (e), (f)] before and [(g), (h), (i)] after etching with HCl:H20 (1:3). In the EDS images, red, green, and yellow correspond to Ga, As, and Bi, respectively. The gray-scale ranges displayed in the AFM images are (c) 10 nm, (f) 160 nm, and (i) 100 nm. Line-cuts of the tip height across the AFM images are shown beneath the images, with height axis from 0 to 250 nm. Reprinted with permission from Ref. 50 (Copyright 2016, AIP Publishing).

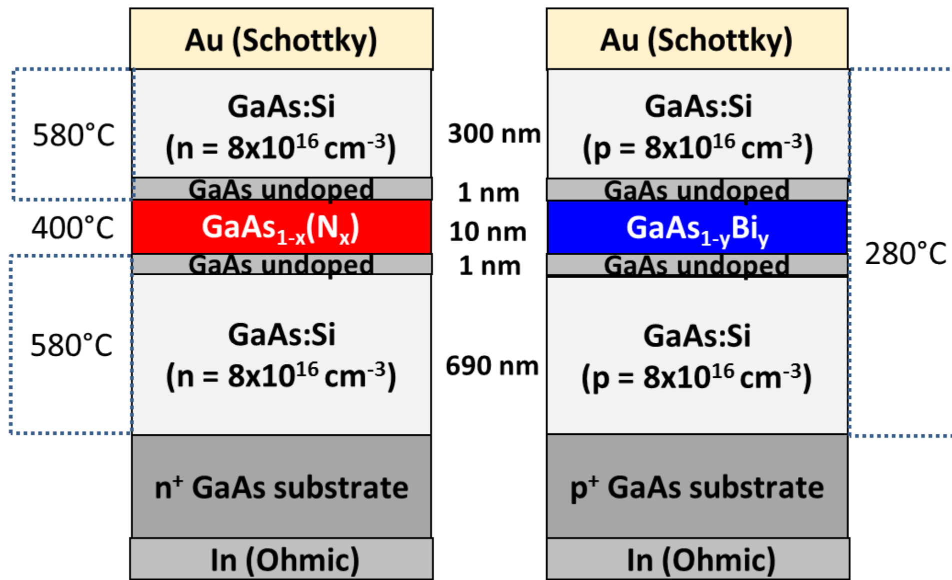

Figure 3.10 Schematic cross-section of the layer structures for n-type and p-type Au/GaAs:Si Schottky diodes containing a single quantum well (QW) of GaAsN or GaAsBi. Silicon was used for both n-type and p-type doping, using the approach described in Section 3.6. For the n-type diodes, the GaAs:Si layers were grown at 580°C while for p-type diodes, GaAs:Si was grown at 280°C.

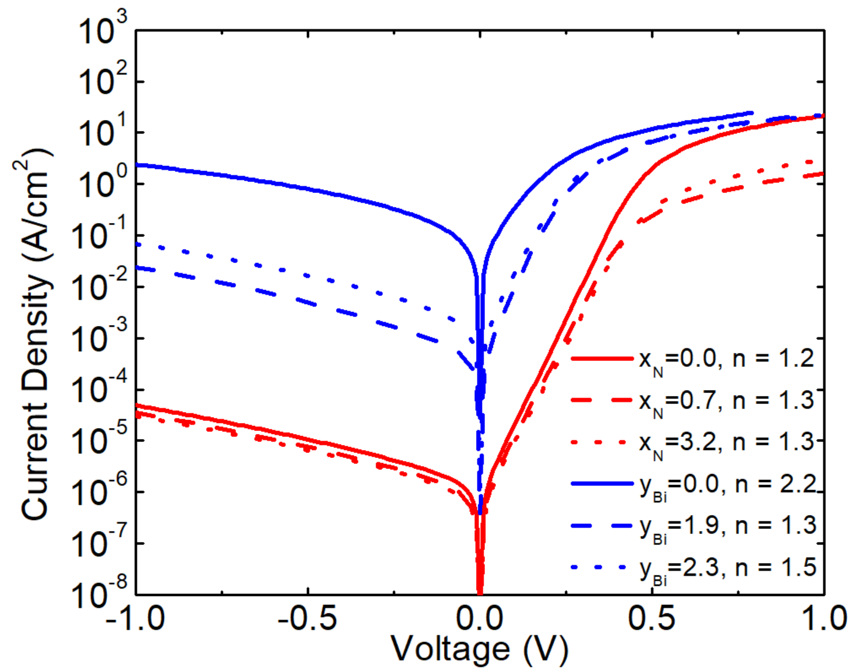

Figure 3.11 Current-voltage curves for n-type (red) and p-type (blue) Au/GaAs:Si Schottky diodes with and without single quantum wells of $GaAs_{1-x}N_x$ or $GaAs_{1-y}Bi_y$. The reverse leakage current densities are two to four orders of magnitude larger for the p-type diodes compared to the n-type diodes.

3.11 References

[1] H. Ito and T. Ishibashi, "Carbon Incorporation in (AlGa)As, (AlIn)As and (GaIn)As Ternary Alloys Grown by Molecular Beam Epitaxy", Jpn. J. Appl. Phys. 30, L944 (1991).

[2] K. Saito, E. Tokumitsu, T. Akatsuka, M. Miyauchi, T. Yamada, M. Konagai, and K. Takahashi, "Characterization of *p* -type GaAs Heavily Doped with Carbon Grown by Metalorganic Molecular-beam Epitaxy", J. Appl. Phys. 64, 3975 (1988).

[3] C. Giannini, A. Fischer, C. Lange, K. Ploog, and L. Tapfer, "Heavy Carbon Doping of GaAs Grown by Solid-source Molecular-beam Epitaxy", Appl. Phys. Lett. 61, 183 (1992).

[4] A.Y. Cho and Hayashi, I., "P-N Junction Formation during Molecular-Beam Epitaxy of Ge-Doped GaAs", J. Appl. Phys. 42, 4422 (1971).

[5] Y. Makita, H. Tanaka, M. Mori, N. Ohnishi, P. Phelan, S. Shigetomi, H. Shibata, and T. Matsumori, "As_4 to Ga Flux Ratio Dependence of the Optical and Electrical Properties of Ge-doped GaAs Grown by Molecular-beam Epitaxy", J. Appl. Phys. 65, 248 (1989).

[6] A.Y. Cho and I. Hayashi, "Epitaxy of Silicon Doped Gallium Arsenide by Molecular Beam Method", Metall. Trans. 2, 777 (1971).

[7] J.H. Neave, P.J. Dobson, J.J. Harris, P. Dawson, and B.A. Joyce, "Silicon Doping of MBE-Grown GaAs Films", Appl. Phys. A 32, 195 (1983).

[8] N. Sakamoto, K. Hirakawa, and T. Ikoma, "Conduction-Type Conversion in Si-Doped (311)A GaAs Grown by Molecular Beam Epitaxy", Appl. Phys. Lett. 67, 1444 (1995).

[9] K. Sato, M.R. Fahy, M.J. Ashwin, and B.A. Joyce, "Silicon Incorporation Behaviour in GaAs Grown on GaAs (111)A by Molecular Beam Epitaxy", J. Cryst. Growth 165, 345 (1996).

[10] S. Subbanna, H. Kroemer, and J.L. Merz, "Molecular-Beam-Epitaxial Growth and Selected Properties of GaAs Layers and GaAs/(Al,Ga)As Superlattices with the (211) Orientation", J. Appl. Phys. 59, 488 (1986).

[11] A.A. Quivy, A.L. Sperandio, E.C.F. da Silva, and J.R. Leite, "P-Type Doping of GaAs(001) Layers Grown by MBE Using Silicon as a Dopant", J. Cryst. Growth 206, 171 (1999).

[12] S. Fukushima, T. Obata, and N. Otsuka, "Electrical Properties of Nearly Stoichiometric GaAs Grown by Molecular Beam Epitaxy at Low Temperature", J. Appl. Phys. 89, 380 (2001).

[13] D. Zhang, K. Radhakrishnan, and S. Yoon, "The Effect of As/Ga Flux Ratio on Si-Doped GaAs Layers Grown by Molecular Beam Epitaxy", J. Cryst. Growth 135, 441 (1994).

[14] D.K. Bowen and B.K. Tanner, *High Resolution X-Ray Diffractometry And Topography* (CRC Press, 2005), p. 18-36.

[15] A. Janotti, S.-H. Wei, and S. Zhang, "Theoretical Study of the Effects of Isovalent Coalloying of Bi and N in GaAs", Phys. Rev. B 65, 115203 (2002).

[16] M. Mayer., W. Eckstein, H. Langhuth, F. Schiettekatte, and U. von Toussaint. "Computer Simulation of Ion Beam Analysis: Possibilities and Limitations", Nucl. Instrum. Meth. B 269, 3006 (2011).

[17] L.J. Van der Pauw, "A Method of Measuring Specific Resistivity and Hall Effect of Discs of Arbitrary Shape", Philips Res. Repts. 26, 220 (1958).

[18] C. X. Zheng, W. X. Tang, and D. E. Jesson, "Asymmetric Coalescence of Reactively Wetting Droplets", Appl. Phys. Lett. 100, 071903 (2012).

[19] C. Somaschini, S. Bietti, N. Koguchi, and S. Sanguinetti, "Fabrication of Multiple Concentric Nanoring Structures", Nano Lett. 9, 3419 (2009).

[20] B.W. Batterman and G. Hildebrandt, "X-Ray Pendellösung Fringes in Darwin Reflection", Acta Crystallograph. A 24, 150 (1968).

[21] P.F. Fewster, "X-Ray Diffraction from Low-Dimensional Structures", Semicond. Sci. Technol. 8, 1915 (1993).

[22] D. F. Reyes, F. Bastiman, C.J. Hunter, D.L. Sales, A.M. Sanchez, J.P.R. David, and D. Gonzalez, "Bismuth Incorporation and the Role of Ordering in GaAsBi/GaAs Structures", Nanoscale Res. Lett. 9, 23 (2014).

[23] X. Liu, A. Prasad, J. Nishio, E.R. Weber, Z. Liliental-Weber, and W. Walukiewicz, "Native Point Defects in Low-Temperature-Grown GaAs", Appl. Phys. Lett. 67, 279 (1995).

[24] J. Betko, P. Kordos, S. Kuklovsky, A. Förster, D. Gregusová, and H. Lüth, "Electrical Properties of Molecular Beam Epitaxial GaAs Layers Grown at Low Temperature", Mater. Sci. Eng. B 28, 147 (1994).

[25] S. O'Hagan and M. Missous, "Effect of As4/Ga Flux Ratio on Electrical and Optical Properties of Low-Temperature GaAs Grown by Molecular Beam Epitaxy", J. Appl. Phys. 75, 7835 (1994).

[26] M. Masnadi-Shirazi, D.A. Beaton, R.B. Lewis, X. Lu, and T. Tiedje, "Surface Reconstructions during Growth of GaAs1−xBix Alloys by Molecular Beam Epitaxy", J. Cryst. Growth 338, 80 (2012).

[27] G. Vardar, S.W. Paleg, M.V. Warren, M. Kang, S. Jeon, and R.S. Goldman, "Mechanisms of Droplet Formation and Bi Incorporation during Molecular Beam Epitaxy of GaAsBi", Appl. Phys. Lett. 102, 42106 (2013).

[28] T. Kita, O. Wada, T. Nakayama, and M. Murayama, "Optical Reflectance Study of the Wetting Layers in (In, Ga)As Self-Assembled Quantum Dot Growth on GaAs (001)", Phys. Rev. B 66, 195312 (2002).

[29] D.J. Chadi, "Atomic Structure of GaAs(100)-(2×1) and (2×4) Reconstructed Surfaces", J. Vac. Sci. Technol. A 5, 834 (1987).

[30] P. Laukkanen, M.P.J. Punkkinen, H.-P. Komsa, M. Ahola-Tuomi, K. Kokko, M. Kuzmin, J. Adell, J. Sadowski, R.E. Perälä, M. Ropo, T.T. Rantala, I.J. Väyrynen, M. Pessa, L. Vitos, J. Kollár, S. Mirbt, and B. Johansson, "Anomalous Bismuth-Stabilized (2 × 1) Reconstructions on GaAs(100) and InP(100) Surfaces", Phys. Rev. Lett. 100, 086101 (2008).

[31] F. Bastiman, A.G. Cullis, J.P.R. David, and S.J. Sweeney, "Bi Incorporation in GaAs(100)-2×1 and 4×3 Reconstructions Investigated by RHEED and STM", J. Cryst. Growth 341, 19 (2012).

[32] A. Ohtake, "Surface Reconstructions on GaAs(001)", Surf. Sci. Rep. 63, 295 (2008).

[33] I. Kamiya, D.E. Aspnes, L.T. Florez, and J.P. Harbison, "Reflectance-Difference Spectroscopy of (001) GaAs Surfaces in Ultrahigh Vacuum", Phys. Rev. B 46, 15894 (1992).

[34] S. Tixier, M. Adamcyk, T. Tiedje, S. Francoeur, A. Mascarenhas, P. Wei, and F. Schiettekatte, "Molecular Beam Epitaxy Growth of GaAs1-xBix", Appl. Phys. Lett. 82, 2245 (2003).

[35] R. N. Kini, L. Bhusal, A. J. Ptak, R. France, and A. Mascarenhas, "Electron Hall Mobility in GaAsBi", J. Appl. Phys. 106, 043705 (2009).

[36] B. Fluegel, R. N. Kini, A. J. Ptak, D. Beaton, K. Alberi, and A. Mascarenhas, "Shubnikov-de Haas Measurement of Electron Effective Mass in GaAs1−xBix", Appl. Phys. Lett. 99, 162108 (2011).

[37] D. A. Beaton, R. B. Lewis, M. Masnadi-Shirazi, and T. Tiedje, "Temperature Dependence of Hole Mobility in GaAs1-xBix Alloys", J. Appl. Phys. 108, 083708 (2010).

[38] R. N. Kini, A. J. Ptak, B. Fluegel, R. France, R. C. Reedy, and A. Mascarenhas, "Effect of Bi Alloying on the Hole Transport in the Dilute Bismide Alloy GaAs1-xBix", Phys. Rev. B 83, 075307 (2011).

[39] K. Kado, T. Fuyuki, K. Yamada, K. Oe, and M. Yoshimoto, "High Hole Mobility in GaAs1-xBix Alloys", Jpn. J. Appl. Phys. 51, 040204 (2012).

[40] J.R. Meyer and F.J. Bartoli, "Ionized-Impurity Scattering in the Strong-Screening Limit", Phys. Rev. B 36, 5989 (1987).

[41] T. Hanada, B. H. Koo, H. Totsuka, and T. Yao, "Anisotropic Shape of Self-Assembled InAs Quantum Dots: Refraction Effect on Spot Shape of Reflection High-Energy Electron Diffraction", Phys. Rev. B 64, 1653071 (2001).

[42] D. W. Pashley, J. H. Neave, and B. A. Joyce, "A Model for the Appearance of Chevrons on RHEED Patterns from InAs Quantum Dots", Surf. Sci. 476, 35 (2001).

[43] C. Somaschini, S. Bietti, S. Sanguinetti, A. Fedorov, N. Koguchi and A. Fedorov, "Self-Assembled GaAs/AlGaAs Coupled Quantum Ring-Disk Structures by Droplet Epitaxy", Nanotechnology 21, 125601 (2010).

[44] A. Okazaki, K. Horibe, K. Maruyama, and S. Miyazima, "Experimental Study of Critical Exponents of Electrical Conductivity in a Two-Dimensional Continuum Percolation System", Phys. Rev. E 61, 6215 (2000).

[45] S. Wagner and A. Pundt, "Conduction Mechanisms during the Growth of Pd Thin Films: Experiment and Model", Phys. Rev. B 78, 155131 (2008).

[46] W. Walukiewicz, "Carrier Scattering by Native Defects in Heavily Doped Semiconductors", Phys. Rev. B 41, 10218 (1990).

[47] J.E. Northrup and S.B. Zhang, "Energetics of the As Vacancy in GaAs: The Stability of the 3+ Charge State", Phys. Rev. B 50, 4962 (1994).

[48] W. Walukiewicz, L. Lagowski, L. Jastrzebski, M. Lichtensteiger, and H.C. Gatos, "Electron Mobility and Free-Carrier Absorption in GaAs: Determination of the Compensation Ratio", J. Appl. Phys. 50, 899 (1979).

[49] D.K. Schroder, *Semiconductor Material and Device Characterization* (John Wiley & Sons, 2006) p.157-161.

[50] R.L. Field, J. Occena, T. Jen, D. Del Gaudio, B. Yarlagadda, C. Kurdak, and R.S. Goldman, "Influence of Surface Reconstruction on Dopant Incorporation and Transport Properties of GaAs(Bi) Alloys", Appl. Phys. Lett. 109, 252105 (2016).

[51] H. Shigekawa, H. Oigawa, K. Miyake, Y. Aiso, Y. Nannichi, T. Hashizume, and T. Sakurai, "Selenium-Treated GaAs(001)-2×3 Surface Studied by Scanning Tunneling Microscopy", Appl. Phys. Lett. 65, 607 (1994).

[52] R.R. Wixom, N.A. Modine, and G.B. Stringfellow, "Theory of Surfactant (Sb) Induced Reconstructions on InP(001)", Phys. Rev. B 67, (2003).

Chapter 4

GaAsNBi Alloys: Influence of Surface Reconstruction on Bi-Enhanced N Incorporation

4.1 Overview

In this chapter, we examine the influence of bismuth (Bi) and nitrogen (N) fluxes on N and Bi incorporation during molecular-beam epitaxy of $GaAs_{1-x-y}N_xBi_y$ alloys. The objective of this work is to understand the influence of surface reconstruction on the atomistic mechanisms of N and Bi co-incorporation in GaAsNBi alloys.

We begin the chapter by reviewing the motivation for co-incorporation of N and Bi, as well as earlier reports of the influence of a Bi flux on N incorporation. We then describe the epitaxial conditions used for growth of GaAsNBi alloys and the combined experimental and computational methods used to investigate N and Bi incorporation. The incorporation of Bi is found to be independent of N flux, while the total N incorporation and the fraction of N atoms occupying non-substitutional lattice sites increase with increasing Bi flux. A comparison of channeling nuclear reaction analysis along the [100], [110], and [111] directions with Monte Carlo-Molecular Dynamics simulations indicates that the non-substitutional N primarily incorporate as $(N\text{-}As)_{As}$ interstitial complexes. We discuss the influence of Bi adatoms on the formation of arsenic-terminated [110]-oriented step-edges on a (1x3) surface reconstruction, and the resulting enhancement in total N

incorporation via the formation of additional $(N\text{-}As)_{As}$. These insights provide a pathway to tailored N incorporation in GaAsNBi and related alloys.

4.2 Background

As discussed in Ch. 1, N-related point defects often lead to degraded minority carrier transport properties and optical efficiencies.[1,2] Co-alloying GaAsN with larger elements such as indium (In), antimony (Sb), and/or Bi allows lattice-matching to GaAs or Ge substrates and is expected to lead to significant bandgap narrowing using a substantially lower N fraction, with a correspondingly lower fraction of N-related defects.[3,4] Bi incorporation into GaAs at a mole fraction of 0.01 is reported to lead to a bandgap reduction of ~84 meV, much larger than the reduction for similar fractions of Sb (21 meV) or In (16 meV), as shown in Ch. 1, Figure 1.1.[5] In addition, the strong spin-orbit splitting induced by Bi is expected to lead to reduced nonradiative Auger recombination for Bi fractions in excess of 0.105.[6] Thus, GaAsNBi is promising for optoelectronic applications operating in the near-infrared range.

For GaAsN and related alloys, bismuth is often reported to surface segregate without incorporating. [7,8,9,10] However, the presence of a Bi flux has been reported to increase or decrease the incorporation of N.[7,8,11, 12,13] For example, metalorganic vapor-phase epitaxy (MOVPE) with a Bi flux has been reported to decrease the N fraction,[12,13] while molecular-beam epitaxy (MBE) with a sufficiently high Bi flux has been reported to increase the N fraction.[7,8,11] Bi-induced decrease in N incorporation during MOVPE has been attributed to a Bi surface coverage blocking N adsorption or inhibiting decomposition of the N precursor.[12,13] On the other hand, it has been proposed that a Bi-induced increase

in N incorporation during MBE may be related to a Bi surface coverage displacing surface As, facilitating N substitution into As sites.[8] To date, the atomistic mechanisms for the influence of Bi flux on N incorporation remain unknown.

4.3 Methods

The $GaAs_{1-x-y}N_xBi_y$ alloy films were grown on semi-insulating (001) GaAs substrates by molecular-beam epitaxy using solid Ga, As, and Bi sources and a radio frequency nitrogen plasma source. The cracking zone of the As source was maintained at a relatively low temperature such that predominantly As_4 was supplied, reducing the dependence of Bi incorporation on the As/Ga ratio, as described in Ch. 1.[14,15] The sample layer structure is shown in Figure 4.1. After an initial 500-nm thick GaAs buffer layer grown at 580ºC, the substrate temperature was held at 580ºC for a 5 minute anneal, then lowered to the GaAsNBi growth temperature and held for another 5 minute anneal.[16] 100 nm thick $GaAs_{1-x-y}N_xBi_y$ films were then grown at 345 ± 15 ºC with As_4/Ga beam equivalent pressure (BEP) ratio of ~ 20 and growth rate of 1 μm/h. A series of films with a range of N and Bi fractions were achieved by independently varying the Bi BEP from 0 to 1×10^{-7} Torr (with N_2 flow rate fixed at 0.25 sccm), and the N_2 flow rate from 0.17 to 0.35 sccm (with Bi BEP fixed at 5.7×10^{-7} Torr), which we will refer to as the "Bi flux series" and the "N flux series", respectively.

To monitor the influence of Bi and N fluxes on surface reconstruction, reflection high-energy electron diffraction (RHEED) patterns were collected along the [110] and [$1\bar{1}0$] directions for the Bi flux series and the N flux series. For all films, a (2 x 4) RHEED pattern [Figure 4.3(a) and Figure 4.3(b)] was observed during growth of the GaAs buffer

layer at 580°C; the pattern transitioned to a (2 x 3) pattern [Figure 4.3(c) and Figure 4.3(d)] as the temperature was ramped under As overpressure to 345 ± 15°C. During GaAsNBi growth with low Bi fluxes, a (1 x 3) pattern [Figure 4.3(e) and Figure 4.3(f)] was observed, consistent with the Bi-induced (1 x 3) reconstruction reported by others for GaAsN growth in the presence of a Bi flux.[7,11] At higher Bi flux, above BEP ~ 5.7×10^{-8} Torr, a (2 x 1) reconstruction was observed instead [Figure 4.3(g) and Figure 4.3(h)]. For the N flux series, with the Bi flux kept constant at 5.7×10^{-8} Torr, all films showed either a (1 x 3) or a (2 x 1) pattern, suggesting that this Bi flux is near the threshold between the (1 x 3) induced by lower Bi fluxes and the (2 x 1) induced by higher Bi fluxes. Growth of GaAsN without a Bi flux resulted in a (2 x 1) pattern similar to Figure 4.3(g) and Figure 4.3(h).

For both the N and Bi flux series of GaAsNBi films, the surface morphologies and compositions were examined using a combination of atomic force microscopy (AFM), HRXRC, RBS, and NRA. AFM images were collected using a Bruker Dimension Icon in tapping mode, as described in Section 2.7. HRXRC measurements were performed using Cu $K\alpha_1$ radiation. A series of $\Delta\omega$ scans were collected near the GaAs (004) and GaAs (224) reflections, as described in Section 2.3. RBS and NRA were performed using a NEC tandem accelerator with a 4.46 MeV He^+ beam, as described in Chapter 2 and Appendix D of the Ph.D. thesis of Dr. Tim Jen.[17] The RBS (NRA) detector was placed at 167° (135°) with respect to the incident beam to detect the backscattered He^+ ions.[18] We used the nuclear reaction $^{14}N(\alpha,p)^{17}O$ to detect the nitrogen atoms.[19] RBS and NRA measurements were performed in [100], [110], and [111] channeling and non-channeling conditions achieved by oscillating the specimen ±4° around the channeling condition in both phi and theta directions during spectra collection. We note that both RBS and NRA data are

analyzed using the simulation of nuclear reaction analysis (SIMNRA) code, an analytical simulation program in which multiple small-angle scattering events are treated as energy broadening.[20] To simulate the channeling NRA spectra, we use a combined Monte Carlo-Molecular Dynamics (MC-MD) approach. More details about the simulation and analysis are provided in Chapter 2 and Appendix D the Ph.D. thesis of Dr. Tim Jen.[17,18]

4.4 Selection of the GaAsNBi growth temperature

A key concern for co-incorporation of N and Bi is selection of an appropriate growth temperature. For N incorporation, there exists a "forbidden window" of temperatures, extending from approximately 450 °C to 550 °C, depending on the growth rate and group V/III flux ratio, at which significant surface roughening occurs.[16,21] Bi incorporation has been shown to drop off steeply as the temperature is increased from 330 °C to 400 °C, with negligible Bi incorporation at growth temperatures > 410 °C.[14] Indeed, the highest Bi fractions incorporated in GaAsBi to date have been achieved at even lower temperatures, < 300 °C.[14,22] However, growth of GaAs at temperatures < 300 °C often leads to incorporation of significant fractions of excess As in the form of As antisites, As_{Ga}, which can suppress both carrier transport and radiative recombination.[23] Because the incorporation of significant concentrations of As antisites expands the lattice parameter relative to that of stoichiometric GaAs, [As_{Ga}] can be quantified from the splitting between the diffraction peaks of a non-stoichiometric GaAs layer and the GaAs substrate,[24] as described in Section 3.5.

Therefore, to identify a GaAsNBi growth temperature with minimal excess As incorporation, we grew a series of 400 nm thick GaAsNBi films, each with a corresponding

non-stoichiometric GaAs buffer layer grown at the same temperature, similar to Figure 3.2, for temperatures ranging from 230 °C to 346 °C. The growth temperatures were measured by a thermocouple attached to the back of the molybdenum substrate holder, calibrated as described in Section 2.2.4. The N and Bi fluxes were held constant for the GaAsNBi films. (004) HRXRC for these films are shown in Figure 4.2. At 230 °C, [As_{Ga}]-induced expansion of the lattice parameter in the non-stoichiometric GaAs buffer layer results in a diffraction peak approximately 100 arcsec lower than that of the GaAs substrate peak. With increasing temperature, the non-stoichiometric GaAs peak moves to higher angle and eventually merges with the GaAs substrate peak, indicating a reduction in the incorporation of excess As. Due to the absence of a separate non-stoichiometric GaAs diffraction peak for growth temperatures > 330 °C, we used a growth temperature of 345 ± 15°C for the GaAs(N)(Bi) films discussed in the remainder of this chapter.

4.5 Influence of N and Bi fluxes on Bi and N fractions

HRXRC of the Bi flux series and N flux series are presented in Figure 4.4(a) and Figure 4.4(b). Due to their compressive and tensile misfit with respect to GaAs, the GaAsBi and GaAsN diffraction peaks appear on the low-angle and high-angle side of the GaAs substrate peak, respectively. For the Bi flux series, the GaAsN(Bi) peak is shifted from the high-angle side with negligible Bi incorporation to the low-angle side as the Bi incorporation is increased. In addition, for the N flux series, the GaAs(N)Bi peak is shifted toward the high-angle side as the N incorporation is increased. AFM images for the Bi flux series and the N flux series are presented in Figure 4.5(a)-(d) and Figure 4.5 (e)-(h) respectively. For both the Bi and N flux series, the surfaces appear featureless, with rms

roughness < 0.5nm, consistent with observations of layer-by-layer growth of GaAsN.[25,26] To confirm the absence of μm-sized surface droplets, SEM images were collected for areas of approximately 400 μm x 500, as shown in Figure 4.5 (i)-(j). Features associated with dust were included in each image to demonstrate the suitable focus condition; the surfaces are otherwise featureless, without droplets.

For the N flux series, shown in Figure 4.4(a), the N mole fraction, *x*, and Bi mole fraction, *y*, determined from analyses of NRA and RBS data respectively, are indicated on the HRXRC plots. As the N_2 flow rate increases, *x* increases monotonically. Meanwhile *y* is unchanged with increasing N_2 flow rate, indicating that Bi incorporation is unaffected by co-incorporation with N. For the Bi flux series, shown in Figure 4.4(b), the *x* and *y* fractions determined from analyses of NRA and RBS are also indicated on the HRXRC plots. As the Bi flux increases, *y* increases monotonically. Furthermore, although the N flux is fixed, *x* also increases with Bi flux, up to a saturation value of ~0.018, as discussed further in Section 4.6.

4.6 Interstitial N concentration

We now discuss the RBS spectra for the Bi flux series and the NRA spectra for the N flux series. For the Bi flux series, the RBS yield vs. backscattered ion energies is plotted in Figure 4.6(a); an enlarged portion is plotted in Figure 4.6(b) with random spectra data overlaid with SIMNRA fitted spectra. Due to the similar atomic masses of Ga and As, the energies of the He ions backscattered from Ga and As are similar, ~3.6MeV, in Figure 4.6(a), and similar RBS yields associated with both atoms are also observed due to their similar atomic numbers. Due to the high atomic mass of Bi, the energies of the He ions

backscattered from Bi are at higher energy, ~4.1MeV. Both the random and channeling RBS yields associated with Bi increase with increasing Bi flux. SIMNRA fits to the random RBS spectra reveal y ranging from 0 to 0.059. In addition, SIMNRA fits, assuming a uniform Bi depth profile, produce Gaussian-shaped RBS yields that match with the measured random spectra, suggesting a uniform incorporation of Bi throughout the GaAsNBi film. For the channeling spectra, the distinct peaks (corresponding to He scattering from Ga and As) near ~3.6MeV and the asymmetric peak (associated with He scattering from Bi) at ~4.1MeV are due to preferential scattering from exposed surface atoms.[27]

For the N flux series, the NRA yield vs. reaction-emitted proton energy is plotted in Figure 4.6(c). Both random and channeling NRA yields associated with N increase with increasing N flux. SIMNRA fits to the random NRA spectra, using a GaAsN standard, reveal x ranging from 0 to 0.017; assuming a uniform N depth profile, SIMNRA fits suggest uniform incorporation of N throughout the GaAsNBi film. The fraction of substitutionally incorporated N atoms, $f_{N\text{-}sub}$, was calculated according to

$$f_{N-sub} = \frac{1-\chi(N)}{1-\chi_{min}(GaAs)} \quad (4.1)$$

where $\chi(N)$ is the ratio of the channeling to the non-channeling NRA yield and $\chi_{min}(GaAs)$ is the ratio of the channeling to the non-channeling RBS yield for the GaAs reference film. To determine the fraction of Bi atoms incorporating substitutionally in GaAs(N)Bi films, $f_{Bi\text{-}sub}$, we used an analogous equation with $\chi(N)$ replaced by $\chi(Bi)$, defined as the ratio of the channeling to the non-channeling Bi-related RBS yield. In Figure 4.7, the total, x, substitutional, x_{sub}, and interstitial, x_{int}, mole fractions of N are plotted for the Bi flux series. As discussed earlier, x increases with increasing Bi BEP. In the GaAsN film (Bi BEP = 0

Torr), the fraction of N occupying substitutional sites, $f_{N\text{-}sub} = x_{sub}/x$, is 0.81, consistent with other literature reports for GaAsN.[16,17,28] As the Bi BEP is increased, $f_{N\text{-}sub}$ decreases, indicating that the fraction of N atoms occupying non-substitutional sites increases with increasing Bi flux. For all Bi-containing films, $f_{Bi\text{-}sub}$ is ≥ 0.90, independent of Bi BEP or N_2 flow rate.

4.7 Dominant interstitial complex in GaAsNBi

To determine the N interstital complex configuration, the measured NRA channeling data are compared with MC-MD simulations of a 3x3 unit cell of GaAsNBi with N-to-Bi incorporation ratio of 1-to-2. Additional details of the MC-MD simulations can be found in Chapter 2 and Appendix D of the Ph.D. thesis of Dr. Tim Jen.[17] Within each cell, each N is positioned at the center of the group V site as either substitutional N, N_{As}; $(N\text{-}N)_{As}$, with N_2 aligned along the [111] direction; or $(N\text{-}As)_{As}$, with the N-As pair aligned along the [010] direction, as illustrated in Figure 4.8.[29,30,31,32] Within each cell, each Bi is positioned at the center of the group V site as substitutional Bi, Bi_{As}. Due to the large size of Bi atoms, we also include atomic displacement of nearest-neighbor Ga, where the Bi-Ga bond length is considered to be 2.63 Å, compared to the As-Ga bond length of 2.46 Å.[33] In Figure 4.9, we present a comparison of the simulated and measured NRA yields for GaAsNBi. For both the N_{sub} and $(N\text{-}N)_{As}$ interstitial complexes, the NRA simulations predict the highest (lowest) yields in the [100] ([111]) directions, as shown in Figure 4.9(a)-(b), leading to a yield trend of $Y_{[100]} > Y_{[110]} > Y_{[111]}$. In contrast, for the interstitial pair $(N\text{-}As)_{As}$, NRA simulations predict the highest (lowest) yield in the [111] ([100]) directions, as shown in Figure 4.9(c), with a yield trend of $Y_{[111]} > Y_{[110]} > Y_{[100]}$. As

shown in Figure 4.9(d), the measured yield trend is $Y_{[111]} > Y_{[110]} > Y_{[100]}$; this particular yield trend is predicted only for the case where $(N\text{-}As)_{As}$ is the dominant interstitial complex. Therefore, our combined computational-experimental approach suggests that $(N\text{-}As)_{As}$ is the dominant interstitial complex in GaAsNBi alloys, consistent with other reports for GaAsN and related dilute nitride alloys. [18,34,35,36,37,38,39]

4.8 Mechanism for Bi-enhanced N incorporation

We next discuss a mechanism for Bi-induced enhancement of N incorporation based upon Bi adatom induced disordering of $[\bar{1}10]$-oriented step edges during growth with a (1x3) reconstruction. Standard MBE growth of GaAs, with a (2x4) reconstruction, typically results in long terraces with step edges oriented along the $[\bar{1}10]$ direction.[40] Dimroth et al. showed that N incorporation is suppressed on (111)A offcut surfaces upon which the density of $[\bar{1}10]$-oriented step edges is increased.[12] On a (2x4) reconstructed GaAs surface, it has been shown that $[\bar{1}10]$ step edges may be disrupted by exposure to Bi, resulting in (1x3) or (4x3) reconstruction consisting of smaller islands with a higher density of [110]-oriented step edges.[41] Thus, for GaAsN, the surface Bi adatoms, which induce the (1x3) reconstruction shown in Figure 4.3(e) and Figure 4.3(f), may increase the density of [110] step edges, allowing increased incorporation of N atoms. Furthermore, the [110] step edge consists of As dangling bonds, such that a N atom incorporating on a [110] step edge would have an increased likelihood of forming a $(N\text{-}As)_{As}$ interstitial complex,[28,29,30,31,32,33] as illustrated in Figure 4.10. Consequently, the Bi adatom induced enhancement in N incorporation would be accompanied by an increased fraction of interstitial N, consistent with our observations.

4.9 Summary and conclusions

In summary, we have investigated the influence of Bi flux on N incorporation in GaAsNBi alloys. Using a combination of Rutherford backscattering spectrometry (RBS), nuclear reaction analysis (NRA), and high-resolution x-ray rocking curves (HRXRC), we showed that both the total N content as well as the fraction of N atoms occupying non-substitutional sites increase with increasing Bi flux. A comparison of channeling NRA measurements along the [100], [110], and [111] directions with Monte Carlo-Molecular Dynamics (MC-MD) simulations indicated that the non-substitutional N primarily occur as $(N\text{-}As)_{As}$ interstitial complexes. The enhancement in both N incorporation and N interstitial formation may be linked to a Bi-adatom- induced increase in the fraction of [110]-oriented step edges with As dangling bonds. This insight provides a pathway to tailored N incorporation in GaAsNBi and related alloys.

4.10 Figures

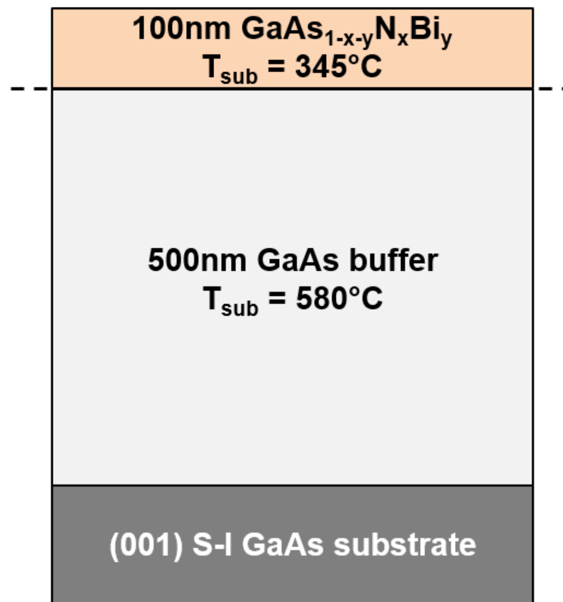

Figure 4.1 Schematic of the sample layer structure for both the N flux series and the Bi flux series. The dashed line indicates a growth interrupt during which the substrate temperature, T_{sub}, was ramped.

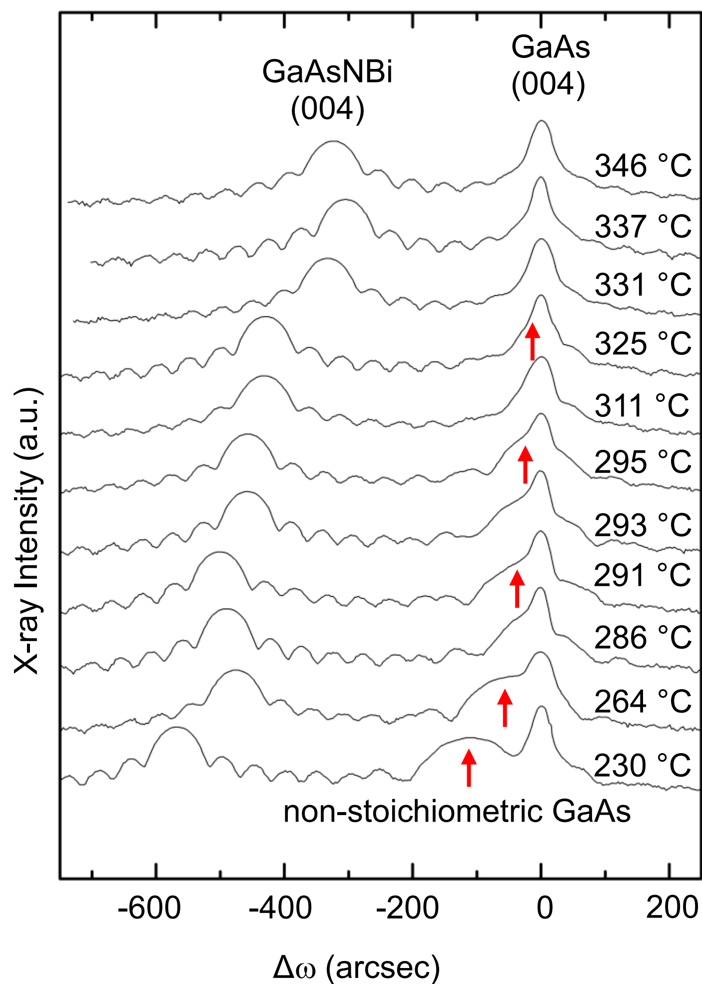

Figure 4.2 (004) high-resolution x-ray rocking curves for GaAsNBi films and GaAs buffer layers at growth temperatures ranging from 230 °C to 346 °C. At 230 °C, expansion of the low-temperature GaAs buffer layer lattice parameter due to excess As incorporation results in a diffraction peak approximately 100 arcsec to the left of the GaAs substrate peak. With increasing temperature, the non-stoichiometric GaAs peak moves to higher angle and eventually merges with the GaAs substrate peak, indicating a reduction in excess As incorporation.

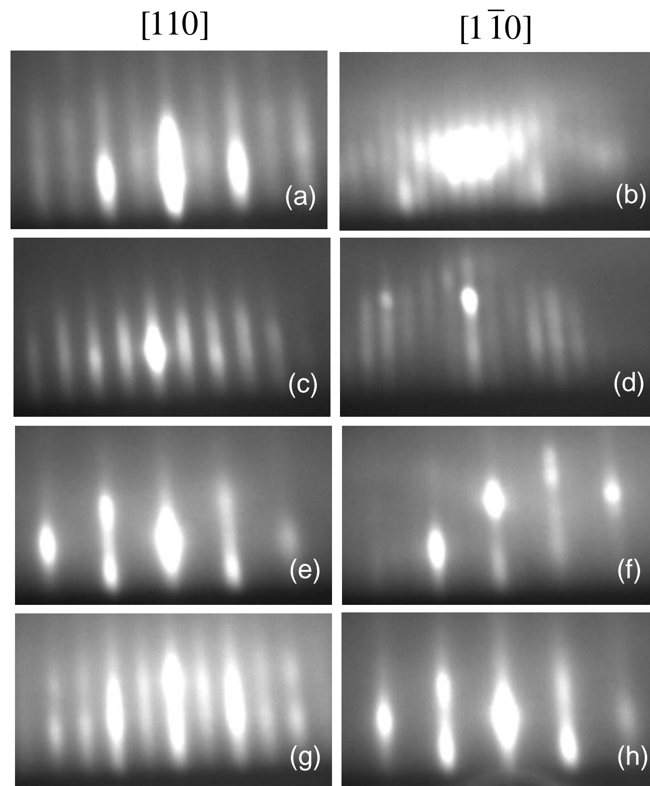

Figure 4.3 Reflection high-energy electron diffraction patterns along the [110] and [1$\bar{1}$0] axes during GaAs(N)(Bi) film growth. [(a), (b)] (2 x 4) pattern following GaAs growth at 580°C; [(c), (d)] (2 x 3) pattern at 345 ± 15°C immediately prior to the GaAs(N)(Bi) growth; [(e), (f)] (1 x 3) pattern during GaAsNBi growth at 345 ± 15°C with Bi flux ≤ 5.7 × 10^{-8} Torr; [(g), (h)] (2 x 1) pattern during GaAsNBi growth with Bi flux ≥ 5.7 × 10^{-8} Torr. Reprinted with permission from Ref. 42 (Copyright 2017, AIP Publishing).

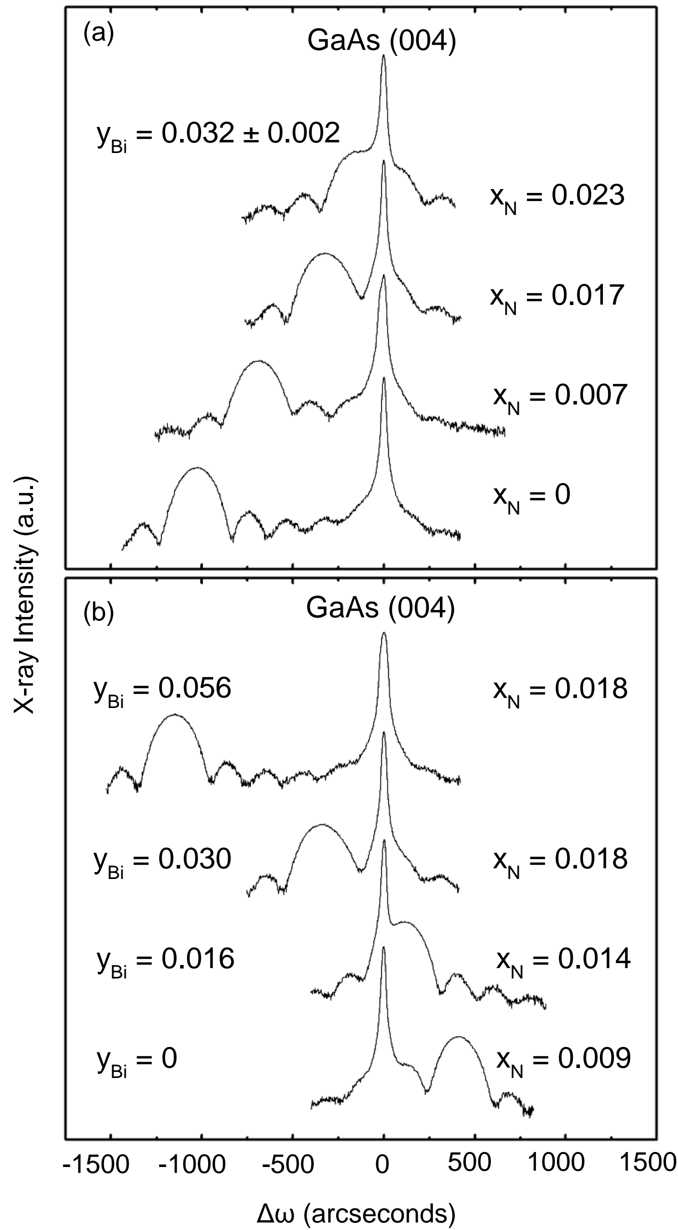

Figure 4.4 (004) high-resolution x-ray rocking curves for the (a) N flux series with x_N ranging from 0 to 0.023 and (b) Bi flux series with y_{Bi} ranging from 0 to 0.056. For all plots, the GaAs substrate peak is set to $\Delta\omega = 0$ arcseconds, thereby facilitating comparison of $\Delta\omega$ between the GaAs substrate and the GaAsNBi epilayers. Within the N flux series, y_{Bi} remains fixed as x_N is increased. However, within the Bi flux series, x_N increases as y_{Bi} increases, suggesting a Bi-induced enhancement of N incorporation. Reprinted with permission from Ref. 42 (Copyright 2017, AIP Publishing).

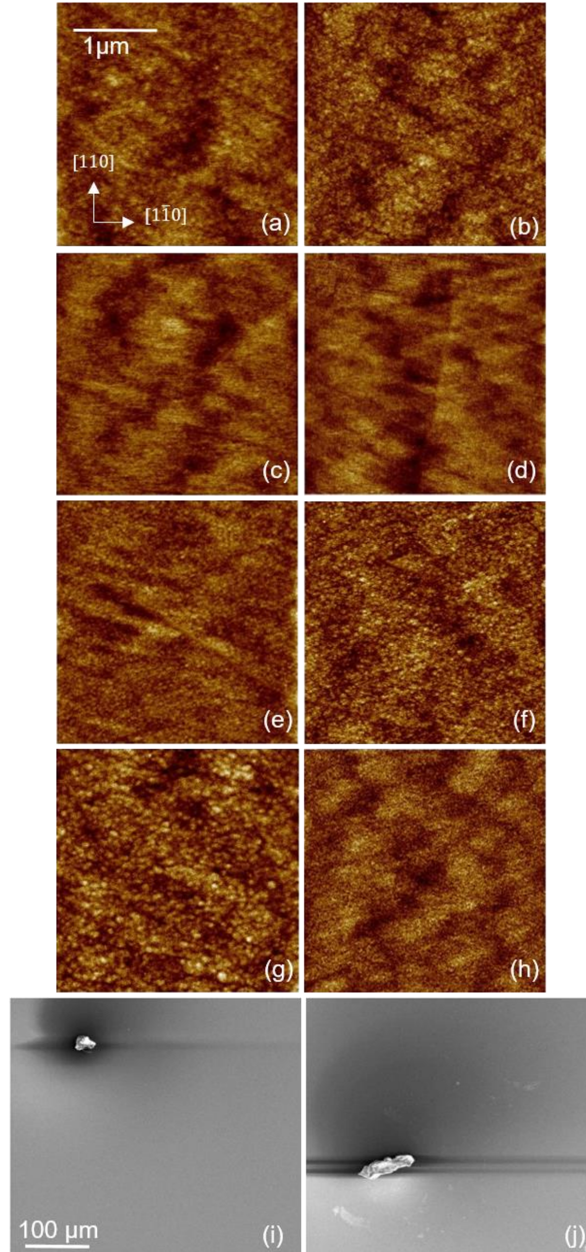

Figure 4.5 AFM images of the Bi flux series ((a)-(d)) and the N flux series ((e)-(f)). The colorscale range displayed is 3nm and the rms roughness is 0.3nm±0.05nm for all images, consistent with the typical <0.5nm rms roughness observed for layer-by-layer growth.[25,26] To confirm the absence of μm-sized surface droplets, SEM images were collected for areas of approximately 400 μm x 500 μm, as shown in (i)-(j). Features associated with dust were included to demonstrate that the images are in focus; the surfaces are otherwise featureless, without droplets. (a) – (h) are reprinted with permission from Ref. 42 (Copyright 2017, AIP Publishing).

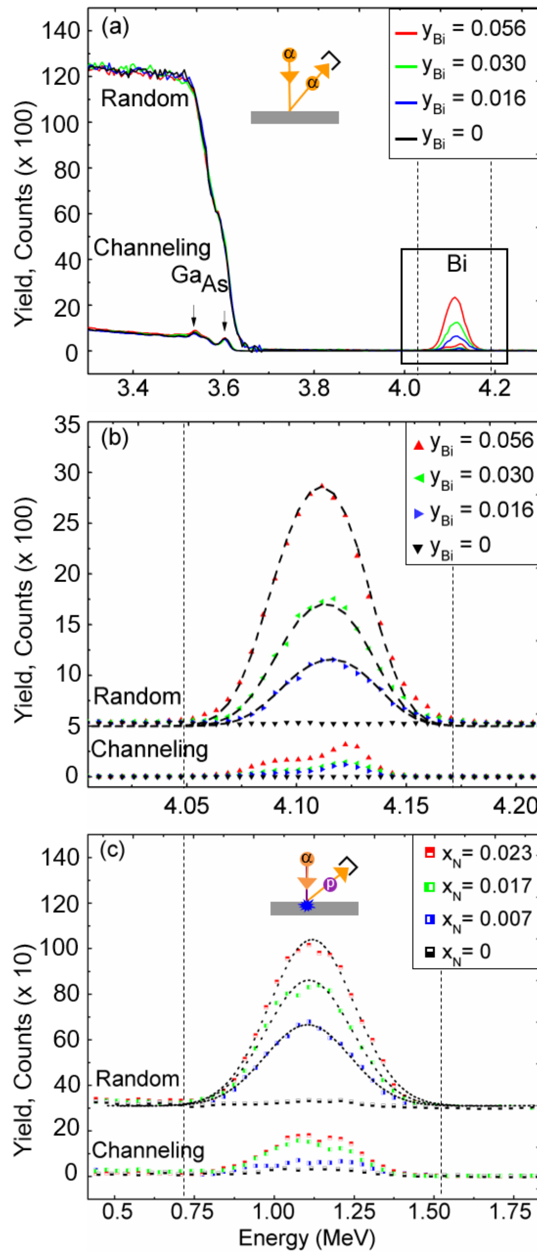

Figure 4.6 Measured RBS yield versus backscattered particle energy for the Bi flux series. The vertical dashed lines indicate the energy window of ions backscattered from Bi atoms. As the Bi flux increases, the resulting Bi signal increases. (b) The portions of the RBS spectra enclosed in the box in (a) are shown in (b). Non-channeling data is overlaid with SIMNRA fitted spectra assuming uniform Bi depth profiles. Fitted Gaussian-shape spectra suggest uniform Bi incorporation throughout the GaAsNBi films. (c) Measured NRA yield versus emitted particle energy for the N flux series. The vertical dashed lines indicate the energy window of the protons emitted during the $^{14}N(\alpha,p)^{17}O$ reaction. As the N flux increases, the resulting N signal increases. Non-channeling data are overlaid with SIMNRA fitted spectra assuming a uniform N depth profile. Fitted Gaussian-shape non-channeling spectra suggest uniform N incorporation throughout the GaAsNBi film. Reprinted with permission from Ref. 42 (Copyright 2017, AIP Publishing).

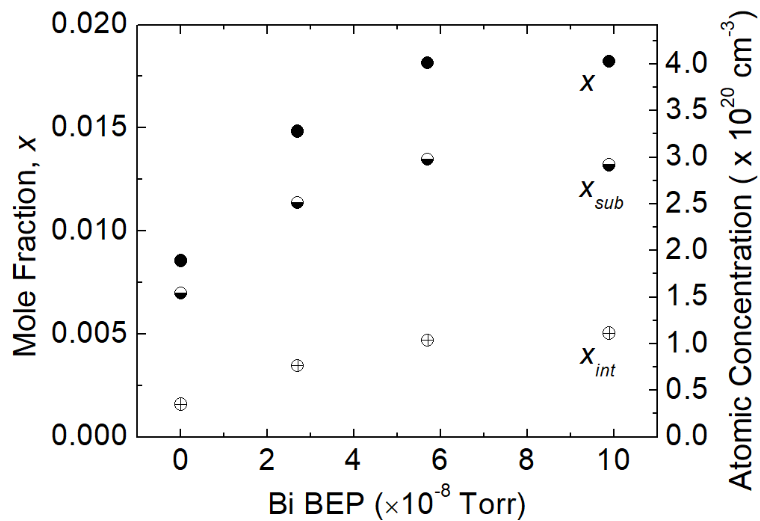

Figure 4.7 Fractions of total N, x, substitutional N, x_{sub}, and interstitial N, x_{int} for the Bi flux series of GaAsN(Bi) films determined by channeling and non-channeling nuclear reaction analysis. The atomic concentrations corresponding to the mole fractions are shown on the right y-axis. Both x and x_{int} increase with Bi flux, suggesting a Bi-induced enhancement of N incorporation, with preferential incorporation in interstitial sites. Reprinted with permission from Ref. 42 (Copyright 2017, AIP Publishing).

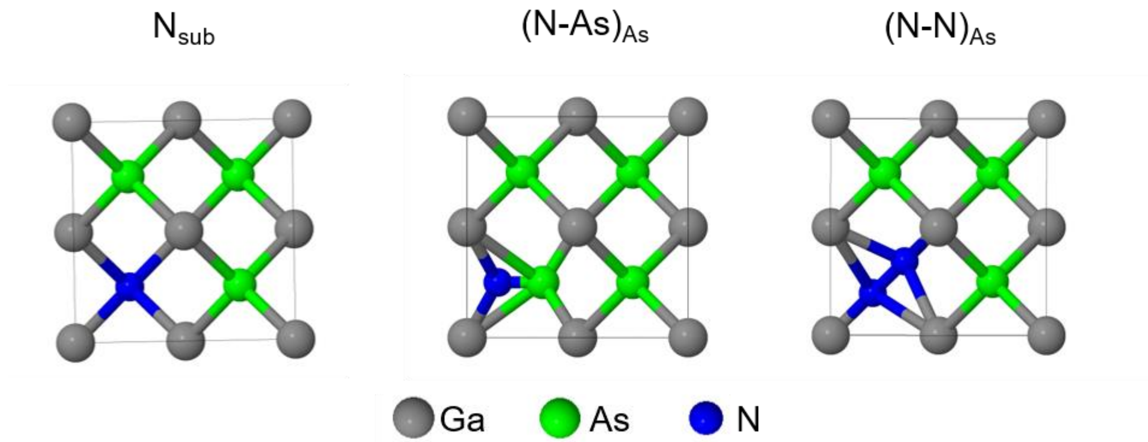

Figure 4.8 Illustration of substitutional N, N_{As}; $(N\text{-}As)_{As}$, with the N-As pair aligned along the [010] direction; and $(N\text{-}N)_{As}$, with N_2 aligned along the [111] direction.

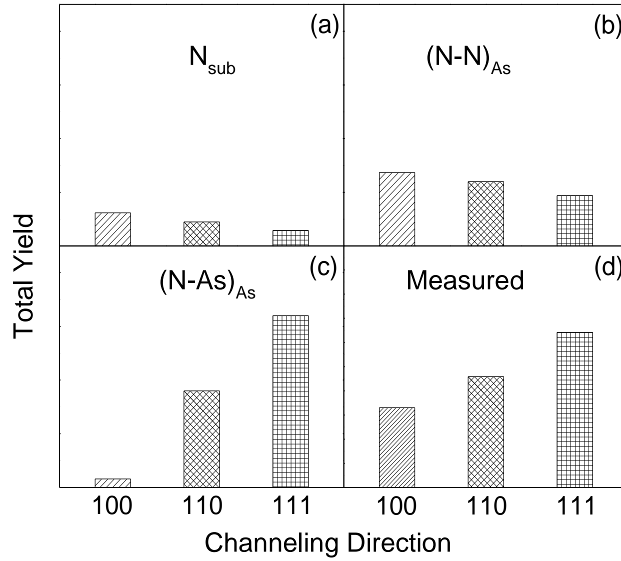

Figure 4.9 Total simulated NRA yields in the [100], [110], and [111] directions for (a) N_{sub}, (b) $(N\text{-}N)_{As}$, and (c) $(N\text{-}As)_{As}$. (d) Measured total NRA yield in each channeling direction. Similar yield trends of $Y_{[111]} > Y_{[110]} > Y_{[100]}$ are observed for (c) and (d), suggesting that $(N\text{-}As)_{As}$ is the dominant interstitial complex in GaAsN alloys. Reprinted with permission from Ref. 42 (Copyright 2017, AIP Publishing).

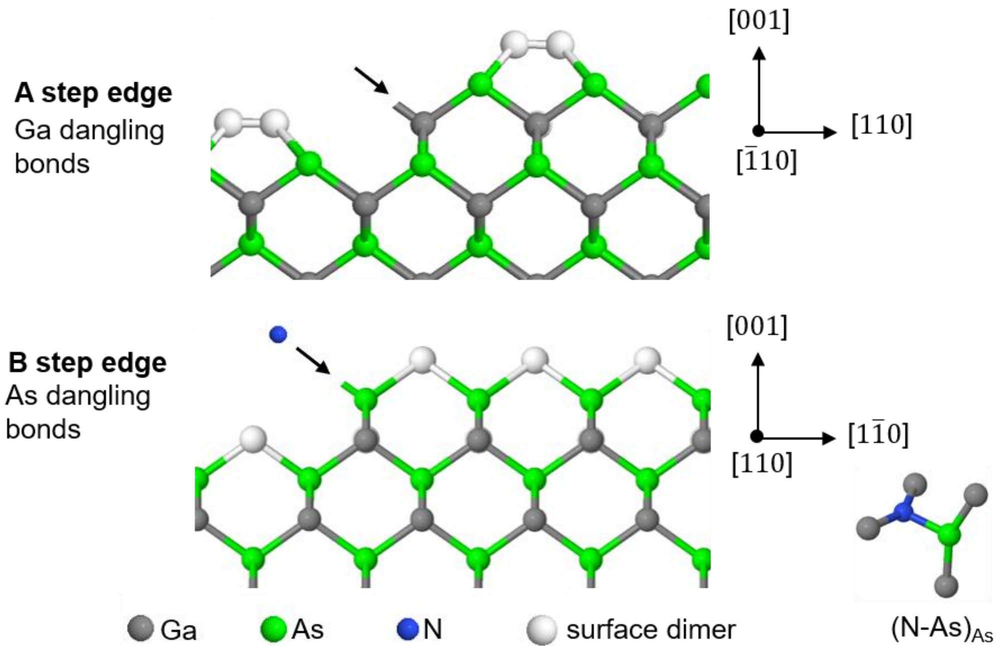

Figure 4.10 Schematic of a [$\bar{1}$10]-oriented A-step with Ga dangling bonds and a [110]-oriented B-step edge with As dangling bonds. Bismuth increases the density of B-step edges with As dangling bonds, facilitating the formation of $(N\text{-}As)_{As}$.

4.11 References

[1] S.R. Kurtz, A.A. Allerman, C.H. Seager, R.M. Sieg, and E.D. Jones, “Minority Carrier Diffusion, Defects, and Localization in InGaAsN, with 2% Nitrogen”, Appl. Phys. Lett. 77, 400 (2000).

[2] E.V.K. Rao, A. Ougazzaden, Y. Le Bellego, and M. Juhel, “Optical Properties of Low Band Gap GaAs(1−x)Nx Layers: Influence of Post-Growth Treatments”, Appl. Phys. Lett. 72, 1409 (1998).

[3] A. Janotti, S.H. Wei, and S.B. Zhang, “Theoretical Study of the Effects of Isovalent Coalloying of Bi and N in GaAs”, Phys. Rev. B 65, 115203 (2002).

[4] A. Mascarenhas, US6815736 B2 (9 November 2004).

[5] S. Tixier, M. Adamcyk, T. Tiedje, S. Francoeur, A. Mascarenhas, P. Wei, and F. Schiettekatte, “Molecular Beam Epitaxy Growth of GaAs1-xBix”, Appl. Phys. Lett. 82, 2245 (2003).

[6] Z. Batool, K. Hild, T.J.C. Hosea, X. Lu, T. Tiedje, and S.J. Sweeney, “The Electronic Band Structure of GaBiAs/GaAs Layers: Influence of Strain and Band Anti-Crossing”, J. Appl. Phys. 111, 113108 (2012).

[7] S. Tixier, M. Adamcyk, E.C. Young, J.H. Schmid, and T. Tiedje, “Surfactant Enhanced Growth of GaNAs and InGaNAs Using Bismuth”, J. Cryst. Growth 251, 449 (2003).

[8] E.C. Young, S. Tixier, and T. Tiedje, “Bismuth Surfactant Growth of the Dilute Nitride GaNxAs1−x”, J. Cryst. Growth 279, 316 (2005).

[9] K. Sakamoto, K. Kyoya, K. Miki, H. Matsuhata, and T. Sakamoto, “Which Surfactant Shall We Choose for the Heteroepitaxy of Ge/Si(001)? –Bi as a Surfactant with Small Self-Incorporation”, Jpn. J. Appl. Phys. 32, L204 (1993).

[10] M.R. Pillai, S.-S. Kim, S.T. Ho, and S.A. Barnett, “Growth of InxGa1−xAs/GaAs Heterostructures Using Bi as a Surfactant”, J. Vac. Sci. Technol. B 18, 1232 (2000).

[11] T. Liu, S. Chandril, A.J. Ptak, D. Korakakis, and T.H. Myers, “Bismuth Surfactant Effects for GaAsN and Beryllium Doping of GaAsN and GaInAsN Grown by Molecular Beam Epitaxy", J. Cryst. Growth 304, 402 (2007).

[12] F. Dimroth, A. Howard, J.K. Shurtleff, and G.B. Stringfellow, “Influence of Sb, Bi, Tl, and B on the Incorporation of N in GaAs”, J. Appl. Phys. 91, 3687 (2002).

[13] Z.L. Bushell, P. Ludewig, N. Knaub, Z. Batool, K. Hild, W. Stolz, S.J. Sweeney, and K. Volz, “Growth and Characterisation of Ga(NAsBi) Alloy by Metal–Organic Vapour Phase Epitaxy”, J. Cryst. Growth 396, 79 (2014).

[14] W. Bennarndt, G. Boehm, and M.-C. Amann, “Domains of Molecular Beam Epitaxial Growth of Ga(In)AsBi on GaAs and InP Substrates”, J. Cryst. Growth 436, 56 (2016).

[15] R.L. Field, J. Occena, T. Jen, D. Del Gaudio, B. Yarlagadda, C. Kurdak, and R.S. Goldman, “Influence of Surface Reconstruction on Dopant Incorporation and Transport Properties of GaAs(Bi) Alloys”, Appl. Phys. Lett. 109, 252105 (2016).

[16] M. Reason, H.A. McKay, W. Ye, S. Hanson, R.S. Goldman, and V. Rotberg, “Mechanisms of Nitrogen Incorporation in GaAsN Alloys”, Appl. Phys. Lett. 85, 1692 (2004).

[17] T. Jen, "Ion Beam Analysis of Solute Incorporation in GaAsN and GaAsNBi Alloys", Ph.D Thesis, University of Michigan, 2017, p. 43-46, 164-179.

[18] T. Jen., G. Vardar, Y. Q. Wang, and R. S. Goldman, “Identifying the Dominant Interstitial Complex in Dilute GaAsN Alloys”, Appl. Phys. Lett. 107, 221904 (2015).

[19] P. Wei, M. Chicoine, S. Gujrathi, F. Schiettekatte, J-N. Beaudry, R. A. Masut, and P. Desjardins, “Characterization of GaAs1−xNx Epitaxial Layers by Ion Beam Analysis”, J. Vac. Sci. Technol. A, 22.3 908 (2004).

[20] M. Mayer., W. Eckstein, H. Langhuth, F. Schiettekatte, and U. von Toussaint, “Computer Simulation of Ion Beam Analysis: Possibilities and Limitations”, Nucl. Instrum. Meth. B 269, 3006 (2011).

[21] S.R. Bank, H. Bae, L.L. Goddard, H.B. Yuen, M.A. Wistey, R. Kudrawiec, and J.S. Harris, “Recent Progress on 1.55-μm Dilute-Nitride Lasers” IEEE J. Quantum Elect. 43, 773 (2007).

[22] R.B. Lewis, M. Masnadi-Shirazi, and T. Tiedje, “Growth of High Bi Concentration $GaAs_{1-x}Bi_x$ by Molecular Beam Epitaxy”, Appl. Phys. Lett. 101, 082112 (2012).

[23] S. O’Hagan and M. Missous, “Effect of As4/Ga Flux Ratio on Electrical and Optical Properties of Low-Temperature GaAs Grown by Molecular Beam Epitaxy”, J. Appl. Phys. 75, 7835 (1994).

[24] X. Liu, A. Prasad, J. Nishio, E.R. Weber, Z. Liliental-Weber, and W. Walukiewicz, “Native Point Defects in Low-Temperature-Grown GaAs”, Appl. Phys. Lett. 67, 279 (1995).

[25] M. Reason, N.G. Rudawski, H.A. McKay, X. Weng, W. Ye, and R.S. Goldman, “Mechanisms of GaAsN Growth: Surface and Step-Edge Diffusion”, J. Appl. Phys. 101, 083520 (2007).

[26] W.K. Cheah, W.J. Fan, S.F. Yoon, S.Z. Wang and W.K. Loke, "X-Ray Reciprocal Space Mapping of Strain Relaxation in GaAs1−xNx on GaAs [100] by Molecular-Beam Epitaxy", J. Appl. Phys. 94, 3828 (2003).

[27] J.R. Tesmer and M.A. Nastasi, *Handbook of Modern Ion Beam Materials Analysis* (Materials Research Society, 1995).

[28] S. Spruytte, M. Larson, W. Wampler, C. Coldren, H. Petersen, and J. Harris, "Nitrogen Incorporation in Group III–Nitride–Arsenide Materials Grown by Elemental Source Molecular Beam Epitaxy", J. Cryst. Growth 227–228, 506 (2001).

[29] P. Carrier, S.-H. Wei, S. B. Zhang, and S. Kurtz, "Evolution of Structural Properties and Formation of N-N Split Interstitials in GaAs 1 − x N x Alloys", Phys. Rev. B 71, 165212 (2005).

[30] K. Laaksonen, H.-P. Komsa, T. T. Rantala, and R. M. Nieminen, "Nitrogen Interstitial Defects in GaAs", J. Phys. Condens. Matter 20, 235231 (2008).

[31] S.B. Zhang and S.H. Wei, "Nitrogen Solubility and Induced Defect Complexes in Epitaxial GaAs:N", Phy. Rev. Lett. 86, 1789 (2001).

[32] E. Arola, J. Ojanen, H.-P. Komsa and T. T. Rantala, "Atomic and Electronic Structures of N Interstitials in GaAs", Phys. Rev. B 72, 045222 (2005).

[33] G. Ciatto, P. Alippi, A. Amore Bonapasta, and T. Tiedje, "How Much Room for Bi_{Ga} Heteroantisites in $GaAs_{1-x}Bi_{x}$?", Appl. Phys. Lett 99, 141192 (2011).

[34] F. Ishikawa, S. Fuyuno, K. Higashi, M. Kondow, M. Machida, H. Oji, J.-Y. Son, A. Trampert, K. Umeno, Y. Furukawa, and A. Wakahara, . "Direct Observation of N-(Group V) Bonding Defects in Dilute Nitride Semiconductors Using Hard x-Ray Photoelectron Spectroscopy", Appl. Phys. Lett 98, 121915 (2011).

[35] K.M. Kim, W.-B. Kim, D. Krishnamurthy, J.H. Ryu, S. Hasegawa, and H. Asahi, "Study on Nitrogen-Induced Defects Formation and Annealing Effects in TlInGaAsN Alloy System", J. Cryst. Growth 368, 35-38 (2013).

[36] J. Chen, G. Ciatto, M. Le Du, J.C. Harmand and F. Glas, "Local Structure of Indium in Quinary (InGa)(AsSbN)/GaAs Quantum Wells", Phys. Rev. B 82, 125303 (2010).

[37] H.T. Pham, S.F. Yoon, K.H. Tan and D. Boning, "Effects of Nitrogen Incorporation in InSb1−xNx Grown Using Radio Frequency Plasma-Assisted Molecular Beam Epitaxy", Appl. Phys. Lett 90, 092115 (2007).

[38] H.P Nair, A.M. Crook, K.M. Yu and S.R. Bank, "Structural and Optical Studies of Nitrogen Incorporation into GaSb-Based GaInSb Quantum Wells", Appl. Phys. Lett 100, 021103 (2012).

[39] J. Buckeridge, D.O. Scanlon, T.D. Veal, M.J. Ashwin, A. Walsh and C.R.A. Catlow. "N Incorporation and Associated Localized Vibrational Modes in GaSb", Phys. Rev. B 89, 014107 (2014).

[40] M. Pashley, K. Haberern, and J. Gaines, "Growth on (001) and Vicinal (001) GaAs Surfaces in a Combined Scanning Tunneling Microscope/Molecular-beam Epitaxy System", J. Vac. Sci. Technol. B 9, 938 (1991).

[41] A. Duzik, J.C. Thomas, J.M. Millunchick, J. Lång, M.P.J. Punkkinen, and P. Laukkanen, "Surface Reconstruction Stability and Configurational Disorder on Bi-Terminated GaAs(001)", Surf. Sci. 606, 1203 (2012).

[42] J. Occena, T. Jen, E.E. Rizzi, T.M. Johnson, J. Horwath, Y.Q. Wang, and R.S. Goldman, "Bi-Enhanced N Incorporation in GaAsNBi Alloys", Appl. Phys. Lett. 110, 242102 (2017).

Chapter 5

Surfactant-Induced Chemical Ordering of GaAsN:Bi

5.1 Overview

In this chapter we examine the influence of an incorporating surfactant, Bi, on chemical ordering in GaAsN:Bi alloys. The objective of this work is to understand the factors influencing the formation of chemical ordering in GaAsN:Bi alloys as a possible route to long-range control of the local atomic configurations of N and Bi solute atoms. This chapter begins with a review of long range ordering in semiconductor alloys. We also review evidence in the literature that the properties of dilute nitride and dilute bismide alloys depend sensitively on the local atomic environments of N and Bi solute atoms. Next, we introduce two sets of GaAsN:Bi alloys, a Bi flux series and a temperature series (T-series), distinct from those in Ch. 4, and examine their surface reconstructions, compositions and surface morphologies. We present evidence from selected-area electron diffraction, x-ray diffraction, and high-resolution scanning transmission electron microscopy for chemical ordering of the {111} planes and correlate it with surface reconstructions observed by reflection high-energy electron diffraction. Finally, we propose a mechanism for chemical ordering in which Bi enhances the formation of dimer rows aligned along the [110] direction in the (2x1) reconstruction, facilitating N incorporation beneath surface dimers and Bi incorporation between dimer rows to form

alternating N-rich and Bi-rich {111} planes. These findings suggest a route to tailoring the local atomic environment of N and Bi atoms in a wide range of emerging dilute nitride-bismide alloys.

5.2 Background

Long range atomic-scale ordering has been reported in a variety of compound semiconductor alloys[1,2,3,4,5,6,7] and can have significant influence on alloy optoelectronic properties.[8] For example, $CuPt_B$-type atomic ordering has been observed to reduce the bandgap of $Ga_{1-x}In_xP$ alloys by up to 160 meV,[9] compared to disordered GaInP alloys. CuPt ordering is proposed to arise according to a dimer-induced strain (DIS) mechanism, in which smaller atoms (Ga) incorporate in compressively strained sites beneath surface dimers while larger atoms (In) incorporate between dimer rows.[10,11] For a surface reconstruction with regular rows of aligned surface dimers, this DIS mechanism results, after growth of multiple atomic layers, in alternating GaP and InP {111} planes. The resulting change in the periodicity and symmetry of the lattice leads to a reduction of the alloy bandgap and a splitting of the valence band.[12] The DIS mechanism is illustrated in Figure 5.1 for the case of a SiGe alloy, in which smaller Si atoms incorporate beneath surface dimers and larger Ge atoms incorporate between dimer rows. Because the emergence of CuPt ordering is thought to be driven by a size mismatch between solute atoms and the host matrix, ordering is an important consideration in highly mismatched III-V semiconductor alloys, in which solute atoms are significantly size-mismatched with the host matrix and have unusually strong influence on the alloy electronic structure. The quaternary alloy $GaAs_{1-x-y}N_xBi_y$ represents both extremes of this scenario, in that both the

smallest and largest group V atoms are substituted for As in the host matrix. However, it remains unknown whether atomic ordering occurs in GaAsNBi alloys or what influence it has on the alloy optoelectronic properties. CuPt ordering has been observed in the ternary alloy $GaAs_{1-y}Bi_y$ for y between 0.03 and 0.10.[13,14] Interestingly, long range ordering has not been reported for $GaAs_{1-x}N_x$ alloys, despite predictions that the DIS mechanism would enhance solubility of N in GaAs.[15]

Furthermore, for dilute nitride alloys, reasonable carrier transport properties[16] and optical efficiencies[17] are only achieved following modifications to the local N atomic configurations via thermal annealing. For dilute bismide alloys, inhomogeneous broadening of spontaneous emission and modal gain spectra has been attributed to variations in the local Bi atomic configuration.[18,19,20] To date, an approach for long-range control of the local atomic configurations of N or Bi has yet to be reported. Here, we identify the influence of an incorporating surfactant on long-range atomic configurations in GaAsN:Bi, namely, long-range chemical ordering of the {111} planes.

5.3 Experimental procedures

Epitaxial GaAsN:Bi films were grown via nucleation and growth of two-dimensional (2D) islands (i.e. layer-by-layer mode) on semi-insulating (001) GaAs substrates by molecular-beam epitaxy (MBE), as described in Section 4.3.[21] Following oxide desorption and the growth of a 500 nm thick GaAs buffer layer at 580°C, the substrate temperature was held at 580°C for 5 minutes, lowered to the GaAsN:Bi growth temperature, $T_{GaAsN:Bi}$, and held at $T_{GaAsN:Bi}$ for another 5 minutes. A series of films with a range of N and Bi fractions were achieved by varying the Bi beam equivalent pressure

(BEP) from 0 to 1.2×10^{-7} Torr (with T_{GaAsN} = 410°C and $T_{GaAsN:Bi}$ = 380°C), which we will refer to as the "Bi flux series". In addition, a series of films with fixed Bi flux were achieved by varying $T_{GaAsN:Bi}$ from 380°C to 260°C (with Bi BEP fixed at 5.7×10^{-8} Torr), which we will refer to as the "T-series". The T-series consists of a multilayer structure with four 400 nm GaAsN:Bi layers, each separated by 100 nm GaAs spacers, as shown in Figure 5.2. The GaAsN:Bi layers were grown in order of decreasing temperature, with a temperature ramp coinciding with the growth of each intervening GaAs spacer.

To monitor the influence of Bi flux and substrate temperature on surface reconstruction, reflection high-energy electron diffraction (RHEED) patterns were collected along the [110] and $[1\bar{1}0]$ directions. For all films, streaky (2x4) patterns [Figure 5.3(a) and Figure 5.3(b)] were observed during the GaAs buffer layer growth; the pattern transitioned to a streaky c(4x4) [Figure 5.3(c) and Figure 5.3(d)] during the 5 minute anneal at $T_{GaAsN:Bi}$. For $T_{GaAsN:Bi}$ < 340°C, a streaky (1x3) pattern [Figure 5.3(e) and Figure 5.3(f)] was observed, consistent with earlier reports for GaAsBi.[22] For $T_{GaAsN:Bi}$ ≥ 340°C, a streaky (2x1) pattern[23] was instead observed [Figure 5.3(g) and Figure 5.3(h)]. For the Bi flux series, with $T_{GaAsN:Bi}$ = 380°C, streaky (1x3), streaky (2x1), and spotty (3x3) patterns were observed for the low, intermediate, and high Bi flux values, respectively. For GaAsN growth without a Bi flux, a streaky (2x1) pattern was observed [Figure 5.3(e) and Figure 5.3(i)].

Following epitaxy, the surface morphologies and compositions were examined using atomic-force microscopy (AFM) and/or scanning electron microscopy (SEM), Rutherford backscattering spectrometry (RBS), high-resolution x-ray diffraction, and transmission electron microscopy (TEM). High-resolution x-ray diffraction measurements

were performed using a Bede D1 and/or Rigaku Smartlab diffractometer with $CuK\alpha_1$ radiation, as described in Section 2.3. AFM images were collected as described in Section 2.7. SEM images were collected using a FEI Nova Nanolab 200 operating at an accelerating voltage of 20 kV and a beam current of 2.4 nA, as described in Section 2.8. RBS measurements were performed using a 4.88 MeV He^+ beam with the detector positioned at 160° with respect to the incident beam, as described in Section 2.6. Bi fractions were determined by fitting the RBS spectra using the simulation of nuclear reaction analysis (SIMNRA) code. In preparation for TEM imaging and selected-area diffraction, cross-sectional specimens normal to the $[110]$ and $[1\bar{1}0]$ directions were prepared by mechanical polishing and low-energy Ar+ ion milling, as described in Section 2.9. Additional cross-sectional specimens were prepared using a focused-ion-beam (FIB) lift-out process consisting of Ga+ FIB followed by low-energy Ar+ ion milling, also described in Section 2.9. The cross-sectional specimens were examined in a FEI Tecnai $G^2$30 Super Twin TEM operating at 300 kV, a FEI Tecnai F20 Ultra Twin scanning TEM (STEM) operating at 200 kV, and a JEOL 3100R05 double C_s-corrected STEM operating at 300 kV. SAD patterns were obtained in the Tecnai $G^2$30. Using layer thicknesses from TEM and Bi fractions from RBS as input, dynamical diffraction simulations using Rocking-Curve Analysis by Dynamical Simulation (RADS) software were used to determine the N fractions in each layer.

5.4 Surface morphologies and compositions

For the Bi flux series, a set of (004) x-ray rocking curves and corresponding AFM and SEM images, with Bi flux values increasing from bottom to top, are shown in Figure

5.4. In Figure 5.4(a), Bi-flux-dependent shifts of the GaAsN:Bi peaks from the high to the low angle side of the GaAs peak indicate tensile and compressive films, respectively. Some of the layers exhibit coherent interference fringes, often termed Pendellösung fringes[24] which are associated with planar surfaces and well-defined epilayer-substrate interfaces.[24,25,26] For the lowest Bi flux, low-amplitude (2nm) periodic (wavelength = 40 nm) surface features [Figure 5.4(c)] and correspondingly weak Pendellösung fringes are apparent. Periodic surface features similar to those in Figure 5.4(c) have been shown to give rise to lateral composition modulations (LCMs) with equivalent periodicity, as will be discussed in Section 5.5. For GaAsN films and intermediate Bi fluxes, featureless surfaces, with RMS roughness <0.5nm, are apparent. Since the Pendellösung fringes are most prominent for intermediate Bi fluxes, we hypothesize that Bi acts as a surfactant,[27,28] enhancing layer-by-layer growth. For the intermediate Bi fluxes, layer-by-layer growth is also suggested by the streaky RHEED patterns [Figure 5.3 (g) and Figure 5.3(h)]. For the highest Bi flux, a significantly broadened epilayer peak is observed, likely related to the presence of surface droplets and islands, as shown in Figure 5.4(f).

Since the GaAsN:Bi T-series consists of a thick sample with multiple layers, we consider ω-2θ x-ray diffraction collected from the entire sample, shown in Figure 5.5, plus an AFM image of the top surface, shown as the inset to Figure 5.5. In the plot of x-ray intensity vs ω-2θ in Figure 5.5, four GaAsN:Bi layer peaks are observed on the low angle side of the GaAs peak. For each successive layer, as the temperature is decreased, x_N remains approximately constant while y_{Bi} increases slightly from 0.06 to 0.07. The AFM image of the top surface of the lowest temperature GaAsN:Bi layer, shown in the inset of

Figure 5.5, reveals a featureless surface, with rms roughness <0.5 nm, suggesting layer-by-layer growth throughout the structure.[29]

5.5 Exploring lateral phase separation

To investigate the possibility of lateral composition modulations (LCMs) induced by the periodic surface features observed on the film grown at the lowest Bi flux, we examine x-ray reciprocal space mapping (RSM) about the GaAs (002) reflection. In Figure 5.6 an RSM collected near the GaAs (002) reflection is shown with Q_z and Q_x axes parallel to the [001] and [110] directions. A peak corresponding to the GaAsNBi epilayer is located near $\Delta Q_z = 10\times10^{-3}$ Å^{-1}, indicating that the GaAsNBi film is under tensile strain with respect to the GaAs substrate. In an (002) RSM, LCMs appear as lateral satellite peaks on either side of the film peak along the [110] direction, with the LCM period, λ, related to the spacing, ΔQ_x, between film peak and each satellite by $\lambda = 2\pi/\Delta Q_x$.[30,31] For the surface features with period 40 nm in Figure 5.4 (c), LCMs would give rise to satellites in the RSM at $\Delta Q_x = \pm\ 16\times10^{-3}$ Å^{-1}. The absence of satellite peaks in Figure 5.6 indicate an absence of LCMs.

5.6 Exploring chemical ordering

In this section, we describe evidence for chemical ordering of the {111} planes in x-ray diffraction, selected-area electron diffraction (SAD), and high angle annular dark field (HAADF) scanning TEM (STEM). We first focus on the intermediate Bi flux (y_{Bi} = 0.020 and y_{Bi} = 0.049) layers with prominent Pendellösung fringes, which we term the tensile and compressive GaAsN:Bi layers. In Figure 5.7, we present ω-2θ x-ray diffraction

about the ½ $(1\bar{1}5)$ reflections for the (a) tensile and (b) compressive GaAsN:Bi layers. The presence of the ½ $(1\bar{1}5)$ reflection, which is a forbidden reflection for the zincblende (ZB) lattice, indicates the formation of a superstructure along the $[1\bar{1}5]$ direction, likely related to long-range ordering of $(1\bar{1}1)$ planes.[32] We use the diffraction peak broadening to estimate ordered domain sizes of 6 nm and 5 nm along the <115> directions for the tensile and compressive GaAsN:Bi layers.[32,33] Similar sizes of ordered domain have been reported for GaInP alloys grown in the layer-by-layer mode on nominally flat (001) GaAs substrates.[32] On the other hand, ordered domain sizes > 100 nm have been reported for GaInP grown in step-flow mode on 6°(111)B offcut substrates.[34]

Further quantification of chemical ordering is obtained from SAD patterns for the compressive GaAsN:Bi layer. For the [110] SAD pattern shown in Figure 5.7(c), {002}, {111}, and {220} reflections typical of a ZB lattice are observed. In addition, ½$(1\bar{1}1)$, ½$(1\bar{1}3)$, and ½$(1\bar{1}5)$ [½$(\bar{1}11)$, ½$(\bar{1}13)$, and ½$(\bar{1}15)$] superstructure reflections, indicating long-range ordering on {111}B planes, i.e. $CuPt_B$ ordering,[35] are apparent. Additional $[1\bar{1}0]$ SAD patterns showed only the allowed ZB reflections, indicating the absence of long-range ordering on the {111}A planes, i.e. a lack of $CuPt_A$ ordering. This observation of $CuPt_B$ ordering without $CuPt_A$ ordering is consistent with earlier reports on GaAsBi alloys.[13,14] Assuming that the elongation of the ½$(1\bar{1}5)$ superstructure reflections along [001] is inversely proportional to the size of the ordered domains,[33] we estimate domain sizes of 1 - 2 nm along the <001> directions for both the tensile and compressive quaternary layers. For ordered GaAsBi on 2° (111)B offcut GaAs (001),[13] our analysis yields larger domains, ~ 3 – 4 nm, presumably due to the enhancement of ordered domain growth facilitated by the B-type[36] step-edges.[11]

For the temperature series, GaAsN:Bi layers are visible as bright layers separated by darker GaAs spacers in the HAADF STEM image in Figure 5.8(a). For each GaAsN:Bi layer in Figure 5.8(a), [110] SAD patterns are shown in Figure 5.8(b) – Figure 5.8(e), where diffraction spots for {002}, {111}, and {220} are marked with closed circles, open circles, and triangles, respectively. For $T_{GaAsN:Bi}$ = 260°C and 300°C, the [110] SAD patterns show only ZB reflections. For $T_{GaAsN:Bi} \geq$ 340°C, superstructure reflections appear in the ½($1\bar{1}1$) and ½($\bar{1}11$) positions, as indicated by arrows in Figure 5.8(d) and Figure 5.8(e), consistent with the presence of $CuPt_B$ ordering.[35] Additional [$1\bar{1}0$] SAD patterns show only ZB reflections, indicating a lack of $CuPt_A$ ordering.

We now present direct observations of the chemically ordered regions (i.e. domains) in real space. In Figure 5.9(a), we show a [110] cross-sectional HAADF STEM image collected near the interface between GaAs and ordered GaAsN:Bi. In Figure 5.9(a), the cyan and magenta arrows indicate example ($1\bar{1}1$) and ($\bar{1}11$) planes with doubled periodicity in the [$1\bar{1}1$] and [$\bar{1}11$] directions. To determine the ordered domain variants and size distributions, we considered several HAADF STEM images, spanning an area >4000 nm^2. For each HAADF STEM image, fast Fourier transforms (FFTs) reveal spots due to the ZB lattice and spots at the ½($1\bar{1}1$) and ½($\bar{1}11$) positions, indicating doubled periodicities in the [$1\bar{1}1$] and [$\bar{1}11$] directions. We selected each conjugate pair of ½($1\bar{1}1$) and ½($\bar{1}11$) spots, circled in cyan and magenta, respectively, in Figure 5.9(b), and performed inverse FFTs to emphasize the ($1\bar{1}1$) and ($\bar{1}11$) ordered domains. For each resulting Fourier-filtered image, we included pixels near the top (18 ± 6%) and bottom (18 ± 7%) of the total grayscale range, with thresholds selected to exclude GaAs regions. In the example Fourier-filtered image shown in Figure 5.9(c), both domain types are narrowed

in the [001] direction and elongated along the $[1\bar{1}0]$ direction, consistent with the [001] elongation of the ½$(1\bar{1}1)$ and ½$(\bar{1}11)$ reflections shown in Figure 5.7(c), Figure 5.8(d), and Figure 5.8(e). Figure 5.9(d) shows a logarithmic-normal (lognormal) fit to the domain size distribution, which yields a median domain size of 1.81 ± 0.01 nm^2. Using this Fourier-filtering analysis, we analyzed the high-resolution TEM image of ordered GaAsBi from Fig. 4 in Ref. 14 and observed similarly shaped domains; a lognormal fit in that case yields a median domain size of 1.8 ± 0.1 nm^2. Both lognormal size distributions are consistent with a domain nucleation and growth process without significant coarsening,[37] as expected for a surface-driven process.

The appearance of both $(1\bar{1}1)$ and $(\bar{1}11)$ domains on the nominally flat substrates is likely related to the growth mode. During layer-by-layer growth, step propagation proceeds away from each 2D island, in both the $[\bar{1}10]$ and $[1\bar{1}0]$ directions. Thus, $(\bar{1}11)$ and $(1\bar{1}1)$ domains will meet when adjacent islands merge, limiting the lateral size of each. In contrast, on surfaces with offcuts toward (111)B, step-flow growth occurs along the B-type step edges; i.e. the $[\bar{1}10]$ or $[1\bar{1}0]$ direction, leading to the formation of large single-variant domains.[11]

5.7 Mechanisms for chemical ordering

In this section, we examine the mechanisms for chemical ordering in GaAsN:Bi. In Figure 5.10, the surface reconstructions for ordered and disordered GaAsN:Bi alloys are shown on a plot of Bi BEP vs $T_{GaAsN:Bi}$. The dashed lines are guides to the eye, enclosing a window in which *both* a (2x1) reconstruction and CuPt ordering are observed. Above the window, a spotty (3x3) reconstruction, with Bi incorporated into surface droplets, shown

in Figure 5.4(f), is observed. Below the window, disordered alloys are observed, including GaAsN and GaAsN:Bi layers grown with (2x1) and (1x3) reconstructions, respectively. Interestingly, for GaAsN growth with a (2x1) reconstruction, but *without* a Bi flux, ordering is not observed. Therefore, it is likely the GaAsN (2x1) lacks sufficient dimer alignment for ordering;[11] however, in the presence of an incorporating surfactant, Bi, the alignment of dimer rows is enhanced. Indeed, the well-defined 2x pattern observed in the (2x1) pattern for GaAsN:Bi films (Figure 5.3(g) and Figure 5.3(h)) compared to that of GaAsN films (Figure 5.3(k) and Figure 5.3(l)) supports this hypothesis.

The observation of only the B-variants of CuPt ordering is consistent with a (2 x 1) reconstruction containing regular rows of surface dimers extending in the [110] direction, with individual dimers oriented along the $[\bar{1}10]$ direction. This result is in good agreement with scanning tunneling microscopy (STM) studies of a Bi-induced (2 x 1) surface reconstruction for Bi deposited on GaAs.[38,39] Furthermore, the absence of CuPt ordering under the (1 x 3) reconstruction in this work is consistent with STM studies of the Bi-induced (1 x 3) and (4 x 3) reconstructions that have previously noted the lack of long-range configurational order that might allow long-range atomic ordering under these reconstructions.[40]

We now present an atomistic mechanism for chemical ordering in GaAsN:Bi. For GaAsN:Bi, we recently reported that up to 30% of N atoms incorporate non-substitutionally, predominantly in the form of $(N\text{-}As)_{As}$ complexes.[21] Thus, the group V sublattice may be occupied by As, Bi, substitutional N, or $(N\text{-}As)_{As}$. Since the N and Bi fractions are low ($x_N < 0.03$, $y_{Bi} < 0.08$), the As fraction is typically high; therefore, arsenic is necessarily incorporated both between and beneath dimer rows. Thus, we hypothesize

that the largest species, Bi, is primarily incorporated between dimer rows due to local tensile strain, while the smallest species, N, tends to incorporate beneath dimer rows due to local compressive strain,[10,11] forming a monolayer superlattice consisting of alternating Bi-rich and N-rich $(\bar{1}11)$ planes, as illustrated in Figure 5.11, in which Bi-rich planes are highlighted in red, and N-rich planes are highlighted in blue. In addition, a significant portion of the N atoms would share sites with As as $(N\text{-}As)_{As}$ complexes.[21] Further work is required to determine whether these complexes are incorporated between or beneath the dimer rows.

5.8 Summary and conclusions

In summary, we have examined the influence of an incorporating surfactant on chemical ordering of GaAsN:Bi during MBE. We show that CuPt ordering is tied to the presence of *both* the incorporating surfactant, Bi, and a (2x1) surface reconstruction. We propose a modified dimer-induced strain mechanism in which Bi enhances the formation of dimer rows aligned along the [110] direction, thereby facilitating N incorporation beneath surface dimers and Bi incorporation between dimer rows to form alternating N-rich and Bi-rich {111} planes. The ordered GaAsN:Bi consists of intersecting $(1\bar{1}1)$ and $(\bar{1}11)$ ordered domains with a lognormal size distribution, consistent with domain formation at surface steps without subsequent coarsening. These findings suggest a route for tailoring local atomic environments through long-range chemical ordering in a wide range of emerging dilute nitride-bismide alloys and heterostructure devices.

5.9 Figures

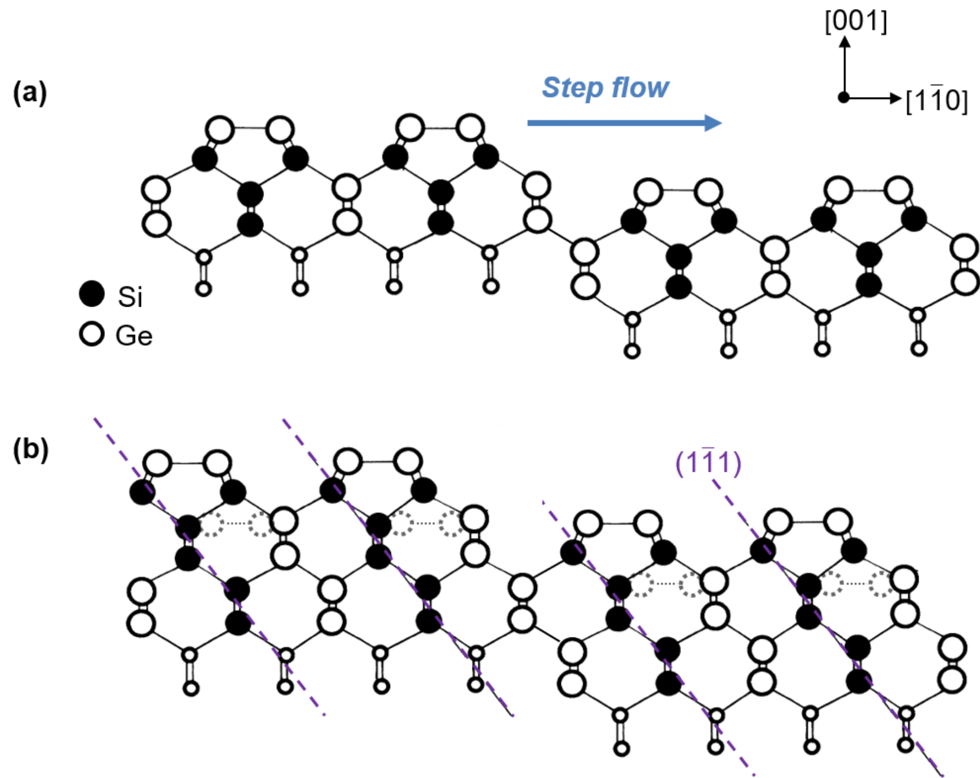

Figure 5.1 Dimer-induced strain (DIS) mechanism[11] for CuPt ordering, illustrated for a SiGe alloy. (a) Smaller Si atoms incorporate at compressively strained sites beneath surface dimers while larger Ge atoms incorporate at sites in tension between dimer rows, resulting in ordered rows of alternating Si and Ge, extending in the [110] direction (b) Upon growth of the next atomic bi-layer, the rows of alternating Si and Ge propagate in the [$\bar{1}$11] direction, forming alternating Si and Ge (1$\bar{1}$1) planes. Adapted with permission from Ref. 10 (Copyright 1990 by the American Physical Society).

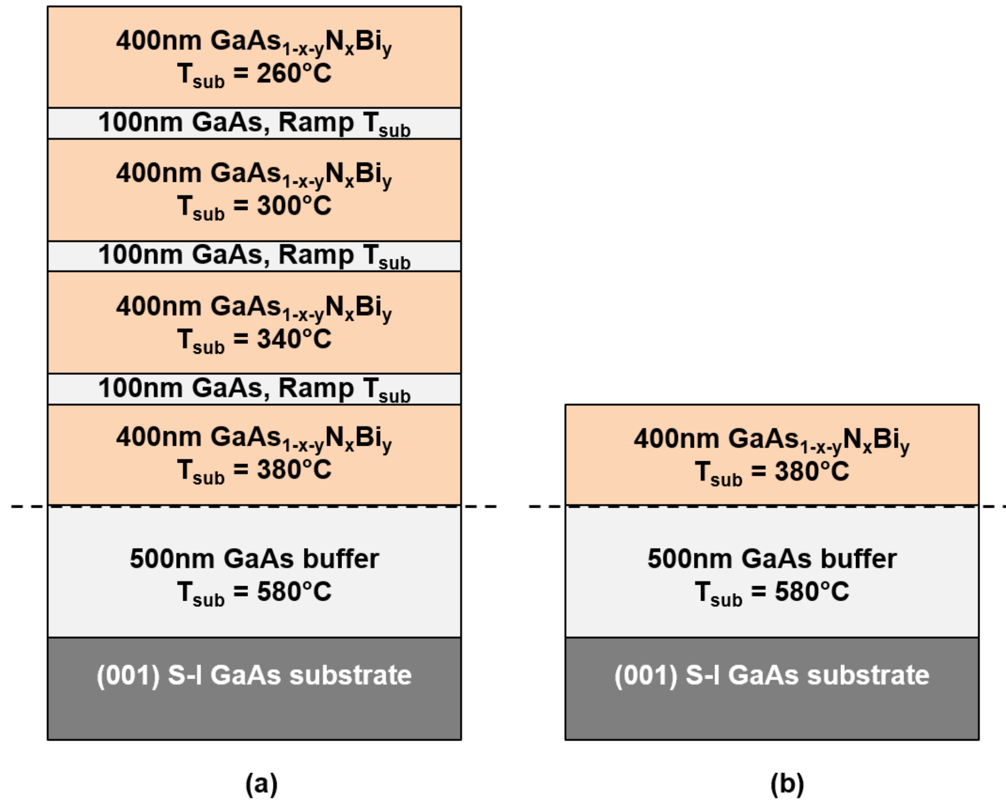

Figure 5.2 Schematic of the layer structures for (a) the temperature series (T-series) and (b) the Bi flux series. Dashed lines indicate growth interrupts during which the substrate temperature, T_{sub}, was ramped.

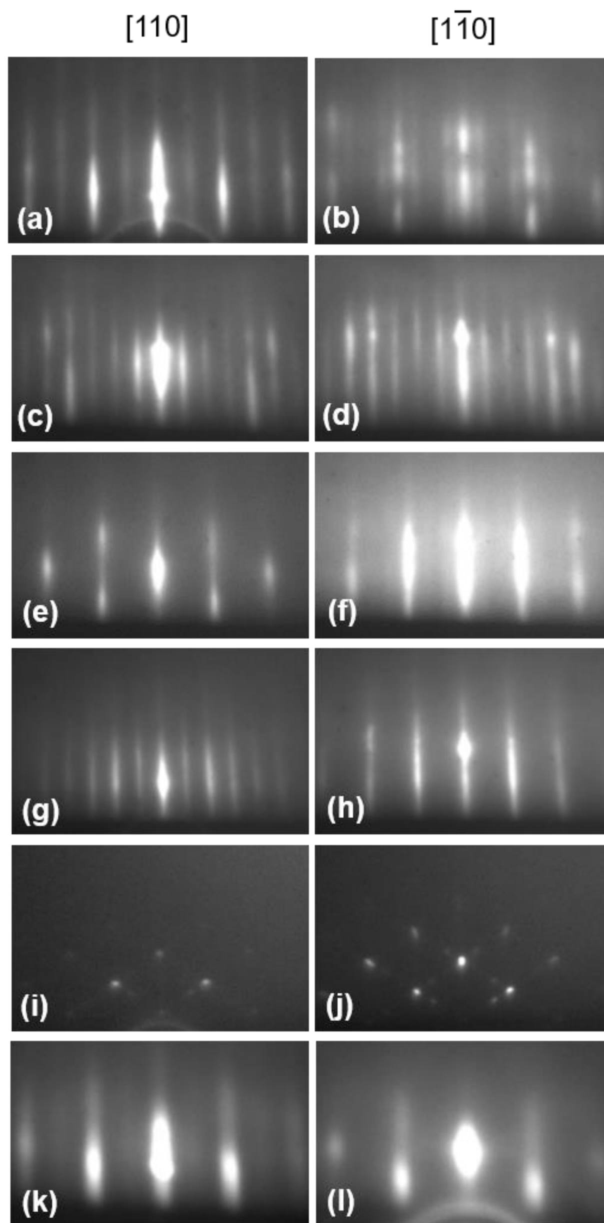

Figure 5.3 Reflection high-energy electron diffraction patterns collected during epitaxy of GaAsN:Bi. Patterns are shown along the [110] and [1$\bar{1}$0] directions in [(a), (b)], [(e), (f)], [(g), (h)], [(i), (j)], and [(k), (l)] and along the [100] and [010] directions in [(c), (d)]. [(a), (b)] streaky (2x4) pattern during GaAs growth at 580°C; [(c), (d)] streaky c(4x4) pattern during annealing at $T_{GaAsN:Bi}$; [(e), (f)] streaky (1x3) pattern during GaAsN:Bi growth at low $T_{GaAsN:Bi}$ or low Bi beam equivalent pressure (BEP) values; [(g), (h)] streaky (2x1) pattern during GaAsN:Bi growth at higher $T_{GaAsN:Bi}$ and moderate Bi BEP values; [(i), (j)] spotty (3x3) pattern during GaAsN:Bi growth with the highest Bi BEP values. [(k), (l)] nearly-streaky (2x1) pattern during GaAsN growth.

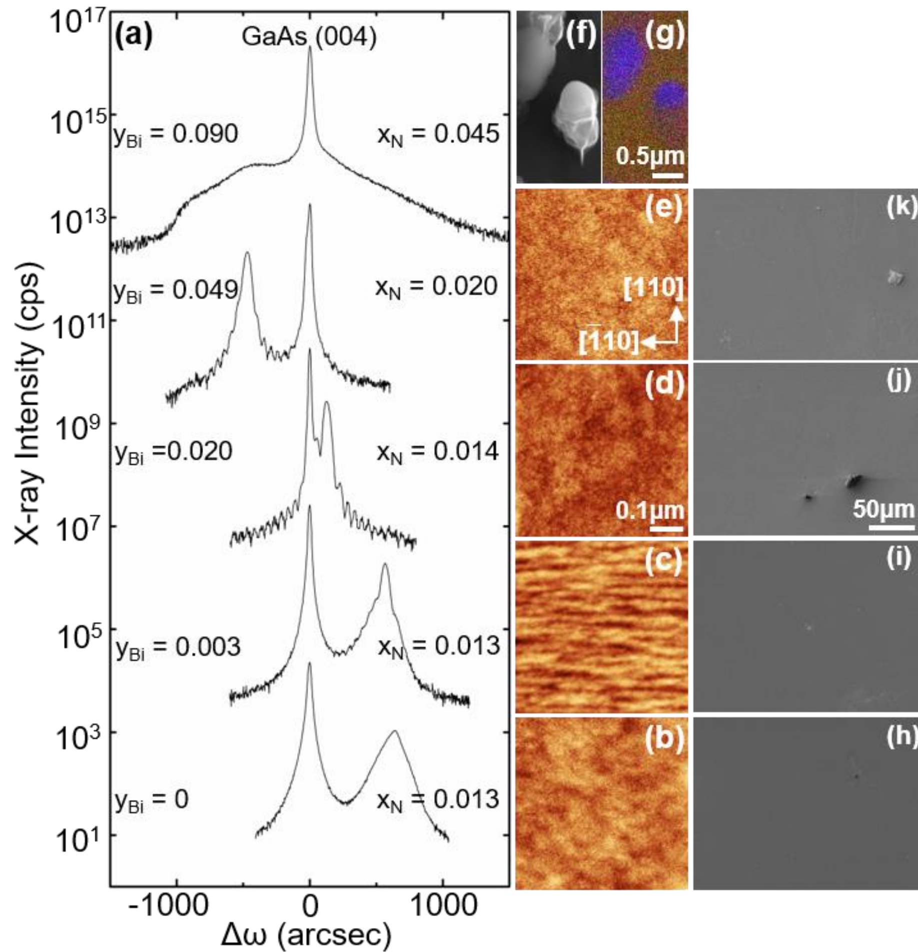

Figure 5.4 Plot of x-ray intensity vs. Δω for rocking curves about the GaAs (004) reflection from the Bi flux series. For all plots, the GaAs substrate peak is set to Δω = 0 arcseconds, thereby facilitating comparison of Δω between the GaAs substrate and the GaAsN:Bi epilayers. Corresponding atomic force microscopy (AFM) or scanning electron microscopy (SEM) images of the surface morphology are shown alongside in (b)-(f). For the AFM images, the colorscale ranges displayed are (b) 2nm, (c) 3 nm, (d) 2 nm, (e) 3 nm. (g) Energy-dispersive x-ray spectroscopy image corresponding to the SEM image in (f). In the mottled red-green region, Ga, As, and N are present, while the blue regions are primarily bismuth. To confirm the absence of μm-sized surface droplets on films shown in (b)-(e), SEM images were collected for areas of approximately 200 μm x 250 μm, as shown in (h)-(k). Features associated with dust were included to demonstrate that the images are in focus; the surfaces are otherwise featureless, without droplets.

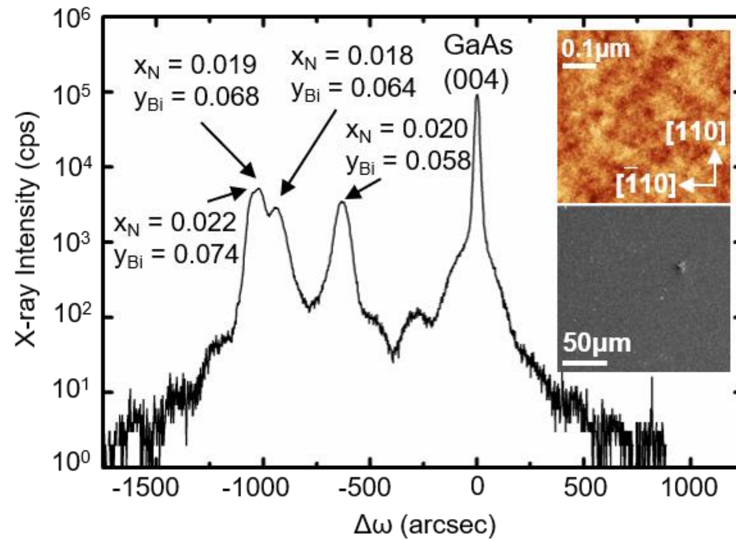

Figure 5.5 Plot of x-ray intensity vs. Δω for a coupled ω-2θ scan about the GaAs (004) reflection for the multilayer structure containing the GaAsN:Bi layers of the T-series. The GaAs substrate peak is set to Δω = 0 arcseconds. For each successive layer, as the temperature is decreased, x_N remains approximately constant while y_{Bi} increases slightly from 0.06 to 0.07. (Inset): Atomic force microscopy image of the top surface of the T-series, with $T_{GaAsN:Bi}$ = 260°C. The colorscale range displayed is 4 nm. To confirm the of absence of µm-sized surface droplets, an SEM image with area of approximately 200 µm x 250 µm is shown in the lower half of the inset. Features associated with dust were included to demonstrate that the image is in focus; the surface is otherwise featureless, without droplets.

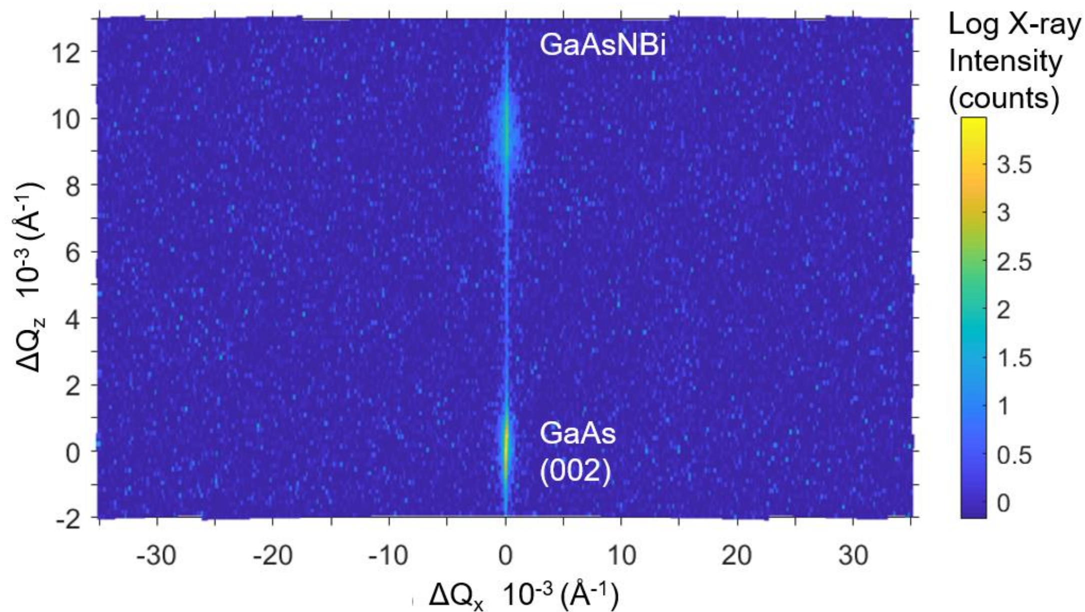

Figure 5.6 X-ray reciprocal space map near the GaAs (002) reflection, with Q_z and Q_x along the [001] and [110] directions, respectively. The GaAs substrate peak is set to $\Delta Q_z = 0$ and $\Delta Q_x = 0$ to facilitate comparison with the GaAsNBi epilayer peak position. The color-scale represents the logarithm of the x-ray intensity. The lack of satellite peaks along the [110] direction about the GaAsNBi peak indicates a lack of lateral composition modulation.

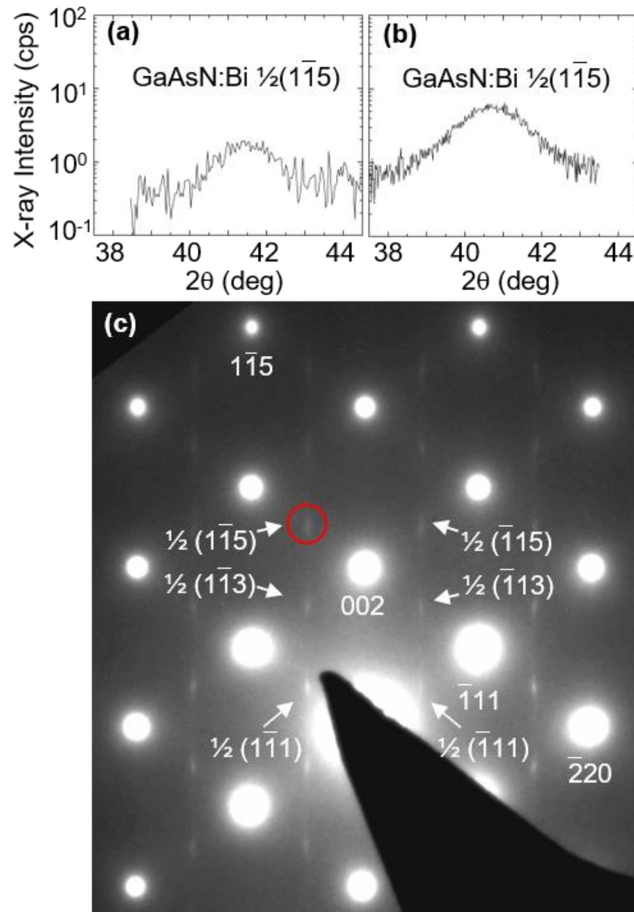

Figure 5.7 Plots of x-ray intensity for ω-2θ scans about the GaAsN:Bi ½ (1$\bar{1}$5) reflections for (a) tensile and (b) compressive GaAsN:Bi films. The presence of the ½ (1$\bar{1}$5) reflection suggests ordering of the (1$\bar{1}$1) planes. (c) representative [110] selected-area diffraction (SAD) pattern for the compressive GaAsN:Bi in (b), showing ½(1$\bar{1}$1), ½(1$\bar{1}$3), and ½(1$\bar{1}$5) [½($\bar{1}$11), ½($\bar{1}$13), and ½($\bar{1}$15)] reflections, indicating long-range ordering on (1$\bar{1}$1) [($\bar{1}$11)] planes. Additional [1$\bar{1}$0] SAD patterns showed only ZB reflections, indicating an absence of long-range ordering on the {111}A planes. Similar SAD patterns were obtained for the tensile GaAsN:Bi.

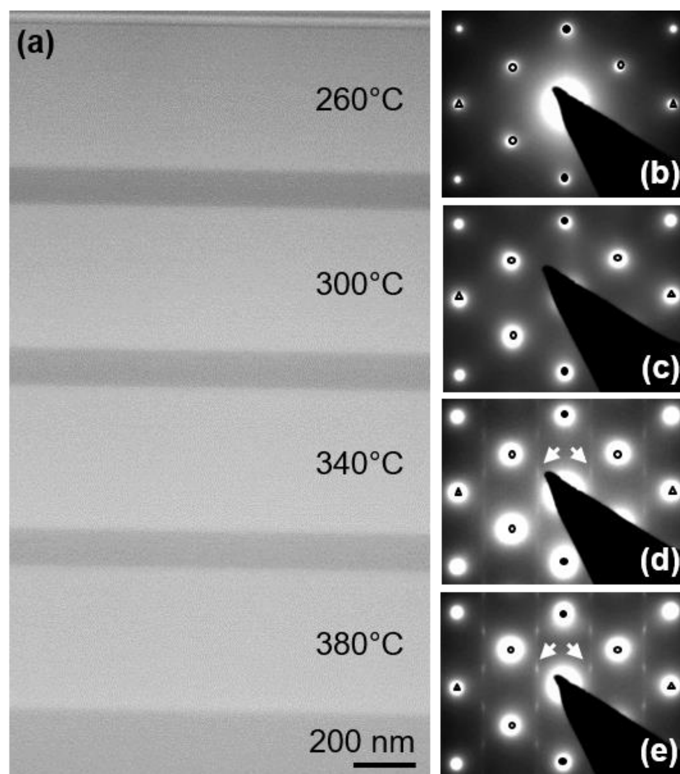

Figure 5.8 High-angle annular dark field scanning transmission electron micrograph of the T-series, with alternating bright and dark layers consisting of GaAsN:Bi and GaAs, respectively. Selected-area diffraction patterns collected along the [110] zone axis for $T_{GaAsN:Bi}$ = 260°C, 300°C, 340°C, and 380°C are shown in (b) – (e), respectively. The diffraction spots for {002}, {111}, and {220} are identified by closed circles, open circles, and triangles, respectively. Arrows in (d) and (e) indicate $\frac{1}{2}(1\bar{1}1)$ and $\frac{1}{2}(\bar{1}11)$ reflections corresponding to $CuPt_B$ ordering.

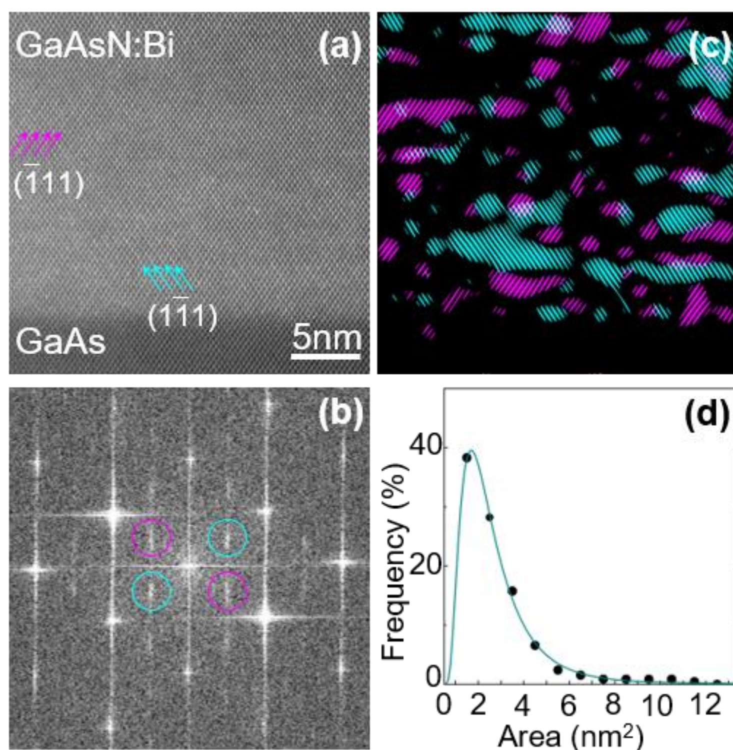

Figure 5.9 (a) High-resolution scanning transmission electron micrograph, collected near an interface between GaAs and ordered GaAsN:Bi. The magenta and cyan arrows in (a) indicate example ($\bar{1}$11) and (1$\bar{1}$1) planes with doubled periodicity in the [$\bar{1}$11] and [1$\bar{1}$1] directions, i.e. ($\bar{1}$11) and (1$\bar{1}$1) ordered domains. (b) Fast Fourier transform (FFT) of the image in (a), showing spots corresponding to the zincblende lattice and those at the ½(1$\bar{1}$1) and ½($\bar{1}$11) positions. Inverse FFTs, using the spots circled in (b), with pixels near the top (18 ± 6%) and bottom (18 ± 7%) of the total grayscale range, are shown in (c), with magenta and cyan regions representing the ($\bar{1}$11) and (1$\bar{1}$1) ordered domains. For both the ($\bar{1}$11) and (1$\bar{1}$1) ordered domains, the distribution of domain sizes, fit with a logarithmic-normal (lognormal) distribution, is shown in (d).

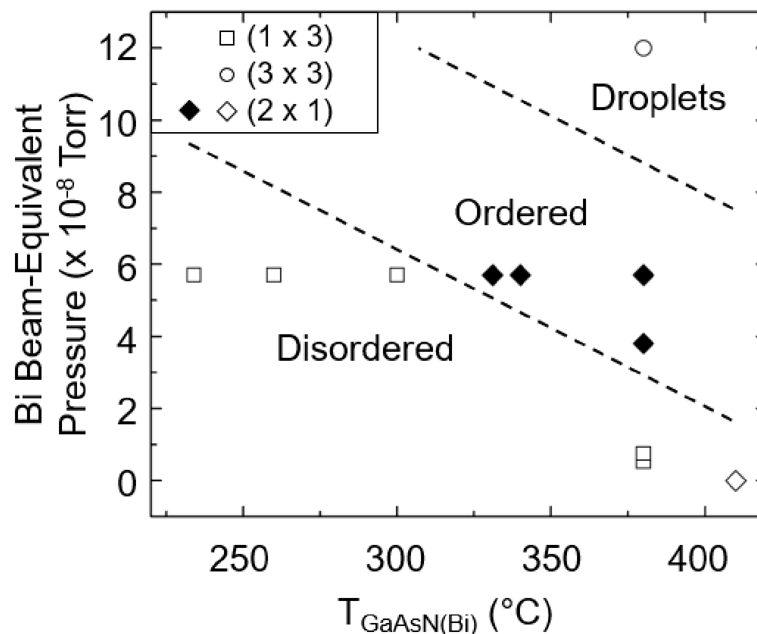

Figure 5.10 Window for $CuPt_B$ ordering in GaAsN:Bi: Bi beam equivalent pressure (BEP) vs $T_{GaAsN:Bi}$. (1x3), (3x3), and (2x1) surface reconstructions are represented by squares, circles, and diamonds, respectively. Solid (open) symbols denote ordered (disordered) films. The dashed lines are a guide to the eye.

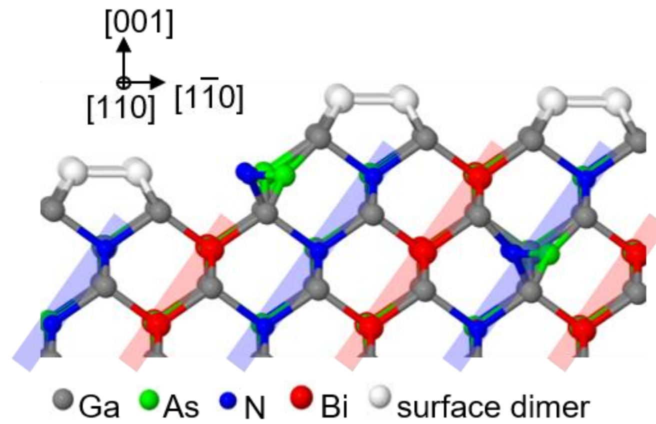

Figure 5.11 Proposed atomistic mechanism for $CuPt_B$ ordering in GaAsN:Bi. White, gray, green, blue, and red circles correspond to surface dimer, Ga, As, N, and Bi atoms, respectively. N and Bi atoms attach at step edges flowing in the [$\bar{1}$10] ([1$\bar{1}$0]) direction, leading to alternating N-rich/Bi-poor and N-poor/Bi-rich ($\bar{1}$11) [(1$\bar{1}$1)] planes, highlighted by blue and red bars respectively. A fraction of N atoms share As lattice sites as $(N\text{-}As)_{As}$ complexes.

5.10 References

[1] D.H. Jaw, G.S. Chen, and G.B. Stringfellow, “Atomic Ordering in $InAs_{0.5}P_{0.5}$ Grown by Organometallic Vapor Phase Epitaxy”, Appl. Phys. Lett. 59, 114 (1991).

[2] G.S. Chen, D.H. Jaw, and G.B. Stringfellow, “Atomic Ordering in GaAsP”, J. Appl. Phys. 69, 4263 (1991).

[3] I.J. Murgatroyd, A.G. Norman, and G.R. Booker, “Observation of {111} Ordering and [110] Modulation in Molecular Beam Epitaxial $GaAs_{1-y}Sb_y$ Layers: Possible Relationship to Surface Reconstruction Occurring during Layer Growth”, J. Appl. Phys. 67, 2310 (1990).

[4] S.R. Kurtz, L.R. Dawson, R.M. Biefeld, D.M. Follstaedt, and B.L. Doyle, “Ordering-Induced Band-Gap Reduction in $InAs_{1-x}Sb_x$ ($x \cong 0.4$) Alloys and Superlattices”, Phys. Rev. B 46, 1909 (1992).

[5] M.A. Shahid, S. Mahajan, D.E. Laughlin, and H.M. Cox, “Atomic Ordering in $Ga_{0.47}In_{0.53}As$ and $Ga_xIn_{1-x}As_yP_{1-y}$ Alloy Semiconductors”, Phys. Rev. Lett. 58, 2567 (1987).

[6] A. Gomyo, K. Makita, I. Hino, and T. Suzuki, “Observation of a New Ordered Phase in $Al_xIn_{1-x}As$ Alloy and Relation between Ordering Structure and Surface Reconstruction during Molecular-Beam-Epitaxial Growth” Phys. Rev. Lett. 72, 673 (1994).

[7] A. Ourmazd and J.C. Bean, “Observation of Order-Disorder Transitions in Strained-Semiconductor Systems”, Phys. Rev. Lett. 55, 765 (1985).

[8] S. Wei, D.B. Laks, and A. Zunger, “Dependence of the Optical Properties of Semiconductor Alloys on the Degree of Long-range Order”, Appl. Phys. Lett. 62, 1937 (1993).

[9] L.C. Su, I.H. Ho, N. Kobayashi, and G.B. Stringfellow, “Order/Disorder Heterostructure in $Ga_{0.5}In_{0.5}P$ with $\Delta Eg = 160$ MeV”, J. Cryst. Growth 145, 140 (1994).

[10] F.K. LeGoues, V.P. Kesan, S.S. Iyer, J. Tersoff, and R. Tromp, "Surface-stress-induced order in SiGe alloy films", Phys. Rev. Lett. 64, 2038 (1990).

[11] B.A. Philips, A.G. Norman, T.Y. Seong, S. Mahajan, G.R. Booker, M. Skowronski, J.P. Harbison, and V.G. Keramidas, “Mechanism for CuPt-Type Ordering in Mixed III–V Epitaxial Layers”, J. Cryst. Growth 140, 249 (1994).

[12] Y. Zhang, A. Mascarenhas, and L.-W. Wang, “Dependence of the Band Structure on the Order Parameter for Partially Ordered $Ga_xIn_{1-x}P$ Alloys”, Phys. Rev. B 63, (2001).

[13] A.G. Norman, R. France, and A.J. Ptak, “Atomic Ordering and Phase Separation in MBE $GaAs_{1-x}Bi_x$”, J. Vac. Sci. Technol. B 29, 03C121 (2011).

[14] D.F. Reyes, F. Bastiman, C.J. Hunter, D.L. Sales, A.M. Sanchez, J.P.R. David, and D. González, "Bismuth Incorporation and the Role of Ordering in GaAsBi/GaAs Structures", Nanoscale Res. Lett. 9, 23 (2014).

[15] S.B. Zhang and A. Zunger, "Surface-Reconstruction-Enhanced Solubility of N, P, As, and Sb in III-V Semiconductors", Appl. Phys. Lett. 71, 677 (1997).

[16] Y. Jin, R.M. Jock, H. Cheng, Y. He, A.M. Mintarov, Y. Wang, C. Kurdak, J.L. Merz, and R.S. Goldman, "Influence of Si–N Complexes on the Electronic Properties of GaAsN Alloys", Appl. Phys. Lett. 95, 062109 (2009).

[17] V. Lordi, H.B. Yuen, S.R. Bank, M.A. Wistey, J.S. Harris, and S. Friedrich, "Nearest-Neighbor Distributions in Ga1−xInxNyAs1−y and Ga1−xInxNyAs1−y−zSbz Thin Films upon Annealing", Phys. Rev. B 71, 125309 (2005).

[18] I.P. Marko, P. Ludewig, Z.L. Bushell, S.R. Jin, K. Hild, Z. Batool, S. Reinhard, L. Nattermann, W. Stolz, K. Volz, and S.J. Sweeney, "Physical Properties and Optimization of GaBiAs/(Al)GaAs Based near-Infrared Laser Diodes Grown by MOVPE with up to 4.4% Bi", J. Phys. D Appl. Phys. 47, 345103 (2014).

[19] L.C. Bannow, O. Rubel, S.C. Badescu, P. Rosenow, J. Hader, J.V. Moloney, R. Tonner, and S.W. Koch, Badescu, S. C., Rosenow, P., Hader, J., Moloney, J. V., Tonner, R., and Koch, S. W. "Configuration Dependence of Band-Gap Narrowing and Localization in Dilute GaAs 1 − x Bi x Alloys", Phys. Rev. B 93, 205202 (2016).

[20] J. Hader, S.C. Badescu, L.C. Bannow, J.V. Moloney, S.R. Johnson, and S.W. Koch, "Extended Band Anti-Crossing Model for Dilute Bismides", Appl. Phys. Lett. 112, 062103 (2018).

[21] J. Occena, T. Jen, E.E. Rizzi, T.M. Johnson, J. Horwath, Y.Q. Wang, and R.S. Goldman, "Bi-Enhanced N Incorporation in GaAsNBi Alloys", Appl. Phys. Lett. 110, 242102 (2017).

[22] R.L. Field III, J. Occena, T. Jen, D. Del Gaudio, B. Yarlagadda, C. Kurdak, and R.S. Goldman, "Influence of Surface Reconstruction on Dopant Incorporation and Transport Properties of GaAs(Bi) Alloys", Appl. Phys. Lett. 109, 252105 (2016).

[23] W. Huang, K. Oe, G. Feng, and M. Yoshimoto, "Molecular-Beam Epitaxy and Characteristics of GaNyAs1−x−yBix", J. Appl. Phys. 98, 053505 (2005).

[24] B.W. Batterman and G. Hildebrandt, "X-Ray Pendellösung Fringes in Darwin Reflection", Acta Crystallograph. A 24, 150 (1968).

[25] L. Tapfer, "High Resolution X-Ray Diffraction in Multilayered Semiconductor Structures and Superlattices", Phys. Scripta 1989, 45 (1989).

[26] G. Mussler, J.-M. Chauveau, A. Trampert, M. Ramsteiner, L. Däweritz, and K.H. Ploog, "Nitrogen-Dependent Optimum Annealing Temperature of Ga(As,N)", J. Cryst. Growth 267, 60 (2004).

[27] S. Tixier, M. Adamcyk, E.C. Young, J.H. Schmid, and T. Tiedje, “Surfactant Enhanced Growth of GaNAs and InGaNAs Using Bismuth", J. Cryst. Growth 251, 449 (2003).

[28] R. Salas, S. Guchhait, K.M. McNicholas, S.D. Sifferman, V.D. Dasika, D. Jung, E.M. Krivoy, M.L. Lee, and S.R. Bank, “Surfactant-Assisted Growth and Properties of Rare-Earth Arsenide InGaAs Nanocomposites for Terahertz Generation”, Appl. Phys. Lett. 108, 182102 (2016).

[29] M. Reason, N.G. Rudawski, H.A. McKay, X. Weng, W. Ye, and R.S. Goldman, “Mechanisms of GaAsN Growth: Surface and Step-Edge Diffusion”, J. Appl. Phys. 101, 083520 (2007).

[30] R.D. Twesten, D.M. Follstaedt, S.R. Lee, E.D. Jones, J.L. Reno, J.M. Millunchick, A.G. Norman, S.P. Ahrenkiel, and A. Mascarenhas, “Characterizing Composition Modulations in InAs/AlAs Short-Period Superlattices”, Phys. Rev. B 60, 13619 (1999).

[31] B. Shin, A. Lin, K. Lappo, R.S. Goldman, M.C. Hanna, S. Francoeur, A.G. Norman, and A. Mascarenhas, “Initiation and Evolution of Phase Separation in Heteroepitaxial InAlAs Films”, Appl. Phys. Lett. 80, 3292 (2002).

[32] Q. Liu, W. Prost, and F.J. Tegude, . “Determination of CuPt-type Ordering in GaInP by Means of X-ray Diffraction in the Skew, Symmetric Arrangement”, Appl. Phys. Lett. 67, 2807 (1995).

[33] E. Morita, M. Ikeda, O. Kumagai, and K. Kaneko, “Transmission Electron Microscopic Study of the Ordered Structure in GaInP/GaAs Epitaxially Grown by Metalorganic Chemical Vapor Deposition”, Appl. Phys. Lett. 53, 2164 (1988).

[34] R.L. Forrest, T.D. Golding, S.C. Moss, Y. Zhang, J.F. Geisz, J.M. Olson, A. Mascarenhas, P. Ernst, and C. Geng, “X-Ray Diffraction and Excitation Photoluminescence Analysis of Ordered GaInP”, Phys. Rev. B 58, 15355 (1998).

[35] A. Gomyo, T. Suzuki, and S. Iijima, “Observation of Strong Ordering in GaxIn1−xP Alloy Semiconductors”, Phys. Rev. Lett. 60, 2645 (1988).

[36] M.D. Pashley, K.W. Haberern, and J.M. Gaines, “Scanning Tunneling Microscopy Comparison of GaAs(001) Vicinal Surfaces Grown by Molecular Beam Epitaxy”, Appl. Phys. Lett. 58, 406 (1991).

[37] R.B. Bergmann and A. Bill, “On the Origin of Logarithmic-Normal Distributions: An Analytical Derivation, and Its Application to Nucleation and Growth Processes”, J. Cryst. Growth 310, 3135 (2008).

[38] F. Bastiman, A.G. Cullis, J.P.R. David, and S.J. Sweeney, . “Bi Incorporation in GaAs(100)-2×1 and 4×3 Reconstructions Investigated by RHEED and STM”, J. Cryst. Growth 341, 19 (2012).

[39] P. Laukkanen, M.P.J. Punkkinen, H.-P. Komsa, M. Ahola-Tuomi, K. Kokko, M. Kuzmin, J. Adell, J. Sadowski, R.E. Perälä, M. Ropo, T.T. Rantala, I.J. Väyrynen, M. Pessa, L. Vitos, J. Kollár, S. Mirbt, and B. Johansson, "Anomalous Bismuth-Stabilized (2×1) Reconstructions on GaAs(100) and InP(100) Surfaces", Phys. Rev. Lett. 100, 086101 (2008).

[40] A. Duzik, J.C. Thomas, A. van der Ven, and J.M. Millunchick, "Surface Reconstruction Stability and Configurational Disorder on Bi-Terminated GaAs(001)", Phys. Rev. B 87, 035313 (2013).

Chapter 6

Composition-Dependence of GaAsNBi Bandgaps

6.1 Overview

In this chapter, we describe our studies of the composition dependence of the energy bandgap and electronic states in GaAsNBi alloys. The objective of this work is to provide a predictive guide for bandgap engineering using GaAsNBi alloys, and to reveal insight into the energetic position of Bi-related states near the valence band edge.

Following a review of conventional alloy behavior, we describe background information, including literature on the composition-dependence of GaAsNBi alloy lattice parameters, energy bandgaps, and Bi impurity states. Then, using our analyses of the N flux series and the Bi flux series of GaAsNBi films from Ch. 4, we present a new map of the out-of-plane misfit, and a new N/Bi ratio for lattice-matching of GaAsNBi alloys with GaAs substrates. Next, we present photoreflectance and photoluminescence data collected from a subset of the samples. Finally, we describe a new map of the composition- and misfit-dependence of the bandgap energy, and present an estimate of the energetic position of Bi-related states.

6.2 Background

As discussed in Ch. 1, the lattice parameters of semiconductor alloys are often described in terms of a linear interpolation between the lattice parameters of their binary constituents. Similarly, composition-dependence of alloy bandgaps is typically described by a linear interpolation between the bandgaps of the binary constituents, modified by a bowing parameter. In the literature, the magic ratio for lattice matching of GaAsNBi with GaAs is predicted to be $x_N/y_{Bi} = 0.59$, based upon a computed value of the GaBi lattice parameter.[1] In addition, the relationship between the composition and the bandgap value is most often determined using x-ray diffraction measurements of strain to determine the alloy composition, assuming the computed value of the GaBi latttice parameter, with films fully strained to the GaAs substrate. For GaAsNBi, it has recently been shown that Bi promotes the formation of $(N\text{-}As)_{As}$ interstitial complexes,[2] which are not accounted for in typical analyses of x-ray diffraction data. Finally, it has been proposed that Bi behaves as an isoelectronic impurity in GaAs. However, there are conflicting reports regarding the energetic position of the Bi impurity state either 0.18 eV above[1] or 0.08 – 0.4 eV below[3,4,5,6,7,8] the valence band maximum.

6.3 Experimental procedures

A series of $GaAs_{1-x-y}N_xBi_y$ films were grown by molecular-beam epitaxy, as described in Section 4.3.[2] A range of N and Bi fractions were achieved by varying the N_2 flow rate from 0 to 0.35 sccm (N flux series) and the Bi beam-equivalent pressure (BEP) from 0 to 1×10^{-7} Torr (Bi flux series). To determine the out-of-plane and in-plane lattice parameters and misfit, (004) and (224) high-resolution x-ray rocking curves (XRC) were

collected as described in Section 2.3. Using the Bragg angle for the GaAs (004) planes, $\theta_B(004)$, and the peak splitting between the film and the GaAs substrate, $\Delta\omega(004)$, the out-of-plane misfit becomes,

$$\varepsilon_{\perp} = \frac{sin(\theta_B(004))}{sin(\theta_B(004)+\Delta\omega(004))} - 1 \tag{6.1}$$

For most films, N and Bi fractions were determined using simultaneous nuclear reaction analysis (NRA) and Rutherford backscattering spectrometry (RBS), in conjunction with simulation of nuclear reaction analysis (SIMNRA) code, as described in Section 4.3.[2,9] For other films, the N fractions were determined using dynamical diffraction simulations, assuming the computed GaBi lattice parameter (6.324),[1] with Bi fractions obtained from RBS/SIMNRA analysis, as described in Section 2.3. To account for interstitial N[2,10] in those samples for which only XRC data was available, we estimate a substitutional N fraction, $f_{N\text{-}sub} = 0.75$,[2] which corresponds to multiplying x_{XRC} by a factor of 1.325.

To measure the photoreflectance (PR) spectra, each sample was mounted on a cold finger in a helium closed cycle refrigerator coupled with a programmable temperature controller, allowing measurements in the 20 - 320 K temperature range. The reflected light from the sample was dispersed by a single grating 0.55 m focal-length monochromator and detected using a thermoelectrically cooled InGaAs p-i-n photodiode. To illuminate the sample, a semiconductor laser (532 nm line) and a 150 W tungsten–halogen bulb were used as the pump and probe beams, respectively, which were focused onto the sample to a diameter of ~2 mm. The pump beam was modulated by a mechanical chopper at a frequency of 290 Hz. Phase sensitive detection of the PR signal was made using a lock-in amplifier. Photoluminescence (PL) spectra were collected using a continuous-wave laser with wavelength of 532 nm and excitation powers of 100 or 300 mW.

6.4 Composition-dependence of out-of-plane misfit

In Figure 6.1, contours of out-of-plane misfit are presented on a plot of y_{Bi} and x_N for $GaAs_{1-x-y}N_xBi_y$ films. For the layers indicated by circular symbols, x_N and y_{Bi} were determined by NRA and RBS respectively. For the layers indicated by square symbols, y_{Bi} was determined by RBS and x_N was determined by the correction to XRC-measured values, as described above. For each composition, the out-of-plane misfit, $\varepsilon_\perp$, determined from (004) x-ray rocking curves, as described in Eqn. (6.1) above, is labeled near each point. Using a planar fit to the data points represented by circular symbols, with R^2 = 0.97, contours of constant $\varepsilon_\perp$, indicated by dashed black lines, reveal a ratio for lattice matching of $x_N/y_{Bi} = 0.83$. For comparison, the predicted lattice-matched ratio of x_N/y_{Bi} = 0.59 from Janotti et al.,[1] as well as the lattice-matched ratio of $x_N/y_{Bi} = 0.49$ estimated using x-ray diffraction determinations of the N fraction by Huang et al.[11] are shown by gray lines. We note that a significant fraction of the N in GaAsNBi has been reported to be incorporated interstitially,[2,12] predominantly in the form of $(N\text{-}As)_{As}$ complexes, which are not accounted for in Janotti's calculations and the x-ray diffraction determinations of x_N by Huang et al.[11] and Tixier.et al.[13] Indeed, a planar fit to $\varepsilon_\perp$, using the substitutional x_N, rather than the total x_N, yields a lattice-matched ratio of $x_N/y_{Bi} = 0.61$, in agreement with the predictions of Janotti et al.[1]

6.5 Photoreflectance

We now consider the optical properties of the N flux series and Bi flux series of GaAsNBi alloys, as shown in the low-temperature (i.e. T = 20 K) PR spectra shown in

Figure 6.2(a) and Figure 6.2(b), respectively. For each PR spectrum, features that are attributed to energy transitions, i.e. resonances, are apparent. To determine the energy, E_0, of each transition and its broadening, the PR spectra were fitted using the Aspnes Formula:[14]

$$\frac{dR}{R}(E) = \mathrm{Re}\left[Ce^{i\vartheta}(E - E_0 + i\Gamma)^{-m}\right], \tag{6.2}$$

where $\frac{dR}{R}(E)$ is the energy dependence of the PR signal, C and ϑ denote the amplitude and phase, and E_0 and Γ are the energy and the broadening parameter of the optical transition, respectively. Assuming $m = 2.5$ for a band-to-band transition, we fit each spectrum with a low and a high energy resonance, shown as black and red vertical dashed lines in the plots in Figure 6.2. For each resonance, further visualization of the transition energies is enabled by plots of the moduli of the PR resonances,[15] shown as grey dashed lines in Figure 6.2:

$$\Delta\rho(E) = \frac{|C|}{[(E-E_0)^2+\Gamma^2]^{\frac{m}{2}}} \tag{6.3}$$

With increasing x_N and/or y_{Bi}, there is a monotonic decrease, i.e. a redshift, of the bandgap to lower energies. For some spectra, a second resonance is apparent at slightly higher energy than the bandgap, likely due to strain-induced splitting of the light-hole and heavy-hole bands.[15] For other spectra, the broadening of the PR resonances and the small degree of splitting makes it difficult to resolve the second transition.

In Figure 6.3, PR spectra for films from the Bi flux series discussed in Ch. 5 are shown, with the N and Bi fractions and the transition energies labeled. For the $y_{Bi} = 0$ film, the PL spectrum is also plotted, indicating that the feature in the PR spectrum at approximately 1.2 eV is attributed to PL emission. As in Figure 6.2, the bandgap energy decreases with increasing x_N or y_{Bi}.

6.6 Composition-dependence of bandgap

In Figure 6.4, contours of bandgap and out-of-plane misfit are presented on a plot of y_{Bi} and x_N for $GaAs_{1-x-y}N_xBi_y$ films. Dashed black lines indicate contours of constant out-of-plane misfit, while circular and square symbols represent individual GaAsNBi films, as described for Figure 6.1. Bandgaps measured by PR for specific films are labeled beside each data point. Solid contours indicate the composition-dependence of the bandgap (in eV), determined by fitting the measured bandgaps and compositions using the parameterization scheme of Tixier et al.:[13]

$$E_{GaAsNBi}(x_N, y_{Bi}) = E_{GaAs} - \Delta_N(x_N) - \Delta_{Bi}(y_{Bi}) - A\Delta_N(x_N)\Delta_{Bi}(y_{Bi}) \quad (6.4)$$

where E_{GaAs} is the bandgap of GaAs at 20K, $\Delta_N(x_N)$ is the N-induced bandgap reduction in GaAsN, $\Delta_{Bi}(y_{Bi})$ is the Bi-induced bandgap reduction in GaAsBi, and A is an adjustable N-Bi coupling parameter. The N-induced bandgap reduction (in eV) is expressed as:

$$\Delta_N(x_N) = x_N(E_{GaAs} - E_{GaN}) + b_{GaAsN}x_N(1 - x_N) \quad (6.5)$$

Where E_{GaN} is the bandgap of GaN and b_{GaAsN} is the bowing parameter (in eV) with a double-exponential dependence on N fraction:[16,17]

$$b_{GaAsN}(x_N) = 9.4 + 23.8e^{-x_N/0.0038} + 11.9e^{-x_N/0.028} \quad (6.6)$$

The double-exponential dependence of the bowing parameter on x_N has been attributed to three regimes of bandgap energy, which are dominated by single-impurity N levels, N pair and cluster states, and alloy behavior, respectively.[17,18,19] To estimate the Bi-induced bandgap reduction, we used our PR determination of the GaAsBi bandgap as $\Delta_{Bi}(y_{Bi}) = 7.3y_{Bi}$ (in eV), which is similar to the average value $7.8y_{Bi}$ from earlier reports.[11,20,21,22,23] Using a non-linear least-squares fit to Eqn. (6.4),[24,25] the N-Bi coupling parameter A = -

0.02 ± 0.10 eV^{-1}, which corresponds to a value of -(1-2) meV for the final term in Eqn. (6.4). Thus, the quaternary bandgap reduction is essentially the sum of the individual bandgap reductions, suggesting that N and Bi independently influence the band edges, as predicted by Broderick et al.[6] but in contrast to earlier reports that indicate non-zero values of A,[1,13] which correspond to additional bandgap reductions of <20 meV[1] and <100 meV.[13]

6.7 Photoluminescence and Stokes shift

We next examine PL spectra for selected $GaAs_{1-x-y}N_xBi_y$ films with PR spectra shown in Figure 6.2 and Figure 6.3. In Figure 6.5(a), PL spectra for a film with $x_N = 0.007$ and $y_{Bi} = 0.034$ are plotted for temperatures ranging from 7 K to 125 K. With increasing measurement temperature, the PL peak energy decreases monotonically. The lineshape of the emission is asymmetric, displaying an extended low-energy tail, which is often attributed to emission from a distribution of localized states.[26,27] In Figure 6.5(b), the PL peak energies as a function of temperature are compared with the bandgap energy of the film determined from PR measurements at 20 K. A solid black line shows a projection of the bandgap to high temperatures using the Varshni model,[28]

$$E(T) = E(0) - \frac{\alpha T^2}{(T+\beta)} \quad (6.7)$$

using the parameters for GaAs (α = 5.41×10^{-4} meV/K, β = 204 K).[29] The ~160 meV difference between the PR-determined low-temperature bandgap, E_{PR}, and the PL-determined low-temperature peak energy, E_{PL}, i.e. the Stokes shift, suggests emission from localized states.

To examine the origins of the localized state emission, we consider PL spectra from several films in Figure 6.6 for (a) the N flux series and (b) the Bi flux series. For all Bi-

containing films, the Stokes shifts range from 0.15 to 0.18 eV. In contrast, for the GaAsN film (i.e. $y_{Bi} = 0$) in Figure 6.6(b), a negligible difference between E_{PL} and E_{PR} is apparent. Taken together, these results suggest the 7 K PL emission is dominated by an optical transition involving a Bi-related state within the bandgap, approximately 0.18 eV above the valence band edge. Interestingly, Janotti et al. have predicted a Bi-induced isovalent defect level at 0.18 eV above the valence band edge of GaAsNBi.[1]

We next consider the influence of chemical ordering on the Bi-related localized states. Figure 6.7 shows PL spectra collected at 4 K for several films from the Ch. 5 Bi flux series, for which the presence or absence of {111} chemical ordering was examined in Section 5.6. The corresponding PR spectra are shown in Figure 6.3, and the Stokes shift, E_{PR} - E_{PL}, is listed alongside each spectrum. In Ch. 5, the presence of {111} chemical ordering was directly correlated with a (2x1) surface reconstruction observed by reflection high-energy electron diffraction (RHEED); therefore, we also list the surface reconstruction observed for each film during growth. Similar to Figure 6.6, a small Stokes shift is observed for $y_{Bi} = 0$ in Figure 6.7; a slightly larger Stokes shift is observed for very small Bi fraction, $y_{Bi} = 0.003$. By considering the Stokes shifts and surface reconstructions for intermediate Bi fractions in both Figure 6.6 and Figure 6.7, it is apparent that films with a (1x3) reconstruction exhibit a Stokes shift of 0.18 eV, while films with a (2x1) reconstruction, expected to contain {111} chemical ordering, exhibit reduced Stokes shifts. The correlation between surface reconstruction and Stokes shift suggests that {111} chemical ordering modifies the energetic positions of the Bi-related states within the bandgap, likely through modification of the Bi local atomic environments.[30,31] Further

work is needed to resolve the atomistic origins of the Bi-related states, as will be further discussed in Section 7.2.4.

6.8 Summary

In summary, we have examined the alloy composition dependence of the energy bandgap and lattice misfit in GaAsNBi alloys. We identify the magic ratio for lattice-matching to GaAs, $x_N/y_{Bi} = 0.83$. Using the substitutional x_N, without including interstitial N, the lattice-matched ratio becomes $x_N/y_{Bi} = 0.61$, in agreement with the predictions of Janotti et al.[1] In addition, a comparison of photoreflectance and photoluminescence measurements suggests the presence of Bi-related states ~0.18 eV above the valence band edge. We suggest that the energetic position of the Bi-related states is modified by the presence of {111} chemical ordering. These findings offer a predictive guide for bandgap engineering using GaAsNBi alloys and provide insight into the combined influence of Bi and N on electronic structure that is likely to extend to other emerging dilute nitride-bismide alloys, such as GaPNBi and InAsNBi.

6.9 Figures

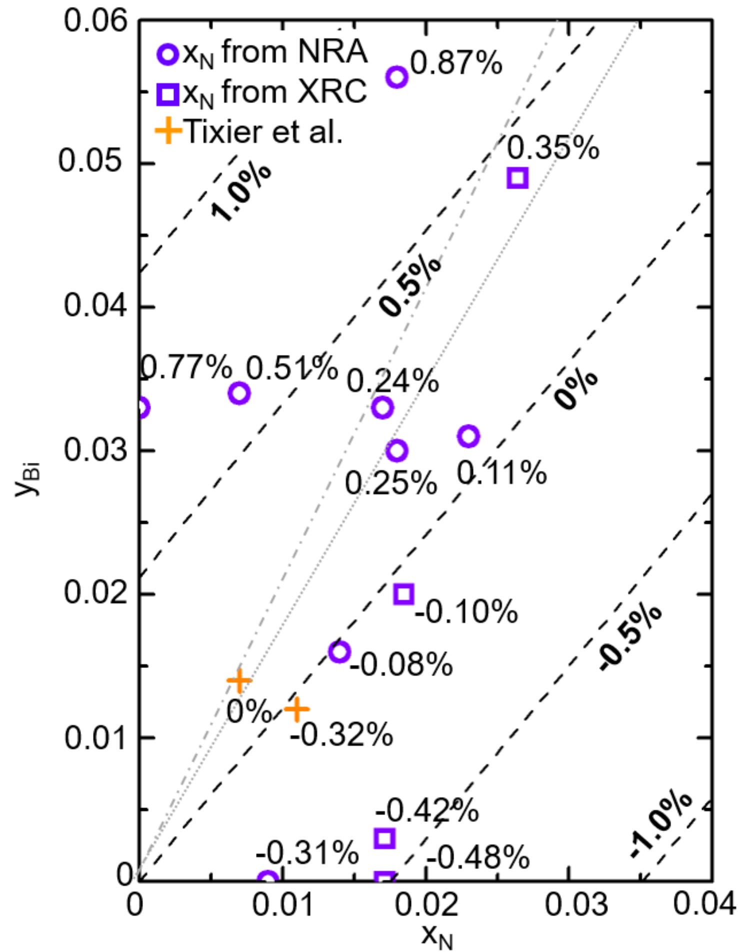

Figure 6.1 Contours of out-of-plane misfit, $\varepsilon_\perp$, presented on a plot of y_{Bi} and x_N for $GaAs_{1-x-y}N_xBi_y$ films. For circular symbols, x_N and y_{Bi} were determined by nuclear reaction analysis and Rutherford backscattering spectrometry (RBS) respectively. For square symbols, y_{Bi} was determined by RBS and x_N was determined by x-ray rocking curves (XRC), corrected to account for interstitial N. The percent out-of-plane misfit, $\varepsilon_\perp$, determined from (004) XRC, is labeled adjacent to each point. Dashed black lines represent contours of constant misfit, determined with a planar fit to the data points, indicating lattice-matching for a ratio $x_N/y_{Bi} = 0.83$. Lattice-matched ratios of $x_N/y_{Bi} = 0.59$ computed by Janotti et al.,[1] and $x_N/y_{Bi} = 0.49$ estimated from x-ray diffraction determinations of x_N by Huang et al.[11] are shown by gray lines. Cross symbols represent GaAsNBi films from Ref. 13. The uncertainty in the $\varepsilon_\perp$ contour lines is ± 0.04%, defined as the standard deviation between the fit and measured values of $\varepsilon_\perp$.

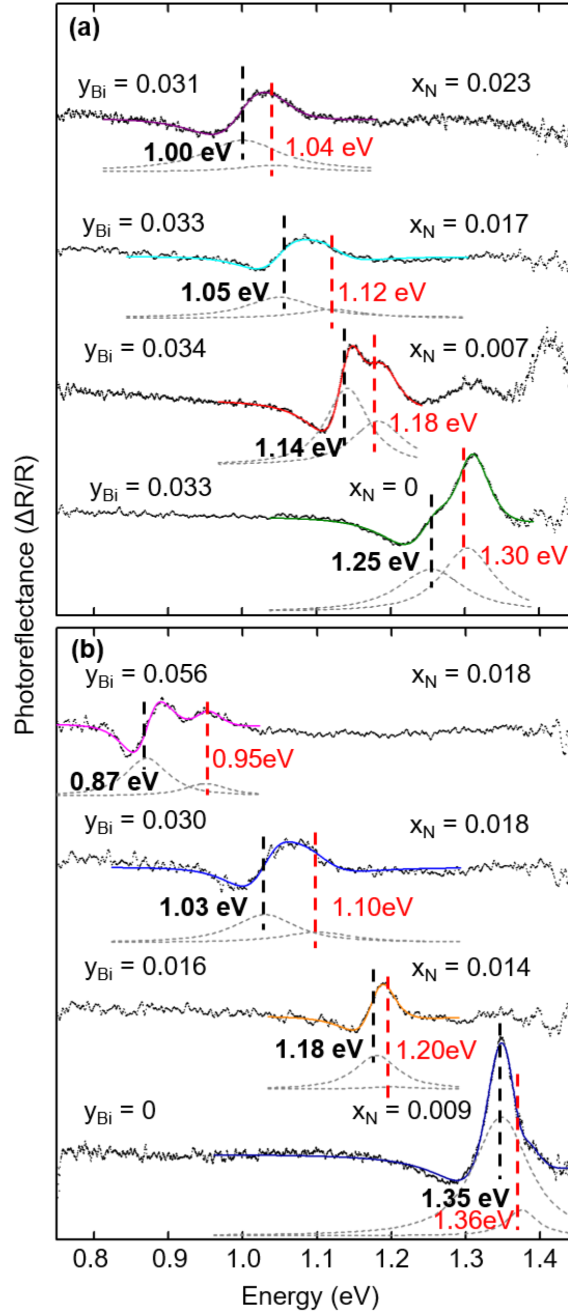

Figure 6.2 Photoreflectance (PR) spectra collected at 20 K from 100 nm thick $GaAs_{1-x-y}N_xBi_y$ films, with corresponding N and Bi fractions, x_N and y_{Bi}, displayed above each spectrum for (a) the N flux series and (b) the Bi flux series. For each spectrum, a PR resonance attributed to the bandgap energy, E_g, is indicated by a black dashed line. With increasing x_N and/or y_{Bi}, the E_g values decrease monotonically. For some spectra, a second transition, attributed to strain-induced splitting of the light-hole and heavy-hole bands, is indicated by a red vertical dashed line. The energy of each resonance was determined by fitting each spectrum with the Aspnes formula[14] (solid lines). The moduli of the PR resonances are shown as gray dashed lines below each PR spectrum.

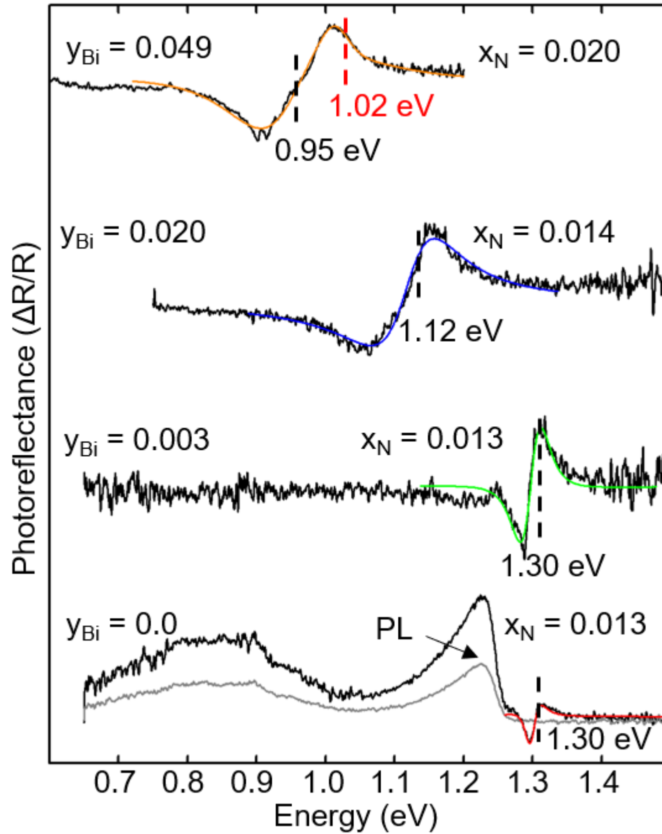

Figure 6.3 Photoreflectance (PR) spectra collected at 20 K from 400nm thick $GaAs_{1-x-y}N_xBi_y$ films from the Ch. 5 Bi-flux series, with corresponding N and Bi fractions, x_N and y_{Bi}, displayed above each spectrum. With increasing x_N and/or y_{Bi}, the E_g values decrease monotonically. For some spectra, a second transition, attributed to strain-induced splitting of the light-hole and heavy-hole bands, is indicated by a red vertical dashed line. The energy of each resonance was determined by fitting each spectrum with the Aspnes formula[14] (solid lines). For the film with y_{Bi} = 0, the photoluminescence (PL) spectrum is plotted in gray, showing that the feature at 1.2 eV in the corresponding PR spectrum is due to PL.

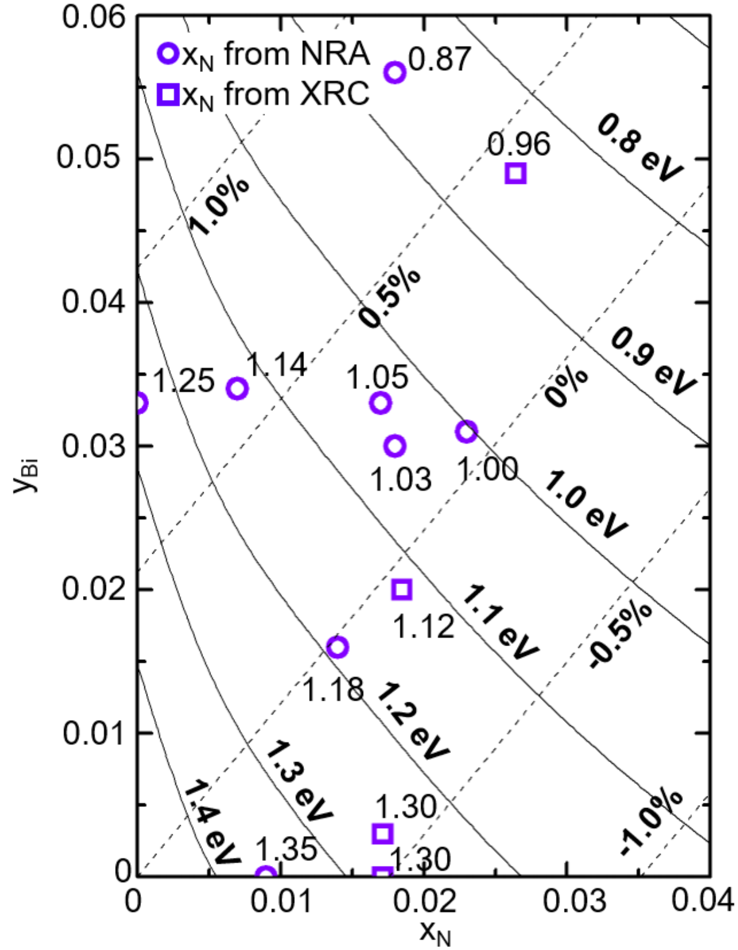

Figure 6.4 Contours of bandgap energies, E_g, and out-of-plane misfit, $\varepsilon_\perp$, presented on a plot of y_{Bi} and x_N for $GaAs_{1-x-y}N_xBi_y$ films. Values of E_g determined from photoreflectance spectra collected at 20 K are labeled adjacent to each point. Solid lines of constant E_g were determined by a non-linear least-squares fit of Eqn. (6.4) to the data points. Dashed lines of constant $\varepsilon_\perp$, were determined as described for Fig. 1, with lattice-matching to GaAs at $x_N/y_{Bi} = 0.83$. The uncertainty in the E_g contour lines is ± 14 meV, defined as the standard deviation between the fit and the measured values of E_g.

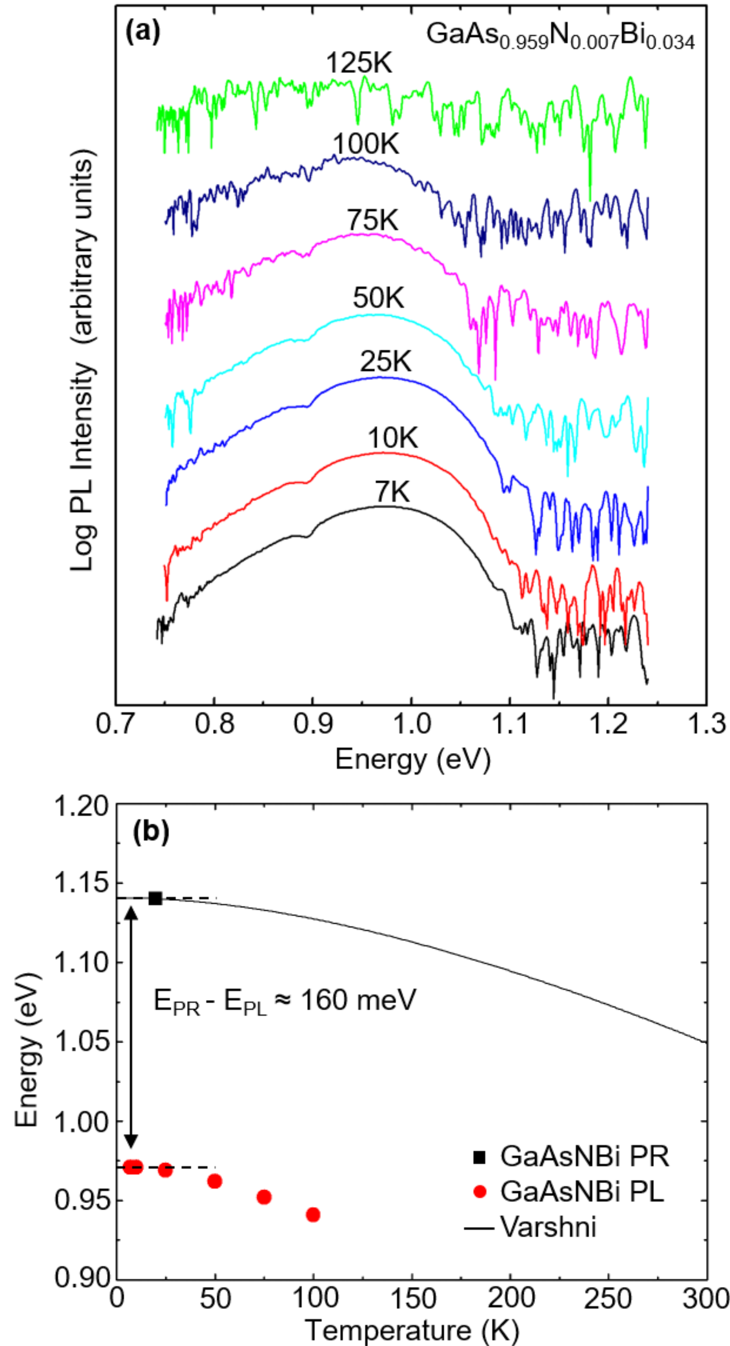

Figure 6.5 (a) Photoluminescence spectra collected from a $GaAs_{0.959}N_{0.007}Bi_{0.034}$ film at measurement temperatures ranging from 7 to 125 K. With increasing measurement temperature, the PL peak energy decreases monotonically. (b) PL peak energy versus measurement temperature, compared to photoreflectance (PR)-determined bandgap energy, E_g, at 20 K. A solid black line shows a projection of the E_g to high temperatures using the Varshni model with the parameters for GaAs.[29]

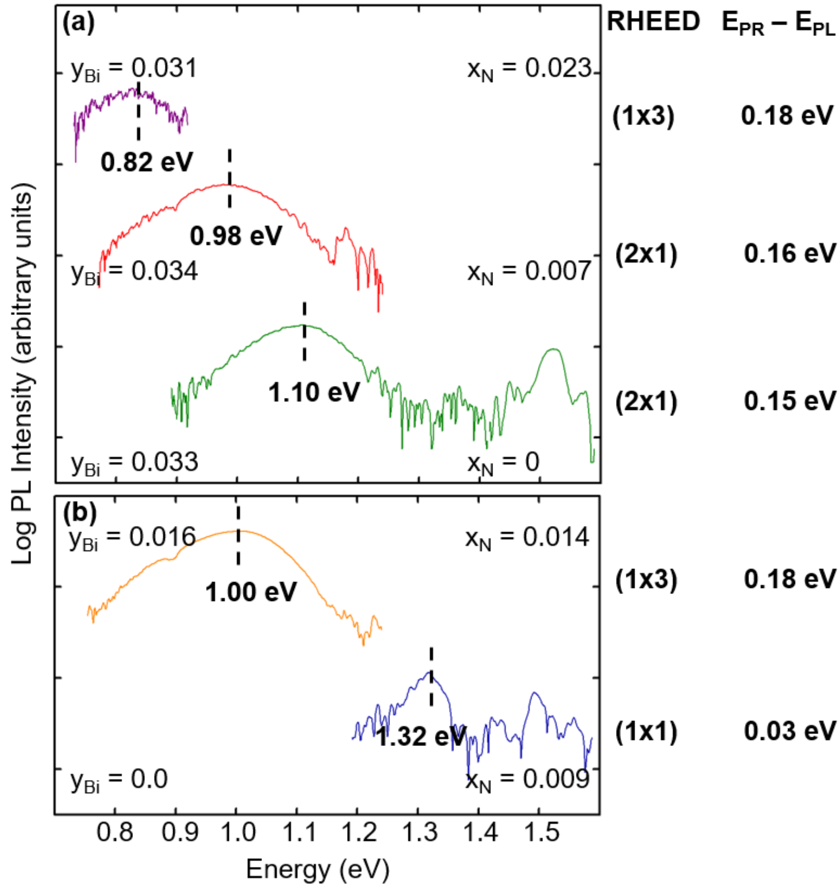

Figure 6.6 Photoluminescence (PL) spectra collected at 7 K for selected $GaAs_{1-x-y}N_xBi_y$ films with photoreflectance spectra shown in Figure 6.2. A comparison of the PL-determined peak energies, E_{PL}, with the PR-determined bandgap energies, E_{PR}, in Figure 6.2 reveals similar values for the GaAsN film. For the GaAsNBi films, the difference between E_{PR} and E_{PL}, i.e. the Stokes shift, ranges from 0.15 to 0.18 eV, likely due to Bi-related states within the bandgap. Films with a (2x1) surface reconstruction observed by RHEED exhibit smaller Stokes shifts than those with a (1x3) reconstruction.

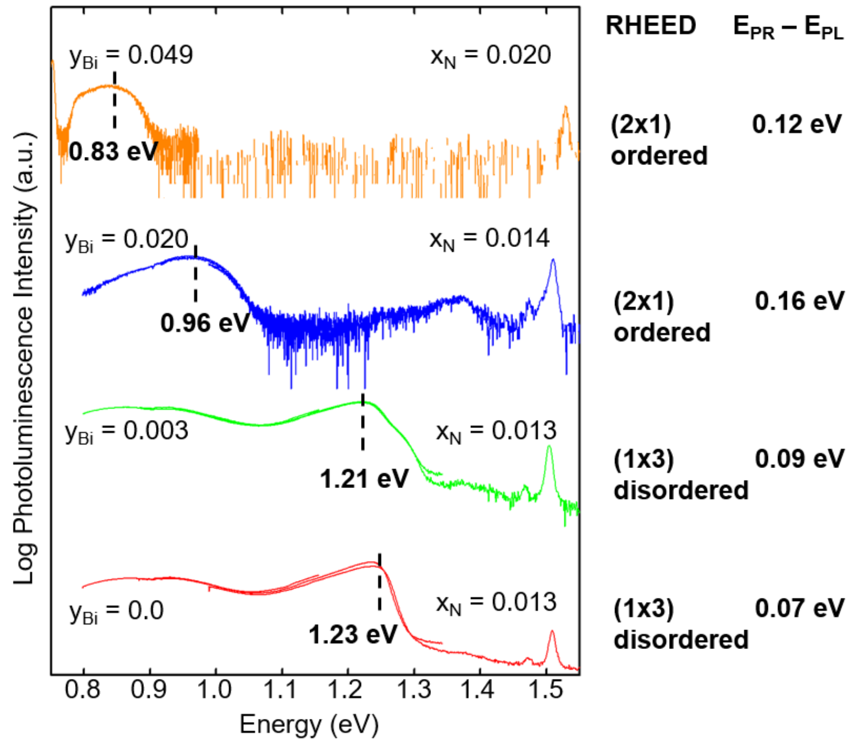

Figure 6.7 Photoluminescence (PL) spectra collected at 4 K from 400 nm thick $GaAs_{1-x-y}N_xBi_y$ films with photoreflectance spectra shown in Figure 6.3. The corresponding PR spectra are shown in Figure 6.3, and the Stokes shift, E_{PR} - E_{PL}, is listed alongside each spectrum, as well as the surface reconstruction observed by RHEED for each film during growth. For intermediate y_{Bi} in Figure 6.6 and Figure 6.7, films with a (2x1) reconstruction exhibit reduced Stokes shifts compared to films with a (1x3) reconstruction.

6.10 References

[1] A. Janotti, S.-H. Wei, and S.B. Zhang, "Theoretical Study of the Effects of Isovalent Coalloying of Bi and N in GaAs", Phys. Rev. B 65, 115203 (2002).

[2] J. Occena, T. Jen, E.E. Rizzi, T.M. Johnson, J. Horwath, Y.Q. Wang, and R.S. Goldman, "Bi-Enhanced N Incorporation in GaAsNBi Alloys", Appl. Phys. Lett. 110, 242102 (2017).

[3] Y. Zhang, A. Mascarenhas, and L.-W. Wang, "Similar and Dissimilar Aspects of III-V Semiconductors Containing Bi versus N", Phys. Rev. B 71, 155201 (2005).

[4] S. Francoeur, S. Tixier, E. Young, T. Tiedje, and A. Mascarenhas, "Bi Isoelectronic Impurities in GaAs", Phys. Rev. B 77, 085209 (2008).

[5] K. Alberi, O.D. Dubon, W. Walukiewicz, K.M. Yu, K. Bertulis, and A. Krotkus, "Valence Band Anticrossing in GaBixAs1−x", Appl. Phys. Lett. 91, 051909 (2007).

[6] C.A. Broderick, M. Usman, and E.P. O'Reilly, "Derivation of 12- and 14-Band k · p Hamiltonians for Dilute Bismide and Bismide-Nitride Semiconductors", Semicon. Sci. Tech. 28, 125025 (2013).

[7] C.-Z. Zhao, H.-Y. Ren, T. Wei, S.-S. Wang, and K.-Q. Lu, Dependence of the Band Gap Energy of Dilute Bismuth and Nitride GaNxBiyAs1−y−z Alloy ($0 \leq x \leq 0.05$, $0 \leq y \leq 0.05$)", J. Electron. Mat. 47, 4539 (2018).

[8] V. Virkkala, V. Havu, F. Tuomisto, and M.J. Puska, "Modeling Bi-Induced Changes in the Electronic Structure of GaAs1−xBix Alloys", Phys. Rev. B 88, 235201 (2013).

[9] T. Jen, G. Vardar, Y.Q. Wang, and R.S. Goldman, "Identifying the Dominant Interstitial Complex in Dilute GaAsN Alloys", Appl. Phys. Lett. 107, 221904 (2015).

[10] M. Reason, H.A. McKay, W. Ye, S. Hanson, R.S. Goldman, and V. Rotberg, "Mechanisms of Nitrogen Incorporation in GaAsN Alloys", Appl. Phys. Lett. 85, 1692 (2004).

[11] W. Huang, K. Oe, G. Feng, and M. Yoshimoto, "Molecular-Beam Epitaxy and Characteristics of GaNyAs1−x−yBix", J. Appl. Phys. 98, 053505 (2005).

[12] P. Wei, S. Tixier, M. Chicoine, S. Francoeur, A. Mascarenhas, T. Tiedje, and F. Schiettekatte, "Ion Beam Characterization of GaAs1−x−yNxBiy Epitaxial Layers", Nucl. Instrum. Meth. B 219–220, 671 (2004).

[13] S. Tixier, S.E. Webster, E.C. Young, T. Tiedje, S. Francoeur, A. Mascarenhas, P. Wei, and F. Schiettekatte, Appl. Phys. Lett. 86, 112113 (2005).

[14] D.E. Aspnes, "Third-Derivative Modulation Spectroscopy with Low-Field Electroreflectance", Surf. Sci. 37, 418 (1973).

[15] R. Kudrawiec and J. Misiewicz, "Optical Modulation Spectroscopy" in *Semiconductor Research*, edited by A. Patane and N. Balkan (Springer Berlin Heidelberg, Berlin, Heidelberg, 2012), pp. 95–124.

[16] M. Reason, "Structure and Properties of Dilute Nitride GaAsN Alloy Films", Ph.D. Thesis, Chapter 5, University of Michigan, 2006, p.140.

[17] U. Tisch, E. Finkman, and J. Salzman, "The Anomalous Bandgap Bowing in GaAsN", Appl. Phys. Lett. 81, 463 (2002).

[18] P.R.C. Kent and A. Zunger, "Theory of Electronic Structure Evolution in GaAsN and GaPN Alloys", Phys. Rev. B 64, 115208 (2001).

[19] R. Field, Y. Jin, H. Cheng, T. Dannecker, R. Jock, Y. Wang, C. Kurdak, and R. Goldman, "Influence of N Incorporation on Persistent Photoconductivity in GaAsN Alloys", Phys. Rev. B 87, (2013).

[20] S. Tixier, M. Adamcyk, T. Tiedje, S. Francoeur, A. Mascarenhas, P. Wei, and F. Schiettekatte, "Molecular Beam Epitaxy Growth of GaAs1-xBix", Appl. Phys. Lett. 82, 2245 (2003).

[21] S. Francoeur, M.J. Seong, A. Mascarenhas, S. Tixier, M. Adamcyk, and T. Tiedje, "Band gap of GaAs1-xBix, $0 < x < 3.6\%$", Appl. Phys. Lett. 82, 3874 (2003).

[22] K. Alberi, O.D. Dubon, W. Walukiewicz, K.M. Yu, K. Bertulis, and A. Krotkus, "Valence Band Anticrossing in GaBixAs1−x", Appl. Phys. Lett. 91, 051909 (2007).

[23] A.R. Mohmad, F. Bastiman, J.S. Ng, S.J. Sweeney, and J.P.R. David, "Room Temperature Photoluminescence Intensity Enhancement in GaAs1-XBix Alloys", Phys. Status Solidi C 9, 259 (2012).

[24] K. Levenberg, "A Method for the Solution of Certain Non-Linear Problems in Least Squares", Quart. Appl. Math. 2, 164 (1944).

[25] D. Marquardt, "An Algorithm for Least-Squares Estimation of Nonlinear Parameters", J. Soc. Ind. Appl. Math. 11, 431 (1963).

[26] S. Imhof, A. Thränhardt, A. Chernikov, M. Koch, N.S. Köster, K. Kolata, S. Chatterjee, S.W. Koch, X. Lu, S.R. Johnson, D.A. Beaton, T. Tiedje, and O. Rubel, "Clustering Effects in Ga(AsBi)", Appl. Phys. Lett. 96, 131115 (2010).

[27] T. Wilson, N.P. Hylton, Y. Harada, P. Pearce, D. Alonso-Álvarez, A. Mellor, R.D. Richards, J.P.R. David, and N.J. Ekins-Daukes, "Assessing the Nature of the Distribution of Localised States in Bulk GaAsBi", Sci. Rep. 8, 6457 (2018).

[28] Y.P. Varshni, "Temperature Dependence of the Energy Gap in Semiconductors", Physica 34, 149 (1967).

[29] I. Vurgaftman, J.R. Meyer, and L.R. Ram-Mohan, "Band Parameters for III–V Compound Semiconductors and Their Alloys", J. Appl. Phys. 89, 5815 (2001).

[30] L.C. Bannow, O. Rubel, S.C. Badescu, P. Rosenow, J. Hader, J.V. Moloney, R. Tonner, and S.W. Koch, Badescu, S. C., Rosenow, P., Hader, J., Moloney, J. V., Tonner, R., and Koch, S. W. "Configuration Dependence of Band-Gap Narrowing and Localization in Dilute GaAs 1 − x Bi x Alloys", Phys. Rev. B 93, 205202 (2016).

[31] Y. Zhang, A. Mascarenhas, and L.-W. Wang, "Dependence of the Band Structure on the Order Parameter for Partially Ordered GaxIn1−xP Alloys", Phys. Rev. B 63, 201312 (2001).

Chapter 7

Summary and Suggestions for Future Work

7.1 Summary

In this dissertation, we described our investigations of surface dimer engineering of $GaAs_{1-x-y}N_xBi_y$ alloys during molecular-beam epitaxy (MBE). We investigated the role of surface reconstruction on the incorporation of Si into group III versus group V sites, and the resulting conductivity type in GaAs(Bi):Si. We linked an enhancement in the concentration of total and interstitial N in GaAsNBi alloys to a Bi-induced modification of the surface step edges on a (1x3) reconstructed surface and mapped the composition-dependence of lattice mismatch and bandgap energy in GaAsNBi alloys. For GaAsNBi alloys, we explored the influence of Bi-induced surface reconstruction on the total N incorporation and atomic ordering on {111}B planes.

In Chapter 3, we investigated the influence of surface reconstruction on silicon dopant incorporation and transport properties during MBE of GaAs and GaAsBi films. We showed that GaAs(Bi) growth with an (n×3) reconstruction leads to n-type conductivity, while growth with a (2×1) reconstruction leads to p-type conductivity. We proposed a mechanism in which the presence or absence of surface arsenic dimers prevents or enables dopant incorporation into arsenic lattice sites, and we investigated the surface morphologies and carrier transport properties of n-type and p-type GaAs(Bi):Si films.

In Chapters 4 and 5, we investigated the role of Bi-induced surface reconstructions on the incorporation of N and Bi into $GaAs_{1-x-y}N_xBi_y$ alloys. Through an examination of Bi-flux series, N-flux series, and temperature series, we revealed new insight into the role of surface dimer alignment on the co-incorporation of N and Bi and chemical ordering on the {111} planes. For intermediate substrate temperature, comparison of the Bi-flux and N-flux series revealed Bi incorporation which is independent of N flux but N incorporation which increases with increasing Bi flux. We hypothesized that the Bi-induced (1x3) reconstruction leads to an increased density of [110]-oriented step edges with As dangling bonds, enhancing the total N incorporation and the formation of $(N\text{-}As)_{As}$.

In Chapter 5, we investigated the role of surface dimers in determining the local atomic environment of N and Bi solute atoms. Through examination of a temperature series and a Bi-flux series (with higher temperature than that in Ch. 4), we showed the influence of Bi as an incorporating surfactant on chemical ordering in GaAsN:Bi alloys. While epitaxy with a (2x1) reconstruction leads to random GaAsN formation, the introduction of a Bi flux induces long-range chemical ordering of the {111} planes of GaAsN:Bi. High-resolution scanning transmission electron microscopy revealed intersecting $(1\bar{1}1)$ and $(\bar{1}11)$ ordered domains with a lognormal size distribution, consistent with domain formation at surface steps without subsequent coarsening. We proposed a mechanism in which Bi enhances the formation of dimer rows aligned along the [110] direction, facilitating N incorporation beneath surface dimers and Bi incorporation between dimer rows to form alternating N-rich and Bi-rich {111} planes. These findings suggest a route to tailoring the local atomic environment of N and Bi atoms in a wide range of emerging dilute nitride-bismide alloys.

In Chapter 6, we examined the alloy composition dependence of the energy bandgap and electronic states in GaAsNBi alloys. Using direct measurements of N and Bi mole fractions, via ion beam analysis, in conjunction with direct measurements of the out-of plane misfit via x-ray rocking curves, we determined a new N/Bi ratio for lattice-matching of GaAsNBi alloys with GaAs substrates. In addition, using a combination of photoreflectance and photoluminescence spectroscopy, we determined a new map of the composition- and misfit-dependence of the energy bandgaps and revealed the presence of of Bi-related states at approximately 0.18 eV above the valence band maximum. These findings offer a predictive guide to bandgap engineering using GaAsNBi alloys and provide insight into the combined influence of Bi and N on electronic structure that may be extended to other emerging dilute nitride-bismide alloys.

7.2 Suggestions for future work

7.2.1 Growth of GaAsNBi on offcut substrates

In Ch. 4 and Ch. 5, we hypothesized that dimer alignment along [$\bar{1}$10] led to an increased density of [110]-oriented step edges and enhanced N incorporation while dimer alignment along [110] led to chemical ordering of the {111}B planes. To test these hypotheses, we propose to examine the influence of substrate offcuts toward (111)A and (111)B, which induce surface terraces with step edges aligned along the [$\bar{1}$10] and [110] directions, respectively,[1] and promote a step-flow growth mode, as shown in Figure 7.1. Through comparison of growth on (111)A and (111)B offcuts, it may be possible to modify

N incorporation by varying the density of [110]-oriented steps according to the mechanism proposed in Ch. 4.

Furthermore, in Ch. 5 we attributed ordered domain sizes of 1-2 nm to the layer-by-layer growth mode on an (001)-oriented substrate, which limits the lateral size of domains due to island propagation in both the $[\bar{1}10]$ and $[1\bar{1}0]$ directions, as discussed in Section 5.6. In contrast, for step-flow growth, step edges propagate in a single direction, facilitating formation of domain sizes > 100 nm.[2] Growth of ordered GaAsNBi alloys on substrates with (111)B offcuts is therefore expected to lead to a stronger degree of ordering, as well as to larger ordered domains.[3]

As a preliminary study of the influence of substrate offcut on N and Bi incorporation, we grew GaAsN and GaAsNBi films on GaAs (001) substrates with offcuts toward (111)A. The films were grown by MBE using a growth sequence nominally identical to that shown in Figure 4.1. The 100 nm thick GaAsN(Bi) films were grown at 340 ± 15 °C with an As_4/Ga beam equivalent pressure (BEP) ratio of ~ 20 and a growth rate of 1 μm/hr. For all films, the Bi/As_4 BEP ratio was fixed at 0.006, and the N plasma source was operated at a N_2 flow rate of 0.25 sccm. To facilitate comparison of multiple substrate offcut angles, groups of three to four samples were indium-mounted on the same molybdenum block and grown simultaneously. The samples were grown in four growth runs, grouped according to alloy and offcut angle as follows: GaAsN (0°, 2°, 6°, 10°), GaAsN (0°, 4°, 8°), GaAsNBi (0°, 2°, 6°, 10°), GaAsNBi (0°, 4°, 8°). We note that the substrates used in this preliminary study were received from Dr. Chris Palmstrom, via Dr. Karen Kavanaugh, circa 2003, and no specifications aside from the substrate orientations were available.

High-resolution x-ray rocking curves (HRXRC) were collected using $CuK\alpha_1$ radiation near the symmetric GaAs (004) and asymmetric GaAs (115) reflections as described in Section 2.3 For GaAsN films, the N fraction was determined using a linear interpolation of the GaAs and GaN lattice parameters. For GaAsNBi films, the Bi fraction was determined by Rutherford backscattering spectrometry (RBS) and the N fraction by nuclear reaction analysis (NRA) using the reaction $^{14}N(\alpha,p)^{17}O$, as described in Section 2.6. RBS (NRA) was performed using a 4.50 MeV He^+ beam with the detector positioned at 170° (165°) with respect to the incident beam.

In Figure 7.2, HRXRC about the GaAs (004) reflection are shown for GaAsN and GaAsNBi films grown on GaAs (001) substrates with offcut toward (111)A ranging from 0° to 10°. For each film, the N fraction, x_N, is listed, determined by HRXRC for GaAsN films and by NRA for GaAsNBi films. For GaAsNBi films, the Bi fraction, y_{Bi}, determined by RBS is also listed. For both GaAsN and GaAsNBi, the measured x_N and y_{Bi} are apparently independent of substrate offcut angle. While NRA spectra were not collected for the GaAsN films, for GaAsN films grown under similar conditions it has been found that ~20% of the N atoms incorporate interstitially, as shown in Section 4.6, and are not accounted for in a linear interpolation of the GaAs and GaN lattice parameters. Interstitial N incorporation may therefore account for the small difference observed here between x_N measured by HRXRC for GaAsN films and x_N measured by NRA for GaAsNBi films.

In Figure 7.2, the full width at half maximum (FWHM) in arcseconds is shown adjacent to each peak. For comparison, films grown with similar layer structure and growth conditions in Figure 4.2 exhibit narrower substrate (20±5 arcsec) and epilayer (191±12 arcsec) peaks. The broadened diffraction peaks and weak or absent Pendellosung fringes

suggest roughened substrate-epilayer interfaces. For future investigations, we suggest using new epi-ready substrates and expanding the study to include GaAs (001) substrates offcut toward (111)B. Through comparison of growth on (111)A and (111)B offcuts, it may be possible to modify N incorporation by varying the density of [110]-oriented steps according to the mechanism proposed in Ch. 4, as well as to significantly alter the ordered domain size in CuPt-ordered alloys, as discussed in Ch. 5.

7.2.2 Band offsets in GaAs/$GaAs_{1-x-y}N_xBi_y$/GaAs quantum wells

As discussed in Sections 1.3 and 1.4, a promising feature predicted for GaAsNBi alloys is the opportunity to independently tune the conduction band offset (CBO) and valence band offset (VBO) over a wide range in semiconductor heterostructures.[4] According to the (valence) band anti-crossing model, N (Bi) primarily lowers (raises) the conduction (valence) band edge,[5,6] forming a type I band alignment at a GaAs/GaAsNBi interface in which the CBO is primarily controlled by the N fraction and the VBO by the Bi fraction. Consequently, GaAsNBi is predicted to enable improved confinement of electrons and holes in GaAs-based double-heterostructure laser diodes.[7] In addition, a strain-balanced type II GaAsN/GaAsBi superlattice structure has been proposed to extend the accessible wavelength range for solar cells and infrared photodetectors.[8,9] However, experimental measurements of the band offsets of GaAsNBi alloys have not been reported. In this section, we describe our progress toward measuring the band offsets in GaAs/$GaAs_{1-x-y}N_xBi_y$/GaAs heterostructures using capacitance-voltage measurements combined with one-dimensional (1-D) Schrödinger-Poisson simulations.

A series of diode structures each containing a single $GaAs/GaAs_{1-x-y}N_xBi_y/GaAs$ quantum well (QW) was grown by MBE on n-type (001) GaAs, with layer structure as shown in Figure 7.3. The substrate temperature was ramped during 10 min. growth interruptions before and after growth of the QW layer. Following MBE growth, Cr/Au (20/200 nm) Schottky contacts were evaporated onto the top surface through a shadow mask with 680 µm diameter circular openings. Indium was used as an Ohmic back contact. The compositions in the $GaAs_{1-x-y}N_xBi_y$ QW layers were examined using a combination of RBS and XRD, as described in Section 2.3. Capacitance-voltage (C-V) measurements were performed as described in Section 2.5 and used to profile the free carrier concentration across the QWs, using the method described in Appendix G.

Accumulation of free carriers inside the QW and depletion of carriers outside the QW leads to a characteristic trough-peak-trough carrier concentration profile, as shown in Figure 7.4. To extract the CBO, 1-D Schrödinger-Poisson simulations are being used to model carrier concentration profiles for QW structures with various CBO for comparison with the measured profiles. An example of a simulated profile for CBO = 320 meV is shown by a dashed line in Figure 7.4. While good agreement is apparent between the measurement and simulation for the first trough, the peak and second trough are overestimated by the simulation. For future simulations, it is suggested that variation in the concentration of fixed charge at each interface of the QW be included to account for the measured difference in the depths of the first and second troughs.[10,11] In addition, a second peak located at ~350 nm in the measured profile is not accounted for in the simulation. It is likely that this second peak is associated with the growth interruption that was used to ramp the substrate temperature between the GaAs and GaAsNBi layers. Accumulation of

species at the growth front during the interruption can lead to delta-doping or the formation of point defects that act as electron traps below the conduction band edge, which have been shown to produce additional peaks in C-V carrier concentration profiles.[12,13,14,15] Further investigation is suggested to identify the source of this peak and its influence on extraction of the CBO. C-V measurements and Schrödinger-Poisson simulations conducted to date have been carried out by Jack Hu and Andra Chen, in collaboration with the author.

Following determination of the CBO, the VBO may be extrapolated using a measurement of the bandgap within the QW, such as by photoluminescence (PL) spectroscopy. PL spectra collected at 4 K for three QW structures with different N fractions are shown in Figure 7.5. The PL measurements were performed by Patricia Dippo at the National Renewable Energy Laboratory. The spectra were collected in three acquisition windows using a 632.8 nm continuous-wave laser operated at excitation power of 0.5 mW for acquisition at 673 – 1153 nm and 5 mW for acquisition at 873 – 1353 nm and 1353 – 1803 nm. For each spectrum, a peak corresponding to emission from the GaAs substrate can be seen near 1.5 eV, with multiple peaks at lower energy associated with emission from the QWs. In future work, self-consistent Schrödinger-Poisson simulations used to fit the carrier concentration profiles may also be used to calculate the expected quantized energy levels for each QW, which may then be correlated with the PL peak energies. Extrapolation of the VBO for each GaAsNBi bandgap for each QW will require consideration of the possible influence of localized states[16,17,18,19,20] on the PL spectra, as well as the temperature difference between the PL and C-V measurements.

Figure 7.6 shows a high-resolution TEM image of a GaAsNBi QW, which appears as a dark band between lighter GaAs layers above and below. The total QW thickness is

approximately 10 nm, as targeted during MBE growth. However, while the top GaAs/GaAsNBi interface appears abrupt, the contrast in the lower half of the QW appears graded, suggesting a graded composition at the lower GaAsNBi/GaAs interface. Bi incorporation has been reported to be a function of the Bi surface coverage;[21,22,23] therefore, the graded composition observed in the lower half of the QW may be understood as corresponding to a gradual increase in the Bi surface coverage in the first few seconds after the Bi shutter is opened, followed by achievement of a steady-state Bi surface coverage which leads to uniform Bi incorporation in the upper half of the QW. Further study of the influence of the compositional grading on the carrier concentration profile is suggested.

7.2.3 Annealing and irradiation of GaAs(N)(Bi) films

7.2.3.1 Background

In this section, we discuss preliminary investigations of rapid thermal annealing (RTA), electron irradiation, and ultra-violet (UV) laser irradiation of GaAsNBi alloys and suggest avenues for further study.

In Ch. 4 and Ch. 6, we examined N interstitial formation and optical properties, respectively, for GaAsNBi alloys. For other dilute nitride HMAs, post-growth rapid thermal annealing (RTA) has been shown to significantly enhance the optical efficiency[24] and electronic transport properties.[25] The enhancement has been attributed to annealing-induced reconfiguration of the N local atomic environments, including a reduction in N interstitials[24,25,26,27] and Si-N complexes[28] in GaAsN:(Si) and an increase in In-N bonds[29] in InGaAsN. Furthermore, irradiating dilute nitride alloys with high-energy electrons prior

to RTA has been found to magnify the RTA-induced enhancement in PL intensity,[30,31] attributed to irradiation-induced formation of point defects, such as Ga vacancies,[32,33] that facilitate reconfiguration of the N local atomic environments via bulk diffusion. Thermal annealing has also been shown to eliminate {111} chemical ordering in GaInP,[34] similar to the {111} ordering we observed for GaAsNBi in Ch. 5. Irradiation of GaAsBi films with UV light during MBE growth has been reported to lead to a reduction in PL linewidth and more abrupt epilayer interfaces compared to samples grown without illumination.[23,35,36,37] UV irradiation with higher laser fluences may also enable localized annealing[38,39] that could be used to locally alter the nearest-neighbor environments of solute atoms through modification of chemical ordering or interstitial concentration.

7.2.3.2 UV irradiation of GaAs(N)(Bi) films

To investigate the influence of post-growth UV irradiation, we examine GaAsNBi, GaAsN, and GaAsBi films, grown by MBE as described in Section 4.3. A GaAs epilayer grown under similar conditions was considered as a reference film. Films were irradiated with a KrF excimer laser with wavelength of 248 nm in Professor John Heron's laboratory. Laser parameters were selected to match the conditions in Ref. 23. Laser pulses with energy 25 mJ were delivered at a frequency of 1 Hz with a spot size of 1.27 cm^2, resulting in a 0.197 J/cm^2 fluence. Films were examined before and after receiving 300 pulses, corresponding to a total energy of 7.5 J delivered to each film. To evaluate the structural changes in the films induced by the UV irradiation, high-resolution x-ray rocking curves (XRC) about the GaAs (004) reflection were used to measure the FWHM of the substrate and epilayer peaks and the substrate-epilayer peak separation. For some films, atomic force

microscopy (AFM) was used to measure the surface roughness before and after irradiation. In Figure 7.7, (004) XRC collected before and after irradiation are shown in black and red, respectively, for GaAs, GaAsBi, GaAsN, and GaAsNBi films, with the FWHM of each peak labeled. The as-grown and irradiated XRC are found to be nearly identical, with negligible change in FWHM, indicating that the irradiation did not have a significant influence on the composition, uniformity, or interface roughness of the films. In Figure 7.8, AFM images of the GaAsNBi film before and after irradiation show negligible change in the surface morphology or the root mean square roughness, R_q. Further investigation is suggested to determine if higher laser fluences or more laser pulses would influence film properties.

7.2.3.3 Influence of RTA and electron irradiation on optical properties

In this section we discuss preliminary investigations of the influence of RTA and electron irradiation on photoluminescence, conducted in collaboration with Dr. Emil-Mihai Pavelescu at IMT-Bucharest. Additional discussion of the PL spectra of as-grown films in this section can be found in Section 6.7.

In Figure 7.9, we examine the PL spectra for several $GaAs_{1-x-y}N_xBi_y$ films before and after RTA. Solid lines represent PL spectra collected from as-grown films while dashed lines represent PL spectra collected following RTA at 650 °C for 1 min. For GaAsNBi films, a small increase in the PL intensity is observed following RTA, with negligible change in peak position. For the GaAsN film ($y_{Bi} = 0$), the RTA-induced enhancement in PL intensity is significantly larger and is accompanied by an increase in PL peak energy, i.e., a blue-shift, suggesting that the presence of Bi modifies the influence of annealing on

luminescence. Further investigation is suggested to understand the atomistic origins of this modification.

In Figure 7.10, we examine the influence of electron irradiation and RTA temperature on PL for a single GaAsNBi film. A solid line indicates the PL spectrum of the as-grown film. Dashed lines indicate PL spectra following RTA, using annealing temperatures ranging from 650 to 850 °C. In all cases, the duration of RTA was 1 min. From 650 to 750 °C, the PL intensity increases with RTA temperature, and the peak energy increases slightly. For RTA temperatures > 750 °C, the PL intensity decreases, and the peak energy is significantly blue-shifted. The dotted line indicates the PL spectrum following irradiation with 6 MeV electrons, while the dot-dash line indicates PL from a film that received electron irradiation followed by RTA at 650 °C. For electron irradiation alone, the PL intensity is reduced compared to the spectrum of the as-grown film. However, for electron irradiation plus RTA at 650 °C, the PL intensity is greater than that of the film that received only RTA at 650 °C, and negligible blue-shift is observed, suggesting that electron irradiation plus RTA enhances the optical efficiency by a different mechanism that RTA alone. To better understand the mechanisms of PL intensity enhancement and blue-shift for electron irradiation versus RTA, we suggest application of the ion beam analysis plus Monte Carlo – molecular dynamics approach described in Section 4.7.

The enhancement in PL intensity induced by electron irradiation and/or RTA may also enable optical measurements of GaAsNBi over a greater range of temperatures than has been possible in as-grown films, allowing further study of the temperature-dependence of the PL peak energy. In Figure 7.11, we show PL spectra collected from a GaAsNBi film at temperatures ranging from 6 to 300 K, following electron irradiation and RTA at 650°C

for 1 min. The excitation power was 100 mW for spectra from 6K to 150K and 300 mW for 300K. The PL peak energy decreases with increasing temperature from 6K to 150K and then increases at 300K, consistent with emission from localized states for measurement temperatures ≤ 150 K,[40,41] as suggested in Section 6.7. For comparison, PL spectra from the same film prior to irradiation plus RTA are shown in Figure 6.4, where the peak cannot be resolved above 100K.

7.2.4 Influence of chemical ordering on electronic structure

In Section 5.7, we proposed that surface dimer-induced {111} chemical ordering could be used to manipulate the local atomic environments of GaAsNBi alloys. Furthermore, in Section 6.7, we revealed the presence of Bi-related states within the GaAsNBi bandgap and suggested that the energetic positions of these states are likely influenced by changes to the local atomic environments in the presence of ordering. To understand the influence of chemical ordering on the electronic structure and optical properties of GaAsNBi alloys, theoretical studies[42,43] of the local atomic environments suggested in Section 5.7 are recommended.

In Figure 7.12, we show possible first- and second-nearest-neighbor (2ndNN) configurations for a Bi solute atom in (a) disordered GaAsNBi, (b) ordered GaAsBi, and (c) ordered GaAsNBi. For disordered GaAsNBi, each 2ndNN position, corresponding to group V lattice sites, may be occupied with equal preference by an As, N, or Bi atom. Due to the small N and Bi fractions present in the GaAs(N)(Bi) alloys studied (x_N, y_{Bi} < 0.10), it is likely that the majority of these sites would be occupied by As atoms. For ordered GaAsBi, 2ndNN sites within the same $(\bar{1}11)$ plane as the center Bi atom are occupied by

Bi or As, while 2ndNN sites in adjacent $(\bar{1}11)$ planes are occupied by only As, forming alternating GaAs and GaAsBi $(\bar{1}11)$ planes. Similarly, for ordered GaAsNBi, the 2ndNN sites in adjacent $(\bar{1}11)$ planes are occupied by As or N, forming alternating GaAsN and GaAsBi $(\bar{1}11)$ planes.

7.2.5 Influence of chemical ordering on transport properties

The application of dilute nitride HMAs in devices has been hindered by severe degradation of the electron mobility with increasing N incorporation.[25,44,45] To date, the only report of electron mobility in GaAsNBi alloys is limited to a single film, but indicates degradation of the electron mobility similar to that reported for other dilute nitride alloys.[46] However, it has been suggested that chemical ordering such as that observed in Ch. 5 may enhance carrier transport parallel to the ordered planes by reducing alloy scattering.[47,48,49,50,51] For example, CuAu-type chemical ordering in InGaAs two-dimensional electron gas structures has been linked to enhanced electron mobility parallel to the {110} ordered planes.[47,48,49] In CuPt-ordered GaInP alloys, longer minority carrier diffusion lengths have been measured along the [110] direction, parallel to {111} ordered planes, than along the orthogonal direction.[50,51] Therefore, we suggest future investigations of carrier transport properties in ordered and disordered GaAsNBi alloys. We hypothesize that carrier transport may be enhanced along the [110] direction, parallel to the ordered $(1\bar{1}1)$ and $(\bar{1}11)$ planes observed in Ch. 5.

7.3 Figures

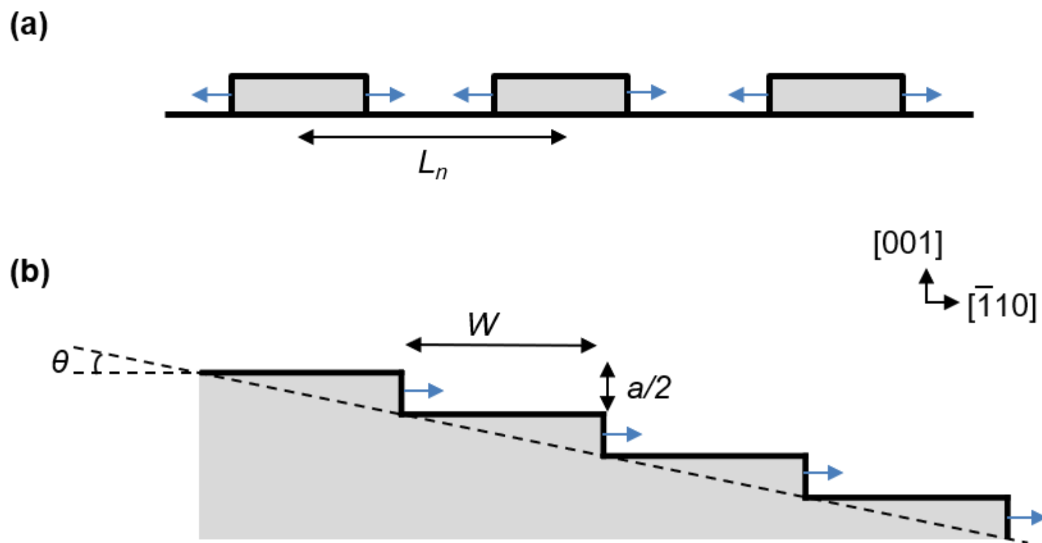

Figure 7.1 Schematic illustration of (a) the layer-by-layer growth mode on an exact (001) substrate, with island separation L_n, and (b) the step-flow growth mode on a substrate with offcut angle, θ, toward (111)B and lattice parameter a. The substrate offcut induces a regular array of terraces with width $W = (a/2)/tan(\theta)$,[1,52] with step edges aligned along the [110] direction.

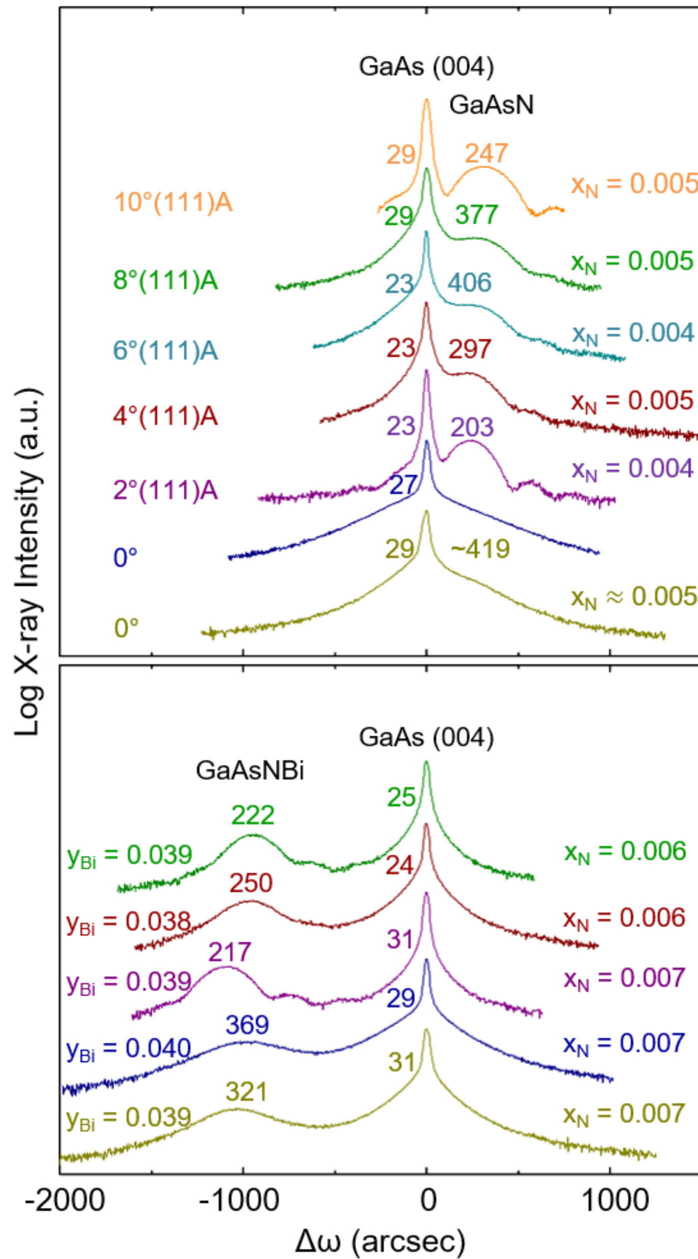

Figure 7.2 (004) high-resolution x-ray rocking curves for 100 nm thick $GaAs_{1-x}N_x$ and $GaAs_{1-x-y}N_xBi_y$ films grown on GaAs (001) substrates with offcuts from 0° to 10°(111)A. For all plots, the GaAs substrate peak is set to $\Delta\omega = 0$ arcseconds to facilitate comparison of $\Delta\omega$ between substrate and epilayer. The values of x_N and y_{Bi} are apparently independent of offcut angle. The full width at half maximum (FWHM) in arcseconds is shown adjacent to each peak. For comparison, films grown with similar layer structure and growth conditions in Figure 4.2 exhibit narrower substrate (20±5 arcsec) and epilayer (191±12 arcsec) peaks. The broadened diffraction peaks and weak or absent Pendellosung fringes suggest roughened substrate-epilayer interfaces.

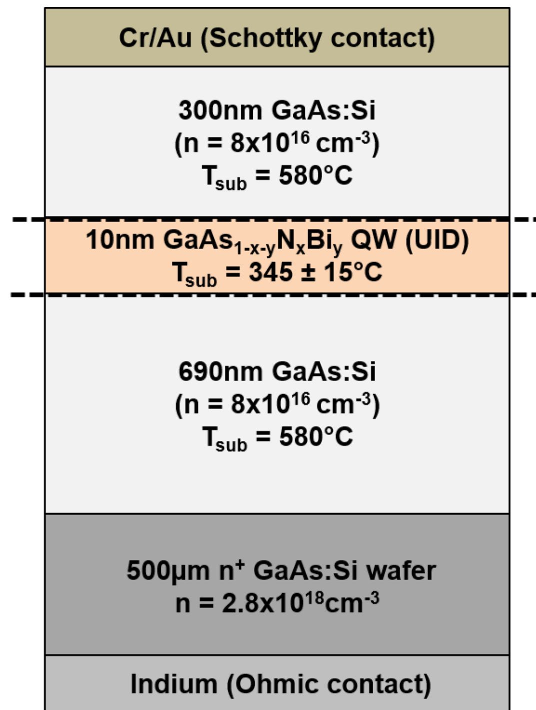

Figure 7.3 Schematic of the layer structure for single quantum well (QW) diodes used in band offset measurements. Dashed lines indicate growth interrupts during which the substrate temperature, T_{sub}, was ramped.

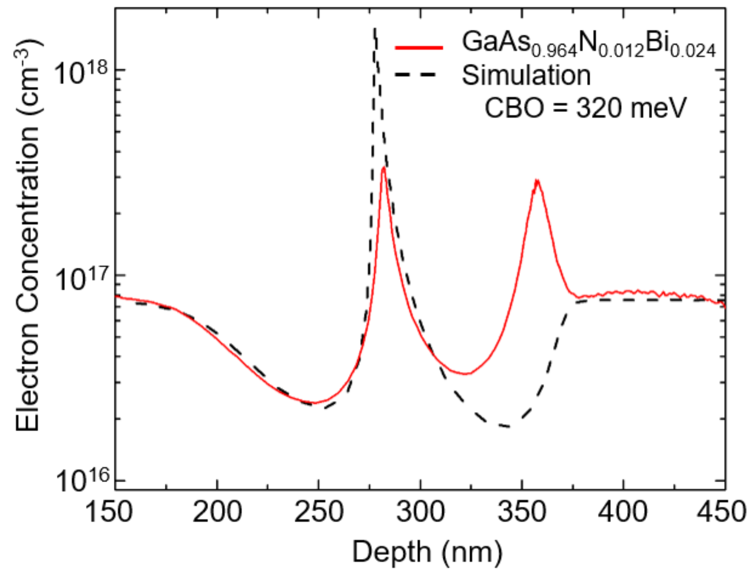

Figure 7.4 Profile of the carrier concentration versus depth from the top Schottky contact of the structure shown in Figure 7.3, determined from capacitance-voltage measurements as described in Appendix G. The dashed black line shows a simulated carrier concentration profile from one-dimensional Schrödinger-Poisson calculations, assuming a conduction band offset (CBO) of 320 meV between GaAs and $GaAs_{0.964}N_{0.012}Bi_{0.024}$.

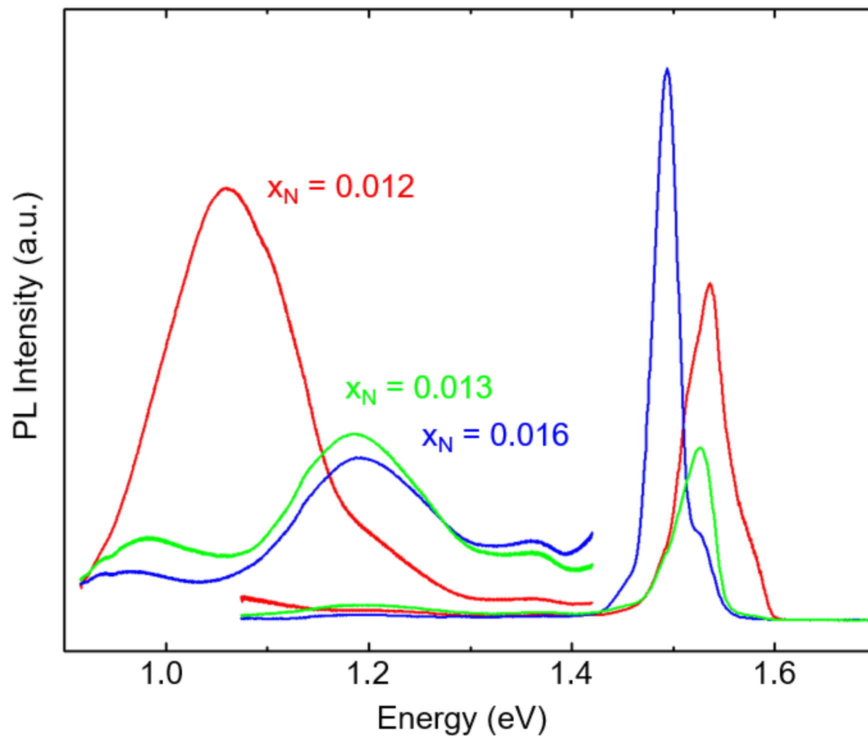

Figure 7.5 Photoluminescence (PL) spectra of GaAs/GaAsNBi/GaAs single quantum well (QW) structures at 4 K, with Bi fraction $y_{Bi} = 0.024$ and N fractions $x_N = 0.012$, 0.013, and 0.016. Emission from GaAs is apparent near 1.5 eV, with multiple features at lower energy associated with emission from the QWs.

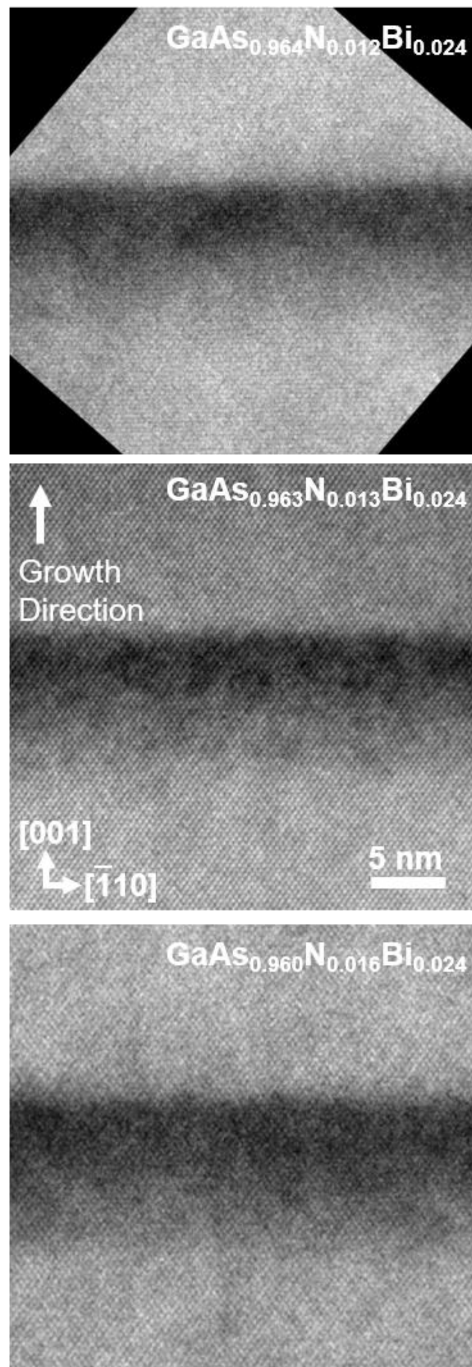

Figure 7.6 High-resolution transmission electron microscopy images collected along the [110] zone axis from GaAs/GaAsNBi/GaAs single quantum well (QW) structures with Bi fraction y_{Bi} = 0.024 and N fractions x_N = 0.012, 0.013, and 0.016. Graded contrast in the lower half of the QWs suggests compositional grading.

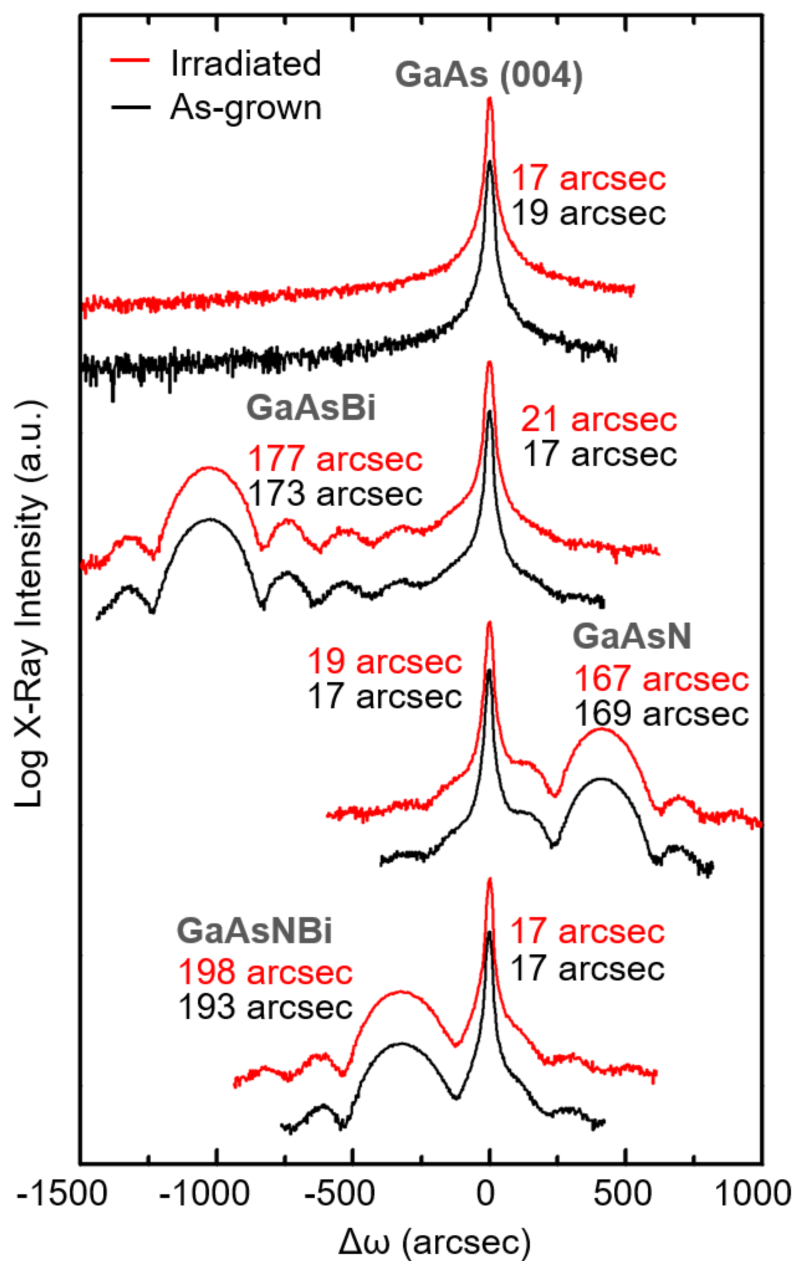

Figure 7.7 (004) high-resolution x-ray rocking curves for $GaAs_{1-x-y}N_xBi_y$ films collected before and after ultraviolet irradiation. For all plots, the GaAs substrate peak is set to $\Delta\omega = 0$ arcseconds to facilitate comparison of $\Delta\omega$ between substrate and epilayer. The full width at half maximum (FWHM) is listed next to each peak. No significant change in the peak FWHM or positions is apparent after irradiation.

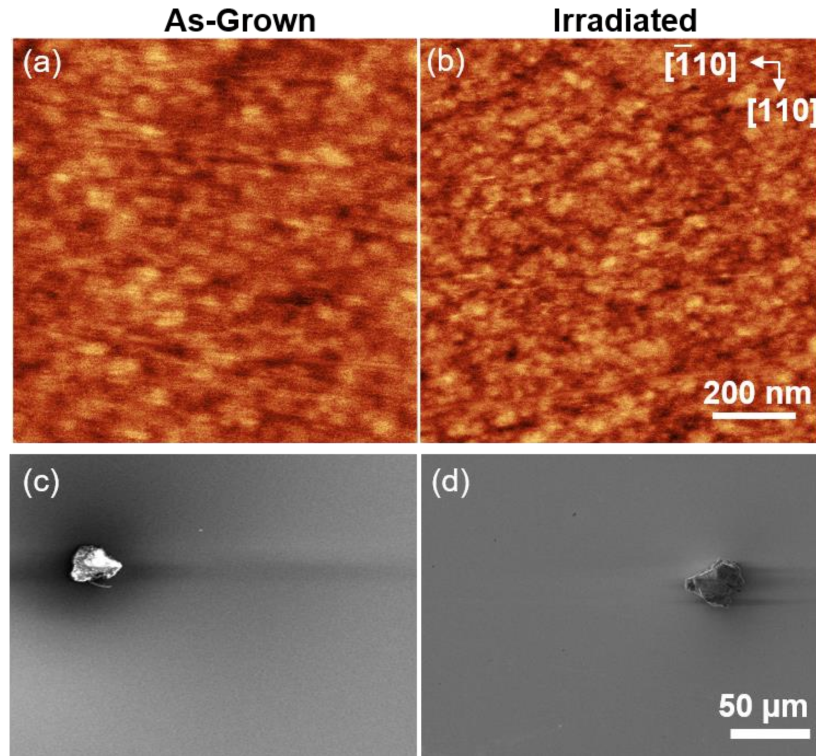

Figure 7.8 Atomic force microscopy images of a GaAsNBi film collected (a) before and (b) after ultraviolet irradiation. The surface morphology and root mean square roughness, $R_q = 0.3$nm, are not significantly changed following irradiation. To confirm the of absence of µm-sized surface droplets, SEM images were collected for areas of approximately 200 µm x 250 µm, as shown in (c)-(d). Features associated with dust were included to demonstrate that the images are in focus; the surfaces are otherwise featureless, without droplets.

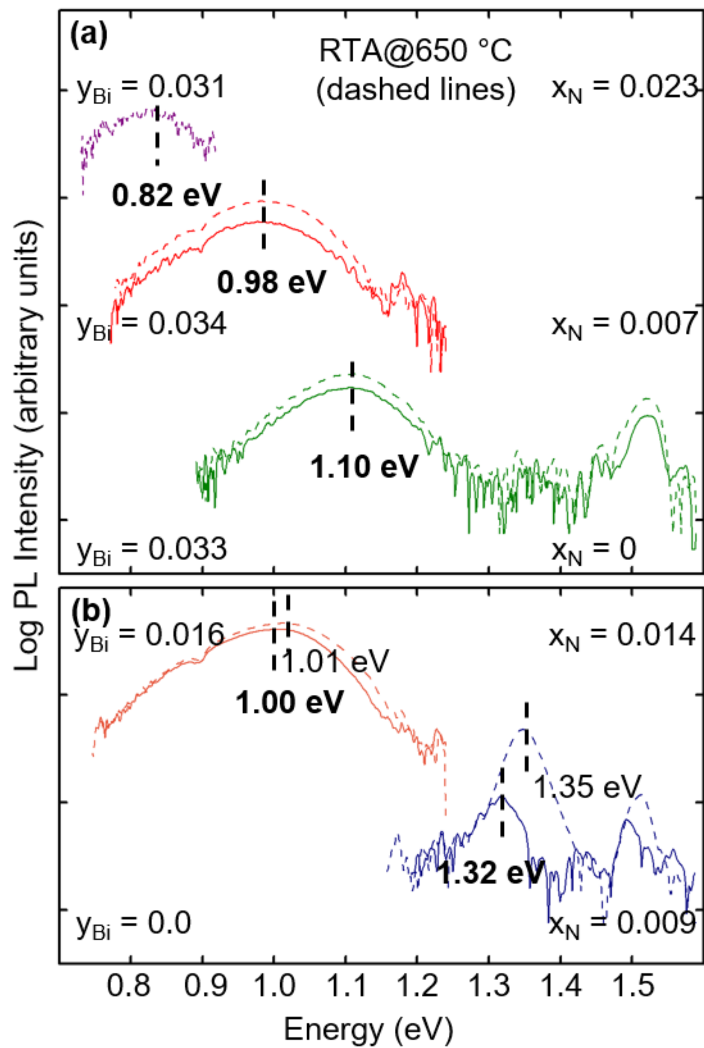

Figure 7.9 Photoluminescence (PL) spectra collected at 7 K for $GaAs_{1-x-y}N_xBi_y$ films from (a) the N flux series and (b) the Bi flux series, both as-grown (solid lines) and following rapid thermal annealing (RTA) for 60 s at 650 °C (dashed lines). For GaAsNBi films, a small increase in the PL peak intensity is observed following RTA, with negligible change in peak position. For the GaAsN film (y_{Bi} = 0), the RTA-induced enhancement in PL intensity is significantly larger and is accompanied by an increase in PL peak energy, suggesting that the presence of Bi modifies the influence of annealing on luminescence. Further discussion of the as-grown film spectra is found in Section 6.7.

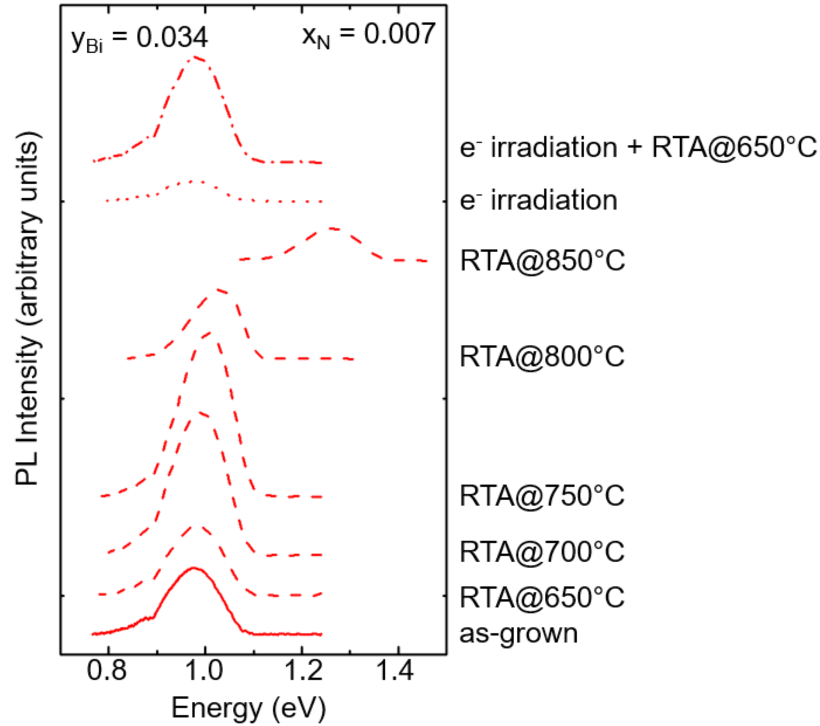

Figure 7.10 Photoluminescence (PL) spectra collected at 7 K from a GaAsNBi film, both as grown as well as following post-growth rapid thermal annealing (RTA) and/or electron irradiation. The PL peak intensity increases with RTA temperature up to 750°C and then decreases. The peak energy increases slightly up to 750°C, with a significant blue-shift for RTA temperature > 750°C. For electron irradiation alone, the PL intensity is reduced compared to the spectrum of the as-grown film. However, for electron irradiation plus RTA at 650 °C, the PL intensity is greater than that of the film that received only RTA at 650 °C, and negligible blue-shift is observed.

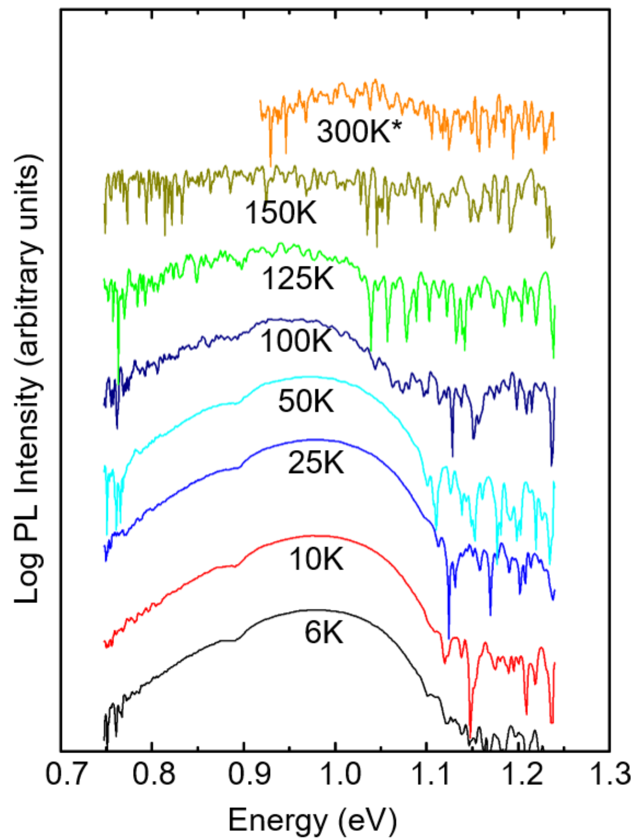

Figure 7.11 Photoluminescence (PL) spectra collected from a $GaAs_{0.959}N_{0.007}Bi_{0.034}$ film at temperatures ranging from 6 to 300 K, following electron irradiation and rapid thermal annealing (RTA) at 650°C for 1 min. The excitation power was 100 mW for spectra from 6K to 150K and 300 mW for 300K. The PL peak energy decreases with increasing temperature from 6K to 150K and then increases at 300K, suggesting the low temperature emission is produced by localized states. For comparison, PL spectra from the same film as-grown are shown in Figure 6.5, where the peak cannot be resolved above 100K.

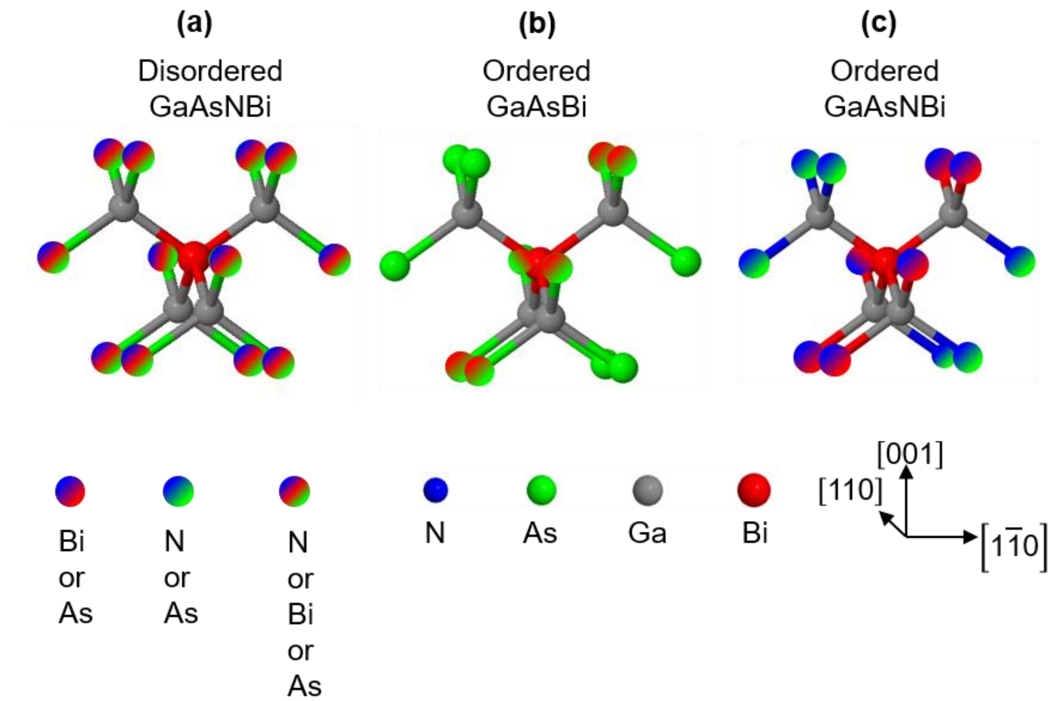

Figure 7.12 First- and second-nearest-neighbor local atomic environments, viewed down the [110] direction, for a Bi solute atom in (a) disordered GaAsNBi, (b) ordered GaAsBi, and (c) ordered GaAsNBi. In the ordered GaAsNBi (GaAsBi) structure, atoms are arranged in alternating GaAsN (GaAs) and GaAsBi $(\bar{1}11)$ planes, as discussed in Section 5.7.

7.4 References

[1] M.D. Pashley, K.W. Haberern, and J.M. Gaines, "Scanning Tunneling Microscopy Comparison of GaAs(001) Vicinal Surfaces Grown by Molecular Beam Epitaxy", Appl. Phys. Lett. 58, 406 (1991).

[2] R.L. Forrest, T.D. Golding, S.C. Moss, Y. Zhang, J.F. Geisz, J.M. Olson, A. Mascarenhas, P. Ernst, and C. Geng, "X-Ray Diffraction and Excitation Photoluminescence Analysis of Ordered GaInP", Phys. Rev. B 58, 15355 (1998).

[3] B.A. Philips, A.G. Norman, T.Y. Seong, S. Mahajan, G.R. Booker, M. Skowronski, J.P. Harbison, and V.G. Keramidas, "Mechanism for CuPt-Type Ordering in Mixed III–V Epitaxial Layers", J. Cryst. Growth 140, 249 (1994).

[4] S.J. Sweeney and S.R. Jin, "Bismide-Nitride Alloys: Promising for Efficient Light Emitting Devices in the near- and Mid-Infrared", J. Appl. Phys. 113, 043110 (2013).

[5] W. Shan, W. Walukiewicz, J. Ager, E. Haller, J. Geisz, D. Friedman, J. Olson, and S. Kurtz, "Band Anticrossing in GaInNAs Alloys", Phys. Rev. Lett. 82, 1221 (1999).

[6] K. Alberi, O.D. Dubon, W. Walukiewicz, K.M. Yu, K. Bertulis, and A. Krotkus, "Valence Band Anticrossing in GaBixAs1−x", Appl. Phys. Lett. 91, 051909 (2007).

[7] C.A. Broderick, M. Usman, S.J. Sweeney, and E.P. O'Reilly, "Band Engineering in Dilute Nitride and Bismide Semiconductor Lasers", Semicon. Sci. Tech. 27, 094011 (2012).

[8] J. Hwang and J.D. Phillips, "Band Structure of Strain-Balanced GaAsBi/GaAsN Superlattices on GaAs", Phys. Rev. B 83, 195327 (2011).

[9] C.A. Broderick, S. Jin, I.P. Marko, K. Hild, P. Ludewig, Z.L. Bushell, W. Stolz, J.M. Rorison, E.P. O'Reilly, K. Volz, and S.J. Sweeney, "GaAs1−xBix/GaNyAs1−y Type-II Quantum Wells: Novel Strain-Balanced Heterostructures for GaAs-Based near- and Mid-Infrared Photonics", Sci. Rep. 7, 46371 (2017).

[10] P. Krispin, S.G. Spruytte, J.S. Harris, and K.H. Ploog, "Admittance Dispersion of N-Type GaAs/Ga(As, N)/GaAs Heterostructures Grown by Molecular Beam Epitaxy", J. Appl. Phys. 90, 2405 (2001).

[11] J.S. Rimmer, B. Hamilton, P. Dawson, M. Missous, and A.R. Peaker, "Correlation between Optical Spectroscopy and Capacitance-voltage Profile Simulation Applied to Interface States in Multilayer GaAs/AlGaAs Heterostructures", J. Appl. Phys. 73, 5032 (1993).

[12] L.C. Kimerling, "Deep Traps at GaAs/GaAs Interface Grown by MBE-Interruption Growth Technique", J.Appl. Phys. 45, 1839 (1974).

[13] F. Wakaya, T. Matsubara, M. Nakayama, J. Yanagisawa, Y. Yuba, S. Takaoka, K. Murase, and K. Gamo, "Interface States Induced in GaAs by Growth Interruption during an in Situ Process", J. Vac. Sci. Technol. B 16, 2313 (1998).

[14] F. Wakaya, T. Matsubara, M. Nakayama, J. Yanagisawa, Y. Yuba, S. Takaoka, K. Murase, K. Gamo, and K. Gamo, "Effects of Growth Interruption in In-Situ Process for Buried Quantum Structures", Microelectron. Eng. 41–42, 591 (1998).

[15] M. Kaniewska and O. Engström, "Deep Traps at GaAs/GaAs Interface Grown by MBE-Interruption Growth Technique", Mat. Sci. Eng. C 27, 1069 (2007).

[16] M.-A. Pinault and E. Tournié, "On the Origin of Carrier Localization in Ga1−xInxNyAs1−y/GaAs Quantum Wells", Appl. Phys. Lett. 78, 1562 (2001).

[17] R. Kudrawiec, M. Syperek, P. Poloczek, J. Misiewicz, R.H. Mari, M. Shafi, M. Henini, Y.G. Gobato, S.V. Novikov, J. Ibáñez, M. Schmidbauer, and S.I. Molina, "Carrier Localization in GaBiAs Probed by Photomodulated Transmittance and Photoluminescence", J. Appl. Phys. 106, 023518 (2009).

[18] S. Imhof, A. Thränhardt, A. Chernikov, M. Koch, N.S. Köster, K. Kolata, S. Chatterjee, S.W. Koch, X. Lu, S.R. Johnson, D.A. Beaton, T. Tiedje, and O. Rubel, "Clustering Effects in Ga(AsBi)", Appl. Phys. Lett. 96, 131115 (2010).

19 A.R. Mohmad, F. Bastiman, C.J. Hunter, R.D. Richards, S.J. Sweeney, J.S. Ng, J.P.R. David, and B.Y. Majlis, "Localization Effects and Band Gap of GaAsBi Alloys: Localization Effects and Band Gap of GaAsBi Alloys", Phys. Status Solidi B 251, 1276 (2014).

20 T. Wilson, N.P. Hylton, Y. Harada, P. Pearce, D. Alonso-Álvarez, A. Mellor, R.D. Richards, J.P.R. David, and N.J. Ekins-Daukes, "Assessing the Nature of the Distribution of Localised States in Bulk GaAsBi", Sci. Rep. 8, 6457 (2018).

21 X. Lu, D.A. Beaton, R.B. Lewis, T. Tiedje, and M.B. Whitwick, 192110 (2008). 1. Lu, X., Beaton, D. A., Lewis, R. B., Tiedje, T., and Whitwick, M. B. "Effect of Molecular Beam Epitaxy Growth Conditions on the Bi Content of GaAs1−xBix", Appl. Phys. Lett. 92, 192110 (2008).

22 R.B. Lewis, M. Masnadi-Shirazi, and T. Tiedje, "Growth of High Bi Concentration GaAs 1−x Bi x by Molecular Beam Epitaxy", Appl. Phys. Lett. 101, 082112 (2012).

23 D.A. Beaton, A. Mascarenhas, and K. Alberi, "Insight into the Epitaxial Growth of High Optical Quality GaAs1–XBix", J. Appl. Phys. 118, 235701 (2015).

24 S.G. Spruytte, C.W. Coldren, J.S. Harris, W. Wampler, P. Krispin, K. Ploog, and M.C. Larson, "Incorporation of Nitrogen in Nitride-Arsenides: Origin of Improved Luminescence Efficiency after Anneal", J. Appl. Phys. 89, 4401 (2001).

[25] Y. Jin, R.M. Jock, H. Cheng, Y. He, A.M. Mintarov, Y. Wang, C. Kurdak, J.L. Merz, and R.S. Goldman, “Influence of N Interstitials on the Electronic Properties of GaAsN Alloys”, Appl. Phys. Lett. 95, 062109 (2009).

[26] R.L. Field, Y. Jin, H. Cheng, T. Dannecker, R.M. Jock, Y.Q. Wang, C. Kurdak, and R.S. Goldman, “Influence of N Incorporation on Persistent Photoconductivity in GaAsN Alloys”, Phys. Rev. B 87, 155303 (2013).

[27] T. Jen, "Ion Beam Analysis of Solute Incorporation in GaAsN and GaAsNBi Alloys", Ph.D Thesis, University of Michigan, 2017, p. 80-94.

[28] Y. Jin, Y. He, H. Cheng, R.M. Jock, T. Dannecker, M. Reason, A.M. Mintairov, C. Kurdak, J.L. Merz, and R.S. Goldman, “Influence of Si–N Complexes on the Electronic Properties of GaAsN Alloys”, Appl. Phys. Lett. 95, 092109 (2009).

[29] V. Lordi, H.B. Yuen, S.R. Bank, M.A. Wistey, J.S. Harris, and S. Friedrich, “Nearest-Neighbor Distributions in Ga1−xInxNyAs1−y and Ga1−xInxNyAs1−y−zSb z Thin Films upon Annealing”, Phys. Rev. B 71, 125309 (2005).

[30] E.-M. Pavelescu, A. Gheorghiu, M. Dumitrescu, A. Tukiainen, T. Jouhti, T. Hakkarainen, R. Kudrawiec, J. Andrzejewski, J. Misiewicz, N. Tkachenko, V.D.S. Dhaka, H. Lemmetyinen, and M. Pessa, “Electron-Irradiation Enhanced Photoluminescence from GaInNAs⁄GaAs Quantum Wells Subject to Thermal Annealing”, Appl. Phys. Lett. 85, 6158 (2004).

[31] E.-M. Pavelescu, R. Kudrawiec, N. Bălţăţeanu, S. Spânulescu, M. Dumitrescu, and M. Guina, “Enhancement in Photoluminescence from 1 EV GaInNAs Epilayers Subject to 7 MeV Electron Irradiation”, Semicon. Sci. Tech. 28, 025020 (2013).

[32] W. Li, M. Pessa, T. Ahlgren, and J. Decker, “Origin of Improved Luminescence Efficiency after Annealing of Ga(In)NAs Materials Grown by Molecular-Beam Epitaxy”, Appl. Phys. Lett. 79, 1094 (2001).

[33] J. Puustinen, M. Wu, E. Luna, A. Schramm, P. Laukkanen, M. Laitinen, T. Sajavaara, and M. Guina, Variation of Lattice Constant and Cluster Formation in GaAsBi”, J. Appl. Phys. 114, 243504 (2013).

[34] P. Gavrilovic, F.P. Dabkowski, K. Meehan, J.E. Williams, W. Stutius, K.C. Hsieh, N. Holonyak, M.A. Shahid, and S. Mahajan, “Disordering of the Ordered Structure in MOCVD-Grown GaInP and AlGaInP by Impurity Diffusion and Thermal Annealing”, J. Cryst. Growth 93, 426 (1988).

[35] D.A. Beaton, C. Sanders, and K. Alberi, “Effects of Incident UV Light on the Surface Morphology of MBE Grown GaAs”, J. Cryst. Growth 413, 76 (2015).

[36] C.E. Sanders, D.A. Beaton, R.C. Reedy, and K. Alberi, “Fermi Energy Tuning with Light to Control Doping Profiles during Epitaxy”, Appl. Phys. Lett. 106, 182105 (2015).

[37] D.A. Beaton, M. Steger, T. Christian, and A. Mascarenhas, “Effects of In-Situ UV Irradiation on the Uniformity and Optical Properties of GaAsBi Epi-Layers Grown by MBE”, J. Cryst. Growth 484, 7 (2018).

[38] G. Fisicaro, M. Italia, V. Privitera, G. Piccitto, K. Huet, J. Venturini, and A. La Magna, “Dopant Activation and Damage Evolution in Implanted Silicon after Excimer Laser Annealing”, Phys. Status Solidi C 8, 940 (2011).

[39] F. Cristiano, M. Shayesteh, R. Duffy, K. Huet, F. Mazzamuto, Y. Qiu, M. Quillec, H.H. Henrichsen, P.F. Nielsen, D.H. Petersen, A. La Magna, G. Caruso, and S. Boninelli, “Defect Evolution and Dopant Activation in Laser Annealed Si and Ge”, Mat. Sci. Semicon. Proc. 42, 188 (2016).

[40] S. Imhof, A. Thränhardt, A. Chernikov, M. Koch, N.S. Köster, K. Kolata, S. Chatterjee, S.W. Koch, X. Lu, S.R. Johnson, D.A. Beaton, T. Tiedje, and O. Rubel, “Clustering Effects in Ga(AsBi)”, Appl. Phys. Lett. 96, 131115 (2010).

[41] T. Wilson, N.P. Hylton, Y. Harada, P. Pearce, D. Alonso-Álvarez, A. Mellor, R.D. Richards, J.P.R. David, and N.J. Ekins-Daukes, “Assessing the Nature of the Distribution of Localised States in Bulk GaAsBi”, Sci. Rep. 8, 6457 (2018).

[42] J. Wang, B. Lukose, M.O. Thompson, and P. Clancy, “*Ab Initio* Modeling of Vacancies, Antisites, and Si Dopants in Ordered InGaAs”, J. Appl. Phys. 121, 045106 (2017).

[43] P.S. Branicio, J.P. Rino, F. Shimojo, R.K. Kalia, A. Nakano, and P. Vashishta, “Molecular Dynamics Study of Structural, Mechanical, and Vibrational Properties of Crystalline and Amorphous Ga1−xInxAs Alloys”, J. Appl. Phys. 94, 3840 (2003).

[44] S.R. Kurtz, A.A. Allerman, C.H. Seager, R.M. Sieg, and E.D. Jones, “Minority Carrier Diffusion, Defects, and Localization in InGaAsN, with 2% Nitrogen”, Appl. Phys. Lett. 77, 400 (2000).

[45] M. Reason, Y. Jin, H.A. McKay, N. Mangan, D. Mao, R.S. Goldman, X. Bai, and C. Kurdak, “Influence of N on the Electronic Properties of GaAsN Alloy Films and Heterostructures”, J. Appl. Phys. 102, 103710 (2007).

[46] D.G. Cooke, F.A. Hegmann, E.C. Young, and T. Tiedje, “Electron Mobility in Dilute GaAs Bismide and Nitride Alloys Measured by Time-Resolved Terahertz Spectroscopy”, Appl. Phys. Lett. 89, 122103 (2006).

[47] A. Chin, T.Y. Chang, A. Ourmazd, and E.M. Monberg, “Partial Ordering and Enhanced Mobility in $Ga_{0.47}In_{0.53}As$ Grown on Vicinal (110)InP”, Appl. Phys. Lett. 58, 968 (1991).

[48] Y. Nakata, O. Ueda, and T. Fujii, “High Two-Dimensional Electron Gas Mobility Enhanced by Ordering in InGaAs/N-InAlAs Heterostructures Grown on (110)-Oriented InP Substrates by Molecular Beam Epitaxy”, Jpn. J. Appl. Phys. 30, L249 (1991).

[49] P. Ramvall, N. Carlsson, P. Omling, L. Samuelson, W. Seifert, M. Stolze, and Q. Wang, "$Ga_{0.25}In_{0.75}As$/InP Quantum Wells with Extremely High and Anisotropic Two-dimensional Electron Gas Mobilities", Appl. Phys. Lett. 68, 1111 (1996).

[50] L. Chernyak, A. Osinsky, H. Temkin, A. Mintairov, I.G. Malkina, B.N. Zvonkov, and Y.N. Saf'anov, "Transport Anisotropy in Spontaneously Ordered GaInP2 Alloys", Appl. Phys. Lett. 70, 2425 (1997).

[51] N.M. Haegel, T.J. Mills, M. Talmadge, C. Scandrett, C.L. Frenzen, H. Yoon, C.M. Fetzer, and R.R. King, "Direct Imaging of Anisotropic Minority-Carrier Diffusion in Ordered GaInP", J. Appl. Phys. 105, 023711 (2009).

[52] Y. Guan, K. Forghani, H. Kim, S.E. Babcock, L.J. Mawst, and T.F. Kuech, "Surface Kinetics Study of Metal-Organic Vapor Phase Epitaxy of GaAs1−yBiy on Offcut and Mesa-Patterned GaAs Substrates", J. Cryst. Growth 464, 39-48 (2017).

Appendix A

Temperature Calibration for $T \ll 580$ °C

In this appendix, we describe the calibration used to relate the CAR thermocouple reading, T_{CAR}, and the pyrometer reading, T_{pyro}, in the Gen II MBE system, enabling measurement of substrate temperatures below the pyrometer's lower detection limit of 400°C. The T_{CAR}-T_{pyro} calibration is performed only after calibration of the pyrometer emissivity, as described in Section 2.2.4. Following oxide desorption, as described in Section 2.2.4, the temperature was decreased from the oxide desorption temperature (typically 600°C) to 450°C in steps of 20-50°C, and both T_{CAR} and T_{pyro} were recorded at each step. Next, T_{pyro} was plotted versus $T_{CAR,}$ and a linear least squares fit was used to express T_{pyro} as a function of T_{CAR}, as shown in Figure A.1. The T_{CAR}-T_{pyro} calibration was performed for each molybdenum block used, yielding a similar slope for all blocks but different y-offsets. For substrate temperatures $T_{sub} > 400$°C, T_{pyro} was considered to accurately represent T_{sub}. For $T_{sub} < 400$°C, T_{sub} was determined from T_{CAR} using an extrapolation of the linear relationship between T_{CAR} and T_{pyro}.

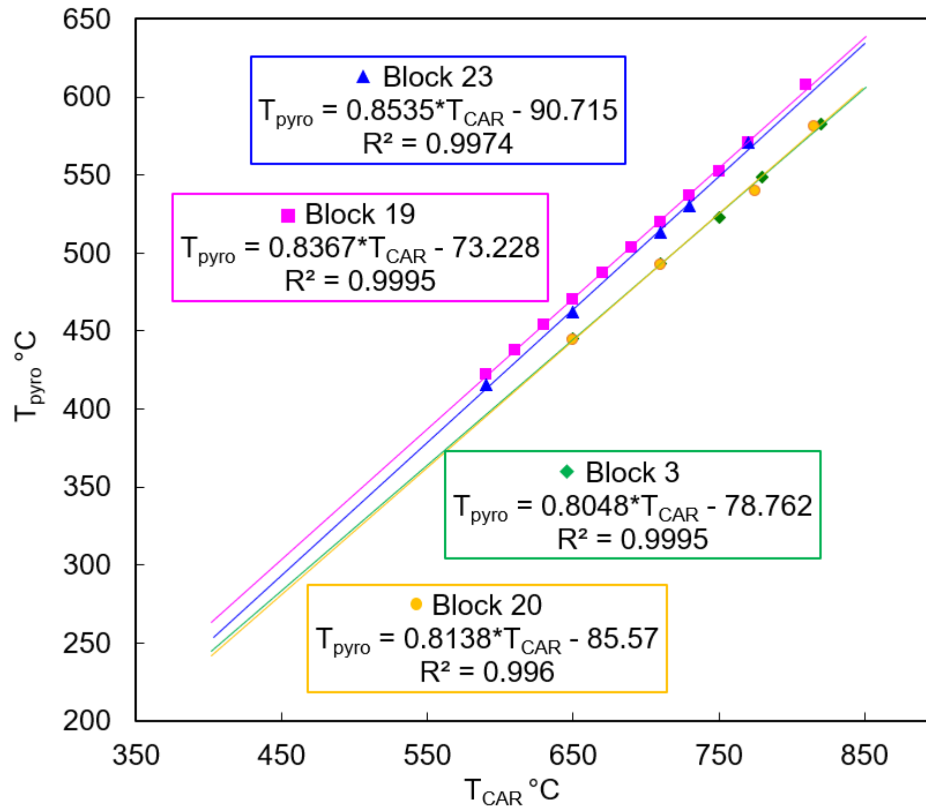

Figure A.1 Pyrometer reading, T_{pyro}, versus CAR thermocouple reading, T_{CAR}, recorded for four molybdenum blocks in the Gen II MBE system. Solid lines represent linear least squares fits to the data points for each block. For substrate temperatures $T_{sub} > 400°C$, T_{pyro} was considered to accurately represent T_{sub}. For $T_{sub} < 400°C$, T_{sub} was determined from T_{CAR} using an extrapolation of the linear relationship between T_{CAR} and T_{pyro}.

Appendix B

Doping Calibration

During MBE growth of doped epilayers, the temperature of the dopant cell is selected to achieve the desired free carrier concentration based on a doping calibration performed on doped GaAs control films. The doping calibration for the silicon dopant cell used to dope the films discussed in Ch. 3, performed in 2013, is described in this appendix. Three control films were grown, using Si cell temperatures of 1050, 1150, and 1250 °C. Each control film consisted of 500 nm of GaAs:Si on a semi-insulating GaAs (001) substrate. Samples were prepared in the van der Pauw geometry, and Hall effect measurements were performed at room temperature as described in Section 2.4. Following determination of the free carrier concentration in each GaAs:Si film, the natural logarithm of the carrier concentration was plotted versus the reciprocal of the Si cell temperature, as shown in Figure B.1, and a linear fit was used to determine the Si cell temperature required to achieve a targeted carrier concentration in future growth of doped films. The Si cell temperatures and free carrier concentrations are tabulated in Table H.3 of Appendix H.

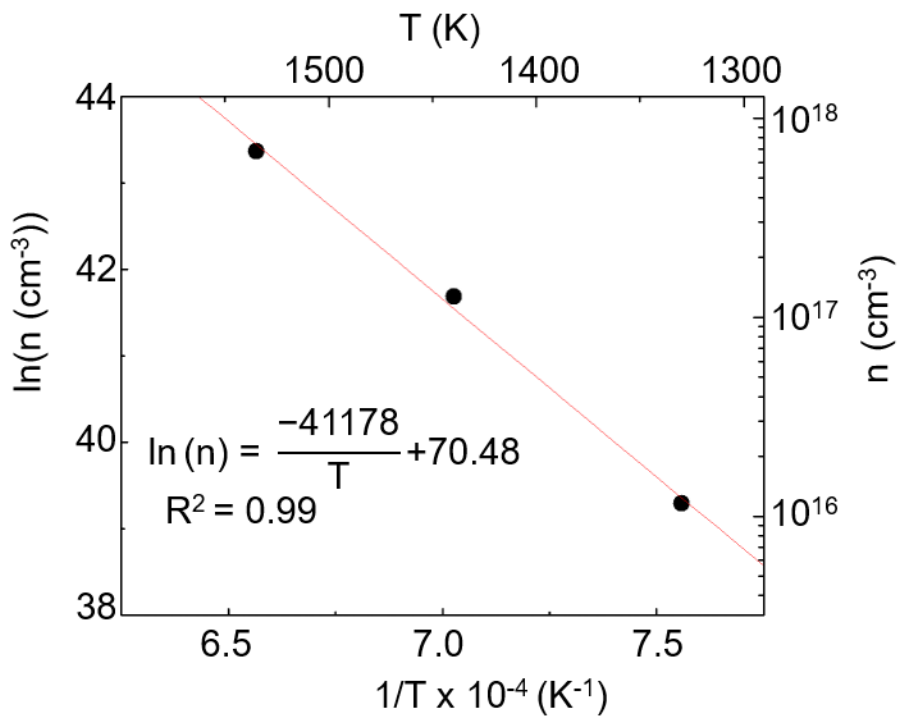

Figure B.1 Natural logarithm of free carrier concentration, *n*, versus reciprocal Si cell temperature, *T*, for three GaAs:Si films. The corresponding temperature and free carrier concentration are shown on the top y-axis and right x-axis, respectively. The solid line is a linear fit to the data extrapolated to fill the full plot range, used to determine the Si cell temperature required to achieve a targeted carrier concentration.

Appendix C

Depletion Correction for Hall Effect Measurements

C.1 Overview

For any semiconductor layer, carrier depletion occurs at the top surface and the layer/substrate interface. Therefore, proper interpretation of Hall measurements requires an iterative process. We initially assume the predicted layer thickness from growth rate calibrations to compute a corresponding carrier concentration from Hall measurements. We then calculate a depletion thickness corresponding to the initial carrier concentration and subtract the depletion thickness from the initial thickness. The depletion thickness, *l*, is calculated as a function of carrier concentration using the equation:[1]

$$l = \left[\frac{2\varepsilon_r\varepsilon_0(V_{BS} - kT/q)}{qn}\right]^{1/2} + \left[\frac{2\varepsilon_r\varepsilon_0(V_{BI} - kT/q)}{qn}\right]^{1/2} \qquad \text{(C.1)}$$

where n is the carrier concentration (cm^{-3}), V_{BS} and V_{BI} are the built-in potentials (V) at the surface and interface, respectively, $\varepsilon_r\varepsilon_0$ is the permittivity of GaAs (F/cm), k is the Boltzman constant (eV/K), q is the elementary charge (C), and T is temperature (K). The carrier concentration is then recalculated from the updated thickness, and the thickness/carrier concentration calculations are iterated until the value of the carrier concentration agrees with the value in the previous iteration to within 0.1%. The following

MATLAB script corrects the measured thickness, resistivity, carrier concentration, and carrier mobility for carrier depletion effects, following the method described in Ref. 1.

C.2 Depletion correction MATLAB script

```
%% File Information
% HallDeplCorrect.m

%% Read in parameters from Hall measurement
clear; close; clc;

filename = input('Enter the filename of the HallEffectCalculationSheet used for data collection: \n(File must be located in same folder as MATLAB script. Filename must be enclosed in single quotes and not include spaces) \n');

B = xlsread(filename,1,'B8'); % Magnetic field strength in Gauss
I_initial = xlsread(filename,1,'B9'); % Current supplied in Amps
roh_initial = xlsread(filename,1,'F23'); % intiial resistivity in Ohm-cm
mu_initial = xlsread(filename,1,'D44'); % intial free carrier mobility in cm^2/(V*s)
Z_initial = xlsread(filename,1,'B10'); % Nominal epilayer thickness in cm
n_initial = xlsread(filename,1,'D39'); % initial free carrier concentration in cm^-3

%% Define constants
eps0 = 8.854e-14; %vacuum permittivity in F/cm
epsr = 13; %relative permittivity for GaAs
q = 1.6e-19; %elementary charge in C
T = 300; %temperature in K
k = 8.617e-5; %Boltzmann constant in eV/K
Vbs = 0.6; %Built-in potential at surface in eV. Usually pinned at 0.6eV for GaAs
Vbi = 0.6; %Built-in potential at epilayer/substrate interface in eV.

%% Calculate depletion thickness
n = n_initial;
Z = Z_initial;
```

```
i = 0; %initial iteration count
n_previous = n*10; %arbitrary starting value for 'n_previous'
that won't end the while loop
compare = n*100; %arbitrary starting value for 'compare' that
won't end the while loop
display('Calculating...')
while abs(compare) > 0.001*n_previous
    i = i+1; %iteration counter
    n_previous = n;

    depl_surf     =     sqrt((2*eps0*epsr*(Vbs-k*T))/(q*n));
%thickness in cm depleted at epilayer surface
%      depl_int = sqrt((eps0*epsr*k*T)/(q*n)); %applies if n
>> trap concentration in substrate
    depl_int = sqrt((2*eps0*epsr*(Vbi-k*T))/(q*n)); %applies
if n << trap concentration in substrate
    depl_total = depl_surf + depl_int; %cm
    Z = Z_initial - depl_total; % adjusted thickness in cm of
conduction portion of epilayer
    roh = roh_initial*Z/Z_initial; %  adjusted resistivity in
Ohm-cm calculated using adjusted thickness
    mu = 1/(n*q*roh); %adjusted mobility
    n  =  n_initial*Z_initial/Z;  %  adjusted  free  carrier
concentration calculated using adjusted thickness

    compare = n-n_previous;

    fprintf('Iteration %i \n',i);
    fprintf('Z: %0.3g cm \n',Z);
    fprintf('n: %0.3g cm^-3 \n \n',n);
end

fprintf('%i iterations \n',i);
fprintf('Corrected electrically active thickness: %0.3g cm
\n',Z);
fprintf('Corrected free carrier concentration: %0.3g cm^-3
\n',n);
fprintf('Corrected resistivity: %0.3g Ohm-cm \n',roh);
fprintf('Corrected mobility: %0.5g cm^2/(V*s) \n',mu);
```

C.3 References

[1] A. Chandra, C.E.C. Wood, D.W. Woodard, and L.F. Eastman, “Surface and Interface Depletion Corrections to Free Carrier-Density Determinations by Hall Measurements”, Solid-State Electron. 22, 645 (1979).

Appendix D

N Interstitial Correction for XRC

In this appendix, we describe the method used to account for interstitial N in GaAsNBi films for which nuclear reaction analysis (NRA) data was not available.

We first consider seven films from the N flux series and Bi flux series in Ch. 4 and Ch. 6, for which both x-ray rocking curves (XRC) and NRA data are available. In Figure D.1, we plot N fractions determined from XRC as described in Section 2.3, x_{XRC}, with N fractions determined from NRA as described in Section 2.6, x_{NRA}. The red line represents a linear least-squares fit, with slope $x_{NRA}/x_{XRC} = 1.325$. Because x_{NRA} includes N in both substitutional and interstitial lattice sites, while x_{XRC} only includes substitutional N, we estimate the substitutional fraction, $f_{N\text{-}sub} = x_{XRC}/x_{NRA} = 0.75$. Therefore, to account for interstitial N in those samples for which only XRC data was available, we estimate a substitutional N fraction, $f_{N\text{-}sub} = 0.75$, which corresponds to multiplying x_{XRC} by a factor of 1.325. For the seven films considered here, substitutional N fractions determined from channeling NRA measurements range from 0.69 to 0.77.

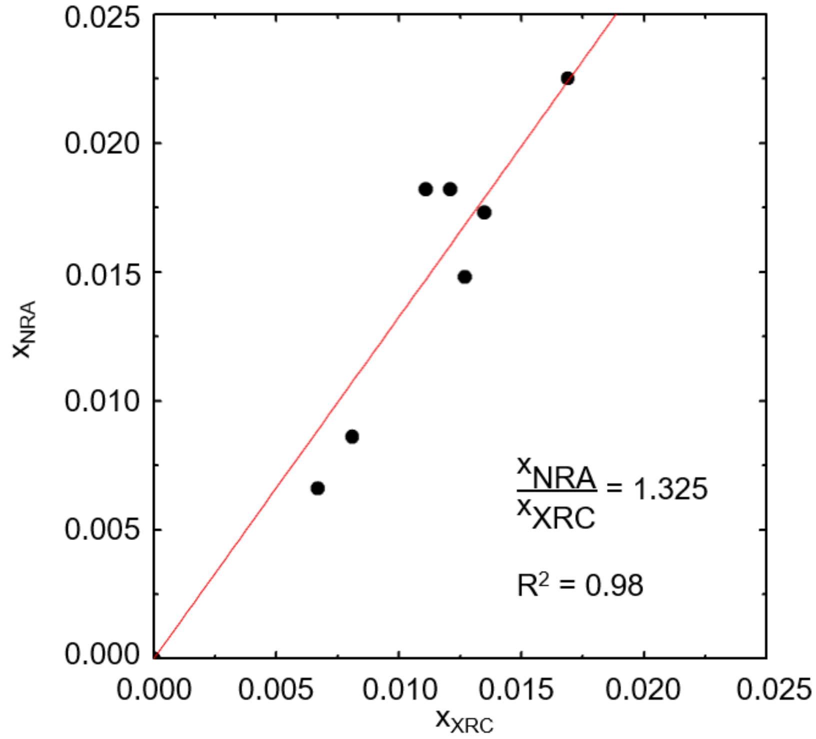

Figure D.1 Nitrogen fractions, x, determined from x-ray rocking curves (XRC) and nuclear reactional analysis (NRA). The red line is a linear least squares fit, with y-intercept fixed at zero to represent the case of a film with zero N, and slope x_{NRA}/x_{XRC} = 1.325. Therefore, to account for interstitial N in those samples for which only XRC data was available, we estimate a substitutional N fraction, $f_{N\text{-}sub}$ = 0.75, which corresponds to multiplying x_{XRC} by a factor of 1.325.

Appendix E

Substrate-Rotation-Induced Composition Modulations

E.1 Overview

In this section, we discuss observations of composition oscillations in the growth direction, termed "composition modulations" at off-rotation-center sample positions. First, we present selected area electron diffraction (SAD) patterns and dark-field transmission electron microscopy (TEM) images that reveal the compositional variations. We then discuss the combined roles of effusion cell configuration and substrate rotation on the formation of composition modulations.

E.2 TEM observations of composition modulations

Figure E.1 shows a SAD pattern collected along the $[\bar{1}10]$ direction for a GaAsNBi film grown at 260 °C in the Gen II MBE, showing {002}, {111}, and {220} reflections typical of a zincblende (ZB) lattice. Several of the ZB reflections are accompanied by a pair of satellite spots aligned along the [001] direction, indicating the presence of a periodic structure along the [001] direction in addition to the periodicity of the ZB lattice. An example of a pair of satellite spots is indicated by red arrows in Figure E.1. As shown by the red dashed lines, the spacing between a ZB reflection and one of its satellites is approximately one sixth the spacing between the (002) reflection and the direct beam,

corresponding to a periodicity of 1.71 nm for the structure giving rise to the satellite spot.[1] In addition, a (002) dark field TEM image of the same region of the GaAsNBi layer is presented in Figure E.2. Interestingly, an intensity modulation along the growth direction, with a period of ~1.7 nm, is apparent. Since the ZB (002) reflection is sensitive to changes in chemical composition,[2] the intensity modulation is likely due to a composition modulation.

E.3 Origin of composition modulations

As described in Figure 2.1, the effusion cell sources are directed at a 33° angle from the surface normal of the sample. Therefore, at a given instant in time, each source supplies a non-uniform flux distribution over the surface of the sample, such that different regions of the sample are exposed to different ratios of the coincident fluxes, as shown in Figure E.3.[3,4,5] To minimize non-uniformity in the sample composition resulting from these non-uniform flux distributions, samples are typically rotated during growth. While the sample is rotating, the composition is fixed in the vicinity of the rotation center, shown by a red dot in Figure E.3. However, at positions away from the rotation center, the relative fluxes of each species vary with time. For example, in Figure E.3, the In flux reaches a maximum when point A passes closest to the In source, and a minimum when A is furthest from the In source, repeating with each revolution of the substrate. The local In fraction at point A is thus modulated as the growth proceeds, with a modulation period equal to the thickness of material grown in the time required for one revolution of the sample.

The GaAsNBi layer shown in Figure E.1 and Figure E.2 was grown with a substrate rotation speed of 10 rpm and a growth rate of 1 μm/h. The expected rotation-induced

composition modulation would therefore have a period of *(6 s)/(1 revolution)* × *(1000 nm)/(3600 s) = 1.67 nm/revolution*. We therefore conclude that the periodic structure with period ~1.7 nm observed in SAD and (002) dark-field TEM is a composition modulation induced by the substrate rotation coupled with the non-uniform flux distributions of each source. The magnitude of the composition modulation is reduced at regions approaching the center of rotation of the sample, as shown in Figure E.4. A cross-sectional specimen taken from the same sample at a location closer to the rotation center does not show satellite spots. Thus, for measurements very sensitive to short-range composition non-uniformities, the sample pieces used should be taken from as close as possible to the center of rotation of the sample.

E.4 Figures

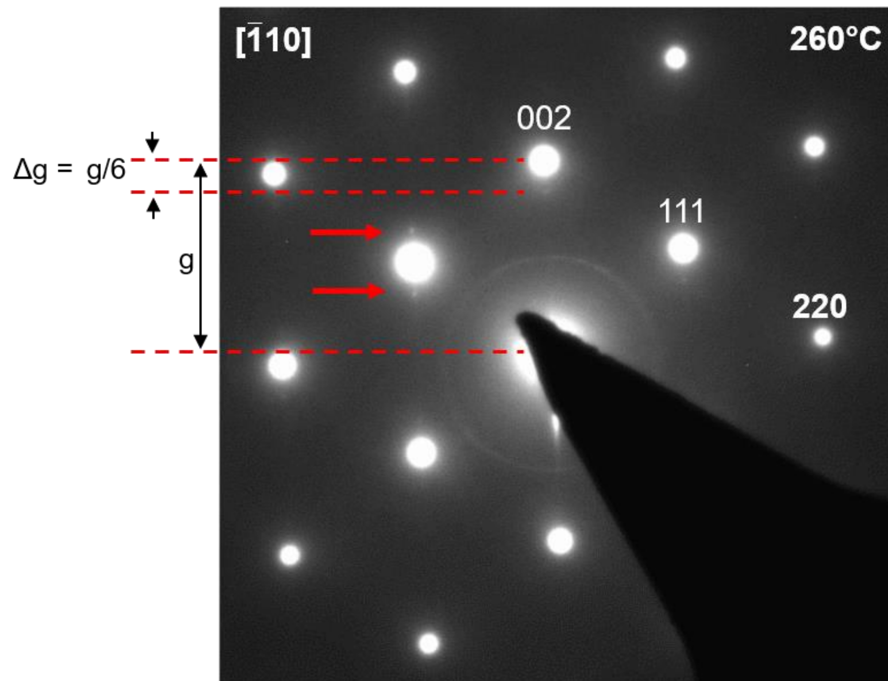

Figure E.1 Selected-area electron diffraction pattern collected along the $[\bar{1}10]$ direction from a GaAsNBi film grown with growth rate of 1 µm/h and substrate rotation speed of 10 rpm. Satellite spots along the [001] direction are indicated by red arrows. The spacing between each reflection and one of its satellite spots is one sixth of the (002) spacing.

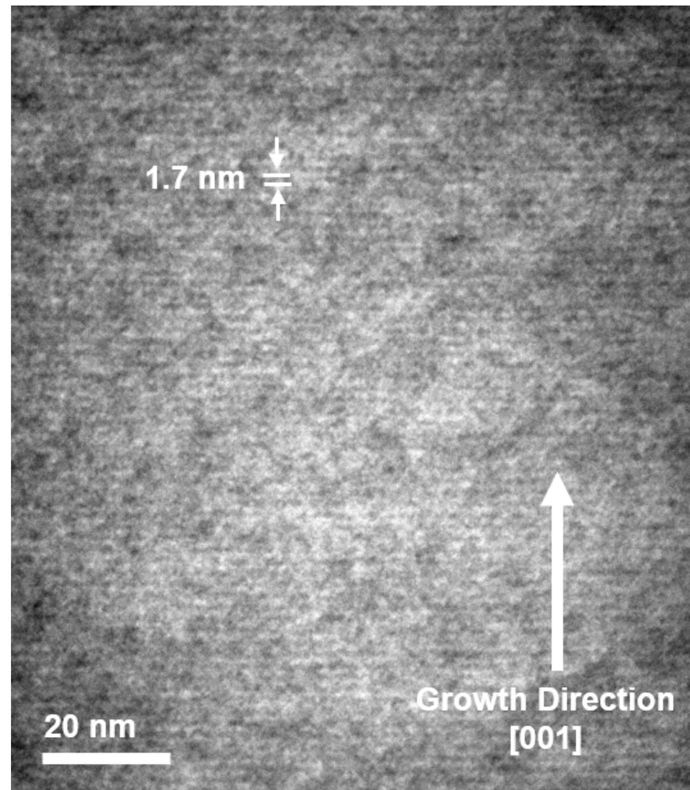

Figure E.2 Chemically-sensitive (002) dark field transmission electron microscopy collected from the film in Figure C.1, showing a composition modulation with period 1.7 nm along the growth direction.

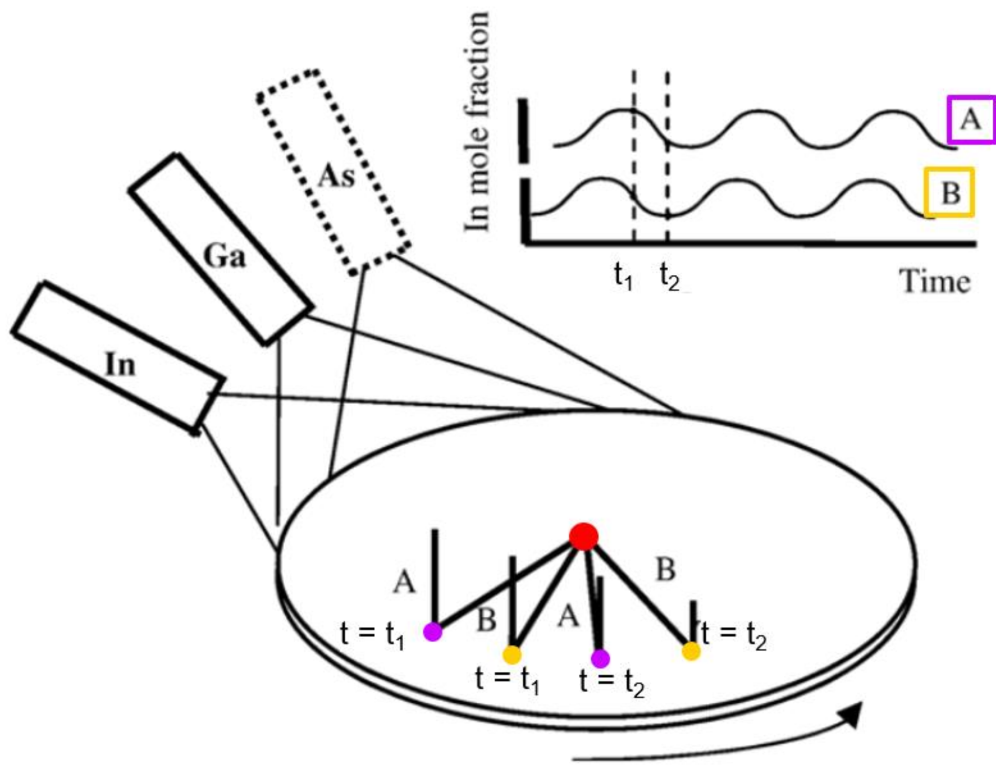

Figure E.3 Schematic showing the position-dependent and time-dependent flux variations as the sample is rotated during molecular-beam epitaxy. At the rotation center, indicated by the red dot, the relative fluxes are independent of time. However, at the off-rotation-center positions, the flux oscillates with a period corresponding to the sample rotation period. Therefore, oscillations in the composition, termed "composition modulations," are observed in the growth direction. Adapted and reprinted with permission from Ref. 4 (Copyright 2007, Elsevier).

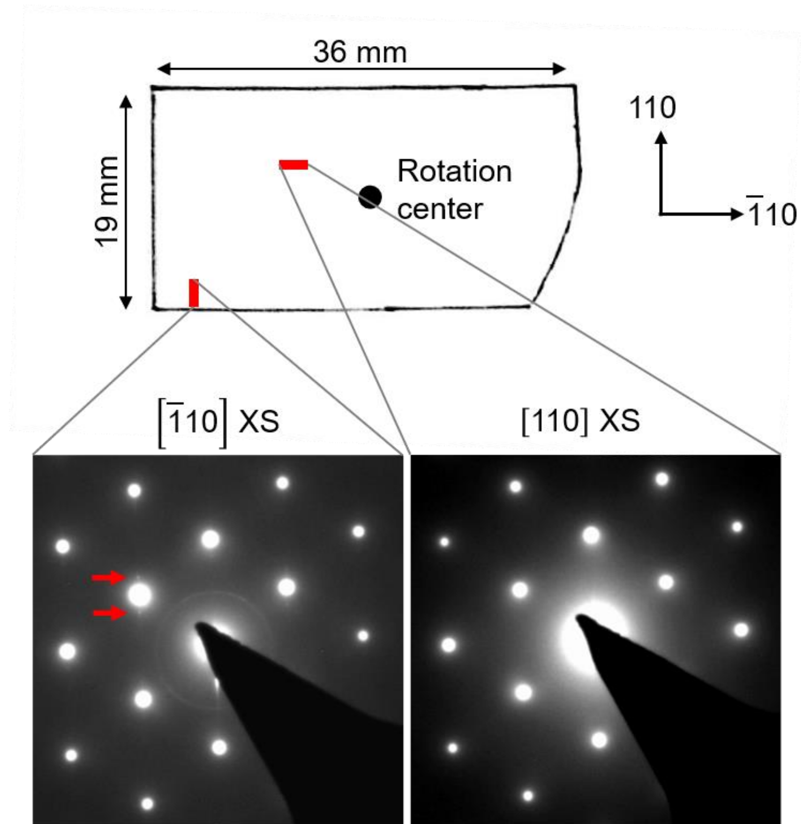

Figure E.4 Schematic of the sample from which the GaAsNBi cross-sectional specimen shown in Figs. C.1 and C.2 was taken. Another specimen taken from the same sample at a location closer to the center of rotation does not exhibit satellite spots corresponding to substrate rotation-induced composition modulation. Relative locations of each specimen are indicated by red bars on the sample schematic.

E.5 References

[1] A.G. Norman and G.R. Booker, "Transmission Electron Microscope and Transmission Electron Diffraction Observations of Alloy Clustering in Liquid-phase Epitaxial (001) GaInAsP Layers", J. Appl. Phys. 57, 4715 (1985).

[2] P.M. Petroff, "Transmission Electron Microscopy of Interfaces in III–V Compound Semiconductors", J. Vac. Sci. Technol. 14, 973 (1977).

[3] S.N.G. Chu, N. Chand, D.L. Sivco, and A.T. Macrander, "Substrate Rotation-induced Composition Modulation in Epitaxial AlGaAs Grown by Molecular-beam Epitaxy", J. Appl. Phys. 65, 3838 (1989).

[4] W.L. Sarney and S.P. Svensson, "Characterization of Compositional Oscillations in InGaAs Films Induced by MBE Cell Configuration and Substrate Rotation", Materials Charact. 58, 284 (2007).

[5] Z.R. Wasilewski, "Studies and Modeling of Growth Uniformity in Molecular Beam Epitaxy", J. Vac. Sci. Technol. B 9, 120 (1991).

Appendix F

FFT Analysis of Ordered Domain Sizes

The distribution of ordered domain sizes in Ch. 5 was quantified through analysis of several high-resolution scanning transmission electron microscope (STEM) images, spanning an area > 4000 nm^2, using the following procedure. For each HAADF STEM image, we performed a fast Fourier transform (FFT) using Gatan DigitalMicrograph, which resulted in both spots corresponding to the zincblende (ZB) lattice and spots at the ½$(1\bar{1}1)$ and ½$(\bar{1}11)$ positions, corresponding to the doubling in periodicity in the $[1\bar{1}1]$ and $[\bar{1}11]$ directions. Figure F.1(b) shows the FFT of the high-resolution STEM image in Figure F.1(a), with both ZB spots, as well as spots at the ½$(1\bar{1}1)$ and ½$(\bar{1}11)$ positions apparent. Next, we used twin-oval masks to select each conjugate pair of ½$(1\bar{1}1)$ and ½$(\bar{1}11)$ spots, circled in blue and green, respectively, in Figure F.1(b), and performed inverse FFTs to emphasize the $(1\bar{1}1)$ and $(\bar{1}11)$ ordered variants. Figure F.2(a) and Figure F.2(b) show the twin-oval mask selections for the ½$(\bar{1}11)$ and ½$(1\bar{1}1)$ spots, with the resulting inverse FFTs shown in Figure F.2(c) and Figure F.2(d). For each inverse FFT image, we included pixels near the top (18 ± 6%) and bottom (18 ± 7%) of the total grayscale range, with thresholds selected to exclude the GaAs regions. Figure F.2(e) and Figure F.2(f) show the inverse FFT images following application of thresholds to the top and bottom of the total grayscale ranges, where we consider each region with stripes of dark contrast to be an ordered

domain. We used the "dilate" function in ImageJ to merge the stripes of contrast in each domain into a continuous region, as shown in Figure F.2(g) and Figure F.2(h). Subsequently, the "analyze particles" function was used to calculate the area of each domain in the [110] projection.

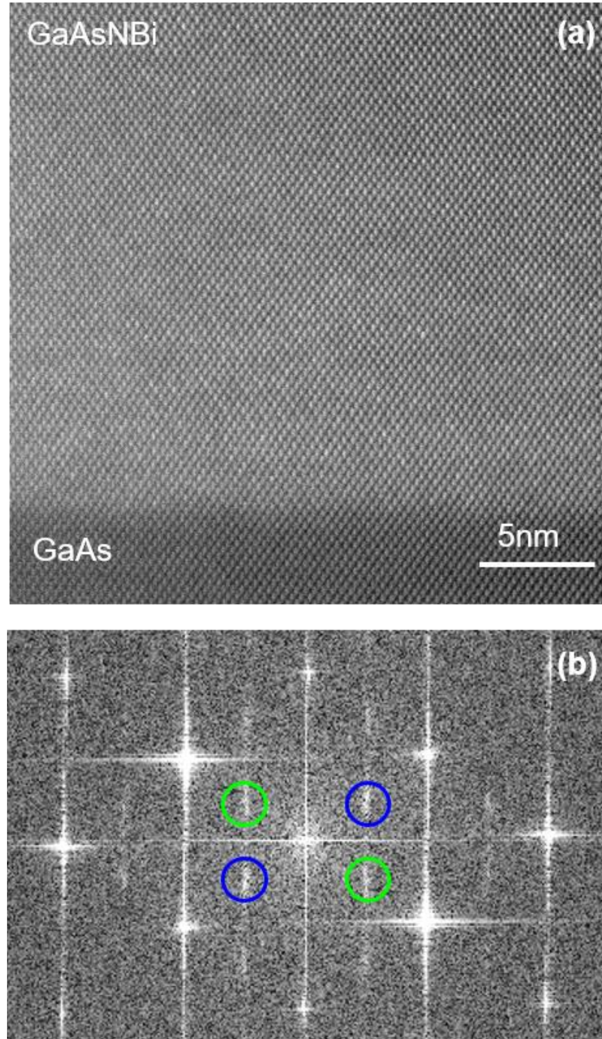

Figure F.1 High-resolution scanning transmission electron micrograph, collected near an interface between GaAs and ordered GaAsNBi. (b) Fast Fourier transform (FFT) of the image in (a), showing spots corresponding to the zincblende lattice and those at the ½$(1\bar{1}1)$ and ½$(\bar{1}11)$ positions, indicating a doubling in periodicity in the $[1\bar{1}1]$ and $[\bar{1}11]$ directions. Green and blue circles indicate the ½$(1\bar{1}1)$ and ½$(\bar{1}11)$ spots, respectively.

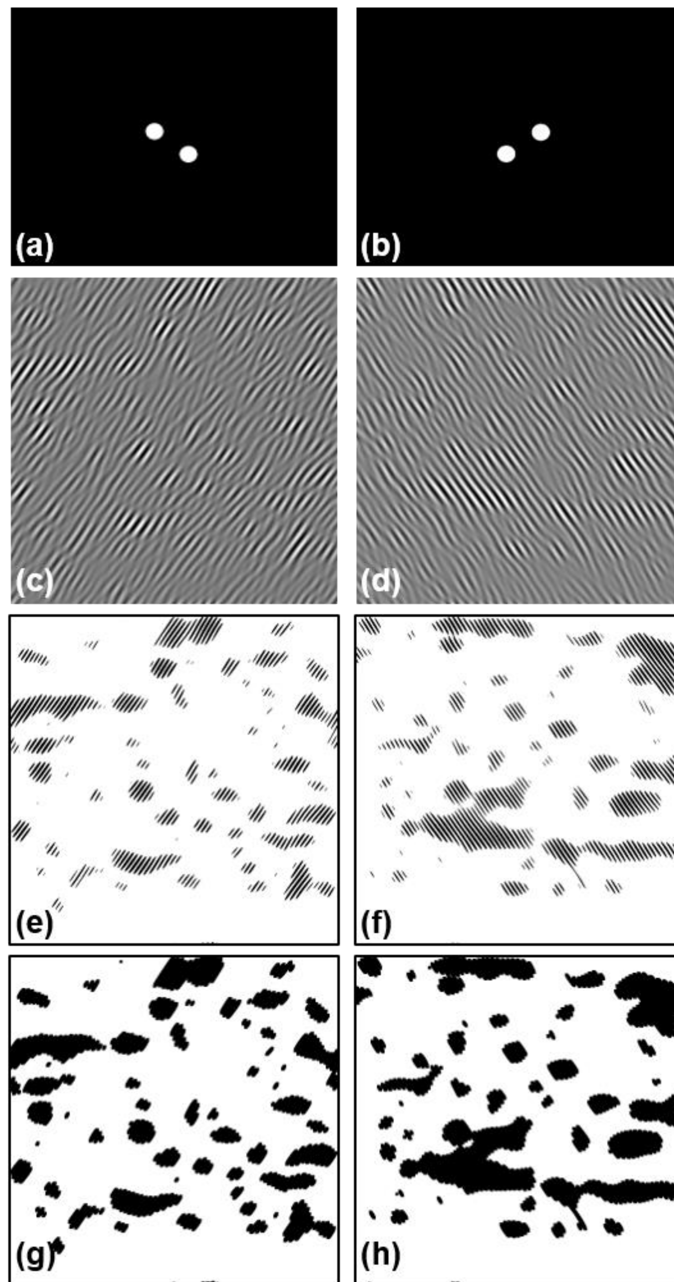

Figure F.2 Conjugate pairs of (a) ½($\bar{1}11$) and (b) ½($1\bar{1}1$) spots in the FFT following application of the twin-oval masks. [(c), (d)] Fourier-filtered images produced by applying an inverse FFT to the conjugate pairs of spots in (a) and (b). [(e), (f)] Thresholded images produced by selecting pixels from the top (18 ± 6%) and bottom (18 ± 7%) of the total grayscale range. [(g), (h)] Images of ordered domains after applying the dilation function to the images in (e) and (f).

Appendix G

Capacitance-Voltage Carrier Concentration Profiling

In this appendix we describe the method used to calculate the depth profile of the free carrier concentration from capacitance-voltage (C-V) measurements of Schottky diodes in Section 7.2.2. Following C-V measurements performed as described in Section 2.5, the carrier concentration, $\hat{n}$, at a depth x from the Schottky contact was calculated using the depletion approximation:[1]

$$x = \frac{K_s \varepsilon_0 A}{C} \tag{G.1}$$

$$\hat{n}(x) = -\frac{2}{q K_s \varepsilon_0 A^2 d(1/C^2)/dV} \tag{G.2}$$

where K_s is the GaAs dielectric constant, ε_0 the permittivity of free space, A the contact area, q the elementary charge, C the measured capacitance, and V the applied DC bias. The depletion approximation assumes that the depletion region of the Schottky junction has well-defined boundaries, with majority carriers fully depleted within the depletion region and neutral charge density outside the depletion region.[1,2]

[1] D.K. Schroder, *Semiconductor Material and Device Characterization* (John Wiley & Sons, 2006) p.65-71.

[2] W.C. Johnson and P.T. Panousis, "The Influence of Debye Length on the C-V Measurement of Doping Profiles", IEEE T. Electron Dev. 18, 965 (1971).

Appendix H

Tabulated Data

H.1 Overview

In this appendix, we provide tabulated data for samples discussed in this dissertation. Table H.1 lists GaAs(Bi) samples grown on the C21 MBE system and discussed in Ch. 3. Table H.2 lists GaAs(N)(Bi) samples grown on the Gen II MBE system and discussed in Ch. 4, 5, and 6. Table H.3 lists the Si cell temperatures and free carrier concentrations for samples used in the doping calibration in Appendix B, and Table H.4 lists the fitting parameters used in analysis of photoreflectance spectra in Ch. 6.

H.2 Growth parameters

Table H.1 Growth parameters for GaAs(Bi):(Si) films grown on the C21 MBE system, including growth rate, epilayer thickness, substrate temperature, As/Ga and Bi/As beam equivalent pressure (BEP) ratios, and silicon cell temperature.

	CMBE	Growth Rate (μm/hr)	Epilayer Thickness (nm)	Substrate Temperature (°C)	As_4 /Ga BEP Ratio	Bi/As_4 BEP Ratio	Si Cell Temperature (°C)
undoped	37	1.2	400	280	20.0	0	--
	30	1.2	400	280	20.0	0.022	--
	32	1.2	400	280	20.0	0.005	--
	33	1.2	400	280	20.0	0.010	--
	34	1.2	400	280	20.0	0.015	--
	36	1.2	400	280	20.0	0.029	--
n-type	45	1.2	400	280	20.0	0	1150
	46	1.2	400	280	20.0	0.005	1150
	65	1.2	400	280	15.0	0.007	1150
	93	0.45	400	280	10.0	0.020	1250
	92	0.28	400	280	10.0	0.020	1250
	62	1.2	400	280	15.0	0.013	1250
	47	1.2	400	280	20.0	0.015	1150
	48	1.2	400	280	20.0	0.030	1150
p-type	66	1.2	400	280	10.0	0	1250
	67	1.2	400	280	10.0	0.010	1250
	64	1.2	400	280	10.0	0.010	1150
	63	1.2	400	280	6.0	0.017	1150
	85	1.45	400	280	10.0	0.020	1250
	84	2.2	400	280	10.0	0.020	1250
	86	1.45	400	280	10.0	0.020	1250
	61	1.2	400	280	10.0	0.020	1250
	60	1.2	400	280	6.0	0.033	1250
	68	1.2	400	280	10.0	0.030	1250

Table H.2 Growth parameters for GaAs(N)(Bi) films grown on the Gen II MBE system, including growth rate, epilayer thickness, substrate temperature, As/Ga and Bi/As beam equivalent pressure (BEP) ratios, and nitrogen flow rate.

	RMBE	Growth Rate (μm/hr)	Epilayer Thickness (nm)	Substrate Temperature (°C)	As_4/Ga BEP Ratio	Bi/As_4 BEP Ratio	N Flow Rate (sccm)
Ch. 4, 6 N Flux Series	1286	1	100	341	20	0.005	0
	1293	1	100	357	20	0.005	0.17
	1294	1	100	351	20	0.005	0.25
	1295	1	100	339	20	0.005	0.35
Ch. 4, 6 Bi Flux Series	1296	1	100	336	20	0.005	0.25
	1285	1	100	340	20	0.002	0.25
	1284	1	100	365	20	0.005	0.25
	1283	1	100	357	20	0.009	0.25
Ch. 5 Temperature Series	1354	1	400	380	21	0.007	0.25
		1	400	340	21	0.007	0.25
		1	400	300	21	0.007	0.25
		1	400	260	21	0.007	0.25
Ch. 5 Bi Flux Series	1244	1	500	409	17	0	0.25
	1368	1	400	380	21	0.001	0.25
	1367	1	400	380	21	0.001	0.25
	1366	1	400	380	21	0.005	0.25
	1353	1	400	380	21	0.007	0.25
	1369	1	400	380	21	0.015	0.25

H.3 Doping calibration data

Table H.3 Si cell temperatures, *T*, and free carrier concentrations, *n*, of GaAs:Si films used in the Si doping calibration.

CMBE	Si Temperature, *T* (°C)	Free carrier concentration, *n*, (cm^{-3})
2	1050	1.16×10^{17}
3	1150	1.26×10^{18}
4	1250	6.84×10^{18}

H.4 Photoreflectance data

Table H.4 Parameters used to fit photoreflectance spectra with two resonances according to the Aspnes formula,[1] $\frac{dR}{R}(E) = \mathrm{Re}\left[Ce^{i\vartheta}(E - E_0 + i\Gamma)^{-m}\right]$, as well as the goodness of fit, R^2. Samples RMBE 1368, 1367, and 1366 were fit with a single resonance.

	Lower Energy Resonance				Higher Energy Resonance				
RMBE	C	ϑ	E_0 (eV)	Γ	C	ϑ	E_0 (eV)	Γ	R^2
1295	-1.01E-08	37.24	1.00	0.070	-1.69E-09	1.04	1.04	0.063	0.960
1294	4.75E-09	-16.43	1.05	0.061	-2.12E-09	1.74	1.12	0.061	0.902
1293	6.16E-09	3.37	1.14	0.040	5.95E-09	3.43	1.18	0.049	0.996
1286	9.89E-09	53.17	1.25	0.061	8.40E-09	-109.87	1.30	0.048	0.990
1283	-3.09E-09	-0.82	0.87	0.040	-1.10E-09	0.40	0.95	0.041	0.921
1284	5.85E-09	27.57	1.03	0.058	-3.00E-09	7.84	1.10	0.066	0.855
1285	-2.82E-09	144.50	1.18	0.040	-1.76E-10	-4.00	1.20	0.040	0.947
1296	-1.87E-08	0.63	1.35	0.052	-9.17E-10	-1.55	1.38	0.029	0.981
1354	2.05E-06	2.31	0.89	0.070	1.24E-06	3.11	0.95	0.083	0.990
1368	-8.55E-09	-7.01	1.30	0.031	-	-	-	-	0.769
1367	2.30E-09	1.47	1.30	0.016	-	-	-	-	0.809
1366	-5.09E-07	-2.09	1.12	0.062	-	-	-	-	0.970
1353	4.27E-06	2.10	0.95	0.119	-1.51E-07	7.68	1.02	0.050	0.979

H.5 References

[1] D.E. Aspnes, “Third-Derivative Modulation Spectroscopy with Low-Field Electroreflectance”, Surf. Sci. 37, 418 (1973).

Appendix I

Materials Parameters

This appendix lists various materials parameters used in this dissertation. Table I.1 contains parameters for GaAs, GaN, and GaBi used in calculations of bandgaps and lattice parameters of GaAs(N)(Bi) alloys. Table I.2 contains additional materials parameters for GaAs, including Varshni parameters used for estimation of the temperature-dependence of the bandgap in Section 6.7, as well as relative permittivity and built-in potentials used for depletion correction calculations in Appendix C.

Table I.1 Lattice parameters, *a,* bandgaps, E_g, and Poisson ratios, *v*, for GaAs, zincblende GaN, and GaBi (predicted).

	a (Å)	E_g, 0 K (eV)	*v*
GaAs	5.653 [1]	1.52 [1]	0.31 [1,2]
GaN	4.50 [3]	3.30 [3]	0.34 [3]
GaBi	-1.45 [4]	-1.45 [4]	0.31 [5]

Table I.2 Additional materials parameters for GaAs, including Varshni parameters,[6] α and β, relative permittivity, ε_r, surface built-in potential, V_{BS}, and interface built-in potential, V_{BI}.

	GaAs
α (meV/K)	5.41×10^{-4} [1]
β (K)	204 [1]
ε_r	13.1 [7]
V_{BS} (V)	0.6 [8]
V_{BI} (V)	0.6 [8]

[1] I. Vurgaftman, J.R. Meyer, and L.R. Ram-Mohan, “Band Parameters for III–V Compound Semiconductors and Their Alloys”, J. Appl. Phys. 89, 5815 (2001).

[2] M. Krieger, H. Sigg, N. Herres, K. Bachem, and K. Köhler, “Elastic Constants and Poisson Ratio in the System AlAs–GaAs”, Appl. Phys. Lett. 66, 682 (1995).

[3] I. Vurgaftman and J.R. Meyer, “Band Parameters for Nitrogen-Containing Semiconductors”, J. Appl. Phys. 94, 3675 (2003).

[4] A. Janotti, S.-H. Wei, and S.B. Zhang, “Theoretical Study of the Effects of Isovalent Coalloying of Bi and N in GaAs”, Phys. Rev. B 65, 115203 (2002).

[5] S.Q. Wang and H.Q. Ye, “First-Principles Study on Elastic Properties and Phase Stability of III–V Compounds”, Phys. Status Solidi B 240, 45 (2003).

[6] Y.P. Varshni, “Temperature Dependence of the Energy Gap in Semiconductors”, Physica 34, 149 (1967).

[7] S. Adachi, “GaAs, AlAs, and $Al_xGa_{1-x}As$: Material Parameters for Use in Research and Device Applications”, J. Appl. Phys. 58, R1 (1985).

[8] A. Chandra, C.E.C. Wood, D.W. Woodard, and L.F. Eastman, “Surface and Interface Depletion Corrections to Free Carrier-Density Determinations by Hall Measurements”, Solid-State Electron. 22, 645 (1979).